Thermal Convection

Differential heating, travelling thermal waves and turbulent superstructures

Philipp Reiter

Thermal Convection

Differential heating, travelling thermal waves and turbulent superstructures

Dissertation

for the award of the degree
"Doctor rerum naturalium"
Division of Mathematics and Natural Sciences
at the Georg-August-Universität Göttingen
within the doctoral degree program

Physics of Biological and Complex Systems
of the Göttingen Graduate School of Neurosciences, Biophysics,
and Molecular Biosciences (GGNB)
of the Georg-August University School of Sciences (GAUSS)

submitted by

Philipp Reiter
from Ustersbach, Germany
Göttingen, 29.12.2021

Abstract

Turbulent thermal convection is ubiquitous in geophysical, astrophysical, and industrial applications. In the present work, various phenomena in the convective paradigm systems of horizontal convection and Rayleigh-Bénard convection are studied, with emphasis on the influence of thermal boundary conditions, scaling laws of heat transport and characterization of large-scale flow structures. The problems are studied theoretically and by means of direct numerical methods.

In chapter 2, the main computational methods are presented with focus on the implementation details of computational codes and numerical solvers for linear stability analysis. A finite-volume code for direct numerical simulations has been improved towards massively parallel simulations and a parallel pseudospectral code has been developed and tested.

In chapter 3, horizontal convection is investigated for various Rayleigh numbers Ra and Prandtl numbers Pr. Several Nusselt number Nu vs. Ra scaling transitions are identified, validating the theoretical scaling model (Shishkina *et al.*, 2016). Examining the global flow structures, we show that the onset of time dependence in horizontal convection is triggered either by oscillations (smaller Pr) or by detaching plumes (larger Pr). We analyze their dependence on Ra and Pr, which is consistent with dimensional-analysis based estimates of their onset.

In chapter 4, the formation of mean zonal flows in convective systems with traveling thermal waves is explored. Excellent agreement of the dependence of zonal flow strength on thermal wave propagation speed between the theoretical model and the fully nonlinear simulations is found for small Ra, while for larger Ra it is overestimated by the model due to nonlinear effects. An important result of this chapter is the reversal of zonal flows from purely retrograde for small Ra to predominantly prograde for large Ra. Stability analysis of convection rolls indicates that the tilted cell instability may play a key role in the formation of zonal flows in convection-dominated flows, even in the presence of traveling thermal waves.

In chapter 5 we study different thermal sidewall boundary conditions in Rayleigh–Bénard convection from the onset of convection to the turbulent regime, with the main goal of mimicking imperfectly adiabatic sidewalls in experiments. Linear sidewall temperatures lead to a premature collapse of the single roll state, while constant sidewall temperatures lead to enhanced single roll stability. Enlargement of corner rolls is identified as the main collapse mechanism, and two distinct corner roll growth rate regimes are obtained. In the intermediate Ra range, vertically stacked double rolls (or double toroidal structures in cylindrical systems) are shown to predominate for linear and adiabatic sidewalls. The different flow structures leave their imprint on the global heat transport, however, at larger Ra heat transport and flow dynamics become increasingly alike for different sidewall boundary conditions, indicating a low sensitivity of very large Ra experiments with respect to spurious sidewall heat fluxes.

In chapter 6 we address the strong spatial inhomogeneity of Rayleigh–Bénard convection arising from the presence of turbulent superstructures by decomposing the flow into large-scale plume ejecting and impacting zones. Using a conditional averaging algorithm based on pattern matching, we show the existence of a crossover in the wall heat transport from impacting-dominated to ejecting-dominated at $Ra \approx 3 \times 10^{11}$ in a two-dimensional laterally periodic configuration with $Pr = 1$ and $\Gamma = 2$. The heat transport increase in the ejecting region arises from the development of a turbulent mixing zone due to the emission of thermal plumes. This mixing

zone reaches its peak heat transport efficiency at about five thermal boundary layer thicknesses and expands vertically and laterally with increasing Ra, becoming more dominant for the total heat transfer.

Contents

Contents

1 Introduction

1.1 Natural convection

Thermal convection is of utmost importance to meteorology, geophysics, astrophysics, industrial processes. It appears in planetary and stellar interiors (Spiegel, 1971; Busse *et al.*, 1998; Hansen *et al.*, 2004), in the Earth's mantle (Getling, 1998; Schubert *et al.*, 2001) and it manages the Earth on a global scale: clouds regulate the temperature through their impact on the energy cycle (Emanuel, 1994) and large-scale ocean circulations retrieve nutrient rich water from the deep sea to the surface (Marshall & Schott, 1999) and act as the largest sink of anthropogenic carbon dioxide (DeVries *et al.*, 2017). Convection is not only deeply rooted in the fundamentals of life, its study is also captivating. Volcanic eruptions reveal some of the most magnificent structures one can witness: from the gigantic umbrella-shaped cloud that raises up tens of kilometres into the sky (Textor *et al.*, 2006) down to the very small turbulent eddies with microscales as small as a hundreds of micrometers. As fluid dynamicists our goal is to shine light on the choreography of these phenomena. We look for patterns, categorize structures and try to distill universal laws from the intrinsic randomness of turbulence. All of which emerges from three seemingly simple laws: the conservation of mass, momentum and energy. This endeavour has rewarded us with remarkable discoveries whose impact exceeds the boundaries of fluid mechanics through its generality. However, many riddles remain. And our understanding of these processes is vital. Without a firm grasp we will fail to recognize the implications of our behavior on nature or to make adequate long-term predictions about the evolution of the climate.

Before we dive into the specific problems that are addressed within this thesis, let us first elucidate on the notion of convection in general. Natural convection refers to a type of flow that is driven by density variations. On Earth, the most common variants of convection are temperature and salinity induced. The equatorial girdling wind belts, i.e. the Hadley cells, are a textbook example. The Hadley cells emanate from the intensely heated equatorial region, which causes warm air to rise, then move poleward and sink at about 30° north/south latitude to flow back to the equator. This tropical atmospheric circulation yields important climatic effects, including the generation of different precipitation zones and the redistribution of thermal energy in the atmosphere. The discovery of the north-south winds of the Hadley cells is deeply intertwined with another associated phenomenon, namely the east-to-west prevailing trade winds, as the next example demonstrates. On his voyage to the New World, Columbus found that once they sailed south of 30° north latitude, the variable European winds ceased and were replaced by steadier easterly winds that greatly aided their westward journey (Emanuel, 2005). Seeking for an explanation, the English physicist Edmond Halley attributed the winds to the diurnal cycle of solar heating as a consequence of the Earth's rotation about its axis (Halley, 1687). Although there is some validity to Halley's theory, as we will discuss in section 1.3, today we know that the effect from the diurnal cycle is far too weak to produce

(a) (b) (c)

Conductive   Laminar   Turbulent
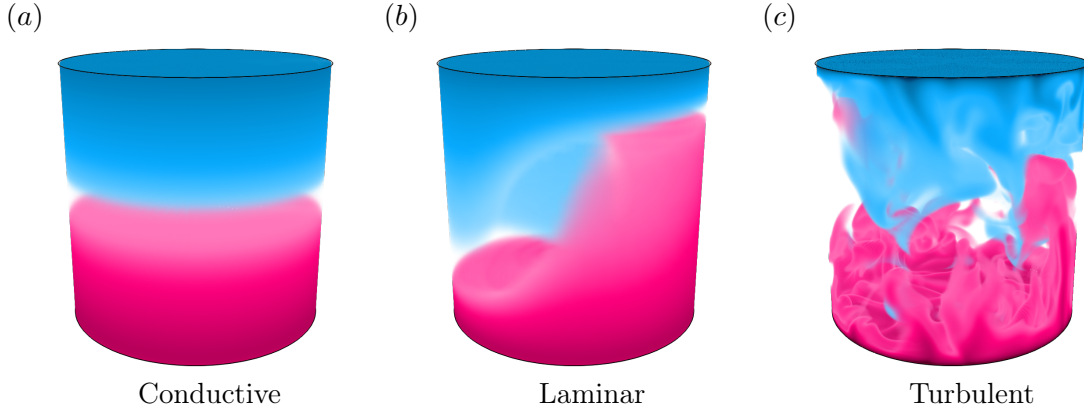
Figure 1.1: Flow phenomenology of Rayleigh–Bénard convection in a cylindrical cell. Shown is the volume rendered temperature field of numerical simulations at different Rayleigh numbers.

the excessive easterly winds that blow with 5-10 metres per second. The correct mechanism was found later by George Hadley (1735). Hadley devised the existence of the aforementioned equatorial wind belts, i.e. the Hadley cells, and conjectured that their equatorial blowing winds must be redirected by the Coriolis force, thus producing the prevailing easterly winds that Columbus experienced.

While these examples illustrate the rich history of the studies of natural convection, the corner stone of contemporary science on convection was laid by the foundational experiments of Henry Bénard (1900) and the theoretical work of Lord Rayleigh (1916) who first demonstrated the onset of thermal instability in a fluid (Chandrasekhar, 1961). The following description leans on the work of Rayleigh; Bénard originally used a slightly different experimental setup[1], but obtained qualitatively similar results. Consider a thin layer of liquid, e.g., water, subjected to a vertical temperature gradient by heating the lower surface to a temperature $T_u + \Delta$ and maintaining the upper surface at a temperature T_u. If the temperature difference Δ is sufficiently small (or negative), the fluid is at rest and heat is transported solely by conduction, i.e. molecular transport. This scenario is illustrated in figure 1.1 (a). However, if the temperature difference Δ surpasses a critical value, the buoyancy force eventually overcomes the adverse viscous forces, the system becomes convectively unstable and convection cells appear (figure 1.1 b). In fact, Lord Rayleigh (1916) has theoretically shown that convection would occur if the quantity

$$Ra \equiv \frac{\alpha g \Delta H^3}{\nu \kappa}, \tag{1.1}$$

now called the Rayleigh number, exceeds a critical value. Here g is the gravitational acceleration, H the layer height, α the volume expansion coefficient, ν the kinematic viscosity and κ the thermal diffusivity. In honor to Bénard and Rayleigh, this convection type is now known as Rayleigh–Bénard convection (RBC) (Siggia, 1994; Bodenschatz *et al.*, 2000; Ahlers *et al.*, 2009b; Lohse & Xia, 2010; Manneville, 2006).

Astonishingly, the critical Rayleigh number above which convection sets is inde-

---

[1]Bénard (1900) studied convection in a liquid layer with a free upper surface in contact with air, where effects of surface tension come into play (Bénard-Marangoni convection).

pendent of the type of liquid or gas, characterized by the Prandtl number $Pr \equiv \nu/\kappa$, and only depends on the boundary conditions (see chapter 5) and the aspect ratio $\Gamma \equiv L/H$ of the setup (Shishkina, 2021). The convection rolls initially grow exponentially until they reach saturatation due to non-linear interactions. The newly formed steady convection cells exhibit a wide variety of different patterns, such as ideal straight rolls, hexagons (Bénard, 1900) or spirals (Morris *et al.*, 1993; Bodenschatz *et al.*, 2000). Although these cells are initially stable, they will undergo further transitions on their way to chaos. Great progress has been made in this area by analyzing the stability of the ideal straight roll solution. This effort culminated in the "Busse Baloon", a representation of the stability boundaries in the Ra - Pr - α parameter space (Busse, 1978), where α denotes a wavenumber. It was found that secondary instabilities, apart from the onset of convection, depend strongly on the Prandtl number. Non-oscillatory instabilities occur predominantly for large Pr fluids (Busse, 1967; Busse & Whitehead, 1971; Busse, 1978), while fluids with low Pr such as gases or liquid metals show oscillatory instabilities (Clever & Busse, 1974).

RBC is also predestined to study the route to chaos. In an attempt to understand the dynamical behavior of deterministic systems, Lorenz (1963) resorted to a low-dimensional representation of RBC derived by Saltzman (1962). He found that for certain parameters of his model the flow developed extremely irregularly and almost unexpectedly exhibited a strong dependence on the initial conditions, a phenomenon that coined the term "butterfly effect" in chaos theory, later immortalised by Hollywood. It reflects that small perturbations in the initial conditions can have an immense impact on the long-term evolution of a system. Lorenz's work became one of the most influential studies on complex systems to date, initiating many of the modern approaches in dynamical system theory.

Thanks to the advent of better technologies, we are today able to delve deeper into the highly turbulent nature of high Ra convection. This is in so far significant as this is the regime where we will acquire the most lasting insights into geophysical and astrophysical systems, which act on scales that currently far surpass our experimental or numerical capabilities. Two of the most daunting questions in this realm, the characterization of turbulent superstructures and the existence of an ultimate regime, are discussed more thoroughly in section 1.4 and in the chapters 5 and 6.

In a nutshell, we have come from the onset of thermal instability in the early 20th century, through pattern formation and secondary instabilities in the second half of the 20th century, to highly turbulent systems in modern times. The multitude of phenomena behind a simple system like RBC accentuates that complexity is inherent in the equations of fluid dynamics themselves. This explains why we can still learn much about the nature of convection by studying its paradigm systems. In the following, we will introduce more thoroughly the main topics of this thesis and give a brief guideline.

1.2 Horizontal convection

Rayleigh–Bénard convection may be the most thoroughly studied system of convection, but it does not always constitute the best representation for a particular practical scenario. Before discussing this in the context of oceanic circulation, let us first consider an alternate example, namely the atmospheric boundary layer (Kaimal *et al.*, 1976). The atmospheric boundary layer is the lowest part of the atmosphere that is in contact with the Earth's surface and above which lies the free atmosphere.
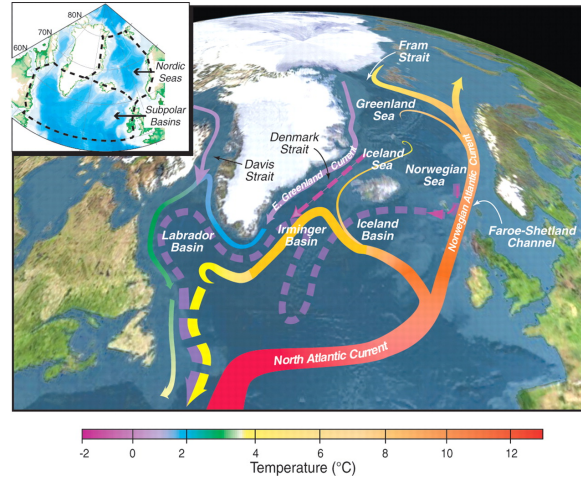
Figure 1.2: Schematic map of the Atlantic meridional overturning circulation in the Nordic Seas with surface currents (solid) and deep currents (dashed). Color represents the water temperature. Source: Curry & Mauritzen (2005).

The lower surface temperature can be well approximated by RBC boundary conditions, using a constant flux instead of a constant temperature. In contrast, the upper free atmospheric surface of the convective boundary layer deviates from the ideal setup and studies have shown that the cooled upper condition of RBC leads to substantially different large-scale structures compared to the convective boundary layer, while a modified system with adiabatic upper conditions, i.e., preventing heat from escaping through the top, exhibits a much better resemblance of statistical properties (Fodor *et al.*, 2019).

A similar reasoning applies to the oceanic basin and the meridional overturning circulation. On top, however, the large spatial extent of the problem additionally refutes the assumption that the temperature is uniformly distributed over the heated area (see figure 1.2). A more suitable model was proposed by Stommel (1962) and experimentally investigated by Rossby (1965). It arose from the dissatisfaction that contemporary ocean models often showed nearly equal sizes of sinking and rising regions, while "substantially all the deep and bottom water in the world ocean, or more than half of all the ocean's mass, comes from two tiny areas - off Greenland, and in the Weddell Sea" (Stommel, 1962). Horizontal convection (HC) accounts for the main thermal characteristics of the ocean, i.e., it is heated non-uniformly along a horizontal surface, mimicking the heating and cooling of the ocean surface that is in contact with the atmosphere, while all other boundaries are kept adiabatic. In this system, all heat enters and leaves through one surface and at equilibrium there is no net vertical heat transport. The asymmetry between sinking and rising regions arises naturally from the relative heat transport efficiencies of convection and conduction. Essentially, the ocean is effectively cooled by convection and inefficiently heated predominantly by conduction, so that downwelling in the North Atlantic occurs over a much smaller area than upwelling in the rest of the ocean.

HC has since been subject to numerous experimental (Stern, 1960; Mullarney *et al.*, 2004; Wang & Huang, 2005) and numerical studies (Beardsley & Festa, 1972; Rossby, 1998; Paparella & Young, 2002; Mullarney *et al.*, 2004; Gayen *et al.*, 2014; Shishkina

& Wagner, 2016; Passaggia *et al.*, 2017; Ramme & Hansen, 2019; Reiter & Shishkina, 2020). It has been studied in combination with other driving mechanism, e.g. rotation (Hignett *et al.*, 1981; Barkan *et al.*, 2013; Gayen & Griffiths, 2022), wind driven through shear stresses (Hazewinkel *et al.*, 2012), tidal forces (Ding *et al.*, 2022) and driven by salinity (Pierce & Rhines, 1996). Wind driven forcing is generally the most dynamic in the ocean (Rahmstorf, 2003). Lunar tidal forces and bottom topography can have a profound impact on the vertical mixing of the ocean, i.e. mixing of dense deep water with lighter surface water (Wunsch, 2000). And thermally and salinity driven currents sustain the global-scale meridional overturning circulation. The studies in this thesis focus on thermally induced effects.

It is somewhat interesting to note that HC has always been surrounded by controversies. The first controversy originates from the studies of Sandstrom (1908) who conjectured, based on his experimental observations and on thermodynamical analogies, that a heating and cooling on the same surface, i.e. on the same geo-potential height, will not be able to sustain a thermally driven circulation. This theory almost impeded the acceptance of HC to be of oceanographic significance, but has since been debunked many times (Jeffreys, 1925; Rossby, 1965; Hughes & Griffiths, 2008; Coman *et al.*, 2006) and can be securely relegated to the stack of misconceptions. Another controversy that has been raised by Paparella & Young (2002) is that HC is not truly turbulent, since it violates the "zeroth" law of turbulence[2] (Frisch, 1995). This statement however is rather elusive. The problem lies within the leeway of the definition of turbulence itself. Scotti & White (2011) suggests that the "zeroth" law is too restrictive as a definition of turbulence, since even RBC - one of the models of turbulence in general - defies this definition. Nevertheless, Paparella's simulations and numerous other works (Mullarney *et al.*, 2004; Sheard & King, 2011; Gayen *et al.*, 2014; Shishkina *et al.*, 2016; Passaggia *et al.*, 2017; Reiter & Shishkina, 2020) show irrefutable signs of local turbulence, starting in the vicinity of the thermally unstable part of the cell and extending further inside the bulk as Ra is increased.

Though HC has gained popularity within the last two decades, the number of reliable numerical simulations covering a large range of parameters is still scarce. More clarity is needed on the scaling of heat and momentum transport and the existence of different scaling regimes. Rossby (1965) found that the global heat transport, expressed by the dimensionless Nusselt number Nu, universally scales as $Nu \sim Ra^{1/5}$, independent of Pr, if the flow is laminar and determined by the boundary layers. More regimes in $Ra - Pr$ space arise, by considering a more elaborated analysis based on the dissipation of kinetic energy and thermal variance (Shishkina *et al.*, 2016), leading to larger heat transport scalings at high Ra and a general Pr dependence, which is consistent with the results obtained by numerical simulations (Shishkina & Wagner, 2016; Ramme & Hansen, 2019; Reiter & Shishkina, 2020). Further, a more thorough understanding concerning the flow structures of HC is desirable, in particular the onset to a time-dependent flow and its parameter dependence. This will be discussed in chapter 3, based on the work Reiter & Shishkina (2020).

1.3 Travelling thermal waves

In the geo- or astrophysical context, zonal flows signify prevailing easterly or westerly winds that twine around planets and stars. Some of the most remarkable zonal

---

[2]The zeroth law states that the mean turbulent kinetic energy dissipation ε should be finite and independent of the kinematic viscosity ν, if $\nu \to 0$ and other parameters are fixed.

(a)   (b)
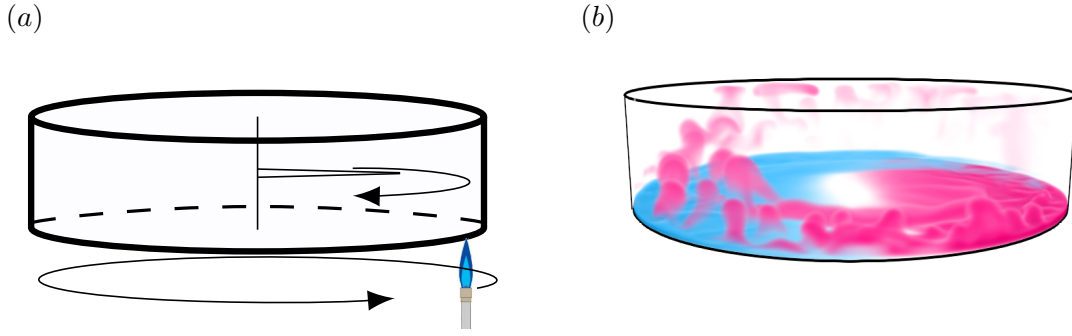
Figure 1.3: (a) Setup of the original moving flame problem. The flame rotates an-
ticlockwise with a constant frequency. This generates a counter-rotating
mean zonal flow in the center, in clockwise direction. (b) Current numer-
ical simulations, showing the temperature field.

structures are evident on the gas giants in our solar system, which consist of multiple
alternating bands of zonal winds flowing in different directions. Although these
structures have attracted much interest and research, much about them remains a
mystery (Kong *et al.*, 2018). Zonal flows are generated either by the Coriolis force of
a thermally driven meridional flow, as we have seen in the case of the trade winds,
or they are produced by Reynolds stresses, i.e., the nonlinear transport of zonal
momentum by radial or vertical flows (Pedlosky, 1987). These (deviatoric) Reynolds
stress components generally arise from symmetry breaking. It is known, for instance,
that in a compressible fluid the expansion of rising fluid and the contraction of sinking
fluid, i.e., a broken vertical symmetry, can induce differential rotation on planets,
as shown by Glatzmaier & Gilman (1982), which would otherwise not occur in an
incompressible medium.

In chapter 4 of this thesis, we demonstrate the generation of zonal flows by travel-
ing thermal waves (Reiter *et al.*, 2021c), another mechanism of symmetry breaking.
This topic arose after Halley (1687) incorrectly attributed the easterly trade winds
to the daily rotation of the Earth, whereupon Thomson (1892) alluded in a footnote
that it would be of great interest to investigate this mechanism by rotating a spirit
flame under a cylinder filled with gas or liquid (see figure 1.3). Fultz *et al.* (1959)
took up this appeal and surprisingly found that the fluid in the cylinder acquired
a mean rotation opposite to the rotation of the flame - somewhat reconciling for
Halley's hypothesis. And although it is unlikely that this mechanism is essential for
the prevailing east-west winds on Earth, the subject attracted attention when Schu-
bert & Whitehead (1969) suggested that it might be important for the atmospheric
superrotation of Venus; a phenomenon in which the planet's atmosphere spins much
faster than the planet itself. (Recent studies by Horinouchi *et al.* (2020) indicate that
the angular momentum necessary for superrotation could be generated by thermal
tidal waves driven by temperature differences between the day and night sides of
Venus and favored by the overall slow rotation of Venus about its axis. In this case,
then, it is a standing wave rather than a traveling wave problem.[3] Nevertheless,
the exact mechanism is still under investigation, including the nature of the relevant
hydrodynamic instabilities. On tidally generated zonal winds, see also the studies

---

[3]The author is aware that the discussion of the superrotation of Venus remains superficial at this
point. This area is not the author's field of expertise and serves primarily to open up to the
reader an area of research that may be unfamiliar to him.

Tilgner (2007) and Morize *et al.* (2010).)

The appeal of the moving flame or traveling thermal wave problem also lies in its simplicity and analytical tractability. Stern (1959) has shown that a mean counter-directed zonal flow is sustained by the presence of Reynolds stresses. To aid understanding, let us attempt a qualitative explanation for the occurrence of counter-directed (retrograde) zonal flows from travelling thermal waves; for simplicity, in a two-dimensional box. Imagine two symmetrical convection cells induced by an initially stationary flame located underneath the system. Let us now assume that the flame starts to move, e.g. to the right, where it heats one of the convection cells more than the other. This lifts up the streamline at the bottom that is directed towards the flame, i.e. against the flame motion, causing a correlation, i.e. a Reynolds stress, between the upward transport (raising of the streamline) and the horizontal transport against the flame motion, which sustains a mean retrograde zonal flow. Davey (1967) showed analytically that the zonal flow strength increases linearly with the speed of the travelling wave for slow waves, but decreases rapidly with the speed of the travelling wave for fast waves. Busse (1972), Whitehead (1972), Young *et al.* (1972) and Hinch & Schubert (1971) further elaborated Davey's analysis and found, for example, that weakly nonlinear effects occurring at larger temperature amplitudes (hotter spirit flame) likely inhibit the zonal flow strength.

What we have omitted so far is that even classical Rayleigh–Bénard exhibits zonal flows in the form of a mean shear flow (Goluskin, 2013; Wang *et al.*, 2020*a*; Winchester *et al.*, 2021) in periodic domains without an imposed thermal wave. This is caused by the tilted cell instability. When convection rolls are tilted initially by a small amount, they can generate a mean shear flow, which in turn enhances their tilt (Busse, 1983; Hartlep *et al.*, 2005). This positive feedback loop continues until saturation. Thompson (1970) argued that the moving flame, in the travelling wave problem, is only relevant at the beginning of the process to initiate an initial shear flow, after which the tilted cell instability takes over. In chapter 4 we discuss both mechanisms of zonal flow generation. We provide evidence for the mechanism described by Stern (1959) and Davey (1967), but show that the tilted the cell instability could play a role in larger Ra regimes. In this context, we discuss the prevalence of counter-rotating zonal flows for small thermal wave amplitudes, as well as the emergence of prograde zonal flows, i.e., waves travelling in the same direction as the thermal wave, for larger thermal wave amplitudes (Reiter *et al.*, 2021*c*).

1.4 Turbulent convection

Turbulence is the most common state of convection in nature. It arises when Ra becomes large enough, for example at about $Ra > 10^7$ for $Pr \approx 1$ in RBC (Castaing *et al.*, 1989), however, many geo- and astrophysical systems operate on scales up to $Ra \gtrsim 10^{20}$ (Sreenivasan & Donnelly, 2001). Figure 1.4 gives an impression of an exemplary flow at $Ra = 10^9$, which is already strongly turbulent, but still far below natural conditions of astro- and geophysical systems. The wall-bounded flow in this regime consists of small-scale turbulent eddies, large-scale structures and boundary layers.

A central debate in convection revolves around the state of the boundary layers. It is anticipated that the laminar boundary layers associated with the large-scale structures will be destabilized by shear instabilities for sufficiently large Ra. On this basis, Kraichnan (1962) postulated that the emerging small-scale turbulence at this
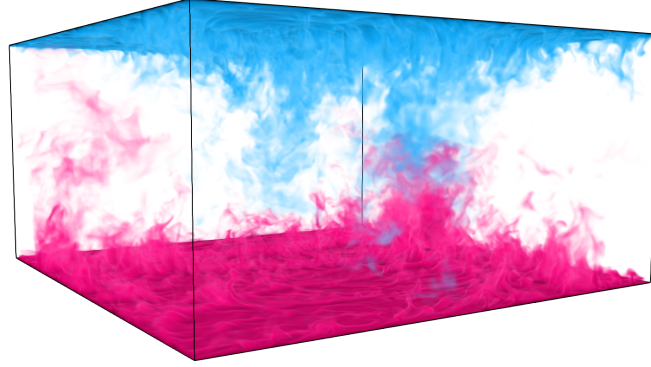
Figure 1.4: Temperature field of highly turbulent three-dimensional turbulent Rayleigh–Bénard convection with periodic sidewalls ($Ra = 10^9$, $Pr = 0.71$, $\Gamma = 2$).

point affects the local heat transport to such an extend that the asymptotic heat transport scaling increases up to $Nu \sim Ra^{1/2}$ (up to logarithmic corrections), i.e., the "ultimate" scaling regime[4]. Laminar boundary layers, on the other hand, imply the "classical" scaling with a limited heat transport efficiency $Nu \sim Ra^{1/3}$ (Malkus, 1954). Thus, there is no universal scaling of Nu with Ra (Grossmann & Lohse, 2000, 2001, 2002; Stevens *et al.*, 2013). The occurrence of shear-induced instabilities depends largely on the Reynolds number, from which Grossmann & Lohse (2002) estimate the onset of the ultimate regime to be about $10^{14} \leq Ra \leq 10^{15}$ for $Pr = 1$ and $\Gamma = 1$.

Intensive research activities are now devoted to the study of the existence of the ultimate regime using experiments (Chavanne *et al.*, 1997; Niemela *et al.*, 2000; Chavanne *et al.*, 2001; Ahlers *et al.*, 2009a, 2012; He *et al.*, 2012b,a; Urban *et al.*, 2014; Roche, 2020), numerical simulations (He *et al.*, 2020; Zhu *et al.*, 2018a, 2019b; Stevens *et al.*, 2020), and upper bound analysis (Howard, 1963; Doering & Constantin, 1996; Kerswell, 2002; Whitehead & Doering, 2011; Wen *et al.*, 2015; Tilgner, 2019). However, experiments in this extremely high Ra regime are notoriously difficult and statistically reliable three dimensional numerical studies still too expensive. To complicate matters, the onset to the ultimate regime depends on the cell geometry (He *et al.*, 2020; Shishkina, 2021; Ahlers *et al.*, 2022) and upper bound studies suggest a profound difference between no-slip (Howard, 1963; Doering & Constantin, 1996; Kerswell, 2002) and free-slip horizontal walls (Whitehead & Doering, 2011; Wen *et al.*, 2015).

Thermal sidewall boundary conditions

Part of the exploration of the ultimate regime is to gain more confidence in experimental data. In chapter 5, we examine the effects of imperfectly insulated/adiabatic sidewalls in Rayleigh–Bénard vessels. Spurious heat flows at the sidewalls are a major

---

[4]By "ultimate" it is understood that there are no other different scaling regimes for $Ra \to \infty$.

difficulty in experiments, which can lead to significant overestimation of heat transport measurements and underestimation of Nusselt number scaling (Ahlers, 2000).

Previous studies have considered heat conduction effects in the solid sidewall, suggesting that global heat transport differences compared to the ideal setup in the low to mid Ra range are due to changes in global flow structures (Verzicco, 2002; Stevens *et al.*, 2014; Wan *et al.*, 2019), while higher Ra show lower sensitivity. This suggests that the sidewall temperature boundary layer has a progressively less controlling influence on the flow structures. However, for smaller Ra, different sidewalls yield remarkably different flow structures, such as double rolls and double-toroidal rolls, which are associated with a significant change in heat and momentum transport properties. In our work, we investigate the entire path from the onset of convection to turbulence using direct numerical simulations for different sidewalls and different Pr. Furthermore, we shed light on the importance of corner rolls for flow transitions in laterally bounded RBC by evaluating steady-state solutions of different flow states which reveal different corner roll growth regimes (Reiter *et al.*, 2021*b*).

Turbulent superstructures

Convection flows show a surprising predominance of large-scale order, so-called turbulent superstructures, even for very large Ra. These superstructures are reminiscent of patterns near the onset of convection and have been described in numerous studies (Hartlep *et al.*, 2003, 2005; Emran & Schumacher, 2015; Stevens *et al.*, 2018; Zhu *et al.*, 2018*a*; Pandey *et al.*, 2018). Their size has been shown to increase with respect to Ra (Krug *et al.*, 2020), which may originate from interactions with the small-scale turbulence causing enhanced turbulent diffusion (Ibbeken *et al.*, 2019).

An important implication of the presence of superstructures is that convection will persist to be highly spatially inhomogeneous. It can even be argued that boundary layers become turbulent earlier in some regions than in others (Zhu *et al.*, 2018*a*). In this case, it is instructive to decompose the flow into different regions. A good method is to distinguish between regions on the plates where the superstructure plumes detach (ejecting region) and regions where the plumes impinge on the other plate (impacting region). In two-dimensional RBC, Zhu *et al.* (2018*a*) obtains different scaling laws for the two regions, i.e., $Nu_{loc} \sim Ra^{0.28}$ in the plume impacting region and $Nu_{loc} \sim Ra^{0.38}$ in the plume ejecting region. Furthermore, Zhu *et al.* report that the total heat transport on the wall for large $Ra \geq 10^{11}$ is dominated by plume ejection. Contrarily, for Ra up to 10^9 and in three-dimensional RBC, Blass *et al.* (2021) demonstrate that the plume impacting regions contribute more to the overall heat transport than the ejecting regions. In chapter 6, we extend the parameter range of Zhu's two-dimensional analysis and present an improved conditional averaging method. Our analysis reconciles the two findings and reveals a crossover of impacting dominated to ejecting dominated heat transport (Reiter *et al.*, 2021*a*).

1.5 Thesis outline

The structure of this thesis is as follows. In chapter 2, the governing equations and computational methods are introduced along with implementation details. This is followed by four chapters presenting the main research studies based on published works.

Chapter 3 reports heat and momentum transport scaling and global flow structure

transitions in horizontal convection (Reiter & Shishkina, 2020). Chapter 4 examines the generation of mean zonal flows by traveling thermal waves in RBC, focusing on the dependence of zonal flow strength on thermal wave speed and the occurrence of the tilted cell instability (Reiter *et al.*, 2021*c*). Chapter 5 explores the emergence of different flow structures, the importance of corner rolls and the global heat transport in RBC with different thermal sidewall boundary conditions from the onset of convection to the turbulent regime (Reiter *et al.*, 2021*b*). Finally, chapter 6 addresses the role of plume impacting and plume ejecting regions in two-dimensional RBC on the heat transport up to very large Ra (Reiter *et al.*, 2021*a*).

The thesis concludes with a summary of the main findings together with an outlook on possible further research directions for each project.

2 Numerical methods

The scope of this section is to introduce the governing equations and present numerical methods for solving the underlying Navier–Stokes equations and the linear stability problem. Finite volume and spectral methods are discussed with a focus on practical implementation; details are left to the given literature references. Most tools developed as part of this work are publicly available and are linked throughout the following explanations.

2.1 Governing equations

The governing equations for an incompressible, viscous buoyancy-driven flow in the Oberbeck–Boussinessq approximation can be described by the conservation of mass, conservation of momentum and conservation of energy for the velocity $\mathbf{u}$, the temperature T and the pressure p:

$$\partial_t \mathbf{u} + \mathbf{u} \cdot \nabla \mathbf{u} + \nabla p = \nu \nabla^2 \mathbf{u} + \alpha g T \mathbf{e}_z, \tag{2.1a}$$

$$\partial_t T + \mathbf{u} \cdot \nabla T = \kappa \nabla^2 T, \tag{2.1b}$$

$$\nabla \cdot \mathbf{u} = 0, \tag{2.1c}$$

where $\mathbf{e}_z$ is the unit vector that points upwards. As explained in the introduction, these equations yield the three independent non-dimensional parameters, the Rayleigh number Ra, the Prandtl number Pr and the aspect ratio Γ:

$$Ra \equiv \frac{\alpha g \Delta H^3}{\nu \kappa}, \quad Pr \equiv \frac{\nu}{\kappa}, \quad \Gamma \equiv \frac{H}{L}. \tag{2.2}$$

The three input parameters reflect the strength of thermal forcing (Ra), the material properties (Pr) and the geometric confinement (Γ).

2.2 Direct numerical simulations

Direct numerical simulation (DNS) is a method to computationally solve the unsteady Navier-Stokes equations (2.1). It differs from other computational methods in fluid mechanics in that small-scale turbulent fluctuations are resolved numerically in space and time and are not represented by turbulence models. Two different methods were used in this thesis, a preexisting finite volume code which was substantially advanced in the context of this work and a pseudospectral code which was developed as part of this thesis.

2.2.1 Finite volume method

The finite volume ansatz (LeVeque, 2002) is particularly elegant when a partial differential equation can be formulated as a conservative law. In this case, the divergence terms can be expressed as surface integrals over a small finite volume.

Let us consider the general conservative law

$$\frac{\partial \mathbf{u}}{\partial t} + \boldsymbol{\nabla} \cdot \mathbf{f}(\mathbf{u}) = 0, \tag{2.3}$$

where $\mathbf{u}$ represents the flow state vector and $\mathbf{f}$ denotes the surfaces fluxes associated with convection or diffusion. We can divide the entire domain into small finite volume cells and average (2.3) over each cell volume V_i, i.e.

$$\int_{V_i} \frac{\partial \mathbf{u}}{\partial t} dV + \int_{V_i} \boldsymbol{\nabla} \cdot \mathbf{f}(\mathbf{u}) dV = 0. \tag{2.4}$$

Defining the volume average $\langle \mathbf{u} \rangle_V = \frac{1}{\Delta V_i} \int_{V_i} \mathbf{u} dV$ and using the divergence theorem, we obtain the finite volume representation

$$\frac{\partial \langle \mathbf{u} \rangle_V}{\partial t} + \frac{1}{\Delta V_i} \int_{S_i} \mathbf{f}(\mathbf{u}) \cdot \mathbf{n} dS = 0, \tag{2.5}$$

where S_i denotes the surface area of the finite volume element. Thus, instead of solving $\mathbf{u}$ at a particular location, as in a finite difference scheme, the finite volume method approximates the solution as volume-averaged quantities. In diffusion-convection problems, the surface flux $\mathbf{f}(\mathbf{u})$ is generally composed of functions depending on $\mathbf{u}$ and its derivative $\mathbf{u}'$, so we need to find the relationship between the volume-averaged values $\langle \mathbf{u} \rangle_V$ and the values given on the surface $\langle \mathbf{u} \rangle_S$ to calculate the fluxes and update the solution. In the following, we assume that our finite volume mesh is structured and curvilinear and for simplicity we consider the one dimension case. For a n-th order finite volume scheme, we evaluate the surface values by constructing a n-th order polynomial, i.e.

$$\mathbf{u}(x) = \sum_{k=0}^{n-1} c_k x^k, \tag{2.6}$$

such that it exactly recovers the volume integrated values $\langle u \rangle_V$ in n neighbouring intervalls $[x_{i-1/2}, x_{i+1/2}]$, i.e.

$$\begin{aligned}
\langle u \rangle_i &= \frac{1}{\Delta x_i} \int_{x_{i-1/2}}^{x_{i+1/2}} \sum_{k=0}^{n-1} c_k x^k dx \\
&= \frac{1}{\Delta x_i} \left[\sum_{k=0}^{n-1} \frac{c_k}{k+1} x^{k+1} \right]_{x_{i-1/2}}^{x_{i+1/2}},
\end{aligned} \tag{2.7}$$

with cell centers (volume averages) indexed as i and cell surfaces indexed as $i \pm 1/2$. In the following we focus on the 4-th order central approximation scheme [1], as implemented in *goldfish* (Kooij *et al.*, 2018). Suppose we want to find the surface values at $\langle u \rangle_{i-1/2}$, then we evaluate the coefficient array $\vec{c} \equiv [c_0 \ \ c_1 \ \ c_2 \ \ c_3]^T$ under the condition eq. (2.7) for the finite volume cells $\vec{u} \equiv [\langle u \rangle_{i-2} \ \ \langle u \rangle_{i-1} \ \ \langle u \rangle_i \ \ \langle u \rangle_{i+1}]^T$. This can be written in matrix form as

$$\vec{u} = \mathbf{A}\vec{c}, \tag{2.8}$$

---

[1] Formally, the scheme is 4th order in space only for equidistant meshes, otherwise 3rd order.

where the 4×4 matrix $\mathbf{A}$ is constructed from eq. (2.7), which resembles a Vandermonde-matrix. We can solve (2.8) by inverting $\mathbf{A}$ which yields the solution of the coefficient array $\vec{c}$, i.e.

$$\vec{c} = \mathbf{A}^{-1}\vec{u}, \tag{2.9}$$

from which we can obtain the surface value $\langle u \rangle_{i-1/2}$ or the derivative $\langle u' \rangle_{i-1/2}$ from eq. (2.6) together with eq. (2.9). This yields

$$
\begin{aligned}
\langle u \rangle_{i-1/2} &= \begin{bmatrix} 1 & x^1_{i-1/2} & x^2_{i-1/2} & x^3_{i-1/2} \end{bmatrix} \vec{c} \\
&= \begin{bmatrix} 1 & x^1_{i-1/2} & x^2_{i-1/2} & x^3_{i-1/2} \end{bmatrix} \mathbf{A}^{-1}\vec{u} \\
&\equiv \vec{\mathcal{I}}^T \vec{u},
\end{aligned}
\tag{2.10}
$$

and

$$
\begin{aligned}
\langle u' \rangle_{i-1/2} &= \begin{bmatrix} 0 & 1 & 2x_{i-1/2} & 3x^2_{i-1/2} \end{bmatrix} \mathbf{A}^{-1}\vec{u} \\
&\equiv \vec{\mathcal{D}}^T \vec{u},
\end{aligned}
\tag{2.11}
$$

with the interpolation coefficient arrays $\vec{\mathcal{I}}$ for the quantity u or $\vec{\mathcal{D}}$ for its derivative u'. These arrays can be stored and the values of u or u' at the surface values can be conveniently computed by the inner product of $\vec{\mathcal{I}}$ or $\vec{\mathcal{D}}$ with the volume averaged values at the cell centers $\vec{u}$.

Time stepping scheme

The Navier–Stokes equations (2.1) are integrated in time using the fractional-step method. In the previous version of *goldfish* (Kooij *et al.*, 2018), the leap-frog scheme was implemented, which has now been extended with a third-order Runge–Kutta method for more accurate time integration. We follow a similar strategy as described in Verzicco & Orlandi (1996). The momentum equation for $\mathbf{u} \equiv (u_x, u_y, u_z)$ is advanced in time as follows

$$\frac{\mathbf{u}^* - \mathbf{u}^i}{\Delta t} = \left[\beta^i \mathbf{H}^i + \lambda^i \mathbf{H}^{i-1} + \alpha^i \frac{\mathbf{L}^* - \mathbf{L}^i}{2} - \alpha^i \boldsymbol{\nabla} \mathbf{p}^i \right] \tag{2.12}$$

where the superscript i denotes the time-step level, α^i, β^i and γ^i indicate the coefficients of the time integration scheme, $\mathbf{u}^*$ is the auxiliary velocity field, $\mathbf{H}$ contains the explicit non-linear convection terms and body forces and $\mathbf{L}$ contains the viscous terms. The coefficients for the third-order Runge–Kutta scheme are taken as in Rai & Moin (1991):

$$
\begin{aligned}
\alpha^1 &= \frac{8}{15}, & \alpha^2 &= \frac{2}{15}, & \alpha^3 &= \frac{1}{3}, \\
\beta^1 &= \frac{8}{15}, & \beta^2 &= \frac{5}{12}, & \beta^3 &= \frac{3}{4}, \\
\gamma^1 &= 0, & \gamma^2 &= -\frac{17}{60}, & \gamma^3 &= -\frac{5}{12}.
\end{aligned}
$$

The correct divergence free velocity field $\mathbf{u}^{i+1}$ is then computed from the auxiliary velocity field $\mathbf{u}^*$ and the scalar pseudo-pressure Φ:

$$\mathbf{u}^{i+1} = \mathbf{u}^* - \Delta t \Phi, \tag{2.13}$$

where Φ is determined by the Poisson equation

$$\boldsymbol{\nabla}^2 \Phi = \boldsymbol{\nabla} \cdot \mathbf{u}^*. \tag{2.14}$$

Ultimately, the new pressure is updated through

$$\mathbf{p}^{i+1} = \mathbf{p}^i - \frac{1}{\alpha^i \Delta t} \Phi - \frac{1}{2} \nu \boldsymbol{\nabla} \cdot \mathbf{u}^*. \tag{2.15}$$

The solution of eq. (2.12) for $\mathbf{u}^*$ deserves further elaboration. Given the definition of the viscous terms $\mathbf{L} \equiv \nu \boldsymbol{\nabla}^2$, we can rewrite (2.12) in terms of a Helmholtz problem:

$$\underbrace{\left(\mathbf{I} - \nu \frac{\alpha^i \Delta t}{2} \boldsymbol{\nabla}^2 \right) \mathbf{u}^*}_{\text{Helmholtz operator}} = \underbrace{\mathbf{u}^i + \Delta t \left[\beta^i \mathbf{H}^i + \lambda^i \mathbf{H}^{i-1} + \alpha^i \frac{\mathbf{L}^i}{2} - \alpha^i \boldsymbol{\nabla} \mathbf{p}^i \right]}_{\text{RHS}}. \tag{2.16}$$

The exact solution of (2.16) is usually quite time consuming for multidimensional systems, but can be avoided by using an approximate factorization technique such as the alternating direction implicit (ADI) method (Douglas, 1962). The idea of the ADI method is to approximate the multidimensional Helmholtz operator by a product of one-dimensional operators (Wang *et al.*, 2013). The approximation of the Helmholtz operator in three dimensions is

$$\left(\mathbf{I} - \nu \frac{\alpha^i \Delta t}{2} \boldsymbol{\nabla}^2 \right) \approx \left(\mathbf{I} - \nu \frac{\alpha^i \Delta t}{2} \boldsymbol{\nabla}_x^2 \right) \left(\mathbf{I} - \nu \frac{\alpha^i \Delta t}{2} \boldsymbol{\nabla}_y^2 \right) \left(\mathbf{I} - \nu \frac{\alpha^i \Delta t}{2} \boldsymbol{\nabla}_z^2 \right), \tag{2.17}$$

which can be solved successively along x, y and z, i.e

$$\left(\mathbf{I} - \nu \frac{\alpha^i \Delta t}{2} \boldsymbol{\nabla}_x^2 \right) \mathbf{T}_1 = \text{RHS},$$

$$\left(\mathbf{I} - \nu \frac{\alpha^i \Delta t}{2} \boldsymbol{\nabla}_y^2 \right) \mathbf{T}_2 = \mathbf{T}_1,$$

$$\left(\mathbf{I} - \nu \frac{\alpha^i \Delta t}{2} \boldsymbol{\nabla}_z^2 \right) \mathbf{u}^* = \mathbf{T}_2, \tag{2.18}$$

where $\boldsymbol{\nabla}_x^2$, $\boldsymbol{\nabla}_y^2$, $\boldsymbol{\nabla}_z^2$ are the discrete operators of the second order derivatives ∂_{xx}, ∂_{yy}, ∂_{zz}. By approximating the derivatives with a centered second-order finite difference scheme, the one-dimensional Helmholtz operators are well-conditioned tridiagonal matrices that can be solved efficiently with the Thomas algorithm (Conte & Boor, 1972). The implicit treatment of the diffusion term leads to a massive improvement in numerical stability for small to medium Ra flows. However, high Ra flows are numerically constrained by the advection term, so the stability gain we get from the implicit method decreases. This means that above a certain Rayleigh number, a simple explicit method such as the forward Euler scheme or the leap frog Euler scheme is again preferable. From experience, this already occurs for about $Ra > 10^8$.
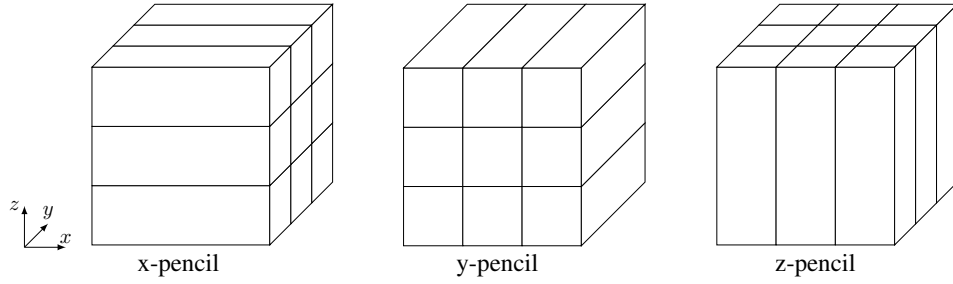
Figure 2.1: 2D Pencil domain decomposition representing x-pencil, y-pencil and z-pencil.

Parallelization and performance

Massively parallel simulations are essential for the study of turbulent flows. Therefore, the direct numerical code *goldfish* was modified from a 1D slab decomposition to a 2D pencil decomposition using the library *2DECOMP* (Li & Laizet, 2010). A sketch of the pencil decomposition for 9 processors is shown in figure 2.1. A 3D domain is partitioned into two dimensions, and each processor contains data contiguous in one dimension. The library defines routines for transferring data from one pencil distribution to another, which is necessary for solving the Helmholtz problem and the pressure Poisson problem. As can be seen in figure 2.2 (*a*), *goldfish* exhibits very good parallel scaling up to several thousand processors. Much work has also been dedicated to optimize numerical performance and achieve a balanced distribution of work without major bottlenecks. The result of these efforts can be seen in figure 2.2 (*b*), where we measured the performance of each routine. In this simulation, we calculated the diffusion terms in the velocity and temperature equations explicitly. As with many Navier-Stokes codes that use the velocity-pressure formulation, solving the pressure Poisson problem takes most of the time. *Goldfish* uses a partial diagonalization method that requires matrix-matrix multiplications for problems with 2 or more non-periodic dimensions (see also section 2.2.2). However, the time required for the pressure solver is now almost the same as the time required for updating the velocity field, which involves only the fairly simple computation of explicit terms. For a large number of processors, performance is limited by the Poisson solver and, in particular, by MPI-all-to-all communication when transposing the pencils. However, the near-ideal scaling for up to 1500 processors on a 512^3 cubic grid shows that the code is now well suited for running large parallel simulations.

2.2.2 Pseudospectral method

Pseudospectral methods are another prominent class of methods to obtain numerical solutions of differential equations (Orszag, 1969). In this method, the solution is expanded in a set of special basis functions and solved for the expansion coefficients (spectral space). A significant advantage of representing a solution with coefficients in function space is the easy differentiability. Moreover, spectral methods generally yield highly accurate solutions, more accurate than finite differences or finite volume methods for the same number of grid points. To avoid the inefficient computation of convolution terms, the nonlinear terms are computed in physical space and then

(a)

(b)
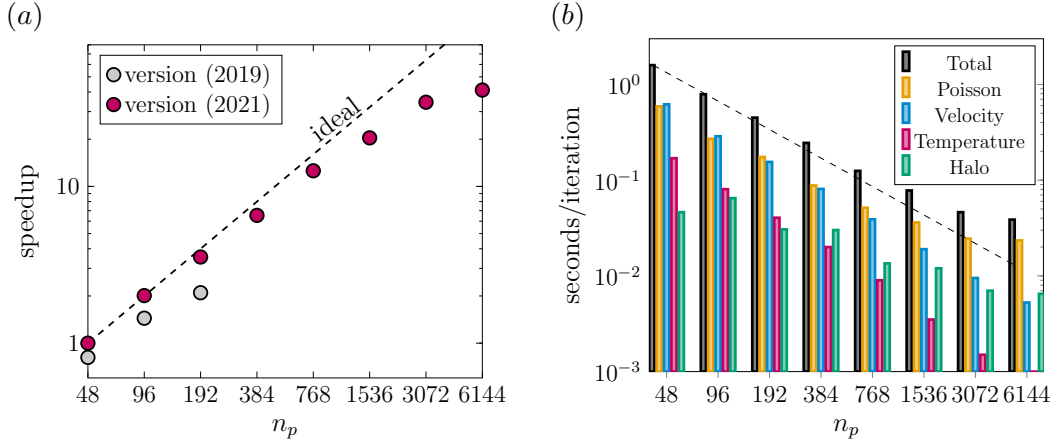
Figure 2.2: (a) Total speedup of *goldfish* versus number of processors n_p on a 512^3 cubic grid. The slab decomposed code from 2019 is limited to 256 processors, while the new pencil distributed version can theoretically run on 256^2 processors for the given grid. (b) Time consumption of individual computational parts: total (black), pressure/poisson solver (yellow), velocity solver (blue), temperature solver (red) and halo/ghost cell communication (green). The update of the diffusion terms in the velocity and temperature solver were performed explicitly in this case. The measurements have been performed on the SuperMUC-NG cluster at Leibniz Supercomputing Centre (www.lrz.de).

transformed into spectral space, hence the naming "pseudo".

Another incentive for developing a pseudospectral numerical solver as part of this thesis was to explore the potential of the modern programming language Rust for high-fidelity numerical simulations. Rust is a high-performance compiled language that offers remarkable memory safety, is rapidly gaining popularity, and could become a good alternative to Fortran and C for the scientific community. The code is available on github (Reiter, 2021). It currently supports two-dimensional domains with Chebyshev expansions for bounded walls or Fourier expansions for periodic walls. In the following description, we focus on the generally more difficult Chebyshev method.

Chebyshev Polynomials

Before discussing the properties of discrete Chebyshev polynomials and transformations, we begin with the general properties of continuous Chebyshev polynomials. This may seem like a dry set of mathematical relations, but they will be needed later to derive the transformation and differentiation methods. There is an extensive body of literature on this subject, see for example: Gottlieb & Orszag (1977); Canuto *et al.* (1988); Hesthaven *et al.* (2007). The following derivation is largely based on Shen *et al.* (2011).

The k-th Chebyshev polynomial of the first kind T_k is defined by

$$T_k(x) = \cos(k \arccos x), \tag{2.19}$$

which can be simplified using the coordinate transform $x \equiv \cos\theta$ to

$$T_k = \cos(k\theta). \tag{2.20}$$

Thus, the Chebyshev polynomials are cosine functions after a change of variables. Equation (2.20) emphasizes the similarity between Chebyshev and Fourier polynomials, from which we can adopt many theoretical and numerical tools. In fact, this is the origin for the popularity of Chebyshev polynomials in numerical computation in non-periodic domains, since it enables the use of fast transforms.

The derivative of the Chebyshev polynomials T_k' with respect to x is

$$T_k' = -k\sin(k\theta)\frac{d\theta}{dx} = \frac{k\sin(k\theta)}{\sin(\theta)}. \tag{2.21}$$

The Chebyshev polynomials are mutually orthogonal with respect to the weighted inner product

$$\int_{-1}^{1} T_k(x)T_m(x)\frac{1}{\sqrt{1-x^2}}dx = \frac{c_n\pi}{2}\delta_{k,m} \tag{2.22}$$

where $c_0 = 2$ and $c_k = 1$ for $k \geq 1$.

The Chebyshev expansion of a function u defined on the interval $x \in [-1, 1]$ is

$$u = \sum_{k=0}^{\infty} \widehat{u}_k T_k, \tag{2.23}$$

where the coefficients $\widehat{u}$ are found by the orthogonality relation, i.e.

$$\widehat{u}_k = \frac{2}{c_n\pi}\int_{-1}^{1} u(x)T_k(x)\frac{1}{\sqrt{1-x^2}}dx. \tag{2.24}$$

Trigonometric identities reveal important properties of the Chebyshev polynomials. First, taking $\cos((k+1)\theta) + \cos((k-1)\theta) = 2\cos(\theta)\cos(k\theta)$ together with eq. (2.20) we obtain the well-known recurrence relation

$$T_{k+1} = 2xT_k - T_{k-1}, \tag{2.25}$$

with $T_0 \equiv 1$ and $T_1 \equiv x$. Thus we can construct any Chebyshev polynomial from its two predecessors. Similarly, the identity $\sin((k+1)\theta) + \sin((k-1)\theta) = 2\sin(\theta)\cos(k\theta)$ together with eq. (2.21) leads to a recurrence relation for the first derivatives, i.e.

$$2T_k = \frac{1}{k+1}T_{k+1}' - \frac{1}{k-1}T_{k-1}', \qquad k \geq 1. \tag{2.26}$$

Discrete Chebyshev transform

We now turn to the discrete Chebyshev transform. Chebyshev methods are most commonly used in conjunction with non-uniformly distributed grid points that are clustered at the end points. Here we consider only Chebyshev–Gauss–Lobatto (CGL) points, which are a particularly well suited choice leading to a highly accurate approximation and allow for efficient transformations. The CGL points are defined

as

$$x_j = -\cos\left(\frac{\pi j}{N}\right),\qquad(2.27)$$

where N is the total number of points and $x \in [-1, 1]$. Note that in the literature, CGL points are usually given without a minus sign in front of eq. (2.27). In this case, the points are ordered from right to left. However, here we deviate from the conventional notation to avoid the mental adjustment and remain coherent with the developed numerical code. For the grid points x_j, the discrete Chebyshev polynomials are as follows:

$$T_k(x_j) = \cos\left(\frac{\pi k j}{N} + k\pi\right) = (-1)^k \cos\left(\frac{\pi k j}{N}\right).\qquad(2.28)$$

where we have used equation (2.19) and the identity $\arccos(-x) = \pi + \arccos(x)$. The term $(-1)^k$ results from the aforementioned minus sign in (2.27) and mirrors practically every odd Chebyshev polynomial. Using Gaussian quadrature, we can approximate the definite integral in eq. (2.24) as a weighted sum of function values at the grid points x_j, i.e.

$$\int_{-1}^{1} f(x) \frac{1}{\sqrt{1 - x^2}} dx \approx \sum_{j=0}^{N} f(x_j) \omega_j, \quad \omega_j = \frac{\pi}{\widehat{c}_j N},\qquad(2.29)$$

where $\widehat{c}_0 = \widehat{c}_N = 2$ and $\widehat{c}_j = 1$ for $j = 1..N - 1$. Note that the weight ω is specific to the CGL points and changes if other quadratures are chosen (Shen *et al.*, 2011). The discrete Chebyshev polynomials are still orthogonal to each other with respect to the weighted sum of (2.29), i.e.

$$\frac{\pi}{N} \sum_{j=0}^{N} \frac{1}{\widehat{c}_j} T_k(x) T_m(x) = \frac{\widehat{c}_n \pi}{2} \delta_{k,m}.\qquad(2.30)$$

Finally, let the Chebyshev expansion of a discrete function $u(x_j)$ be given, i.e.

$$u(x_j) = \sum_{k=0}^{N} \widehat{u}_k T_k,\qquad(2.31)$$

using eq. (2.28), the orthogonality property of eq. (2.30) and the Gaussian quadrature formula (2.29), we obtain the *forward discrete Chebyshev transform*

$$\widehat{u}_k = (-1)^k \frac{2}{\widehat{c}_k N} \sum_{j=0}^{N} \frac{1}{\widehat{c}_j} u(x_j) \cos\left(\frac{k j \pi}{N}\right), \quad 0 \le k \le N.\qquad(2.32)$$

and the *backward discrete Chebyshev transform*

$$u(x_j) = (-1)^k \sum_{k=0}^{N} \widehat{u}_k \cos\left(\frac{k j \pi}{N}\right), \quad 0 \le j \le N.\qquad(2.33)$$

Both transforms can be efficiently performed by the discrete cosine transformation (Type-I) in $\mathcal{O}(N \log N)$ operations.

Differentiation in Spectral Space

Differentiation in Chebyshev space is somewhat more complex than in Fourier space, but still very efficient. From (2.26) one can derive

$$
\begin{aligned}
u' &= \sum_{k=1}^{N} \widehat{u}_k T_k' \\
&= \sum_{k=0}^{N} \widehat{u}_k^{(1)} T_k \quad \text{(with } \widehat{u}_N^{(1)} = 0) \\
&= \widehat{u}_0^{(1)} + \widehat{u}_1^{(1)} T_1 + \sum_{k=2}^{N} \widehat{u}_k^{(1)} \left(\frac{T_{k+1}'}{2(k+1)} - \frac{T_{k-1}'}{2(k-1)} \right) \\
&= \frac{\widehat{u}_{N-1}^{(1)}}{2N} T_N' + \sum_{k=1}^{N-1} \frac{1}{2k} \left(c_{k-1} \widehat{u}_{k-1}^{(1)} - \widehat{u}_{k+1}^{(1)} \right) T_k'.
\end{aligned}
$$

where $\widehat{u}^{(1)}$ are the Chebyshev coefficients of the derivative u', $\widehat{c}_0 = \widehat{c}_N = 2$ and $\widehat{c}_j = 1$ for $j = 1..N-1$ (see also Shen *et al.* (2011)). The last line simply follows from a manipulation of the summation term. Since T_k' is also mutually orthogonal, we can now compare the expansion coefficients of T_k' between the first and the last line to obtain a recurrence relation for the Chebyshev coefficients of the first derivative

$$
\begin{aligned}
\widehat{u}_N^{(1)} &= 0, \\
\widehat{u}_{N-1}^{(1)} &= 2N \widehat{u}_N, \\
\widehat{u}_{k-1}^{(1)} &= \left(2k \widehat{u}_k + \widehat{u}_{k+1}^{(1)} \right) / c_{k-1}, \quad k = N-1, ..., 1,
\end{aligned}
$$

which can be simplified to

$$
\widehat{u}_k^{(1)} = \frac{2}{c_k} \sum_{\substack{p=k+1 \\ p+m \text{ odd}}}^{N} p \widehat{u}_p. \tag{2.34}
$$

Thus, for given Chebyshev coefficients, the derivative can be calculated via (2.34) and higher-order derivatives can be calculated recursively. For instance, the second derivative is

$$
\widehat{u}_k^{(2)} = \frac{2}{c_k} \sum_{\substack{p=k+2 \\ p+m \text{ even}}}^{N} p \left(p^2 - k^2 \right) \widehat{u}_p. \tag{2.35}
$$

Higher order relations are given in the appendix in Hesthaven *et al.* (2007). The determination of the (first) derivative of a function $u(x)$ is done in three steps

- Forward transform eq. (2.32), $u \to \widehat{u}$;

- Compute spectral derivative eq. (2.34), $\widehat{u} \to \widehat{u}^{(1)}$;

- Backward transform eq. (2.33), $\widehat{u}^{(1)} \to u'$.

Galerkin Method

There are several ways to implement spectral methods for solving differential equations. The most common are the Galerkin method, the tau method, and the collocation method. For brevity, we will focus on the description of the Galerkin method. In the Galerkin method, the solution is expressed by a finite set of basis functions, and each basis function must satisfy the boundary conditions of the problem. These special basis functions can be found, for example, by recombining orthogonal bases such as Chebyshev or Fourier. Well-conditioned Galerkin basis functions based on Chebyshev polynomials are derived by Shen (1995), i. e.

$$\phi_k = T_k - T_{k+2}, \qquad k = 0..N - 2, \tag{2.36}$$

for Dirichlet BCs and

$$\phi_k = T_k - \frac{k^2}{(k+2)^2} T_{k+2}, \qquad k = 0..N - 2, \tag{2.37}$$

for Neumann BCs. So we can represent our function u in two different ways

$$u(x) = \begin{cases} \sum_{k=0}^{N} \widehat{u}_k T_k, \\ \sum_{k=0}^{N-2} \widehat{v}_k \phi_k, \end{cases} \tag{2.38}$$

where we call the first representation the Chebyshev or orthogonal representation and the second the Galerkin or composite representation. Since the Galerkin basis functions are just linear combinations of the orthogonal Chebyshev basis functions, we can easily map between the two representations:

$$\widehat{\mathbf{u}} = \mathbf{S}\widehat{\mathbf{v}}, \tag{2.39}$$

where $\mathbf{S} \in \mathbb{R}^{(N-2) \times N}$ denotes a (sparse) transformation matrix, or stencil, defined by the relations (2.36) or (2.37). For example, for $N = 5$ the Dirichlet and Neumann stencils $\mathbf{S}$ are

$$\underbrace{\begin{bmatrix} 1 & 0 & 0 \\ 0 & 1 & 0 \\ -1 & 0 & 1 \\ 0 & -1 & 0 \\ 0 & 0 & -1 \end{bmatrix}}_{\text{Dirichlet}} \quad \text{and} \quad \underbrace{\begin{bmatrix} 1 & 0 & 0 \\ 0 & 1 & 0 \\ 0 & 0 & 1 \\ 0 & -\frac{1}{9} & 0 \\ 0 & 0 & -\frac{1}{4} \end{bmatrix}}_{\text{Neumann}}.$$

A function is first transformed from physical space to orthogonal space and from there to composite space via eq. (2.39) exploiting the sparseness of the stencil operator. Therefore, we can continue to take advantage of the fast Chebyshev transform, so that the transformation from physical to Galerkin space is still efficient.

1-D Poisson equation

When solving the Navier–Stokes equations, we often deal with a Poisson-type equation $\nabla^2 u = f$ for the pressure term, or a Helmholtz-type equation $(\gamma \mathbf{I} - \nabla^2)u = f$ (where γ is a positive scalar) for an implicitly treated diffusion term. Let us first focus on the one-dimensional case for the Chebyshev-Galerkin system with Dirichlet or Neumann bases according to (2.36) and (2.37). The Poisson equation in spectral
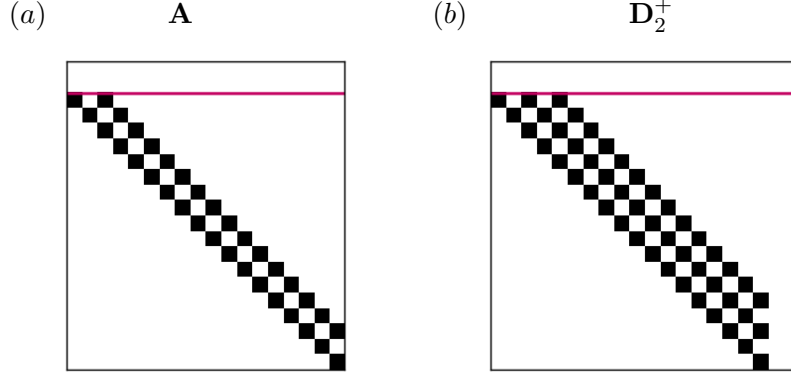
Figure 2.3: Sparsity patterns of (a) $\mathbf{A} \equiv \mathbf{I}_2\mathbf{S}$ and (b) the pseudo inverse matrix $\mathbf{D}_2^+$ arising in the 1D Poisson eq. (2.42) with $N = 20$. Red line shows the discarded first two rows.

space can be approximated as

$$\mathbf{D}_2\widehat{\mathbf{u}} = \mathbf{D}_2\mathbf{S}\widehat{\mathbf{v}} = \widehat{\mathbf{f}}. \tag{2.40}$$

The operator $\mathbf{D}_2$ is the discrete version of the Laplacian $\boldsymbol{\nabla}^2$ in spectral space. It can be derived from eq. (2.35) and is an upper triangular matrix. Therefore, the solution of eq. (2.40) can be solved by back substitution in $\mathcal{O}(N^2)$ operations. However, a more efficient way to solve this system is the so-called quasi-inversion technique (Julien & Watson, 2009; Oh, 2019). This method exploits the fact that the operator $\mathbf{D}_2^+$, which is the pseudo-inverse to $\mathbf{D}_2$, is itself sparse and can be constructed as follows:

$$\mathbf{D}_{2\ i,j}^+ = \begin{cases} \frac{c_{i-2}}{4i(i-1)} & \text{if } i = j - 2 \\ \frac{-b_i}{2(i^2-1)} & \text{if } i = j \\ \frac{b_{i+2}}{4i(i+1)} & \text{if } i = j + 2, \end{cases} \tag{2.41}$$

for $i = 2, 3, ..., N$, where $c_0 = 2$ and $c_k = 1$ for $k \geq 1$ and $b_k = 1$ for $k = 2, 3, .., N - 2$ and $b_{N-1} = b_N = 0$ (Oh, 2019). Applying $\mathbf{D}_2^+$ to (2.40) yields

$$\mathbf{I}_2\mathbf{S}\widehat{\mathbf{v}} \equiv \mathbf{A}\widehat{\mathbf{v}} = \mathbf{D}_2^+\widehat{\mathbf{f}}, \tag{2.42}$$

where $\mathbf{I}_2$ is the pseudo identity matrix. It is equal to the identity matrix except for the first two diagonal elements, which are zero, i.e. $\mathbf{D}_2^+\mathbf{D}_2 = \mathbf{I}_2 \equiv \mathrm{diag}([0\ 0\ 1\ ...\ 1])$. Note that the pseudoinverse is not a real inverse, since the matrix $\mathbf{D}_2$ is singular and thus not invertible. The reason for this is that the second derivatives of the first two Chebyshev polynomials, i.e. $T_0 \equiv 1$ and $T_1 \equiv x$, are zero. Figure 2.3 shows the sparsity patterns of $\mathbf{A}$ and $\mathbf{D}_2^+$. The first two lines are zero and can be discarded, reducing the system from order N to order $M = N - 2$. The right-hand side $\mathbf{D}_2^+\widehat{\mathbf{f}}$ can be evaluated by sparse matrix multiplication, and the linear system with the two-diagonally banded matrix $\mathbf{A}$ to yield $\widehat{\mathbf{v}}$ can be more efficiently solved in $\mathcal{O}(N)$ operations, compared to $\mathcal{O}(N^2)$ operations given the original upper triangular matrix.

2 Numerical methods

1-D Helmholtz equation

The solution of the Helmholtz problem $(\gamma\mathbf{I} - \boldsymbol{\nabla}^2)u = f$ is very similar to that of the Poisson problem. The Helmholtz equation in spectral space can be written as

$$(\gamma\mathbf{I} - \mathbf{D}_2)\mathbf{S}\widehat{\mathbf{v}} = \widehat{\mathbf{f}}. \tag{2.43}$$

Multiplying both sides by $\mathbf{D}_2^+$ yields

$$(\gamma\mathbf{D}_2^+\mathbf{S} - \mathbf{I}_2\mathbf{S})\widehat{\mathbf{v}} = \mathbf{D}_2^+\widehat{\mathbf{f}}, \quad \text{or}$$
$$(\gamma\mathbf{B} - \mathbf{A})\widehat{\mathbf{v}} = \mathbf{D}_2^+\widehat{\mathbf{f}}, \tag{2.44}$$

where $\mathbf{A} \equiv \mathbf{I}_2\mathbf{S}$ and $\mathbf{B}_2 \equiv \mathbf{D}_2^+\mathbf{S}$. The only differences to the Poisson problem is that the left-hand side $(\gamma\mathbf{B} - \mathbf{A})$ is now four-diagonal with elements on the diagonals $[-2, 0, 2, 4]$, which can also be solved efficiently in $\mathcal{O}(N)$ operations.

2-D Poisson equation

We now move on to multidimensional problems. For simplicity, we choose the same number of grid points in x and y, i.e. $N_x = N_y = N$. A convenient way to represent multidimensional problems is to use Kronecker products. The two-dimensional Poisson problem in spectral space can be written as

$$[(\mathbf{D}_2 \otimes \mathbf{I}) + (\mathbf{I} \otimes \mathbf{D}_2)]\,\widehat{\mathbf{u}} = \widehat{\mathbf{f}}, \quad \text{or}$$
$$[(\mathbf{D}_2\mathbf{S} \otimes \mathbf{S}) + (\mathbf{S} \otimes \mathbf{D}_2\mathbf{S})]\,\widehat{\mathbf{v}} = \widehat{\mathbf{f}}, \tag{2.45}$$

where $\widehat{\mathbf{v}}$ and $\widehat{\mathbf{f}}$ are column vectors of size N^2 and $\otimes$ denotes the Kronecker product. For simplicity we use the same derivative operator $\mathbf{D}_2$ and stencil $\mathbf{S}$ in x and y, but the following derivation applies also to the more general case where the number of dimensions or the chosen bases differs between the dimensions. Unlike for a system discretized by Fourier polynomials, the Poisson problem as defined in eq. (2.45) does not decouple the dimensions and thus can't be solved efficiently. A commonly applied strategy is to decouple, or diagonalize, one of the two spatial dimensions by means of an eigendecomposition. Let us outline this procedure. As before, we multiply both sides (and both dimensions) of (2.45) with the pseudo inverse operator $\mathbf{D}_2^+$, which yields

$$\left[(\mathbf{I}_2\mathbf{S} \otimes \mathbf{D}_2^+\mathbf{S}) + (\mathbf{D}_2^+\mathbf{S} \otimes \mathbf{I}_2\mathbf{S})\right]\widehat{\mathbf{v}} = (\mathbf{D}_2^+ \otimes \mathbf{D}_2^+)\widehat{\mathbf{f}} \tag{2.46}$$

or more concisely with $\mathbf{A} \equiv \mathbf{I}_2\mathbf{S}$ and $\mathbf{B}_2 \equiv \mathbf{D}_2^+\mathbf{S}$ we obtain

$$[(\mathbf{A} \otimes \mathbf{B}) + (\mathbf{B} \otimes \mathbf{A})]\,\widehat{\mathbf{v}} = (\mathbf{D}_2^+ \otimes \mathbf{D}_2^+)\widehat{\mathbf{f}}. \tag{2.47}$$

Multiplying from the right by $(\mathbf{B}^{-1} \otimes \mathbf{I})$ gives

$$\left[(\mathbf{A}\mathbf{B}^{-1} \otimes \mathbf{B}) + (\mathbf{I} \otimes \mathbf{A})\right]\widehat{\mathbf{v}} = \widehat{\mathbf{g}}, \tag{2.48}$$

where $\widehat{\mathbf{g}} \equiv (\mathbf{D}_2^+\mathbf{B}^{-1} \otimes \mathbf{D}_2^+)\widehat{\mathbf{f}}$. To fully separate the dimensions in eq. (2.48) we make use of the eigendecomposition

$$\mathbf{A}\mathbf{B}^{-1} = \mathbf{Q}\boldsymbol{\Lambda}\mathbf{Q}^{-1}, \tag{2.49}$$

where $\mathbf{Q}$ is a dense matrix containing the eigenvectors as columns and $\mathbf{\Lambda}$ is the diagonal eigenvalue matrix. Substituting (2.49) in (2.48), we obtain

$$\left[(\mathbf{Q}\mathbf{\Lambda}\mathbf{Q}^{-1} \otimes \mathbf{B}) + (\mathbf{I} \otimes \mathbf{A})\right]\widehat{\mathbf{v}} = \widehat{\mathbf{g}}, \tag{2.50}$$

and finally after multiplying from the left by $(\mathbf{Q}^{-1} \otimes \mathbf{I})$ we get

$$\left[(\mathbf{\Lambda} \otimes \mathbf{B}) + (\mathbf{I} \otimes \mathbf{A})\right]\widehat{\mathbf{v}}^* = \widehat{\mathbf{g}}^*, \tag{2.51}$$

where $\widehat{\mathbf{v}}^* \equiv (\mathbf{Q}^{-1} \otimes \mathbf{I})\widehat{\mathbf{v}}$ and $\widehat{\mathbf{g}}^* \equiv (\mathbf{Q}^{-1} \otimes \mathbf{I})\widehat{\mathbf{g}}$. Since $\mathbf{\Lambda}$ and $\mathbf{I}$ are both diagonal matrices, the first dimension is now fully diagonal, therefore we can solve the problem independently for each lane along the second dimension. If we define $\widehat{v}_j^*$ and $\widehat{g}_j^*$ as the j-th lane (contiguous along the second dimension) of the respective two-dimensional fields and λ_j as the j-th diagonal element of $\mathbf{\Lambda}$, we obtain

$$(\lambda_j\mathbf{B} + \mathbf{A})\widehat{v}_j^* = \widehat{g}_j^*, \tag{2.52}$$

with $j = 0, 1, .., N - 2$. This system consists of $N - 2$ one-dimensional Helmholtz equations as defined in eq. (2.44), and can be solved in $\mathcal{O}(N^2)$ operations. However, multiplication of the right-hand side by the eigenvector matrix $\widehat{\mathbf{g}}^* \equiv \mathbf{Q}^{-1}\widehat{\mathbf{g}}$ and the inverse of $\widehat{\mathbf{v}}^*$, i.e. $\widehat{\mathbf{v}} \equiv \mathbf{Q}\widehat{\mathbf{v}}^*$ is more costly, so the overall performance of this algorithm depends on the performance of the matrix multiplications.

Finally, let us outline the algorithm for solving the 2D Poisson problem:

- Calculate the right-hand side: $\widehat{\mathbf{g}} \equiv \mathbf{D}_2^+ \mathbf{B}\widehat{\mathbf{f}}\mathbf{D}_2^{+T}$,

- Transform $\widehat{\mathbf{g}}$ along x: $\widehat{\mathbf{g}}^* \equiv \mathbf{Q}^{-1}\widehat{\mathbf{g}}$,

- Solve the banded system along y: $(\lambda_j\mathbf{B} + \mathbf{A})\mathbf{v}_j^* = \widehat{g}_j^*$,

- Inverse transform $\widehat{\mathbf{v}}$ along x: $\widehat{\mathbf{v}} \equiv \mathbf{Q}\widehat{\mathbf{v}}^*$,

which yields the desired spectral coefficients $\widehat{\mathbf{v}}$.

2D Helmholtz equation

The 2D Helmholtz equation

$$\left[\gamma(\mathbf{I} \otimes \mathbf{I}) - (\mathbf{D}_2 \otimes \mathbf{I}) - (\mathbf{I} \otimes \mathbf{D}_2)\right]\widehat{\mathbf{u}} = \widehat{\mathbf{f}}, \tag{2.53}$$

can be treated in the same way. Eq. (2.51) becomes

$$\left[(\gamma\mathbf{I} \otimes \mathbf{B}) - (\mathbf{\Lambda} \otimes \mathbf{B}) - (\mathbf{I} \otimes \mathbf{A})\right]\widehat{\mathbf{v}}^* = \widehat{\mathbf{g}}^*, \tag{2.54}$$

which leads to a set of one-dimensional equations of the following form

$$\left[(\gamma - \lambda_j)\mathbf{B} - \mathbf{A}\right]\widehat{v}_j^* = \widehat{g}_j^*. \tag{2.55}$$

However, in practice, the multidimensional Helmholtz system is solved using an implicit alternating direction method (ADI) (Douglas, 1962) in the implicit computation of the diffusion term, as described in section 2.2.1. Preconditioning eq. (2.53)
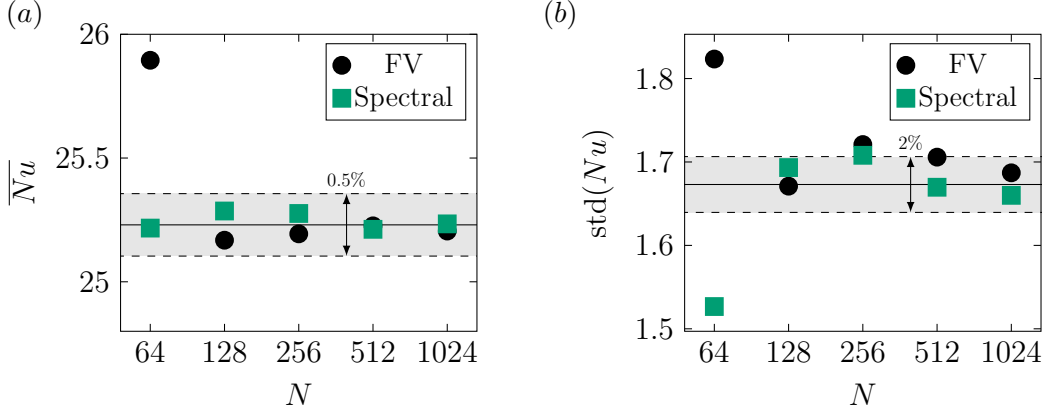
(a)

(b)

Figure 2.4: Comparison of the numerical accuracy of the finite volume code *goldfish* versus the pseudospectral code *rustpde* (Reiter, 2021) for 2D RBC with adiabatic sidewalls, $Ra = 10^8$, $Pr = 1$, $\Gamma = 1$ on a square grid with $N_x = N_y = N$ cells. Statistics were collected over 3500 free-fall time units in the statistically stationary regime. (a) Mean Nusselt number. (b) Standard deviation of Nusselt number. The shaded area marks $\pm 0.5\%$ ($\pm 2.0\%$) of the converged solution of the averaged Nusselt number (the standard deviation).

with $\mathbf{D}_2^+$ and applying the ADI decomposition yields

$$
\left(\gamma \mathbf{D}_2^+ \mathbf{S} - \mathbf{I}_2 \mathbf{S}\right) \Psi_i = \widehat{h}_i,
$$
$$
\left(\gamma \mathbf{D}_2^+ \mathbf{S} - \mathbf{I}_2 \mathbf{S}\right) \widehat{v}_j = \Psi_j, \tag{2.56}
$$

where $\widehat{\mathbf{h}} \equiv (\mathbf{D}_2^+ \otimes \mathbf{D}_2^+)\widehat{\mathbf{f}}$. The first equation is solved N times along the first dimension and the second equation is solved N times along the second dimension. The advantage of the ADI approach is that it decouples the spatial dimensions, resulting in $2N$ one-dimensional Helmholtz problems (in 2D). Therefore, it scales as $\mathcal{O}(N^2)$, which is faster than the matrix multiplications of the exact method described earlier.

2.2.3 Validation

In the following, the pseudospectral code is cross-validated with the finite volume code. The finite volume code *goldfish* has been used in numerous scientific studies and has been validated against other numerical codes in the context of RBC (Kooij *et al.*, 2018). In addition, the following comparison is also intended to evaluate the Rust programming language in the context of computational fluid dynamics.

As a comparison case, we use 2D RBC with $Ra = 10^8$, $Pr = 1$, and $\Gamma = 1$ in a laterally confined domain. At $Ra = 10^8$, the flow is already sufficiently turbulent and data were collected over 4000 time units, of which the first 500 time units were discarded, leaving 3500 time units in statistical steady state for averaging. Figure 2.4 shows the average and standard deviation of the Nusselt number on different square grids with $N_x = N_z = N$. Both codes show very good agreement. As expected, the spectral code gives slightly more accurate results on an under-resolved grid. However, we also note that the correctness of the mean Nusselt number observed for the spectral code at $N = 64$ may be deceptive and not indicative of a well-resolved simulation, as we see from the larger error in the standard deviation of Nu.
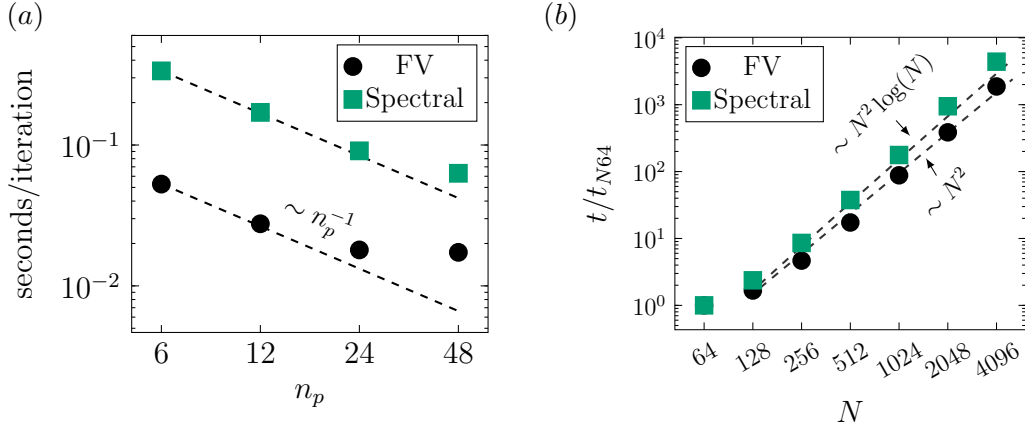
Figure 2.5: Comparison of the performance of the finite volume code *goldfish* versus the pseudospectral code *rustpde*. (*a*) Time per iteration for different number of processors on a 1024^2 grid. Dashed lines indicate ideal scaling. (*b*) Execution time for various two-dimensional grids N^2, normalized by execution time at $N = 64$.

The performance comparison is shown in figure 2.5. The performance of *goldfish* has already been discussed separately in section 2.2.1. There we demonstrated excellent parallel scaling with respect to the number of processors and showed that the code itself has been greatly optimized over the years. Although much less time has been spent on the pseudospectral code, it still shows quite good performance. From figure 2.5 (*a*), it can be seen that the code scales almost ideally when run on multiple processors. The finite volume code *goldfish* is still about $6 \sim 8$ times faster on the same grid, which is reasonable given the higher numerical complexity of pseudospectral methods compared to finite volume or finite difference approaches. It is also consistent with the comparison of Kooij *et al.* (2018), which showed that finite difference and finite volume methods can be > 10 times faster per iteration compared to a spectral element method. The trade-off, however, is that finite volume methods require a larger number of grid points for the same numerical accuracy. In figure 2.5 (*b*) we show the scaling of both codes with respect to the number of grid points $N_x = N_y = N$. The $N^2 \log(N)$ scaling of the spectral code shows that it is limited by the fast Fourier transform; a good sign that makes the existence of other bottlenecks less likely. Ultimately, for even larger Ra and in fully bounded domains, we expect the bottleneck of both codes to be the cost of the matrix multiplications in the pressure Poisson part, see section 2.2.2. In summary, we find the developed pseudospectral code is competitive and the Rust programming language is well suited for use in computational fluid dynamics.

2.3 Linear stability analysis

The concept of a linear stability analysis is to obtain the stability of a fixed point from a nonlinear equation by perturbing the equilibrium state. Starting from the nonlinear Navier–Stokes equations (2.1) and decomposing the flow field quantities $\mathbf{q} = (\mathbf{u}, p, T)^T \equiv \overline{\mathbf{q}} + \mathbf{q}'$ into an equilibrium state $\overline{\mathbf{q}}$ and perturbations $\mathbf{q}'$, neglecting second order terms and subtracting the mean field equations we obtain the equations

for the perturbations of the linearized Oberbeck-Boussinessq equations:

$$\partial_t \mathbf{u}' + \mathbf{u}' \cdot \nabla \overline{\mathbf{u}} + \overline{\mathbf{u}} \cdot \nabla \mathbf{u}' + \nabla p' = \nu \nabla^2 \mathbf{u}' + T' \mathbf{e}_z, \qquad (2.57\text{a})$$

$$\partial_t T' + \mathbf{u}' \cdot \nabla \overline{T} + \overline{\mathbf{u}} \cdot \nabla T' = \kappa \nabla^2 T', \qquad (2.57\text{b})$$

$$\nabla \cdot \mathbf{u}' = 0. \qquad (2.57\text{c})$$

(Note that throughout section 2.3 a primed quantity does not refer to a derivative, but to perturbations.) The goal is to determine the evolution of the disturbances for a given equilibrium state and evaluate whether the disturbances decay or grow. There are several strategies to solve this problem. The most common is to search for modal solutions of the form

$$\mathbf{q}'(\mathbf{x}, t) \equiv \tilde{\mathbf{q}}(\mathbf{x}) e^{-i\sigma t}, \qquad (2.58)$$

with the amplitude function $\tilde{\mathbf{q}}$ and an undulating time evolution. Here $\sigma = \sigma_r + \sigma_i$ denotes a complex frequency and the time growth is determined by its imaginary part σ_i. Substituting (2.58) into (2.57), one obtains

$$i\sigma \tilde{\mathbf{u}} = \tilde{\mathbf{u}} \cdot \nabla \overline{\mathbf{u}} + \overline{\mathbf{u}} \cdot \nabla \tilde{\mathbf{u}} + \nabla \tilde{p} - \nu \nabla^2 \tilde{\mathbf{u}} - \tilde{T} \mathbf{e}_z,$$

$$i\sigma \tilde{T} = \tilde{\mathbf{u}} \cdot \nabla \overline{T} + \overline{\mathbf{u}} \cdot \nabla \tilde{T} - \kappa \nabla^2 \tilde{T},$$

$$0 = \nabla \cdot \tilde{\mathbf{u}}.$$

which yields a generalized eigenvalue problem of the form

$$\sigma \mathcal{B} \tilde{\mathbf{q}} = \mathcal{A}(\overline{\mathbf{q}}) \tilde{\mathbf{q}}, \qquad (2.60)$$

with eigenvalues σ and eigenvectors $\tilde{\mathbf{q}}$. An equilibrium is stable if all eigenvalues have a negative temporal growth rate, i.e. $\sigma_i < 0$. And an equilibrium is unstable if at least one eigenvalue has a positive imaginary part, i.e. $\sigma_i > 0$. In the following, we describe the technical details of the matrix-based linear stability analysis as used in the studies of Shishkina (2021), Reiter *et al.* (2021*c*), Reiter *et al.* (2021*b*), Wang *et al.* (2021) and Ahlers *et al.* (2022), i.e., the collocation method and the Galerkin method. An alternative matrix-free strategy to obtain the strongest perturbation is to integrate the equations (2.57) forward in time like the Navier-Stokes equations in a classical direct numerical simulation, which we will not elaborate on here.

2.3.1 Collocation method

The collocation method enforces the governing equations (2.57) at each discrete grid point in the *physical space* (Uhlmann, 2004). For a two-dimensional domain with $\mathbf{q} \equiv (u, v, p, T)^T$, where u (v) denotes the horizontal (vertical) velocity component, the discrete eigenvalue problem (2.60) can be written as

$$\underbrace{\begin{bmatrix} \mathbf{L}_{2D} + \mathbf{D}_x \overline{u} & \mathbf{D}_y \overline{u} & \mathbf{D}_x & 0 \\ \mathbf{D}_x \overline{v} & \mathbf{L}_{2D} + \mathbf{D}_y \overline{v} & \mathbf{D}_y & -\mathbf{I} \\ \mathbf{D}_x & \mathbf{D}_y & 0 & 0 \\ \mathbf{D}_x \overline{T} & \mathbf{D}_y \overline{T} & 0 & \mathbf{K}_{2D} \end{bmatrix}}_{\mathcal{A}} \underbrace{\begin{bmatrix} \tilde{u} \\ \tilde{v} \\ \tilde{p} \\ \tilde{T} \end{bmatrix}}_{\tilde{\mathbf{q}}} = i\sigma \underbrace{\begin{bmatrix} \mathbf{I} & 0 & 0 & 0 \\ 0 & \mathbf{I} & 0 & 0 \\ 0 & 0 & 0 & 0 \\ 0 & 0 & 0 & \mathbf{I} \end{bmatrix}}_{\mathcal{B}} \underbrace{\begin{bmatrix} \tilde{u} \\ \tilde{v} \\ \tilde{p} \\ \tilde{T} \end{bmatrix}}_{\tilde{\mathbf{q}}}, \qquad (2.61)$$

where

$$\mathbf{L}_{2D} \equiv \overline{u}\mathbf{D}_x + \overline{v}\mathbf{D}_y - \nu\left(\mathbf{D}_x^2 + \mathbf{D}_y^2\right),$$
$$\mathbf{K}_{2D} \equiv \overline{u}\mathbf{D}_x + \overline{v}\mathbf{D}_y - \kappa\left(\mathbf{D}_x^2 + \mathbf{D}_y^2\right).$$

(Note that all terms referring to one-dimensional matrices, such as $\mathbf{D}_x\overline{u}$ or $\overline{u}$, are expanded to diagonal matrices). The discrete operators for the first derivative $\mathbf{D}_i$ and the second derivative $\mathbf{D}_i^2$ depend on the discretization. A common choice for wall-bounded domains is to expand the solution in terms of Chebyshev polynomials. The construction of the Chebyshev differentiation matrix is shown in Trefethen (2000) and higher order derivatives can be constructed by repeated matrix multiplication, for example $\mathbf{D}_i^2 = \mathbf{D}_i\mathbf{D}_i$. If the problem is fully constrained and we use Chebyshev discretization in x and y directions, then the eigenvalue problem is (2.61) of size $4N_xN_y$. The multidimensional operators can be conveniently constructed using Kronecker products. For example, we can form the derivative in x-direction by $\mathbf{D}_x = (D_x \otimes I_y) \in \mathbb{R}^{N_xN_y \times N_xN_y}$, where $D_x \in \mathbb{R}^{N_x \times N_x}$ denotes the one-dimensional Chebyshev differentiation matrix and $I_y \in \mathbb{R}^{N_y \times N_y}$ denotes the identity matrix. Boundary conditions can be included by removing the rows corresponding to the particular grid point with the discrete form of the boundary conditions.

For problems with periodic walls, discretization with Fourier polynomials is a common choice. In this case, we can replace the respective derivatives (say in x) by $\mathbf{D}_x \to ik_x$ and $\mathbf{D}_x^2 \to -k_x^2$, where k_x is a free parameter representing a spatial wavenumber. Assuming we use a Chebyshev discretization in y and a Fourier approach in x, this reduces the dimensionality of the system (2.61) to an eigenvalue problem of size $4N_y$, but adds the additional independent parameter k_x. The linear stability code for the collocation method is available on github (Reiter, 2020a).

2.3.2 Galerkin method

As briefly explained in 2.2.2, the Galerkin method enforces the governing equations in an integral sense. This method can also be used for linear stability analysis. The eigenvalue problem (2.60) is then solved in *spectral space*.

However, this method is less common in the literature. A major technical difficulty of Galerkin-based linear stability analysis is that the spectral transformation of the multiplication terms lead to the appearance of convolution terms, i.e., $\mathcal{T}(\mathbf{ab}) = \widehat{\mathbf{a}} * \widehat{\mathbf{b}}$, where $\mathcal{T}$ denotes the Chebyshev transform, $\widehat{\mathbf{a}}$ are the spectral coefficients of f, and $*$ is the convolution operator associated with the spectral transform. For Chebyshev polynomials defined on the Gauss-Lobatto points, the discrete Chebyshev transform is related to the discrete cosine transform (DCT-I), as we have shown in section 2.2.2. Thus, in what follows, the operator $*$ refers to the convolution operator of the DCT-I transform (Baszenski & Tasche, 1997). The complication is that in order to obtain an eigenvalue formulation, we must re-express the convolution term in matrix form. Therefore, we need to find a relationship between the convolution and a matrix multiplication, i.e.

$$\widehat{\mathbf{a}} * \widehat{\mathbf{b}} = \mathcal{C}(\widehat{\mathbf{a}})\widehat{\mathbf{b}} \tag{2.62}$$

where we call $\mathcal{C}$ the circulant matrix. This step is quite tedious, but it is outlined in greater detail in Baszenski & Tasche (1997). The following explanations focuses on the practical implementation.

Let us consider the one-dimensional problem with N grid points. We define a

matrix $\mathbf{P}_m \in \mathbb{R}^{N \times N}$, which is called a shift matrix related to DCT-I as follows

$$\mathbf{P}_0 \equiv \delta_{i,j}, \quad \mathbf{P}_N \equiv \delta_{i,N-j},$$

and for $m = 1..N - 2$

$$\mathbf{P}_m \equiv \begin{cases} 1/2(\delta_{m-i,j} + \delta_{m+i,j}), & i \leq m \wedge i < N - m \\ 1/2(\delta_{i-m,j} + \delta_{m+i,j}), & i > m \wedge i < N - m \\ 1/2(\delta_{m-i,j} + \delta_{2(N-1)-i-m,j}), & i \leq m \wedge i \geq N - m \\ 1/2(\delta_{i-m,j} + \delta_{2(N-1)-i-m,j}), & i > m \wedge i \geq N - m \end{cases} \quad (2.63)$$

for $i, j \in \{0, .., N - 1\}$. For example, the shift matrix for $N = 6$ and $m = 3$ looks like

$$\mathbf{P}_3 = \begin{bmatrix} & & & 1 & & \\ & & 0.5 & & 0.5 & \\ & 0.5 & & & & 0.5 \\ 0.5 & & & & 0.5 & \\ & 0.5 & & 0.5 & & \\ & & 1 & & & \end{bmatrix},$$

where blank spaces denote zero entries. Then, the circulant matrix with respect to the DCT-I for any vector $\widehat{\mathbf{a}} = \widehat{a}_{j \in \{0,...,N-1\}} \in \mathbb{R}^N$ yields

$$\mathcal{C}(\widehat{\mathbf{a}}) = \sum_{j=0}^{N} e_j \widehat{a}_j \mathbf{P}_j, \quad (2.64)$$

where $e_0 \equiv e_{N-1} \equiv 0.5$ and $e_k \equiv 1$ for $1 \leq k \leq N - 2$. Therefore, together with (2.62) we now have the recipes to express the convolution terms as matrix multiplications.

The discrete eigenvalue problem (2.60), transformed into spectral space, can be written as

$$\underbrace{\begin{bmatrix} \widehat{\mathbf{L}}_{2D} + \mathcal{C}(\widehat{\mathbf{D}_x \overline{u}}) & \mathcal{C}(\widehat{\mathbf{D}_y \overline{u}}) & \widehat{\mathbf{D}}_x & 0 \\ \mathcal{C}(\widehat{\mathbf{D}_x \overline{v}}) & \widehat{\mathbf{L}}_{2D} + \mathcal{C}(\widehat{\mathbf{D}_y \overline{v}}) & \widehat{\mathbf{D}}_y & -\mathbf{I} \\ \widehat{\mathbf{D}}_x & \widehat{\mathbf{D}}_y & \widehat{\mathbf{D}} & 0 \\ \mathcal{C}(\widehat{\mathbf{D}_x \overline{T}}) & \mathcal{C}(\widehat{\mathbf{D}_y \overline{T}}) & 0 & \widehat{\mathbf{K}}_{2D} \end{bmatrix}}_{\mathcal{A}} \underbrace{\begin{bmatrix} \widehat{u} \\ \widehat{v} \\ \widehat{p} \\ \widehat{T} \end{bmatrix}}_{\widehat{\mathbf{q}}} = i\sigma \underbrace{\begin{bmatrix} \mathbf{I} & 0 & 0 & 0 \\ 0 & \mathbf{I} & 0 & 0 \\ 0 & 0 & 0 & 0 \\ 0 & 0 & 0 & \mathbf{I} \end{bmatrix}}_{\mathcal{B}} \underbrace{\begin{bmatrix} \widehat{u} \\ \widehat{v} \\ \widehat{p} \\ \widehat{T} \end{bmatrix}}_{\widehat{\mathbf{q}}},$$

$$(2.65)$$

where

$$\widehat{\mathbf{L}}_{2D} = \mathcal{C}(\widehat{\overline{u}})\widehat{\mathbf{D}}_x + \mathcal{C}(\widehat{\overline{v}})\widehat{\mathbf{D}}_y - \nu\left(\widehat{\mathbf{D}}_x^2 + \widehat{\mathbf{D}}_y^2\right),$$

$$\widehat{\mathbf{K}}_{2D} = \mathcal{C}(\widehat{\overline{u}})\widehat{\mathbf{D}}_x + \mathcal{C}(\widehat{\overline{v}})\widehat{\mathbf{D}}_y - \kappa\left(\widehat{\mathbf{D}}_x^2 + \widehat{\mathbf{D}}_y^2\right).$$

Here $\widehat{\mathbf{D}}_{i=x,y}$ denotes the spectral derivative operator. For Chebyshev polynomials on Gauss-Lobatto quadrature points, the first derivative $\widehat{\mathbf{D}}_i$ and the second derivative $\widehat{\mathbf{D}}i^2$ are obtained from eq. (2.34) and eq. (2.35). Moreover, the identity $\widehat{\mathbf{D}_i u_j} = \widehat{\mathbf{D}}_i \widehat{u}_j$ with $i, j = x, y$ holds. In eq. (2.65), $\widehat{\mathbf{q}}$ denotes the spectral coefficients in orthogonal space (see also 2.2.2). In the Galerkin method, we apply the boundary conditions
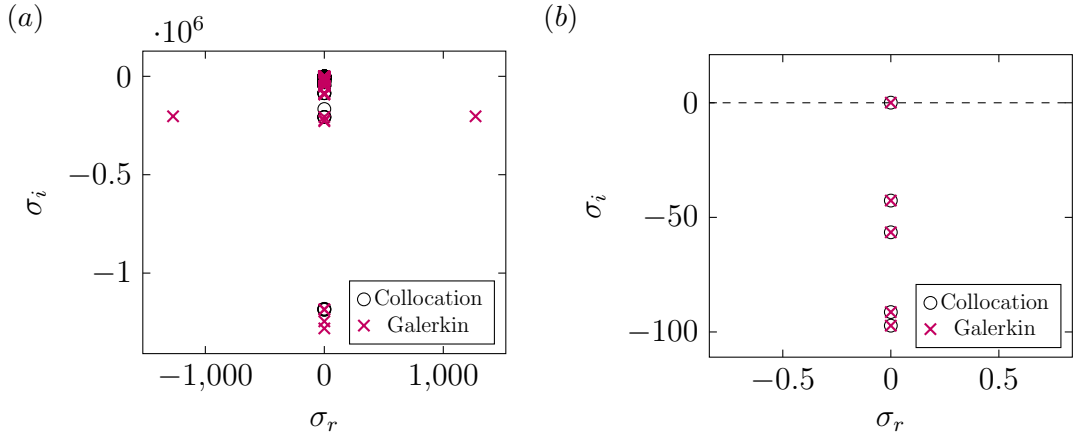
Figure 2.6: Eigenvalues of laterally unbounded RBC with parameters $Ra = 1715$, $Pr = 1$ and $k_x = 3.14$ with resolution $N = 41$. (a) Full spectrum and (b) magnification to the most dominant eigenvalues.

by projecting the solution vectors onto a lower-dimensional space, as we elaborated in 2.2.2. For this purpose, we use the definition of eq. (2.39), i.e. in this case $\widehat{\mathbf{q}} = \mathbf{S}\widehat{\underline{\mathbf{q}}}$, to transform from the orthogonal coefficients $\widehat{\mathbf{q}}$ to the low-dimensional Galerkin coefficients $\widehat{\underline{\mathbf{q}}}$, so that we end up solving the following eigenvalue problem based on (2.65):

$$\mathbf{S}^T \mathcal{A} \mathbf{S}\widehat{\underline{\mathbf{q}}} = \sigma \mathbf{S}^T \mathcal{B} \mathbf{S}\widehat{\underline{\mathbf{q}}}, \tag{2.66}$$

with the stencil matrices

$$\mathbf{S} \equiv \begin{bmatrix} \mathbf{S}_u & 0 & 0 & 0 \\ 0 & \mathbf{S}_v & 0 & 0 \\ 0 & 0 & \mathbf{S}_p & 0 \\ 0 & 0 & 0 & \mathbf{S}_T \end{bmatrix}, \quad \mathbf{S}^T \equiv \begin{bmatrix} \mathbf{S}_u^T & 0 & 0 & 0 \\ 0 & \mathbf{S}_v^T & 0 & 0 \\ 0 & 0 & \mathbf{S}_p^T & 0 \\ 0 & 0 & 0 & \mathbf{S}_T^T \end{bmatrix}.$$

As explained in section 2.2.2, the stencil matrices are chosen depending on the boundary conditions of the field variables. The linear stability code for the Galerkin method is available on github (Reiter, 2020b).

Collocation vs. Galerkin

We now compare the developed collocation and Galerkin method. For this purpose, we study the onset of convection in Rayleigh–Bénard flows. We set all mean velocities to zero and apply a constant negative mean temperature gradient in the vertical direction. We then test stability for an infinitely extended domain (one-dimensional) and a laterally bounded domain (two-dimensional).

For the infinitely extended case, we can apply the Fourier approach and reduce the two-dimensional eigenvalue problem to a one-dimensional problem, with an additional parameter k_x denoting the lateral wavenumber. We fix $k_x = 3.14$ and analyze the stability for $Ra = 1715$, $Pr = 1$ (although the onset of convection is Pr-independent) and use $N = 41$ grid points, i.e. spectral coefficients. The eigenvalue spectrum for both methods is shown in figure 2.6. The full spectrum in figure 2.6 (a) shows marginal differences between the two methods, but the most physically relevant eigenvalues near $\sigma_i = 0$ show perfect agreement, as seen in figure 2.6 (b). For
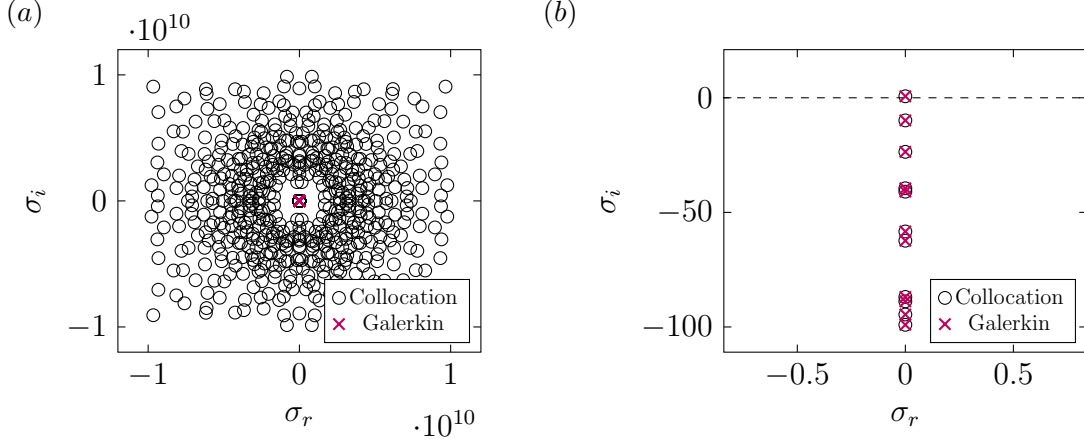
(a)

(b)

Figure 2.7: Eigenvalues of laterally bounded two-dimensional RBC with parameters $Ra = 2700$, $Pr = 1$ and $\Gamma = 1$ with resolution $N_x = N_z = 25$. (a) Spectrum with eigenvalues $|\sigma_r| < 10^{10}$ and $|\sigma_i| < 10^{10}$. (b) Spectrum zoomed to physically relevant eigenvalues. The collocation method shows an abundance of spurious eigenvalues, but the physically relevant ones are well captured.

$Ra = 1715$ we capture exactly one positive eigenvalue, and indeed it is known that laterally unbounded RBC becomes unstable at $Ra \approx 1708$ (Lord Rayleigh, 1916).

When we consider laterally bounded RBC, we are forced to solve a 2D eigenvalue problem. If we set $N_x = N_y = 25$, we obtain an EVP of size $4N_xN_y = 1250$ for the collocation method and $4(N_x - 2)(N_y - 2) = 1058$ for the Galerkin method, which is reflected in the slightly lower memory requirement of the Galerkin method for small N, shown in the table 2.1. Here we analyze the parameters $Ra = 2700$, $Pr = 1$ and the aspect ratio $\Gamma = 1$. The eigenvalue spectrum for both methods is shown in Figure 2.7. The collocation method shows an abundance of spurious eigenvalues of very large magnitude. However, looking at the physically relevant eigenvalues in figure 2.6 (b), we again see perfect agreement between the two methods. This behavior is also described in Uhlmann & Nagata (2006). Filtering out the spurious eigenvalues in the collocation method is usually not difficult, and we find that both methods consistently reproduce the most important eigenvalues. However, the Galerkin method is often more reliable and therefore our preferred approach.

Table 2.1: Comparison of wall-clock time and peak memory consumption of collocation and Galerkin method for a two-dimensional RBC stability problem with grid resolution $N_x = N_z = N$.

N	Collocation		Galerkin	
	Time (s)	Memory (GB)	Time (s)	Memory (GB)
11	0.8	0.09	1.3	0.09
21	0.8	0.28	0.9	0.24
31	2.0	0.99	2.7	0.88
41	5.3	2.8	7.7	2.6
51	16.2	6.5	19.5	6.3
61	21.2	13.0	35.5	13.1

3 Classical and symmetrical horizontal convection: detaching plumes and oscillations

Classical and symmetrical horizontal convection is studied by means of direct numerical simulations for Rayleigh numbers Ra up to 3×10^{12} and Prandtl numbers $Pr = 0.1, 1$ and 10. For both setups a very good agreement in global quantities with respect to heat and momentum transport is attained. Similar to Shishkina & Wagner (2016), we find Nusselt number Nu vs. Ra scaling transitions in a region $10^8 \leq Ra \leq 10^{11}$. Above a critical Ra, the flow undergoes either a steady – oscillatory transition (small Pr) or a transition from steady state to a transient state with detaching plumes (large Pr). The onset of the oscillations takes place at $Ra Pr^{-1} \approx 5 \times 10^9$ and the onset of detaching plumes at $Ra Pr^{5/4} \approx 9 \times 10^{10}$. These onsets coincide with the onsets of scaling transitions.

3.1 Introduction

In a horizontal convection (HC) system, heating and cooling takes place over a single horizontal surface of a fluid layer. In 1908, Sandstrom argued that due to the absence of a pressure gradient, a closed circulation can not be maintained in such systems. However, six decades later, Rossby (1965) demonstrated in his experiments that HC alone, independent from any other sources, is able to create a circulation of a fluid and therefore a net convective buoyancy flux. Over the last decades Rossby's setup became a popular paradigm case to study this important type of natural convective systems (Hughes & Griffiths, 2008; Griffiths *et al.*, 2013), which is relevant in geo-physical flows like the meridional overturning circulation in the ocean (Munk, 1966; Killworth, 1983; Cushman-Roisin & Beckers, 2011; Scott *et al.*, 2001; Scotti & White, 2011), in astrophysical flows (Spiegel, 1971) and engineering applications (Gramberg *et al.*, 2007). Investigations of HC systems are also necessary for understanding the effect of polar amplification on the ocean circulation (Holland & Bitz, 2003), i.e. a phenomenon of global warming that decreases the temperature contrast between the poles and mid-latitudes.

In any convective system, a naturally arising question is: How do the global heat transport (Nusselt number Nu) and momentum transport (Reynolds number Re) depend on the main input parameters (Rayleigh number Ra and Prandtl number Pr). While considering a laminar boundary layer (BL) and balancing buoyancy and viscous dissipation terms inside the BL, Rossby (1965) proposed a relation $Nu \sim Ra^{1/5}Pr^0$. The existence of the $\sim Ra^{1/5}$ regime was supported by various numerical and experimental studies (e.g. Gayen *et al.*, 2014; Mullarney *et al.*, 2004), but the predicted Pr-invariance of Nu does not hold for small Pr (e.g. Shishkina & Wagner, 2016). By considering the dynamics to be driven by a turbulent endwall plume, Hughes *et al.* (2007) proposed the scaling $Nu \sim Ra^{1/5}Pr^{1/5}$, but as it was shown in Shishkina & Wagner (2016), the proposed Pr-scaling is too strong and is not supported by direct numerical simulations (DNS). Whereas the Rossby model is based solely on the BL-scalings, the model by Shishkina *et al.* (2016) (SGL), which is an extension of the Grossmann & Lohse (2000, 2001, 2004) theory to HC, is able to account for laminar regimes as well as for regimes where the mixing is governed by turbulent processes. In particular, the SGL model suggests $Nu \sim Pr^0Ra^{1/4}$ for large Pr and $Nu \sim Pr^{1/10}Ra^{1/5}$ for small Pr laminar flows, which was supported by several numerical studies (Shishkina & Wagner, 2016; Ramme & Hansen, 2019).

However, verification of the other regimes needs further investigations. For this, high Ra DNS or experiments are needed, which turn out to be challenging tasks. On the one hand, the very slow diffusion in the system is a critical problem for the DNS of (almost) steady flows. On the other hand, in experiments, unwanted heat losses through the vertical walls can affect the scaling results significantly (Ahlers, 2000). Therefore in this work we focus on two setups: classical horizontal convection (CHC) and symmetrical horizontal convection (SHC), which can be more suitable for future experiments. Here we report 3D DNS results for $Ra \leq 3 \times 10^{12}$ and $Pr = 0.1, 1$ and 10.

3.2 Theoretical background

We consider a fluid layer which is confined in a rectangular box and heated and cooled locally from the bottom. In the CHC setup, heating and cooling is applied
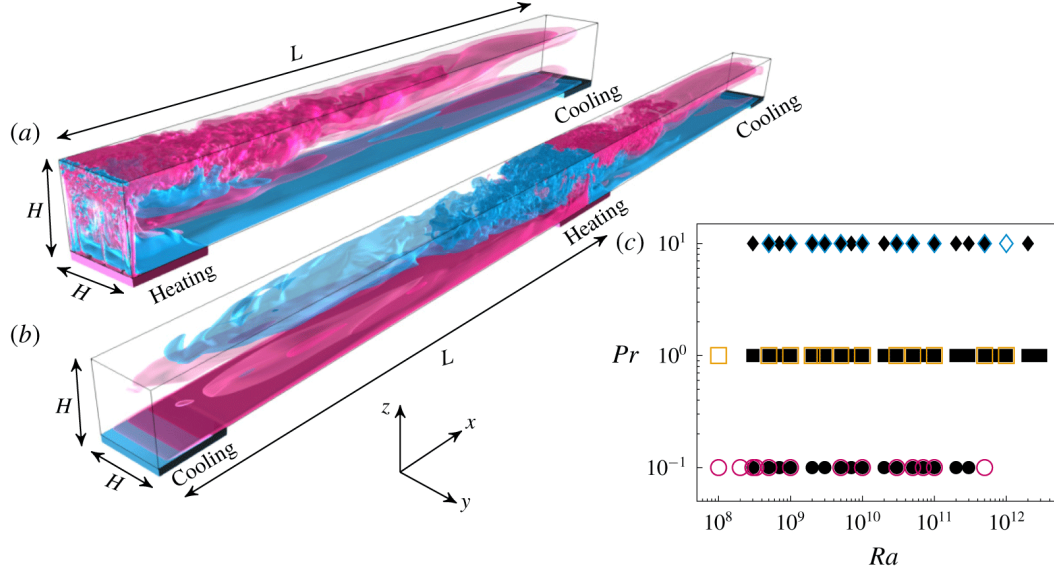
Figure 3.1: Sketch of (a) CHC and (b) SHC setups. Colours inside the cells represent the lengthwise velocity $u_x : u_x > 0$ (pink) and $u_x < 0$ (blue). (c) shows the studied parameter range for CHC (closed symbols) and SHC (open symbols).

to the opposite bottom ends (figure 3.1 a), while in the SHC setup the bottom is cooled at the ends and heated in the central part (figure 3.1 b). The advantage of the SHC setup over the HC one is the absence of the vertical endwall attached to the heated plate, which is difficult to isolate thermally in experiments. For both setups we conducted extensive 3D DNS over the range of parameters shown in figure 3.1 (c), where the DNS data for CHC and $Ra < 3 \times 10^{11}$ are taken from Shishkina (2017).

The governing equations in the Oberbeck – Boussinessq approximation for the dimensionless velocity $\mathbf{u}$, temperature θ and pressure p read as follows:

$$
\begin{aligned}
\mathrm{d}\mathbf{u}/\mathrm{d}t + \mathbf{u} \cdot \nabla\mathbf{u} + \nabla p &= \sqrt{Pr/Ra}\nabla^2\mathbf{u} + \theta\mathbf{e}_z, \\
\mathrm{d}\theta/\mathrm{d}t + \mathbf{u} \cdot \nabla\theta &= 1/\sqrt{PrRa}\nabla^2\theta, \quad \nabla \cdot \mathbf{u} = 0.
\end{aligned}
$$

The equations were made dimensionless using the free-fall velocity $u_{ff} \equiv (\alpha g\Delta L)^{1/2}$, the free-fall time $t_{ff} \equiv L/u_{ff}$, the temperature difference $\Delta \equiv T_+ - T_-$ between heated (T_+) and cooled (T_-) plates and L the cell length (CHC) or half cell length (SHC). The dimensionless parameters Ra, Pr and the aspect ratio Γ are then defined as:

$$
Ra \equiv \alpha g\Delta L^3/(\kappa\nu), \qquad Pr \equiv \nu/\kappa, \qquad \Gamma \equiv L/H = 10,
$$

where H is the cell height, ν the kinematic viscosity, α the isobaric thermal expansion coefficient, κ the thermal diffusivity and g the acceleration due to gravity. In the CHC configuration the temperature boundary conditions (BCs) at the bottom are $\theta = 0.5$ for $0 \leqslant x \leqslant 0.1$ and $\theta = -0.5$ for $0.9 \leqslant x \leqslant 1$. The other walls are adiabatic, $\partial\theta/\partial\vec{n} = 0$ where $\vec{n}$ is the wall-normal vector. The velocity BC are no-slip everywhere. In the SHC setup, the small vertical endwall near the heated plate is removed and the whole cell is extended by reflection of the cell with respect to the removed endwall. The used finite-volume code is Goldfish (Kooij *et al.*, 2018). A list

33

	I_l^*	I_l	II_l	III_∞	IV_u	IV_l
$Nu \sim$	$Pr^0 Ra^{1/4}$	$Pr^{1/10} Ra^{1/5}$	$Pr^{1/6} Ra^{1/6}$	$Pr^0 Ra^{1/4}$	$Pr^0 Ra^{1/4}$	$Pr^{1/3} Ra^{1/3}$
$Re \sim$	$Pr^{-1} Ra^{1/2}$	$Pr^{-4/5} Ra^{2/5}$	$Pr^{-2/3} Ra^{1/3}$	$Pr^{-1} Ra^{1/2}$	$Pr^{-2/3} Ra^{1/3}$	$Pr^{-2/3} Ra^{1/3}$

Table 3.1: Limiting scaling regimes in HC, according to Shishkina *et al.* (2016).

of all simulations, their spatial resolutions and averaging times are included in the supplementary materials.

The SGL model proposes different scaling regimes based on an assumption that in HC, the globally averaged kinetic (ϵ_u) and thermal (ϵ_θ) dissipation rates,

$$\langle \epsilon_u \rangle_V = \alpha g \langle u_z \theta \rangle_V \leq \alpha g \kappa \Delta/(2H) = (\Gamma/2)(\nu^3/L^4) Ra Pr^{-2}, \qquad (3.1)$$

$$\langle \epsilon_\theta \rangle_V = -(\kappa/H)\langle \theta \partial \theta/\partial z \rangle_{z=0} = (\Gamma/2)(\kappa \Delta^2/L^2) Nu, \qquad (3.2)$$

are determined by either the BLs (laminar flows) or the bulk (turbulent flows). Here $\langle \cdot \rangle_V$ denotes the time- and volume-average and $\langle \cdot \rangle_{z=0}$ the time- and area-average at $z = 0$. All this leads to different scaling regimes of Nu and Re vs. Ra and Pr (see table 3.1).

3.3 Results

3.3.1 Global heat and momentum transport

We start our analysis with Ra-dependencies of Nu and Re, using the definitions

$$Nu \equiv \langle |\partial_z \theta| \rangle_{z=0}/\langle |\partial_z \theta_c| \rangle_{z=0}, \qquad Re \equiv \sqrt{\langle \mathbf{U}^2 \rangle_V} L/\nu,$$

where $\langle |\partial_z \theta_c| \rangle_{z=0}$ is the magnitude of the heat flux considering a pure conductive system subjected to the same BCs (here $\frac{1}{2}\langle |\partial_z \theta_c| \rangle_{z=0} \approx 1.12$) and Re is based on the total kinetic energy. The results are presented in figure 3.2. First we observe that Nu and Re in CHC (solid black) and SHC (open colour) match remarkably well, with nearly equal absolute values over the whole parameter range. Therefore both setups can be used for the investigation of the global heat and momentum transport in HC. However, there exist differences in the flow structures which will be discussed in §3.3.2.

The DNS reveal a rather complex scaling dependence with multiple transitions. Starting from left to right in figure 3.2 (a) we find: $Nu \sim Ra^{1/4}$ for lower Ra, which corresponds to regime I_l^* in the SGL model, previously supported by Shishkina & Wagner (2016) and Ramme & Hansen (2019). As Ra increases, all three sets of data for different Pr show a rather sharp transition to a scaling $Nu \sim Ra^{1/5}$. Note that the critical Ra, where this transition occurs, increases with increasing Pr. The $\sim Ra^{1/5}$ scaling seems to persist up to our highest Ra for $Pr = 0.1$. Regime II_l of the SGL-model was not observed in our DNS, because $Pr = 0.1$ is still too large for this regime (Passaggia *et al.*, 2018). For $Pr = 1$ and 10 the curves rise again at higher Ra, leading to a scaling exponent of about 0.24 and 0.23. Figure 3.2 (b-d) shows $Re \sim Ra^{2/5}$ for small Ra (regime I_l) and $Re \sim Ra^{1/3}$ for larger Ra and no I_l^* regime in low Pr. However, when Re is based on $\langle \mathbf{U}^2 \rangle_+$, where $\langle \cdot \rangle_+$ denotes average in time and over the volume exclusively above the heated plate(s), we find scaling transitions consistent with the $Nu - Ra$ transitions of figure 3.2 (a). In general, the Re scaling
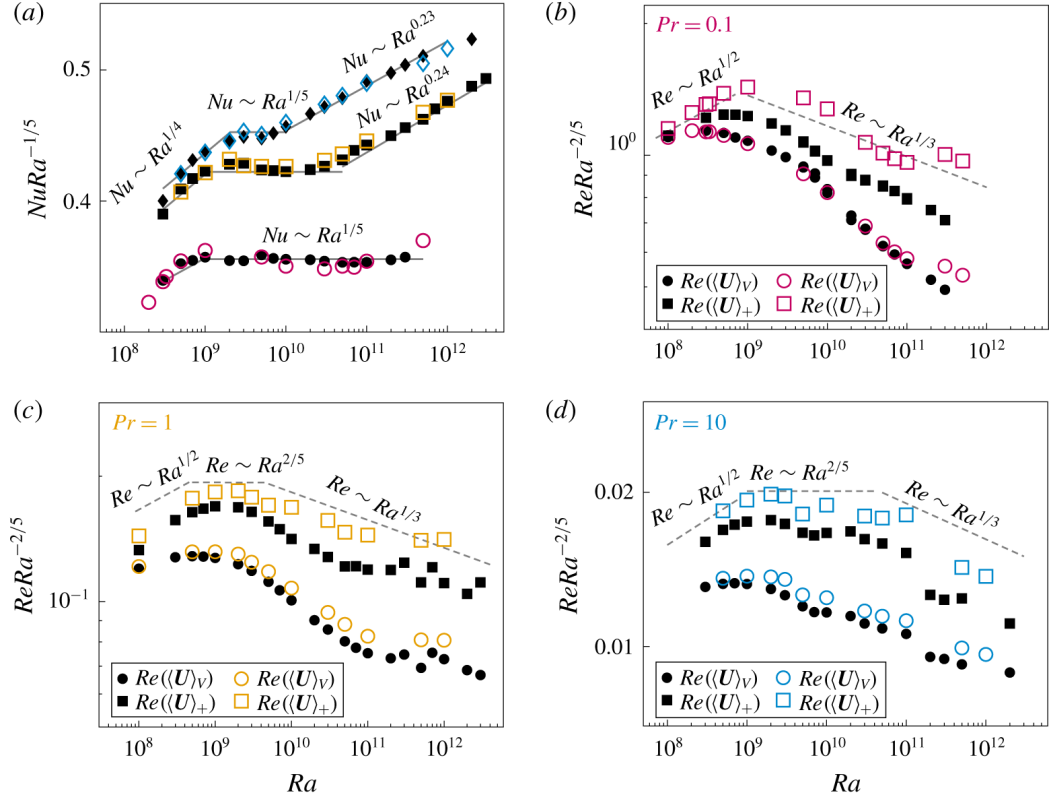
Figure 3.2: (a) Nu vs. Ra (log-log plot) for Pr=0.1 (circles), Pr=1 (squares) and Pr=10 (diamonds) for CHC (closed symbols) and SHC (open symbols). (b-d) Re based on $\langle \mathbf{U}^2 \rangle_V$ (circles) and Re_+ based on $\langle \mathbf{U}^2 \rangle_+$ (squares), the kinetic energy average only above the heated plate. The first onsets in the scalings coincide with the instability onsets found in §3.2, as well as other irregularities correspond to changes in the flow regimes - e.g. (c) $Ra \approx 10^{11}$ and onset to plume regime - as shown in figure 3.4. The straight scaling lines are put as a guide to the eye.

is sensitive to its spatial averaging domain. This displays the inhomogeneous nature of HC flows. To explain the scaling transitions, we further will have a closer look at the flow topology and its changes and relate them to the transitions in the scaling relations.

3.3.2 Dynamics: plumes and oscillations

In general, the HC dynamics are rich in flow structures and instability transitions. Paparella & Young (2002) observed that HC flows become unsteady with growing Ra, while higher Pr flows are stable over a broader range of Ra. Chiu-Webster *et al.* (2008) and Ramme & Hansen (2019) noticed the existence of time-dependent flows for highly viscous flows. Gayen *et al.* (2014) showed for $Pr = 5$ and varying Ra that the flow goes through a sequence of stability transitions, starting with the growth of plumes in the BL, followed by convective rolls at higher Ra and finally show fully 3D turbulence within a region above the hot BL at $Ra \approx 5 \times 10^{11}$. The linear stability analysis of Passaggia *et al.* (2017) for $Pr = 1$ supports these findings and suggests that there exists a competition between 3D rolls around a stream-wise axis and 2D
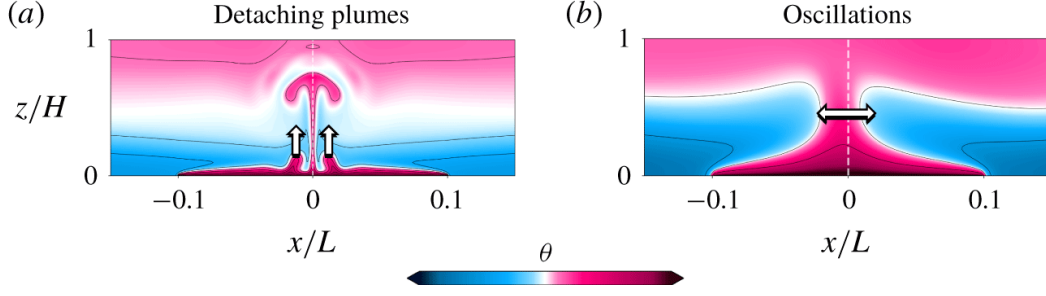
Figure 3.3: Snapshots of the temperature field for a) detaching plumes ($Pr = 10$, $Ra = 10^{10}$) and b) oscillations ($Pr = 0.1$, $Ra = 3 \times 10^8$) in SHC.

Rayleigh-Taylor (RT) instability. The former one seem to be dominant in wider cells, as it was found by Sukhanovsky *et al.* (2012), whereas the latter one seems to be most relevant for no-slip BC in narrow cells. Sheard & King (2011) found that the onset to unsteady flows is independent of vertical confinement for $0.16 \leq \Gamma \leq 2$ and Passaggia *et al.* (2018) observed the maximum growth for the two-dimensional plume instabilities at $\Gamma = 6$. HC instability was studied also for the cases of a BL synthetic jet (Leigh *et al.*, 2016), 2D HC (Tsai *et al.*, 2016) and different temperature BCs (Tsai *et al.*, 2020).

In our DNS we found the existence of 2D RT instabilities, which manifest themselves as sheared plumes that arise above the heated plate and which travel towards the endwall (CHC) or the center (SHC), as shown in figure 3.3 (a). However, for small Pr and especially in SHC flows, we found a different time-dependent behaviour prior to plumes emerging, which is an oscillatory instability, that breaks symmetry in SHC (3.3 b). These plume and oscillatory induced transitions to the unsteady state are explained below.

Plumes

In terms of timescales, detached plumes can occur if the time scale of the development of RT-instabilities T_{RT} is shorter than the advection timescale T_{wind} of the large-scale wind: $T_{RT}/T_{wind} < C_p$, for a certain constant C_p. The e-folding time scale of RT-instabilities (a characteristic timescale for RT-instabilities to grow by the factor $1/e$) equals $T_{RT} \sim \nu^{1/3}/(\alpha g \Delta)^{2/3}$ (Chandrasekhar, 1981) and the time scale of the wind velocity equals $T_{wind} \sim L^2/(Re\nu)$, which leads to an estimate

$$T_{wind}/T_{RT} = Ra^{2/3}/(RePr^{2/3}). \tag{3.3}$$

As the plumes detaching regime is anticipated for large Pr, we make use of the scaling relation $Re \sim Pr^{-1}Ra^{1/2}$ of the regime I$_l^*$ (see table 3.1), which gives $T_{wind}/T_{RT} \sim Pr^{1/3}Ra^{1/6}$. Thus, a certain critical value of $Pr^{1/3}Ra^{1/6}$, or an equivalent critical value of Pr^2Ra, determines the onset of the detached plumes. Note that the absolute value of the constant C_p can be determined from simulations or experimental data. This relation shows that for low Pr, the critical Ra increases. Physically explained, the larger wind speed of low Pr flows advects growing plumes faster to the endwall (CHC) or the center (SHC) before they become distinguishable from the thermal BL.

The solid red curves $Pr^2Ra \approx 10^{11}$ in figures 3.4 (a) and (b) give a rough estimate of the Pr and Ra dependence of the onset of the plume dominated regime. However,
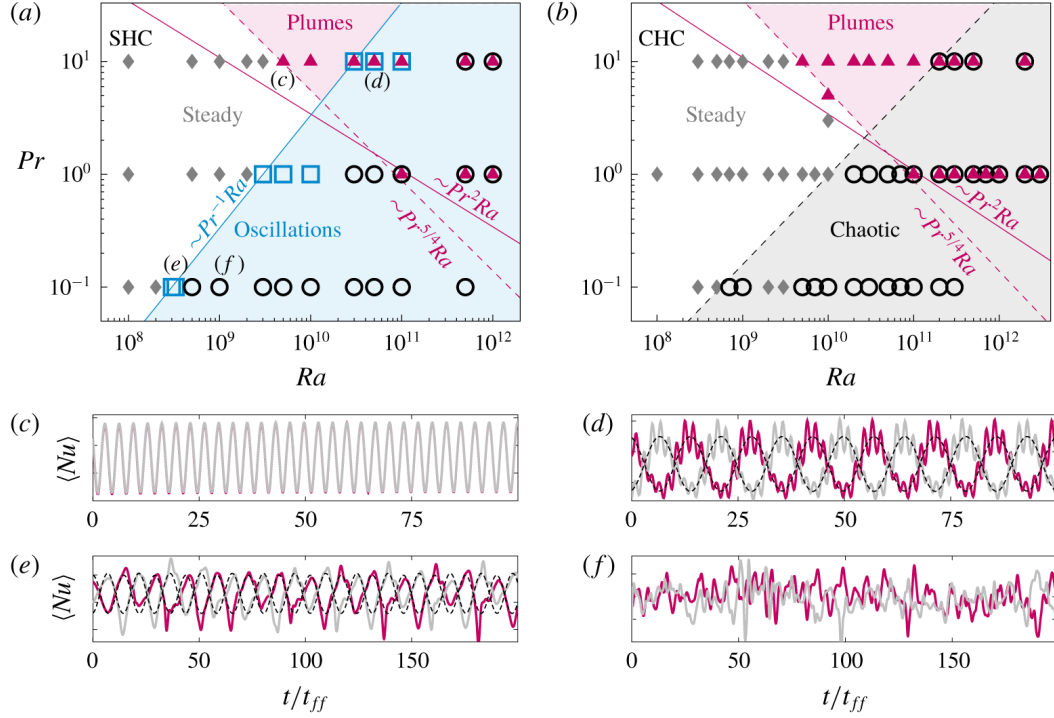
Figure 3.4: *Ra-Pr* phase space of the flow dynamics: steady (diamonds), oscillations (open squares), plumes (triangles) and chaotic (open circles). The solid lines in (a,b) show the theoretical predicted onsets of oscillation and plume regime, the red dashed line the semi-empirical predicted plume regime onset. The other four plots (c,d,e,f) show the evolution of the heat flux that enters the left half (red) and the heat flux that enters through the right half of the heated plate (grey), which in the oscillatory regime are anti-phase (represented by dashed lines d,e). The normalized frequencies for plume detaching f_p and oscillatory movement f_o are (c) $f_p \approx 0.298$, (d) $f_p \approx 0.522$ and $f_o \approx 0.070$, (e) $f_o \approx 0.068$ and (f) chaotic.

using Re scaling relations from the DNS instead of the SGL model, namely $Re \sim Ra^{2/5}$ (figure 3.2 b) and $Re \sim Pr^{-1}$ (Shishkina & Wagner, 2016), together with (3.3) we obtain $\sim Pr^{5/4}Ra$. And indeed, DNS (dashed curves in figure 3.4) supports that a constant $Pr^{5/4}Ra \approx 9 \times 10^{10}$ determines the onset of the detached plumes regime.

At higher Ra, plumes will detach faster and for sufficiently large Ra one finds multiple plumes detaching from the thermal BL. This phenomena was reported in Passaggia *et al.* (2017) for $Ra = 9 \times 10^{14}$, where plumes were visible immediately after entering the convectively unstable region.

Oscillations

A laminar flow in SHC can be thought as a configuration of two convective flows in sub-cells meeting in the center and circulating in opposite directions. While talking about oscillations, we refer to a horizontal movement of these two large structures and analyse an oscillatory movement at the location where the two rolls meet. This location oscillates periodically around the geometric center of the cell and thus breaks its symmetry.

Following the same strategy as in the previous section, the onset of oscillations can

be described in a simplified way as follows. Assume there exists a temperature fluctuation in one of the sub-cells near the centerline, which, due to buoyancy forces, leads to a local velocity change Δv of a flow parcel travelling upwards (relative to the base flow) against the viscous forces. As the speed increases, the pressure drops according to Bernoulli's theorem, which consequently initiates a horizontal pressure gradient between the two convective sub-cells. This essentially reflects the underlying role of the pressure term in the Navier-Stokes equations, which can transfer energy between modes of different directions (Batchelor, 1953). Therefore a vertically directed force (buoyancy) can induce horizontal oscillations.

The characteristic velocity of this Stokes type flow is $\Delta v \sim (\alpha g \Delta L^2)/\nu$ and the time scale is $T_p \approx L/(\Delta v) = \nu/(\alpha g \Delta L)$. The stabilizing antagonist here is the viscous force, which acts preserving for the symmetric flow profiles and the viscous time scale is $T_\nu = L^2/\nu$. The oscillations happen as soon as the shear time scale becomes large, unable to smooth-out the asymmetric flow profiles at a certain constant value of T_ν/T_p:

$$T_\nu/T_p = Ra/Pr = Gr \tag{3.4}$$

Our DNS results (figures 3.4 a, b) indicate that the critical value is $Ra/Pr \approx 5 \times 10^9$, supporting the afore described physical picture. This is consistent with the results of Paparella & Young (2002), who found that the transition to a time-dependent flow occurs at $Ra/Pr \approx 1.6 \times 10^8$. The discrepancy in the prefactors is explained by different BCs and that their simulations were 2D. Two remarks to figure 3.4 should be made. First, especially for low Pr, periodic oscillations exist only near the onset of the instability (figure 3.4 e). With increasing Ra, the flow becomes chaotic (figure 3.4 f). Second, we cannot identify regime of oscillations in CHC, but found the onset to a time-dependent and not plume determined flow with a similar trend.

The different plots (c,d,e,f) in figure 3.4 show the time signals of the vertical heat flux, averaged over the heated plates. As discussed, low Pr flows show oscillations and chaotic behaviour, while for large Pr we find the presence of plumes and a combination of plumes and oscillations. In general, the frequency of detaching plumes is by an order of magnitude larger than the oscillatory frequency (see captions of figure 3.4). It remains to be noted, that the locations of onsets to time-dependent flows shown in figure 3.4 (a,b) coincide with Nu and Re transitions as seen in figure 3.2 (a,b).

3.3.3 Dissipation rates

To study how the transition to a time-dependent flow can affect the global scalings (analysed in §3.3.1), we now analyse the kinetic (ϵ_u) and thermal (ϵ_θ) dissipation rates and assess the results in the context of the SGL model. Following Ng *et al.* (2015), we decompose the dissipation rates into their mean and fluctuating part: $\langle \epsilon_u \rangle_V = \langle \overline{\epsilon_u} \rangle_V + \langle \epsilon'_u \rangle_V = \nu \left[\langle (\partial U_i/\partial x_j)^2 \rangle_V + \langle (\partial u'_i/\partial x_j)^2 \rangle_V \right]$. This will give us a qualitative understanding about the role that fluctuations have on the mixing process. Additionally, we consider the volume averages restricted to the domain part above the heated plate, $\langle \cdot \rangle_+$, where we expect the most turbulent fluctuations.

For $\langle \epsilon_u \rangle_V$ one can expect either the BL scalings $\sim Re^2$, $\sim Re^{5/2}$ or bulk scaling $\sim Re^3$. Figure 3.5 shows a non-monotonic behaviour in all cases. First, for the lowest Re, the scaling shows approximately a $\langle \epsilon_u \rangle_V \sim Re^2$ behaviour, which corresponds to regime I_l^* with $Nu \sim Ra^{1/4}$. As Re increases, we observe a rather rapid increase
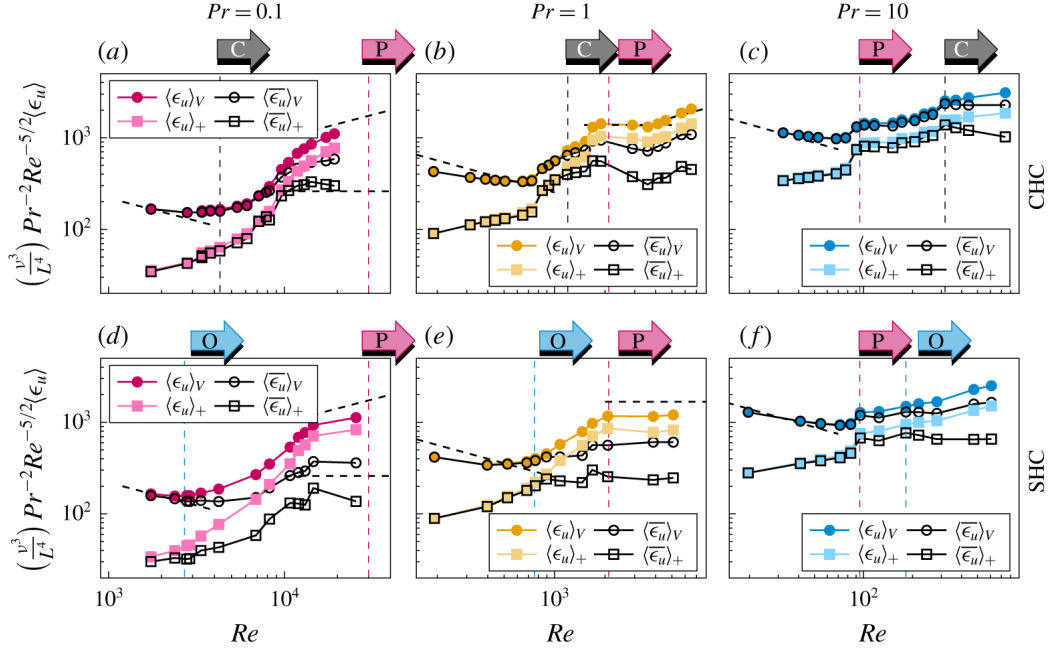
Figure 3.5: Kinetic dissipation rate vs. Re (as defined in §3), for (a,d) $Pr = 0.1$, (b,e) $Pr = 1$ and (c,f) $Pr = 10$ in CHC (a,b,c) and SHC (d,e,f). Vertical dashed lines indicate the corresponding onsets of oscillations (O) and plumes (P). Shown are total dissipation rate (ϵ_u) and contributions from the mean flow ($\overline{\epsilon_u}$) averaged over the whole domain $\langle\cdot\rangle_V$ or averaged specifically over the domain above the heated plate $\langle\cdot\rangle_+$. Negative slopes (inclined dashed lines) show $\epsilon_u \sim Re^2$; positive slopes $\epsilon_u \sim Re^3$.

of $\langle\epsilon_u\rangle_V$ leading to positive slopes in the compensated plot. The sudden increase in $\langle\epsilon_u\rangle_V$ is accompanied by a region, where the dissipation of the mean flow starts to drop. The total kinetic dissipation rate in the region above the heated plate $\langle\epsilon_u\rangle_+$ increases even stronger and for high Ra, most of the energy dissipates inside this region. The value of Re, where the first dissipation increase occurs, correlates strongly with the transition to a time-dependent flow, as indicated by the vertical dashed lines. Subsequently, the curves drop again to slopes in between $\sim Re^{5/2}$ and $\sim Re^3$. For high Re and especially for low Pr we observe that the contribution from the mean flow $\langle\overline{\epsilon_u}\rangle_V$ is no longer dominant, which matches the observations of Mullarney *et al.* (2004) and Scotti & White (2011), that turbulent fluctuations start to become dominating in HC. For our highest Ra and $Pr = 1$ (figure 3.5 b) a transition to a turbulent regime $\sim Re^3$ appears, but more data points at higher Re are needed to extend this trend. Another observation one can make from figure 3.5 (a, d) is that for increasing Re, $\langle\epsilon_u\rangle_V$ and $\langle\epsilon_u\rangle_+$ first converge and than slightly diverge again. This is explained by the fact that the region, where a turbulent flow is present, starts above the heated plate, but then spreads over an increasingly larger volume of the domain.

In figure 3.6 the thermal dissipation rate is analysed in a similar way. Other than for the kinetic dissipation, there is no observable effect from the onset of the instabilities. Moreover it is evident that the contributions of turbulent fluctuations is small for all studied Ra and that the total thermal dissipation is well described by its mean field contribution. Only for our largest Ra and only above the heated
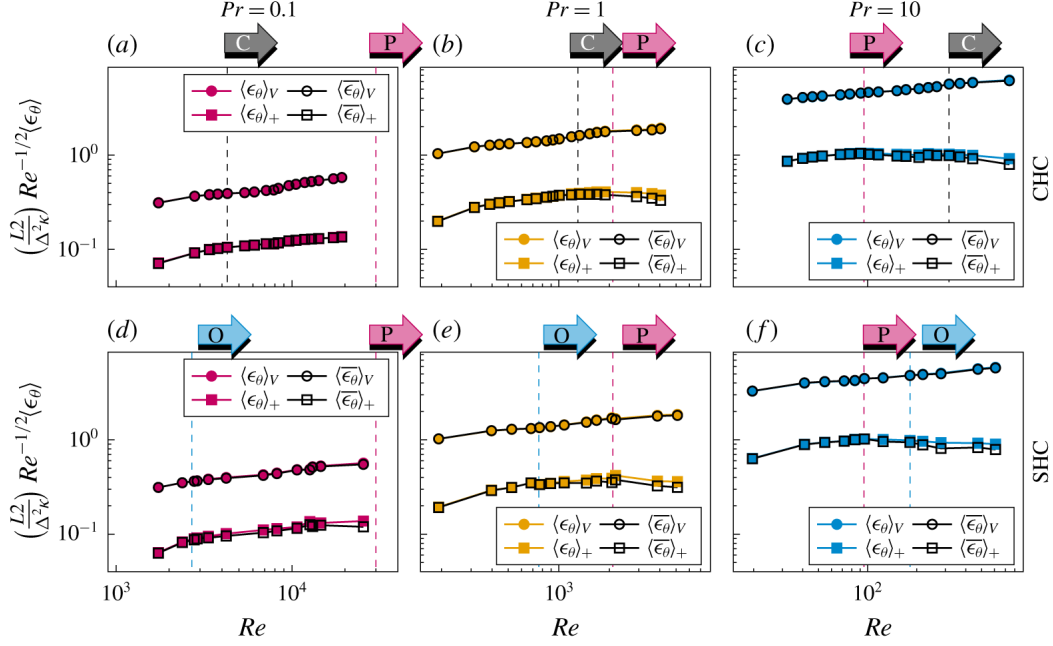
Figure 3.6: Thermal dissipation rate vs. Re (as defined in §3), for (a,d) $Pr = 0.1$, (b,e) $Pr = 1$ and (c,f) $Pr = 10$ in CHC (a,b,c) and SHC (d,e,f). Vertical dashed lines indicate the corresponding onsets of oscillations (O) and plumes (P). Shown are total dissipation rate (ϵ_θ) and contributions from the mean flow ($\overline{\epsilon_\theta}$) averaged over the whole domain $\langle\cdot\rangle_V$ or averaged specifically over the domain above the heated plate $\langle\cdot\rangle_+$.

plate the mean flow dissipation deviates slightly from the total thermal dissipation. The scaling is approximately $\epsilon_\theta \sim Re^{1/2}$ to $\epsilon_\theta \sim Re^{3/4}$ and nearly constant.

In summary, we found a strong enhancement of ϵ_u in the vicinity of the onset of the first instabilities. This locally occurring changes can cause the sharp scaling transitions, as observed in §3.3.1, suggesting not a "scale-free" region. The contributions of the mean dissipation $\overline{\epsilon_u}$ gradually decreases and for large Re we observe $\epsilon_u \sim Re^3$, which hints toward a transition to a turbulent regime. The temperature fluctuations, for all studied Ra, contribute little to the total thermal dissipation rate in contrast to the situation of the kinetic dissipation.

3.4 Conclusions

Long run-time DNS were conducted for several decades of Ra and $Pr = 0.1, 1$ and 10, for classical and symmetrical HC, in order to investigate the global scaling relations and the flow dynamics. The obtained results can be summarised as follows.

First, for the same parameters (Ra, Pr), SHC and CHC systems provide nearly the same heat and momentum transport (Nu, Re). Thus, we conclude that SHC setups can serve as a good alternative to CHC in studying HC-systems, which may give a better experimental accuracy, since it gets along without isolating the critical hot wall. The Nu vs. Ra scaling analysis for both setups showed evidence for regimes I_l and I_l^*, according to Shishkina *et al.* (2016), as found previously in Shishkina & Wagner (2016) and Ramme & Hansen (2019). Further, the Nu evolution suggests another transition phase for $Ra > 10^{10}$ and $Pr \geq 1$, which we found to be presumably

related to the transition from a steady to a time-dependent bulk flow. For our highest $Ra = 3 \times 10^{12}$, both Pr showing a slope of $Nu \sim Ra^{0.24}$.

Second, the analysis of the dynamics of HC systems reveals three different unsteady flow regimes: detached plume regime, oscillatory regime in SHC and chaotic regime. The onset of the former two instabilities have been obtained theoretically up to a constant and were confirmed by our DNS data. Detaching plumes dominate high-Pr flows and are found above a critical $RaPr^{5/4} \approx 9 \times 10^{10}$, while the oscillatory instability starts at a $Ra/Pr \approx 5 \times 10^{9}$ and is therefore dominating especially in small Pr fluids. A subsequent examination of the kinetic and thermal dissipation rates showed that the onsets of these instabilities coincide with a strong increase in the total kinetic dissipation and a simultaneous decrease in its mean field contribution. Our DNS show also that velocity fluctuations become the dominating part of $\langle \epsilon_u \rangle_V$, while the temperature fluctuations contribute only a little to $\langle \epsilon_\theta \rangle_V$ (less than 5%). Further experimental or numerical investigations for $Ra > 10^{12}$ are absolutely crucial for verifying of the other regimes of the SGL model and for the understanding of the role of buoyancy forcing on the ocean dynamics.

4 Generation of zonal flows in convective systems by travelling thermal waves

This work addresses the effect of travelling thermal waves applied at the fluid layer surface, on the formation of global flow structures in two-dimensional (2-D) and 3-D convective systems. For a broad range of Rayleigh numbers ($10^3 \leq Ra \leq 10^7$) and thermal wave frequencies ($10^{-4} \leq \Omega \leq 10^0$), we investigate flows with and without imposed mean temperature gradients. Our results confirm that the travelling thermal waves can cause zonal flows, i.e. strong mean horizontal flows. We show that the zonal flows in diffusion dominated regimes are driven purely by the Reynolds stresses and end up always travelling retrograde. In convection dominated regimes, however, mean flow advection, caused by tilted convection cells, becomes dominant. This generally leads to prograde directed mean zonal flows. By means of direct numerical simulations we validate theoretical predictions made for the diffusion dominated regime. Furthermore, we make use of the linear stability analysis and explain the existence of the tilted convection cell mode. Our extensive 3-D simulations support the results for 2-D flows and thus provide further evidence for the relevance of the findings for geophysical and astrophysical systems.

4.1 Introduction

The problem of the generation of a mean (zonal) flow in a fluid layer due to a moving heat source is an old one. Halley (1687) was probably the first to perceive that the periodic heating of the Earth's surface, due to the Earth's rotation, could be the reason for the occurrence of zonal winds in the atmosphere. Nearly three centuries later, experiments by Fultz *et al.* (1959), in which a Bunsen flame was rotated around a cylinder filled with water, verified Halley's hypothesis. The moving flame caused zonal flows and the fluid started to move opposite to the direction of the flame. Since then, several experimental and theoretical studies have appeared, which illuminated this phenomenon.

Thus, Stern (1959) repeated Fultz's experiments using a cylindrical annulus. His observations confirmed the previous result that the fluid acquires a net vertical angular momentum through the rotation of a flame, this time despite the suppression of radial currents in such a domain. Stern then provided a simple two-dimensional (2-D) model, showing that the mean motion is maintained through the presence of the Reynolds stresses. Davey (1967) extended Stern's model and provided a theoretical explanation that, in an enclosed domain, diffusion dominated flows always acquire a net vertical angular momentum in a direction opposite to the rotation of the heat source. His model provided asymptotic scalings for the dependency of the time- and space-averaged mean horizontal velocity, $\langle U_x \rangle_V$, with the characteristic frequency of the moving heat source Ω: $\langle U_x \rangle_V \sim \Omega^1$ for $\Omega \to 0$ and $\langle U_x \rangle_V \sim \Omega^{-4}$ for $\Omega \to \infty$. The topic gained further attention when Schubert & Whitehead (1969) suggested that the 4 day retrograde rotation of the Venus atmosphere might be driven by such a periodic thermal forcing. By using a low Prandtl number (Pr) fluid, they observed that the induced mean flow rotated rapidly and exceeded the rotation speed of the heat source, which was rotated below a cylindrical annulus filled with mercury ($Pr \ll 1$), by up to 4 times. This validated the linear analysis by Davey, who predicted the speed of the fluid to increase as Pr becomes small. However, at this time, it became clear that the induced rapid mean flows may exceed the range of validity of Davey's linear theory. Consequently, Whitehead (1972), Young *et al.* (1972) and Hinch & Schubert (1971) studied the influence of weakly non-linear contributions. They concluded that the small higher-order corrections rather tend to suppress the induced retrograde zonal flows and that the occurring secondary rolls transport momentum in the direction of the moving heat source. It therefore seemed unlikely that the mean flows become much faster than the heat source phase speed, even for small Pr, as soon as convective processes come into play.

The preceding analysis certainly lacked the complexity of convective flows, and therefore Malkus (1970), Davey (1967) and other authors anticipated that convective and shear instabilities could alter the entire character of the solution. In particular, Thompson (1970) showed that the interaction of a mean shear with convection can lead to a tilt of the convection rolls and thus to the transport of the momentum along the shear gradient and thereby amplifies the mean shear flow. In this scenario, the convective flow is unstable to the mean zonal flow even in the absence of a modulated travelling temperature variation, which suggests that the mean zonal flows might be the rule and not the exception to periodic flows that are thermally or mechanically driven. However, the direction of this mean zonal flow would be solely determined by a spontaneous break of symmetry; it could either move counter (retrograde) to the imposed travelling wave (TW) or in the same directions as the TW (prograde).

The existence of mean flow instabilities in internally heated convection and in rotating Rayleigh–Bénard convection (RBC) (Ahlers *et al.*, 2009*b*) was studied theoretically by Busse (1972, 1983) and Howard & Krishnamurti (1986), but has not been observed in laboratory experiments. In classical RBC, a zonal flow, if imposed as an initial flow, can survive (Goluskin *et al.*, 2014), but only if the ratio of the horizontal to vertical extension of the domain is smaller than a certain value, see Wang *et al.* (2020*b*) and Wang *et al.* (2020*a*). Also, several studies examined the effects of time-dependent sinusoidal perturbations in RBC. Venezian (1969) showed that the onset of convection can be advanced or delayed by modulation, while Yang *et al.* (2020*a*) and Niemela & Sreenivasan (2008) demonstrated a strong increase of the global transport properties in some cases.

Its general nature makes the travelling thermal wave problem appealing to study, however, to our knowledge, there are only a few studies recently published that are related to the original "moving flame" problem. Therefore, in the present study we revisit the existing theoretical models, specifically Davey's model, and validate it by means of state of the art direct numerical simulations (DNS). Furthermore, we study a set-up with a non-vanishing vertical mean temperature gradient (as in RBC), to study the influence of the travelling thermal wave on convection dominated flows and discuss the absolute strength and the direction of the induced zonal flows. Despite the substantial advances over the years, it remains unanswered, whether the thermal TW problem is merely of academic interest or, indeed, of practical relevance in the generation of geo- and astrophysical zonal flows (Maximenko *et al.*, 2005; Nadiga, 2006; Yano *et al.*, 2003). For this purpose, in chapter 2, we complement our analysis with thorough 3-D DNS. For the sake of generality, we choose a classical RBC set-up. Ultimately, we analyse the absolute angular momentum in 3-D flows (respectively, horizontal velocity in 2-D flows) and provide insight into the mean flow structures.

4.2 Methods

4.2.1 Direct numerical simulations

The governing equations in the Oberbeck–Boussinesq approximation for the dimensionless velocity $\mathbf{u}$, temperature θ and pressure p read as follows:

$$
\begin{aligned}
\mathrm{d}\mathbf{u}/\mathrm{d}t + \mathbf{u} \cdot \nabla \mathbf{u} + \nabla p &= \sqrt{Pr/Ra}\nabla^2\mathbf{u} + \theta\mathbf{e}_z, \\
\mathrm{d}\theta/\mathrm{d}t + \mathbf{u} \cdot \nabla \theta &= 1/\sqrt{PrRa}\nabla^2\theta, \quad \nabla \cdot \mathbf{u} = 0.
\end{aligned}
$$

Here, t denotes time and $\mathbf{e}_z$ the unit vector in the vertical direction. The equations have been non-dimensionalised using the free-fall velocity $u_{ff} \equiv (\alpha g\Delta\hat{H})^{1/2}$, the free-fall time $t_{ff} \equiv \hat{H}/u_{ff}$, Δ the amplitude of the thermal TW and $\hat{H}$ the cell height. The dimensionless parameters Ra, Pr and the aspect ratio Γ are defined by:

$$
Ra \equiv \alpha g\Delta\hat{H}^3/(\kappa\nu), \qquad Pr \equiv \nu/\kappa, \qquad \Gamma \equiv \hat{L}/\hat{H},
$$

where $\hat{L}$ is the length of the domain, ν is the kinematic viscosity, α the isobaric thermal expansion coefficient, κ the thermal diffusivity and g the acceleration due to gravity. This set of equations is solved using the finite-volume code *goldfish* (Kooij *et al.*, 2018; Shishkina *et al.*, 2015), which employs a fourth-order discretisation scheme in space and a third order Runge–Kutta, or, alternatively, an Euler-leapfrog scheme in time. The code runs on rectangular and cylindrical domains and has been

advanced for a 2-D pencil decomposition for a highly parallel usage. The spatial grid resolution of the simulations was chosen according to the minimum resolution requirements of Shishkina *et al.* (2010). A stationary state is ensured by monitoring the volume-averaged, the wall-averaged and the kinetic dissipation based Nusselt numbers.

In this study, the following notations are used: temporal averages are indicated by an overline or by a capital letter, thus the Reynolds decomposition of the velocity reads $u = U + u'$, decomposing u into its mean part U and fluctuating part u'. Unless specifically stated, time averages are carried out over a long period of time, however, in section 4.3.1, the averaging period was deliberately restricted to only a few wave periods to achieve a time scale separation. Further, the spatial averages are denoted by angular brackets $\langle \cdot \rangle$, followed by the respective direction of the average, e.g. $\langle \cdot \rangle_x$ denotes an average in x; $\langle \cdot \rangle_V$ denotes a volume average. And ultimately, the velocity vector definitions $\mathbf{u} \equiv (u_x, u_y, u_z) \equiv (u, v, w)$ are used interchangeably.

4.2.2 Theoretical model

Already the earliest models proposed by Stern (1959) and Davey (1967) gave a considerable good understanding of the moving heat source problem. Although there are more complex models (Stern, 1971) based on adding higher-order non-linear contributions (Whitehead, 1972; Young *et al.*, 1972; Hinch & Schubert, 1971; Busse, 1972), this section focuses on revisiting the main arguments of Davey's original work, which is expected to give reasonably good results in the limit of small Ra. Besides, a more complete derivation and concrete analytical solutions are provided in Appendix 4.A.

Given the linearised Navier–Stokes equations in two dimensions and averaging the horizontal momentum equation in the periodic x-direction and over time t, one can derive the following balance:

$$\sqrt{Pr/Ra}\,\partial_z^2 \langle U \rangle_x = \partial_z \langle \overline{u'w'} \rangle_x + \langle W \partial_z U \rangle_x. \tag{4.1}$$

Evidently, a mean zonal flow $\langle U \rangle_x$ is maintained by the momentum transport due to the Reynolds stress component $\overline{u'w'}$ and by mean advection through $W \partial_z U$. The theory further advances by assuming that no vertical mean flow exists ($W = 0$), which reduces equation (4.1) to the balance between viscous mean diffusion and Reynolds stress diffusion. Furthermore, by neglecting convection and variations in x, the linearised equations can be written as a set of ordinary differential equations, that can be solved sequentially to find u' and w' and ultimately the Reynolds stress term $\overline{u'w'}$. This procedure is shown in Appendix 4.A. Given the Reynolds stress field, equation (4.1) has to be integrated twice to obtain the mean zonal flow $U(z)$. Integrating that profile again finally gives the total mean zonal flow $\langle U \rangle_V$, which is an important measure of the amount of horizontal momentum or, respectively, angular momentum in cylindrical systems, that is generated due to the moving heat source. The last step can be solved numerically, however, following Davey (1967), the limiting relations can be calculated explicitly
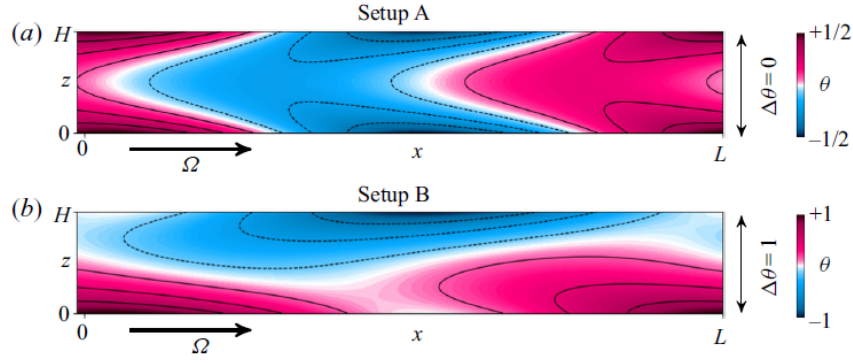
Figure 4.1: Sketch of the 2-D numerical set-up. The colour represents the dimension-less temperature distribution for the purely conductive cases ($\Omega = 0.1$). The thermal wave is imposed at the top and bottom plates, propagating to the right, in the positive x-direction. (a) Set-up A: no mean temperature gradient is imposed between the top and the bottom. (b) Set-up B: with (unstably stratified) mean temperature gradient, as in RBC. The figure shows temperature snapshots, while the time-averaged conduction temperature field depends linearly on z.

$$\langle U_x \rangle_V = -\frac{\pi}{2} \frac{k^3 Ra^2 Pr^{-2}(Pr+1)}{12!} \Omega + \mathcal{O}(\Omega^3) \text{ for } \Omega \to 0, \tag{4.2}$$

$$\langle U_x \rangle_V = -\frac{k^3 Ra^{-1/2} Pr^{-3/2}}{256\pi^4(Pr+1)} \Omega^{-4} + \mathcal{O}(\Omega^{-9/2}) \text{ for } \Omega \to \infty, \tag{4.3}$$

where the horizontally TW, $\theta(x,t) = 0.5\cos(kx - 2\pi\Omega t)$, is applied to the bottom and top plate. We would like to add that this theoretical model is, as determined by its assumptions, expected to be limited to diffusion dominated, small-Ra flows. However, when momentum and thermal advection take over, its validity remains questionable. We will show later that, after the onset of convection, where eventually mean advection takes over, the neglect of the $W\partial_z U$-contribution is no longer justified.

4.3 Two-dimensional convective system

As described by Stern (1959), the generation of a laminar zonal flow by a TW can be successfully explained in a 2-D system, which makes it a good starting point. The temperature boundary conditions (BCs) are time and space dependent,

$$\theta(x, z = 0, t) = 0.5\left[\cos(x - 2\pi\Omega t) + \Delta\theta\right],$$
$$\theta(x, z = H, t) = 0.5\left[\cos(x - 2\pi\Omega t) - \Delta\theta\right].$$

Here, Ω indicates the temporal frequency of the TW in free-fall time units. For example, $\Omega = 10^{-1}$ describes a wave with a period of 10 free-fall time units τ_{ff}, and $\Delta\theta$ is introduced as a control parameter for the strength of the mean temperature gradient.

In the following, two different set-ups are considered. In set-up A (figure 4.1 a)
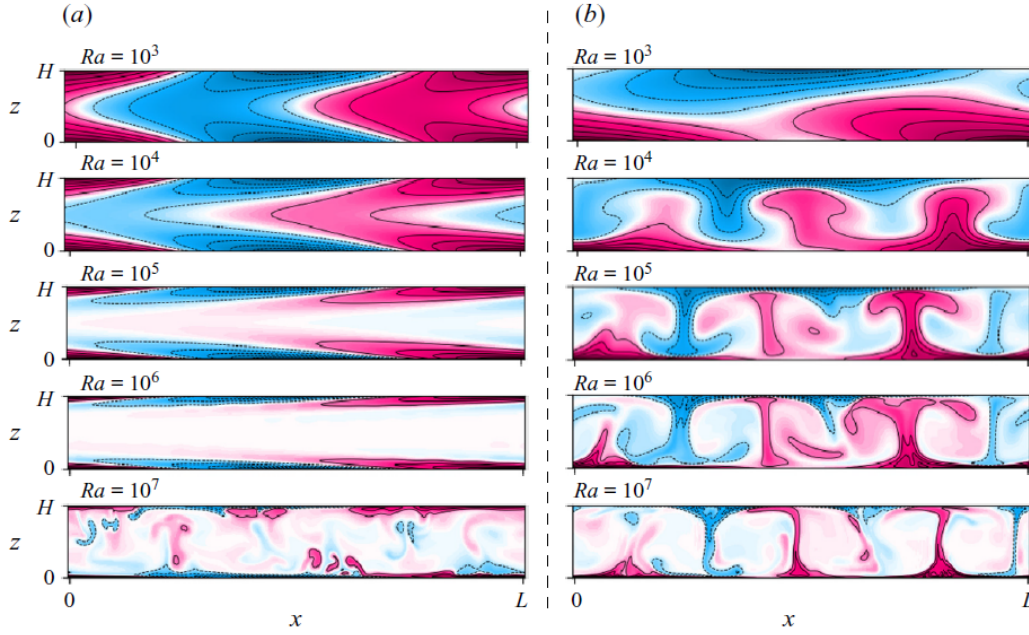
Figure 4.2: Snapshots of the temperature field θ at a fixed TW speed $\Omega = 0.1$ (propagating to the right). (a) Set-up A and (b) Setup B. The plumes in set-up B travel either retrograde or prograde (see supplementary movies).

– the one originally examined by Davey (1967) – no mean temperature gradient exists ($\Delta\theta = 0$) and the top and bottom plate temperatures are equal, whereas in set-up B (figure 4.1 b) a mean, unstable temperature gradient is applied ($\Delta\theta = 1$). For simplicity, the mean temperature gradient is set equal to the amplitude of the thermal wave. In this set-up, effects of convection are expected to become dominant. Averaged over time, this set-up resembles RBC, therefore, it can be regarded as a spatially and temporally modulated variant of RBC. Further, no-slip conditions are applied at the top and bottom plates, the x-direction is periodic and the domain has a length $L = 2\pi$ and height $H = 1$. In upcoming studies, one might introduce a second Rayleigh number based on the mean temperature gradient (as in RBC), namely $Ra_{\Delta\theta} \equiv \alpha g \Delta\theta \hat{H}^3/(\kappa\nu)$. However, in this work the connection to Ra is simply $Ra_{\Delta\theta} = 0$ for set-up A and $Ra_{\Delta\theta} = Ra$ for Set-up B.

The overall focus in this study lies on variations of the zonal flow with Ra and Ω. Thus, the parameter space spans $10^3 \leq Ra \leq 10^7$ and $10^{-4} \leq \Omega \leq 10^0$, while the aspect ratio and Prandtl number are kept constant ($\Gamma = 2\pi$, $Pr = 1$). Exemplary temperature fields at a fixed $\Omega = 0.1$ are shown in figure 4.2.

4.3.1 Results

The theoretical model, as presented in Appendix 4.A, aims to explain the generation of the total mean momentum $\langle U_x \rangle_V$ for a given Ra and wave frequency Ω. Moreover, it predicts that the generated mean momentum will be directed opposite, i.e. retrograde, to the travelling thermal wave. In this section we study the validity of the model and reveal its limitations.

Figure 4.3 shows the numerical data from the DNS together with the respective results of the theoretical model, for different Ra. Worth noting first is, that the maximum of the theoretical model is located at a fixed frequency, if the frequency
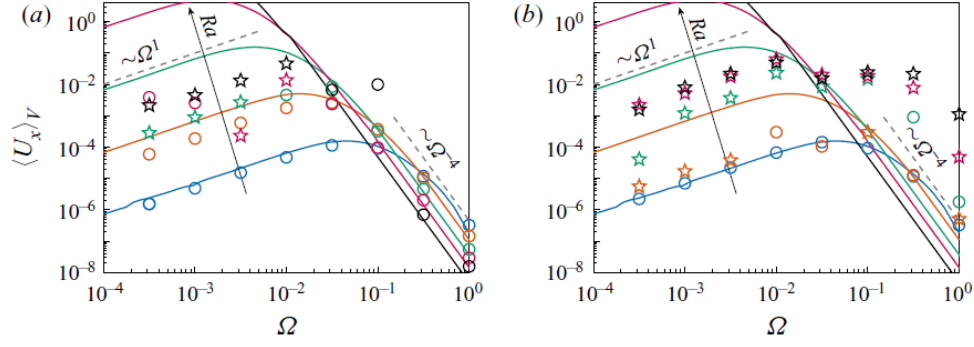
Figure 4.3: Mean velocity of the zonal flow vs. the wave frequency Ω for $Ra = 10^3$ (blue), 10^4 (orange), 10^5 (green), 10^6 (red) and 10^7 (black). Circles (stars) denote a retrograde (prograde) mean zonal flow, the solid lines of the corresponding colour show the results of the theoretical model by Davey (1967). (a) Set-up A and (b) set-up B.

is expressed in terms of the diffusive time scale rather than the free-fall time scale $\Omega_{\kappa,max} = \Omega/\sqrt{RaPr} \approx 0.66$. This indicates that the model predictions could be collapsed onto a single curve. Nonetheless, this was avoided here for the sake of clarity.

We begin our discussion with the results of set-up A, shown in figure 4.3 (a). The theoretical model by Davey (1967), indicated by the solid lines, gives accurate results for $Ra = 10^3$ and a good agreement for $Ra = 10^4$, although, evidently, the model systematically overestimates the mean momentum generation for higher Ra. In fact, this is consistent with Whitehead (1972), Young *et al.* (1972) and Hinch & Schubert (1971) who observed that corrections of higher-order non-linear contributions tend to suppress the induced retrograde zonal flows. Also it suggests that an induced mean flow does not strengthen itself, i.e. there is no positive feedback mechanism between the mean flow and Reynolds stresses. While all low Ra flows and high Ra flows in the limit of large Ω are well predicted by the model, the large Ra flows are mostly over predicted (except $Ra = 10^7$ and $\Omega = 0.1$, the only flow of that set-up that becomes truly turbulent, despite similar initial conditions). Presumably, even more important is that some of the flows for $Ra \geq 10^5$ exhibit a positive/prograde mean flow, indicated by a star symbol, which is especially prevalent at small Ω.

Turning the focus to set-up B, shown in figure 4.3 (b), the differences become even more obvious, since adding a mean temperature gradient enhances the effects of convection further. For $Ra = 10^3$ the picture is clear, as it is below the onset of convection $Ra_c \approx 1708$ for classical RBC even for the unbounded domains. The Reynolds stresses remain dominant, which preserves the development of a mean flow opposite to the TW direction. However, for $Ra \geq 10^3$, all but a few of the simulations end up with a prograde mean flow final state. In order to understand the role of the mean flow, we analyse the two terms on the right side of equation (4.1), which are presented in figure 4.4. The model neglects mean advection, it only captures contributions of $\overline{u'w'}$. As seen in figure 4.4 (a), this is justified for a flow without strong convection effects and the model predictions agree well with the Reynolds stresses obtained in the simulations. This is different from the situation in figure 4.4 (b), where obviously mean flow advection $W\partial_z U$ starts to take over. The shape of the mean flow advection curve is antiphase to the Reynolds stress curve and contributes
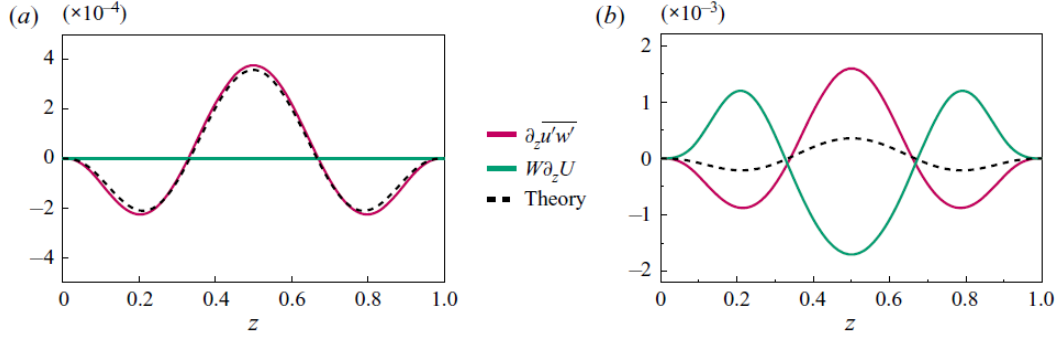
49

Figure 4.4: Mean profiles of Reynolds stress vs. mean flow advection contribution for $Ra = 10^4$ and $\Omega = 0.1$ for (a) $\Delta\theta = 0$ and (b) $\Delta\theta = 1$, where mean advection dominates. The flow in (a) moves retrograde due to the Reynolds stress contribution, while the flow in (b) shows a prograde mean flow ($\sqrt{Pr/Ra}\partial_z^2\langle U\rangle_x = \partial_z\langle\overline{u'w'}\rangle_x + \langle W\partial_z U\rangle_x$).

the most. This explains the reversal of the mean flow, from retrograde in figure 4.4 (a) to prograde in figure 4.4 (b).

The underlying reason for that will be examined in more detail in the next section. But briefly, the main argument is that there exist two competing mechanisms, one induced by the TW and the other induced by convection rolls, which act on different time scales. At small Ra, as convection rolls move considerably slower, an average over a few TW time periods can reliably separate both structures, so that the Reynolds stresses reflect mainly the TW contributions, while the mean field represents the convection rolls. Therefore, the dominant mean flow advection in figure 4.4 (b) reflects the dominance of advection by convection rolls as Ra increases.

A few more interesting observations can be deduced from figure 4.3 (b). First, compared to the theory, the simulations show significantly larger values at high Ra. Apparently, the mean zonal flow can be substantially stronger than expected and its velocity can exceed the TW phase velocity. Second, while the theory predicts the location of the maximum zonal flow at a constant diffusive time scale, the DNS indicates a coupling with the free-fall time rather than with the diffusive time and the maximum is found in the region $0.01 \leq \Omega \leq 0.1$. This is important, since natural flows often fall within this parameter range. We show this in the context of the Earth's atmosphere in section 4.4. Finally the instantaneous fields most often show three plumes (figure 4.2 b), while a classical RBC simulation with the same initial conditions would develop four plumes. Presumably, either the sinusoidal temperature distribution at the plates, or a pre-existing shear flow (before Rayleigh–Taylor instabilities develop) reduces the number of plumes. On this basis, we tested the linear stability of the Rayleigh–Taylor instabilities with an imposed shear flow, and found indeed that the wavelength of the most unstable mode decreases.

In figure 4.5 we show the total kinetic $E_{tot} = \frac{1}{2}\langle\overline{u_x^2 + u_z^2}\rangle_V^{1/2}$ and horizontal (zonal flow) kinetic energy $E_{hor} = \frac{1}{2}\langle\overline{u_x^2}\rangle_V^{1/2}$ in order to elucidate the energetic impact of the present zonal flows and to evaluate the strength of the vertical and horizontal motions. Set-up A (a) is clearly dominated by the horizontal kinetic energy throughout the whole parameter range. For $\Omega > 10^{-1}$, the kinetic energy drops close to zero and the temperature is transported by conduction only above this limit. However, before the kinetic energy drops, the curves show an energy enhancement. The location of
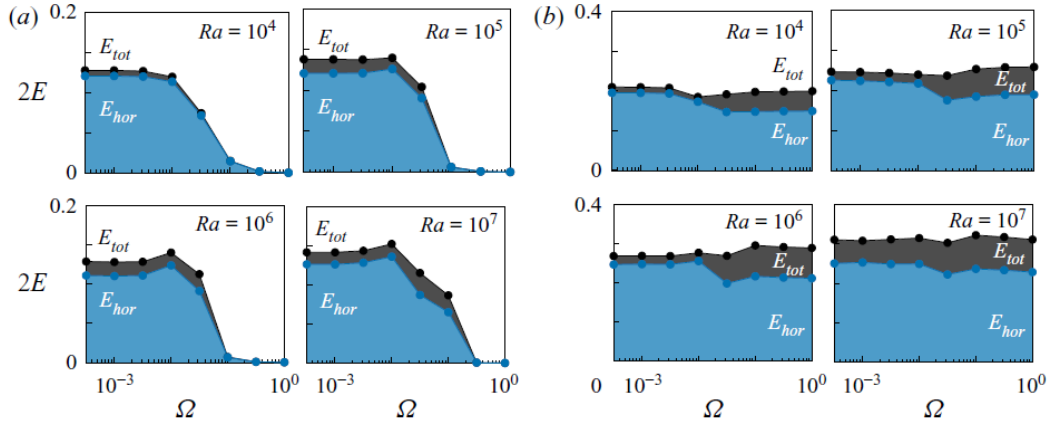
Figure 4.5: Total kinetic energy E_{tot} (black) and horizontal kinetic energy E_{hor} (blue) for (a) set-up A and (b) set-up B.

the energy maximum coincides with the maximum of the zonal flow (figure 4.3 a), which indicates that the zonal flows can have a significant imprint in the energy of the system. Likewise, set-up B (figure 4.5 b) is also dominated by horizontal kinetic energy. However, obviously for larger Ra and larger Ω, the magnitude of the vertical kinetic energy becomes increasingly important. This further supports that the neglect of the vertical velocity component W is eventually no longer justified for these parameter regimes.

Origin of prograde flows in convection dominated flows

In order to understand how prograde flows can emerge, we looked at the route from small to large Ra for a specific configuration. Set-up B and $\Omega = 0.1$ is well suited for this purpose, since the transition from a retrograde flow to a prograde flow appears early, already below $Ra = 10^4$ (figure 4.3 b). Thus, a simulation was initiated at $Ra = 1000$ and then Ra was progressively increased by 1000 each time after a steady state had settled. The time evolution of the total mean zonal flow is given in figure 4.6 (a). At the lowest Ra, the mean flow is retrograde. Increasing Ra to 2000 enhances its strength further, as anticipated. But already at $Ra = 3000$ the zonal flow breaks down and its vertical profile, as seen in figure 4.6 (b), flattens. Ultimately, at $Ra \geq 4000$ this profile flips over and the total zonal flow turns into a prograde state.

As we have shown in the preceding analysis (figure 4.4 b), in the presence of convection cells, the mean zonal flow can be fed by the base flow itself, in particular it is fed by the vertical advection of horizontal momentum $W\partial_z U$. Now, let us consider perfectly symmetric convection cells; although locally, at a position in x, momentum may be transported up- or downward, the symmetry, however, would balance this transport at another location and the net transport would become zero. Therefore there must be a symmetry breaking in the convection cells, which correlates W with $\partial_z U$. A possible mechanism, even discussed in the context of the moving heat source problem, was described by Thompson (1970) and theoretically analysed by Busse (1972), who showed that, in a periodic domain, convection rolls can become unstable to a mean shear flow. This mean shear tilts the convection cells such that their asymmetric circulation maintains a shear flow. In the following this mean flow instability will be called tilted cell instability. Busse (1972) showed the existence of
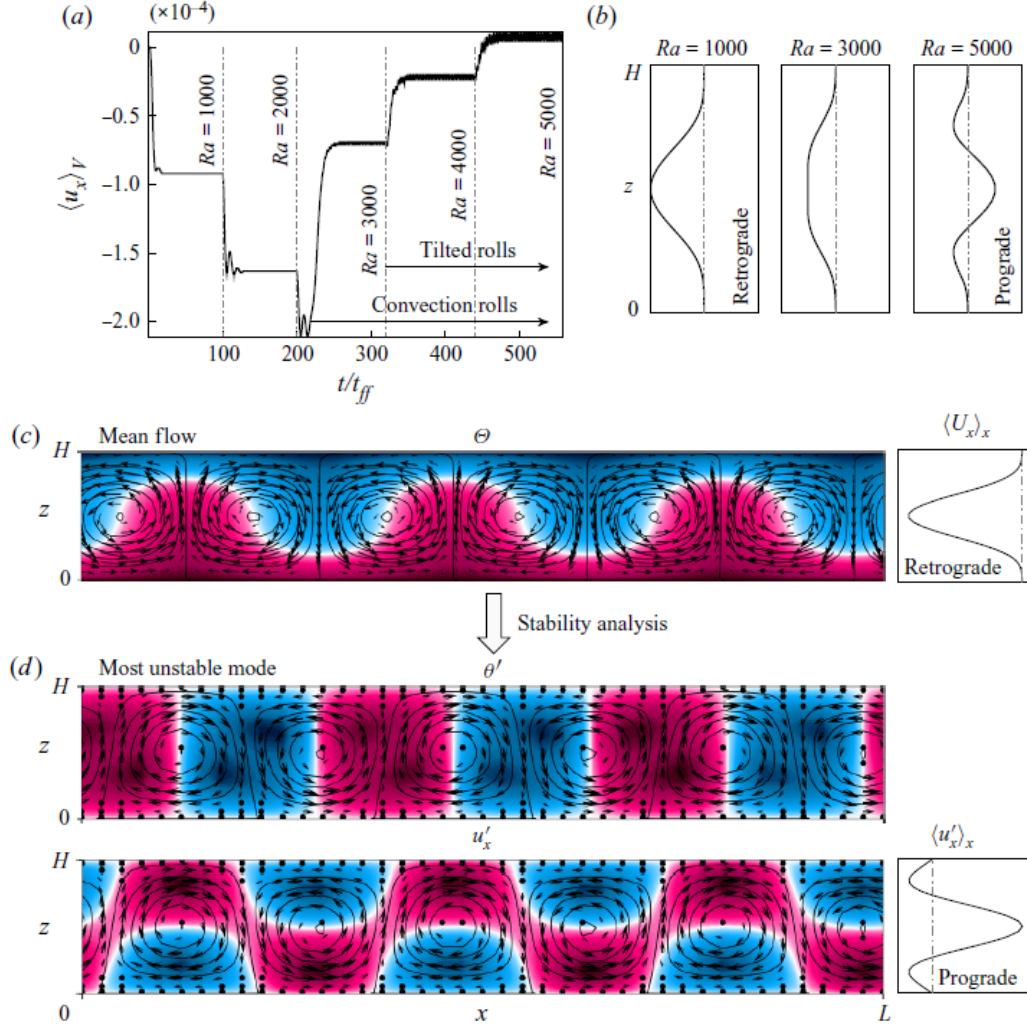
Figure 4.6: Path from a retrograde flow to a prograde flow. (a) Time evolution of the mean zonal flow; Ra was increased stepwise. For $Ra \geq 3000$ convection rolls form; for $Ra \geq 4000$ the rolls tilt significantly, and the mean zonal flow becomes positive. (b) The u_x profiles for $Ra = 1000, 3000, 5000$. (c) Mean flow extracted at $Ra = 3000$ (averaged over one TW period). (d) Result of the global stability analysis for the mean flow of (c), that becomes unstable for $Ra \geq 4000$ to tilted convection rolls.

this instability on a analytic base flow field. Differently, in the following we conduct a stability analysis on a base flow extracted from the DNS.

The first rise of the curve in figure 4.6 (a) at $Ra = 3000$ coincides with the observed onset of convection, which is slightly delayed compared to classical, unmodulated RBC ($Ra_c \approx 1708$). The convection cells at that point appear to be standing still, almost unaffected from the TW and clearly orders of magnitudes slower than the TW. Therefore a short time average, over one wave period, was applied to separate both time scales, which results in the base flow, as shown in figure 4.6 (c). Based on this base flow, a linear, temporal stability analysis of the full 2-D linearised Navier-Stokes equations was conducted. Details therefore are given in appendix 4.C. While no unstable mode was detected for $Ra = 3000$, for $Ra = 4000$ the mean flow becomes unstable, to the mode presented in figure 4.6 (d). The growth rate of it is

$\sigma \approx 0 + 0.2i$, suggesting no oscillatory behaviour (real part is zero) but exponential temporal growth (imaginary part larger than zero). This mode shares characteristics with the tilted cell instability described by Thompson (1970), in the sense that the mode induces a mean shear flow (see profile in figure 4.6 d). However, rather than the "pure" shear flows as presented by Thompson (1970) and Busse (1972, 1983) with a vanishing total net momentum when integrated vertically, the fluctuation profile found in our study (figure 4.6 d on the right) shows a more directed flow, negative in the vicinity of the plates and stronger positive in the centre. And especially interesting, its momentum profile has a similar shape as the final state solution of typical prograde flows, e.g. the profile on the right in figure 4.6 (b). A few more notes are necessary. The difference between the shape of the mode found in this work, compared to the ones from Thompson and Busse might be explained by different BCs, as both authors applied free-slip conditions at the plates, in contrast to our no-slip conditions. In addition, in their seminal works and in the work of Krishnamurti & Howard (1981), it was already remarked that the mean flow transition is caused by a spontaneous symmetry breaking and therefore the direction of the shear flow is somewhat arbitrary as it depends on the initial conditions. Indeed, a change in the grid size of the stability analysis led to a most unstable mode with a reversed shear flow profile compared to the mode shown in figure 4.6 (d). And finally, even though in figure 4.6 (a) tilted rolls are shown to start later as convection rolls, it actually is likely that the convection cells tilt as soon as convection sets in, it is just not clearly visible from the flow fields at that point.

In a nutshell, the mean flow is unstable – even in the absence of a boundary temperature modulation – to a mode with tilted convection cells and non-zero total mean horizontal velocity. Both modes, prograde and retrograde, are found in the global stability analysis, thus it remains unanswered why the DNS at high Ra almost exclusively end up moving in the same direction as the TW. The disturbance velocity profiles resemble those of the final mean flow velocity profiles, therefore, the presented mean flow instability is a plausible mechanism for the generation of moderate strong zonal flows after onset of convection, then dominating over the Reynolds stress mechanism, that is inherent to diffusion dominated flows.

Space–time structures

The flows found in this study revealed surprisingly rich formations. Therefore this part will be completed with examples of some space–time structures that have been observed in the 2-D system and, already ahead of the next part, in the 3-D cylindrical system. In addition, movies are provided as supplementary material.

In general, in two dimensions, as can be seen from figure 4.2, the temperature field is either symmetric around the horizontal mid-plane (set-up A), or not; in this case there exist plumes (set-up B). In the latter case, there are usually three up- and three down-welling plumes identifiable. In the 3-D case, the flow consists of rising and falling plumes, which together form a large scale circulation (LSC). If the TW propagates slowly (small Ω), the plumes (two dimensions) or respectively the LSC plane (three dimensions) drift with the same speed as the TW and both structures appear to be connected. However, as Ω increases and, hypothetically, the TW time scale τ_Ω becomes small compared to thermal diffusion τ_κ ($\tau_\kappa/\tau_\Omega = \sqrt{PrRa}\,\Omega$), the plumes (two dimensions) or LSC (three dimensions) "break-off" from the TW, forming two separate structures, acting on different time scales.

Figure 4.7 shows the space–time structures of the temperature field, evaluated at
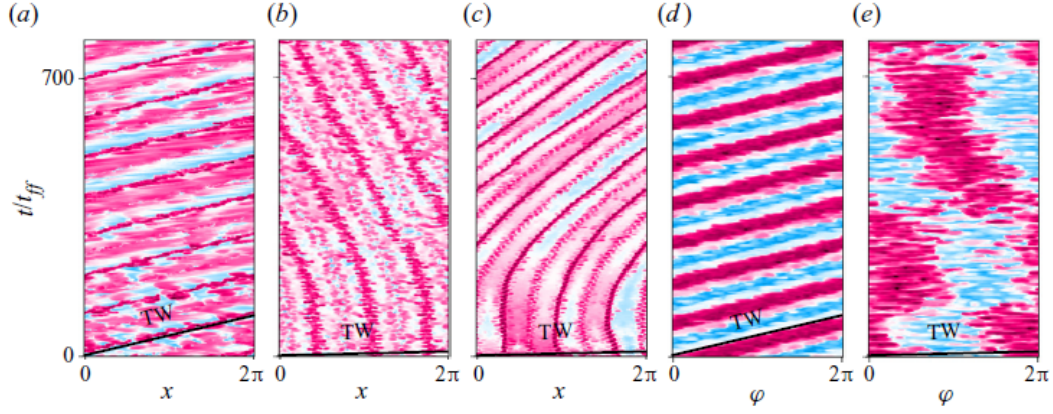
Figure 4.7: Evolution of the temperature at mid-height $z = H/2$, for (a-c) 2-D flows and (d,e) 3-D RBC ($r = 0.99R$) flows. (a) $\Omega = 0.01$, set-up A, (b) $\Omega = 0.1$, set-up A, (c) $\Omega = 0.1$, set-up B, (d) $\Omega = 0.01$, 3-D RBC and (e) $\Omega = 0.1$ 3-D RBC. All panels show $Ra = 10^7$. The black solid line in each plot indicates the TW speed.

mid-height, and in the 3-D case at mid-height and near the sidewall. The structures at mid-height either (i) travel with the same speed (but a phase difference) as the thermal wave (a,d), or travel with phase speeds different to the thermal wave and in this case either (ii) retrograde (b,e) or (iii) prograde (c). Regime (i) is expected for small Ra and/or small Ω parameters, (ii) is found for large Ra and large Ω, if no mean temperature is present and (iii) exists in strongly convection dominated flows for large Ra and large Ω, especially if a mean temperature gradient is present. Furthermore it is striking that temperatures between the left and right regions in the vicinity of the plumes centre (hottest or coldest regions in figure 4.7) do not necessarily fill with the same temperature (c). This gives further evidence of a mean flow instability, as it features similarities of the temperature field of the unstable mode given in figure 4.6 (d), due to which a plume loses its horizontal symmetry. Considering the speed of the drifting plumes (b,c), we observe initially exponential growth, as anticipated from an instability, followed by a, possibly, non-linear saturation.

4.4 Three-dimensional convective systems

The preceding part, as most of the existing literature, is confined to 2-D flows. Now we will discuss the moving heat source problem in the context of more complicated 3-D convective flows. In general, TW solutions are common amongst 3-D convective systems. Bensimon *et al.* (1990); Kolodner *et al.* (1988); Kolodner & Surko (1988) observed convection rolls propagating azimuthally in a large aspect ratio annulus near the onset of convection. Their drift velocity was of the order of magnitude 10^{-4} to 10^{-3}, however, drift velocity is not necessarily equal to the mean azimuthal flow. Another kind of TW solution in RBC systems are the spiral patterns found in large aspect ratio cells (Bodenschatz *et al.*, 1991, 2000). These spirals are rotating in either direction, although corotating spirals are more numerous (Cross & Tu, 1995), and are known to be coupled with an azimuthal mean flow (Decker *et al.*, 1994). Furthermore, in rotating systems travelling wave structures are quite common (Knobloch & Silber, 1990). These structures are strongly geometry dependent (Wang *et al.*, 2012) and
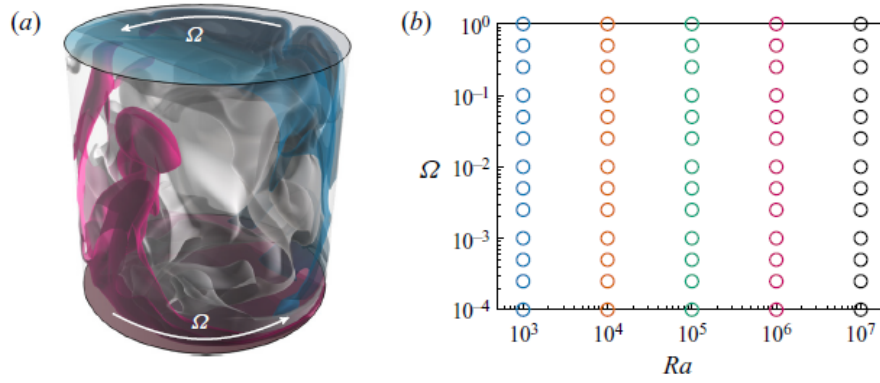
Figure 4.8: (a) Sketch of the cylindrical domain and imposed TW. (b) Studied parameter space. The mesh sizes $n_r \times n_\varphi \times n_z$ of the DNS are $48 \times 130 \times 98$ for $Ra = 10^3$, $96 \times 260 \times 196$ for $Ra = 10^4, 10^5, 10^6$ and $128 \times 342 \times 256$ for $Ra = 10^7$.

known to induce mean zonal flows that propagate pro- and retrograde (Zhang *et al.*, 2020).

Despite the vast literature on these phenomena, quantitative data on mean flows that are induced by external travelling thermal waves in 3-D flows seem to be rare. Therefore our main goal in this part is to gain insight into the strength and structure of such mean flows, and discuss whether their order of magnitude is relevant in natural flows. For this purpose we took the paradigm convective system cylindrical RBC and studied it by means of DNS.

4.4.1 Numerical set-up: cylindrical RBC

The set-up is essentially motivated by the original experiments of Fultz *et al.* (1959), where a heat source rotated around a cylinder with the radius R (diameter D), except, in our case, thermal waves travel at the bottom and top and a mean temperature gradient was applied, as in set-up B of the previous part. In particular, the temperature distribution is linear in the radial r-direction and consists of one wave period in φ that travels counterclockwise:

$$\theta(\varphi, r, z = 0, t) = 0.5 \left[\frac{r}{R} \cos(\varphi - 2\pi\Omega t) + 1 \right],$$

$$\theta(\varphi, r, z = H, t) = 0.5 \left[\frac{r}{R} \cos(\varphi - 2\pi\Omega t) - 1 \right].$$

Again, the mean temperature gradient, averaged over time, is the same as in classical RBC. The cell is shown in figure 4.8 (a). Furthermore, top and bottom plates are free slip ($\partial \mathbf{u}/\partial \mathbf{n} = 0$) and no-slip conditions are applied at the sidewall ($\mathbf{u} = 0$). All simulations are carried out for the parameters $Pr = 1$ and the aspect ratio $\Gamma \equiv D/H = 1$. The rather large aspect ratio is a sacrifice, in return, more simulations could be conducted and the parameter space in the region of interest is well resolved, as shown in figure 4.8 (b).
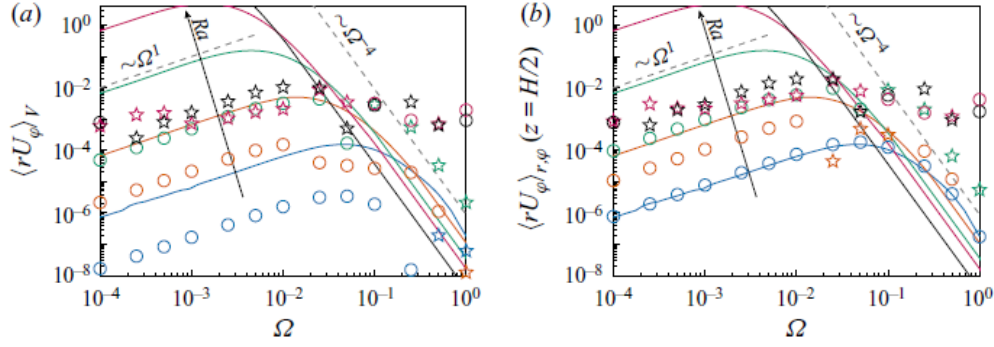
Figure 4.9: (a) Time- and volume-averaged zonal flow as a function of the heat source frequency Ω, (b) zonal flow at mid-height for 3-D RBC data: $Ra = 10^3$ (blue), 10^4 (orange), 10^5 (green), 10^6 (red) and 10^7 (black). Circles (stars) denote a retrograde (prograde) mean zonal flow, the solid lines of the corresponding colour show the results of the theoretical model by Davey (1967).

4.4.2 Results

Previously, we have shown that travelling thermal waves generate a mean horizontal, or, synonymously, a zonal flow. The same can be observed in the cylindrical system, where a zonal flow now refers to non-vanishing azimuthal mean flow. In the following, we evaluate its strength and direction and discuss the results in the context of the 2-D results. As no specific adjustments to the theoretical model have been made, from this point on, the model results are intended to serve mainly as references to the previous results. A brief remark beforehand: evaluating the time and volume average of u_φ proves problematic, as often flows are not purely pro- or retrograde. Therefore, rather than give precise scaling laws, the primary purpose of the subsequent analysis is to explore the parameter space, demonstrate the overall strength of the zonal flows and find the most critical wave frequencies and determine the critical Ra above which the results deviate substantively from the predictions.

Figure 4.9 shows (a) the total mean azimuthal momentum $\langle U_\varphi \rangle_V$ and (b) the value of $\langle U_\varphi \rangle_{r,\varphi}$ at the mid-height. As before, circles denote a retrograde, stars a prograde mean flow and the solid lines are the 2-D model solutions from Davey (1967), without modifications for no-slip walls. The obtained flows for small $Ra \leq 10^5$ share distinct features with the 2-D flows. The mean momentum converges to the asymptotic scalings, and, in fact, the data of figure 4.9 b collapse under a transformation with Ra remarkably well. For larger Ω, in particular $\Omega \geq 10^{-1}$, the most flows are found to be directed prograde, even for $Ra = 10^3$, which is different from the 2-D case. And as in two dimensions, the flow structures reveal a transition in this Ω-region. As was discussed in section 4.3.1, the plane of the LSC drifts with the same speed as the TW $(= \Omega)$, if the TW speed is small compared to thermal diffusion speed, and the LSC breaks off from the TW at larger Ω, forming separate structures, acting on different time scales. It is in the regime of this break-off above which a prograde flow is present. This process hints towards a similar mean flow instability, as discussed in §4.3.1, where the mean flow is now a slow LSC.

As Ra exceeds 10^5, turbulent fluctuations increase and the data in figure 4.9 become increasingly scattered. The asymptotic scalings are hardly determinable,
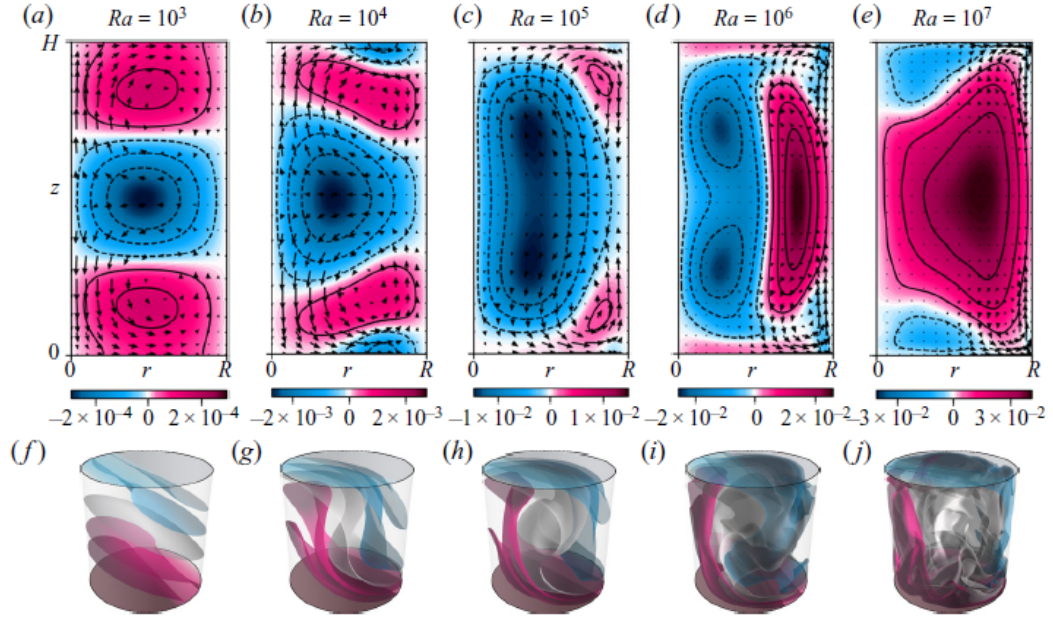
Figure 4.10: For a fixed TW frequency $\Omega = 0.01$. The azimuthally averaged mean azimuthal velocity $\langle U_\varphi \rangle_\varphi$ (top row) and the corresponding snapshots of the temperature θ (bottom row). As Ra increases, the core zonal flow becomes first stronger retrograde ($Ra = 10^4, 10^5$), then switches its state to a prograde flow originating from the sidewall ($Ra \geq 10^6$), while still increasing its strength (see colour bar).

even though $\langle U_x \rangle_V \sim \Omega^1$ for $\Omega \to 0$ appears still valid. The fluctuations can exceed their mean values, especially for small and large Ω. Despite the strong fluctuations, in regions of maximal zonal flow, i.e. $\Omega \approx 10^{-2}$, the mean values are highly significant and can induce zonal flows of the same order of magnitude as the TW frequency, $\langle U_\varphi \rangle_V \approx \mathcal{O}(10^{-2})$. Furthermore, similarly to the 2-D case, in three dimensions the zonal flows at high Ra are most of the time directed prograde, contrary to small Ra. From the vertical planes of the azimuthally and time-averaged azimuthal velocity, shown in figure 4.10, the dominance of prograde motion at large Ra becomes more obvious. Moreover, these figures reveal a complex, inhomogeneous flow, with strong differential rotation and poloidal mean velocities.

Vertical and radial momentum transport

In the following, we assess the contributing terms of the mean flow azimuthal momentum equation. For clarity, let us write the equation for u_φ explicitly

$$\partial_t u_\varphi + \frac{1}{r}\frac{\partial r u_\varphi u_r}{\partial r} + \frac{1}{r}\frac{\partial u_\varphi u_\varphi}{\partial \varphi} + \frac{\partial u_\varphi u_z}{\partial z} = $$
$$\frac{\partial p}{\partial \varphi} + \sqrt{\frac{Pr}{Ra}}\left[\frac{1}{r}\frac{\partial}{\partial r}\left(r\frac{\partial u_\varphi}{\partial r}\right) + \frac{1}{r^2}\frac{\partial^2 u_\varphi}{\partial \varphi^2} + \frac{\partial^2 u_\varphi}{\partial z^2} - \frac{u_\varphi}{r^2} + \frac{2}{r^2}\frac{\partial u_r}{\partial \varphi}\right].$$
$$(4.4)$$

First, we consider how U_φ changes in the vertical direction and, second, how it changes radially. Therefore, decomposing eq. (4.4) into its mean and fluctuating

components, and averaging over φ and r gives the following balance:

$$\sqrt{\frac{Pr}{Ra}} \left(\frac{\partial^2 \langle U_\varphi \rangle_{r,\varphi}}{\partial_z^2} - \frac{\langle U_\varphi \rangle_{r,\varphi}}{r^2} \right) =$$

$$\frac{\partial \langle \overline{u_\varphi' u_z'} \rangle_{r,\varphi}}{\partial_z} + \frac{\partial \langle U_\varphi U_z \rangle_{r,\varphi}}{\partial_z} + \langle \frac{\overline{u_\varphi' u_r'}}{r} \rangle_{r,\varphi} + \langle \frac{U_r U_\varphi}{r} \rangle_{r,\varphi}. \tag{4.5}$$

Analysing the radial dependence, on the other side, averaging over φ and z gives

$$\sqrt{\frac{Pr}{Ra}} \left(\frac{1}{r^2} \frac{\partial^2 \langle U_\varphi \rangle_{\varphi,z}}{\partial_r^2} - \frac{\langle U_\varphi \rangle_{\varphi,z}}{r^2} \right) =$$

$$\frac{1}{r} \frac{\partial r \langle \overline{u_\varphi' u_r'} \rangle_{\varphi,z}}{\partial_r} + \frac{1}{r} \frac{\partial r \langle U_\varphi U_r \rangle_{\varphi,z}}{\partial_r} + \langle \frac{\overline{u_\varphi' u_r'}}{r} \rangle_{\varphi,z} + \langle \frac{U_r U_\varphi}{r} \rangle_{\varphi,z}. \tag{4.6}$$

The right-hand side terms of these equations are evaluated for $\Omega = 10^{-2}$, which are shown in figure 4.11. We ensured, that in the simulations, the data were averaged over an integer number of TW periods, to prevent artefacts of the TW in the mean fields (the exact time values can be found in the supplementary material). When we compare the individual mean velocities for (a) $Ra = 10^3$ and (b) $Ra = 10^4$, it becomes clear that the mean field transport in both, vertical and radial, directions is rather negligible. Hence, the non-linear Reynolds stress sustains the mean zonal flow, just as in the 2-D case for small Ra (see figure 4.4 a), as expected (Stern, 1959; Davey, 1967). The small mean field contributions even reinforce the zonal flow, since the shape of the mean advection curves matches the shape of the Reynolds stress curve. Comparing further the vertical and the radial transports, we find that the former dominates the latter one by an order of magnitude. This proves that in this case the neglect of the radial currents, as suggested by Stern (1959), is justified, and therefore the mean momentum scalings (figure 4.9) match remarkably well with their 2-D analogue (figure 4.3), and the difference in the prefactors can presumably be explained by the different velocity BCs.

The situation for larger Ra (figure 4.11 c-e) is vastly different. First, the problem becomes considerably three-dimensional and the radial transport now reaches the same order of magnitude as the vertical transport (e.g. figure 4.11 c-e), which suggests that the validity of the 2-D analogy at large Ra is no longer justified. Furthermore, the mean field advection contributions, which can be partially seen from figure 4.10, increase significantly. As a matter of fact, locally, it can even exceed the Reynolds stress contributions. Furthermore, whereas for small Ra, vertical and radial momentum transports are present throughout the whole domain, at large Ra it becomes strongly confined to the boundaries. In particular, the vertical transport peaks close to the top and bottom boundaries and is less pronounced in the centre. The radial transport, on the other side, shows an interesting feature in the region $0.95 \leq r/R \leq 1$ (figure 4.11 d,e). All terms are simultaneously positive, which causes an enhanced zonal transport close to the sidewall. This may explain why a prograde flow first appears close to the sidewall (figure 4.10, $Ra = 10^6$) and, from there, spreads further inwards (figure 4.10, $Ra = 10^7$).

Sensitivity to the BCs and aspect ratio

The systems studied in this paper allow many variations of the velocity and temperature boundary conditions as well as geometrical characteristics of the system.
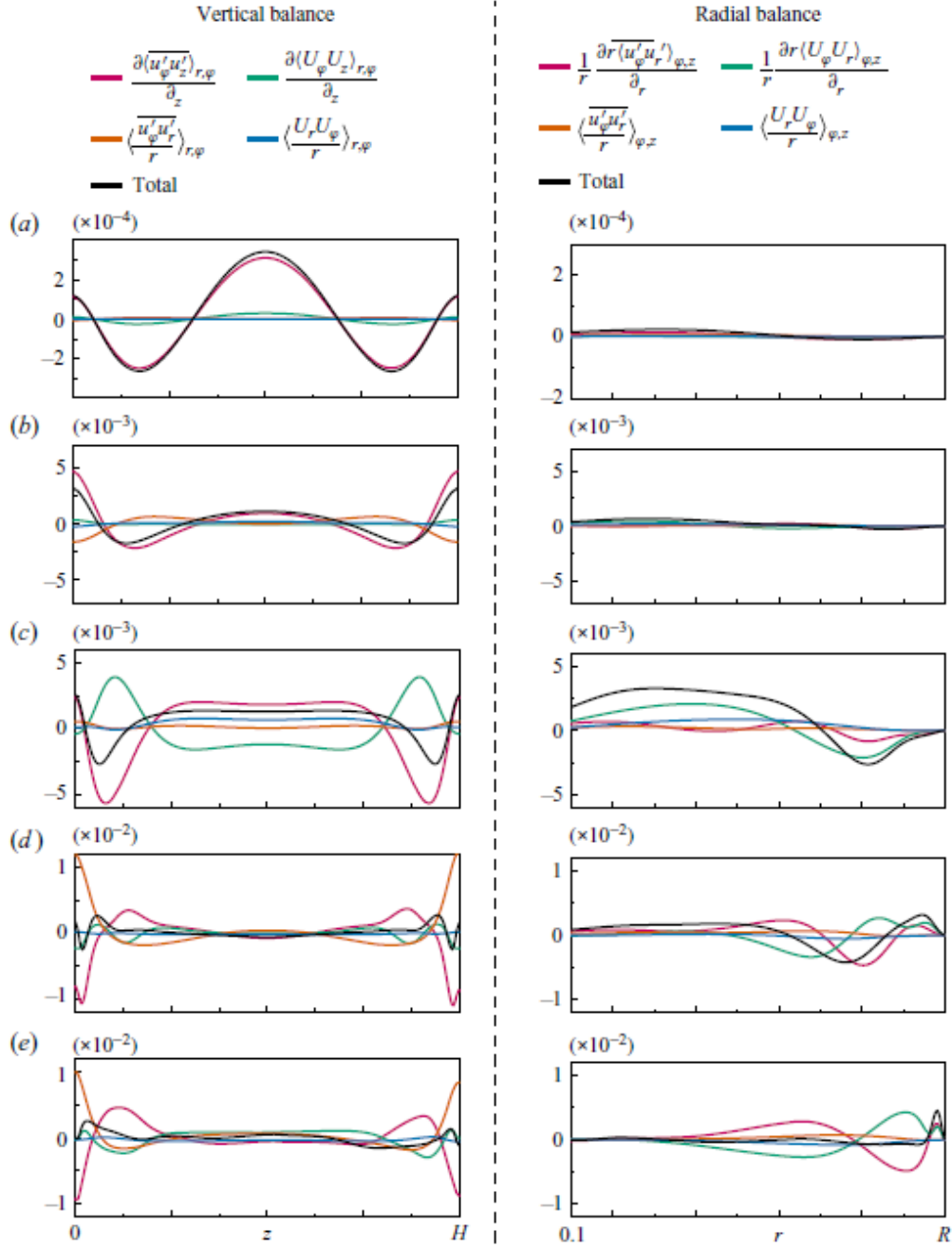
Figure 4.11: Components of the vertical momentum transport, eq. (4.5), (left) and the radial momentum transport, eq. (4.6), (right). Parameters: $\Omega = 10^{-2}$ and Ra: (a) 10^3, (b) 10^4, (c) 10^5, (d) 10^6 and (e) 10^7.

Discussing all of them goes beyond the scope of a single study. Nevertheless, in order to provide some preliminary intuition, we examine selected variations and their effects on the generation of the zonal flows. We do this for a single baseline simulation at $Ra = 10^5$ and $\Omega = 10^{-1}$. The mean angular momentum profiles are shown in figure 4.12.

First, we consider the effects of the aspect ratio. From classical RBC it is known that zonal flow properties depend strongly on Γ (Wang *et al.*, 2020a). In our case, a
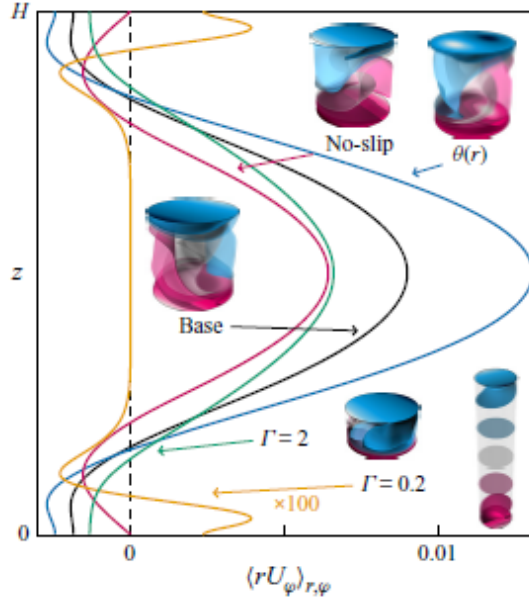
Figure 4.12: Mean angular momentum profile for $Ra = 10^5$ and $\Omega = 10^{-1}$. The curves show the effects of different imposed BCs and aspect ratios: baseline simulation (black, free-slip BCs, $\theta \sim r/R$ and $\Gamma = 1$), sinusoidal radial temperature BCs (blue, free-slip BCs, $\theta \sim sin(\pi r/R)$ and $\Gamma = 1$), no-slip (red, no-slip BCs, $\theta \sim r/R$ and $\Gamma = 1$), $\Gamma = 0.2$ (yellow, free-slip BCs, $\theta \sim r/R$ and $\Gamma = 0.2$) and $\Gamma = 2$ (green, free-slip BCs, $\theta \sim r/R$ and $\Gamma = 2$).

decrease of the aspect ratio from $\Gamma = 1$ to $\Gamma = 0.2$ (slender cell) weakens the zonal flow considerably by a factor of 100. Furthermore, the zonal flow becomes confined to the top and bottom plates, while no zonal flow is observed in the centre of the cell. On the other hand, increasing the aspect ratio to $\Gamma = 2$ has only minor impact on the zonal flow. We must note that for the case of $\Gamma = 0.2$, convection has yet not started and subsequent studies would be necessary to conclusively elucidate on the aspect ratio dependence.

The effects of the BC variations on the formation of zonal flows can be formulated as follows. No-slip conditions at the top and bottom plates lead to a slightly weaker, but qualitatively similar zonal flow. Likewise, replacing the linear radial temperature distribution at the plates by a sinusoidal distribution ($\theta \sim sin(\pi r/R)$) shows still a qualitatively similar angular momentum profile, although the strength of the zonal flow in the centre of the cell increases by a factor of about 1.5. This indicates that the system is rather sensitive to variations of the temperature BCs.

4.4.3 Example: Atmospheric boundary layer

Finally, we would like to illustrate the strength of the induced zonal flows on a concrete example. Assume an atmospheric boundary layer with a height of $\hat{H} = 500m$ and a vertical temperature difference of $\Delta T = 3°C$. Given a mean temperature of $10°C$, the material properties of air are approximately $\kappa = 2.0 \times 10^{-5}$ m^2/s, $\nu = 1.4 \times 10^{-5}$ m^2/s and $\alpha = 3.6 \times 10^{-3}$K^{-1}. From that, we find $Pr \approx 0.7$ and $Ra \approx 10^{16}$ and the free-fall units $u_{ff} \equiv \sqrt{\alpha g \hat{H} \Delta \theta} \approx 7$m/s, $t_{ff} \equiv \hat{H}/u_{ff} \approx 70$s.

This system is exposed to a travelling thermal wave through the solar radiation with a period of 24h, or, in dimensionless units $\Omega \approx 10^{-3}$. For simplicity, we say, the day and night difference is also about 3°C, which is likely to be a rather conservative estimate. Our study does not conclusively show how the zonal flows scale up to $Ra = 10^{16}$, but the results suggest a saturation at higher Ra, therefore we proceed using the maximum order of magnitude, which is $U_{\varphi} \approx 10^{-2}$ (for the given Ω it might be smaller). With these values, the thermal variation of the Earth's surface would induce a prevailing zonal flow of around 0.07m/s, or equivalently 0.3km/h. However, locally, it could exceed this value (see figure 4.10) multiple times, therefore speeds of 1km/h are conceivable. Nevertheless, the variance of this estimate is rather high. Subsequent studies have to examine the influence of Ra, Pr and the geometry, in order to make more confident statements about natural systems.

4.5 Conclusions

We have explored the original moving heat source problem by means of direct numerical simulations in 2-D and 3-D systems, for varying Rayleigh numbers Ra and travelling thermal wave frequency Ω. In the seminal works of Fultz *et al.* (1959) and Stern (1959), it was discovered that a system subjected to such a TW generates Reynolds stresses, which induce a large scale mean horizontal, or equivalently zonal, flow directed counter to the propagating thermal wave. Therefore, in the first part, we revisited the theoretical model proposed by Davey (1967) and found excellent agreement with the theory for low Ra flows, where even the absolute magnitude of the zonal flows is reproduced remarkably well. As Ra increases, the theoretical model overestimates the DNS data, which is consistent with the effects of higher-order nonlinear contributions (Whitehead, 1972; Young *et al.*, 1972; Hinch & Schubert, 1971).

However, when an unstable mean temperature gradient is added to the system, the flows deviate substantially from the initial predictions and often reverse their direction to a prograde moving zonal flow. Such a behaviour was theorised before to be the result of a mean flow instability caused by the tilt of convection cells (Thompson, 1970; Busse, 1972, 1983). Therefore, we have conducted a global linear stability analysis of a base flow near onset of convection and confirmed this hypothesis. The most unstable mode can give rise to a reverse of the horizontal velocity profile. Despite the strong plausibility, that this mean flow instability is the dominating mechanism at large Ra, the question remains open as to why prograde flow are more numerous than retrograde flows, while the mean flow instability suggests a spontaneous break of symmetry and therefore a more balanced distribution. In this context, it would be interesting to study in the future the interaction between the TW induced and convection rolls induced fields.

In the second part we have examined the moving heat source problem in the context of a 3-D cylindrical RBC system. The asymptotic scalings $\langle U_{\varphi} \rangle_V \sim \Omega^1$ for $\Omega \to 0$ and $\langle U_{\varphi} \rangle_V \sim \Omega^{-4}$ for $\Omega \to \infty$ of the 2-D theoretical model (Davey, 1967) still hold in this system, especially at small Ra. An analysis of the vertical and radial momentum transport contributions suggests that the radial transport is negligible at small Ra, (which justifies a 2-D approximation) but becomes relevant as Ra increases. Furthermore, again, large Ra is found to predominantly induce a prograde mean zonal flow. This gives more evidence that the prograde prevalence is likely not fully explained by the mean flow instability picture and further studyies are required to explain its origin.

The studied problem is sufficiently general and can be extended to more complicated systems (Whitehead, 1975; Shukla *et al.*, 1981; Mamou *et al.*, 1996). A more generalised theoretical framework already exists, which includes the influence of a basic stability and rotation (Stern, 1971; Chawla & Purushothaman, 1983), however, as this study showed, the theoretical models most often cannot fully explain the phenomena in convection dominated systems. Furthermore, the moving heat source problem might help to understand the ubiquitous structures present in rotating systems. In rotating RBC systems, the flow structures near the sidewall (Favier & Knobloch, 2020; Zhang *et al.*, 2020) are similar to a certain extent to those structures accounting due to the imposed TW.

Ultimately, this study also revealed that the estimates of the order of magnitudes are still afflicted with too large variances to make reliable statements about natural systems. A naive approach showed that atmospheric currents, caused by solar radiation and the Earth's rotation, can actually generate prevailing zonal flows of about 1.0 km/h. However, the variance of this estimate is rather high, it therefore is pivotal for subsequent studies to examine the sensitivities with Ra, Pr and the geometry in greater detail.

Appendix

4.A Theory for diffusion dominated flows

We follow the theory of Davey (1967), but solve the equations in a more general way, to allow for flexibility in the chosen BCs; for more details, the reader is referred to Davey (1967) or Kelly & Vreeman (1970). Neglecting the mean vertical velocity component, assuming the mean horizontal velocity to be independent of x and neglecting the contributions from the mean temperature field $\overline{\theta}$, the linearised, non-dimensionalised Navier-Stokes equations in two dimensions read

$$\partial_t u' + (U + u')\partial_x u' + w'\partial_z(U + u') = -\partial_x p + \nu^* \left(\frac{\partial^2 U}{\partial z^2} + \frac{\partial^2 u'}{\partial x^2} + \frac{\partial^2 u'}{\partial z^2} \right), \quad (4.7)$$

$$\partial_t w' + (U + u')\partial_x w' + w'\partial_z(w') = -\partial_z p + \nu^* \left(\frac{\partial^2 w'}{\partial x^2} + \frac{\partial^2 w'}{\partial z^2} \right) + \theta', \quad (4.8)$$

$$\partial_x u' + \partial_z w' = 0. \quad (4.9)$$

Here, u' and w' are, respectively, the horizontal and vertical components of the velocity fluctuations with respect to their time averages, i.e. U and $W = 0$, and θ' is the temperature fluctuation. For non-dimensionalisation we have used the free-fall velocity $u_{ff} \equiv (\alpha g \Delta \hat{H})^{1/2}$, the height $\hat{H}$ and the amplitude of the thermal TW, Δ, so that $\nu^* = \sqrt{Pr/Ra}$. Let us consider a single wave mode in the horizontal x-direction and in time t, e.g.:

$$w'(x, z, t) = \frac{1}{2} \left(\hat{w}(z)e^{+i(kx-2\pi\Omega t)} + \hat{w}^*(z)e^{-i(kx-2\pi\Omega t)} \right), \quad (4.10)$$

$$u'(x, z, t) = -\int \partial_z w' dx = \frac{i}{2k} \left(\partial_z \hat{w}(z)e^{+i(kx-2\pi\Omega t)} - \partial_z \hat{w}^*(z)e^{-i(kx-2\pi\Omega t)} \right), \quad (4.11)$$

$$\theta'(x, z, t) = \frac{1}{2} \left(\hat{\theta}(z)e^{+i(kx-2\pi\Omega t)} + \hat{\theta}^*(z)e^{-i(kx-2\pi\Omega t)} \right), \quad (4.12)$$

where the asterisk denotes the complex conjugate of a function. We will consider two

BCs (different scenarios), Scenario 1 describes a set-up, where two travelling thermal waves are imposed at the top and the bottom (whithout any phase difference). This case was considered in the present work. Scenario 2, on the other hand, describes a set-up, where the thermal wave travels only at the bottom, while the dimensionless top temperature equals zero.

Step 1: calculate $\hat{\theta}(z)$.

Neglecting dissipation in x, all convective terms and mean temperature contributions, the linearised non-dimensional energy equation reads

$$\partial_t \theta' = \kappa^* \left(\frac{\partial^2 \theta'}{\partial z^2} \right),$$

where $\kappa^* = 1/\sqrt{RaPr}$. This, together with eq. (4.12), leads to the following equation for the wave amplitude equation $\hat{\theta}(z)$:

$$\frac{d^2\hat{\theta}}{dz^2} - \lambda^2 \hat{\theta} = 0; \quad \lambda^2 = \frac{2\pi i \Omega}{\kappa^*}. \tag{4.13}$$

The solution to eq. (4.13), for the two scenarios is:

Scenario 1

$$\text{For } \hat{\theta}|_{z=-1/2} = \hat{\theta}|_{z=1/2} = \frac{1}{2}:$$
$$\hat{\theta}(z) = \frac{\cosh(\lambda z)}{2\cosh(\lambda/2)}.$$

Scenario 2

$$\text{For } \hat{\theta}|_{z=-1/2} = \frac{1}{2}, \hat{\theta}|_{z=1/2} = 0:$$
$$\hat{\theta}(z) = \frac{\sinh(\lambda/2 - \lambda z)}{2\sinh(\lambda)}.$$

Step 2: calculate $\hat{w}(z)$.

Eliminate the pressure term by cross-differentiation of (4.7) and (4.8), substitute (4.10)-(4.12), neglect convective terms and assume that the thermal wavelength is much larger than the height of the cell ($kH \ll 1$) to obtain

$$\frac{\partial^4 \hat{w}}{\partial z^4} - \alpha^2 \frac{\partial^2 \hat{w}}{\partial z^2} = k^2 \hat{\theta}, \quad \alpha^2 = \frac{2\pi i \Omega}{\nu^*}. \tag{4.14}$$

For $\hat{w}|_{z=1/2} = \hat{w}|_{z=-1/2} = \partial_z \hat{w}|_{z=1/2} = \partial_z \hat{w}|_{z=-1/2} = 0$, the solution to (4.14) is:

$$\hat{w}(z) = \frac{c_1}{\alpha^2} \cosh(\alpha z) + \frac{c_2}{\alpha^2} \sinh(\alpha z) + c_3 z + c_4 + c_5 \cosh(\lambda z) + c_6 \sinh(\lambda z).$$

Scenario 1

$$A = \frac{k^2}{2\nu^*\lambda^2(\lambda^2 - \alpha^2)},$$

$$c_1 = -\lambda\alpha A \frac{\tanh(\lambda/2)}{\sinh(\alpha/2)},$$

$$c_2 = 0,$$

$$c_3 = 0,$$

$$c_4 = A\left(\frac{\lambda}{\alpha}\frac{\tanh(\lambda/2)}{\tanh(\alpha/2)} - 1\right),$$

$$c_5 = \frac{A}{\cosh(\lambda/2)},$$

$$c_6 = 0.$$

Scenario 2

$$A = \frac{k^2}{4\nu^*\lambda^2(\lambda^2 - \alpha^2)},$$

$$c_1 = -\lambda\alpha A \frac{\tanh(\lambda/2)}{\sinh(\alpha/2)},$$

$$c_2 = \frac{-\alpha A\left(\frac{\lambda}{\tanh(\lambda/2)} - 2\right)}{(2/\alpha)\sinh(\alpha/2) - \cosh(\alpha/2)},$$

$$c_3 = -\frac{c_2}{\alpha}\cosh(\alpha/2) + \frac{\lambda A}{\tanh(\lambda/2)},$$

$$c_4 = A\left(\frac{\lambda}{\alpha}\frac{\tanh(\lambda/2)}{\tanh(\alpha/2)} - 1\right),$$

$$c_5 = \frac{A}{\cosh(\lambda/2)},$$

$$c_6 = \frac{-A}{\sinh(\lambda/2)}.$$

Step 3: calculate $U(z)$.

Averaging equation (4.7) over time and over one wavelength in x, we obtain the following equation for the mean flow $U(z)$:

$$\nu^*\frac{d^2U}{dz^2} = \frac{d}{dz}(\overline{u'w'}), \tag{4.15}$$

which can be solved via numerical integration using the no-slip BCs at the plates.

4.B Heat and momentum transport

The Nusselt number Nu and Reynolds number Re, based on the wind velocity, are defined as

$$Nu \equiv -\left\langle\left.\frac{\partial\bar{\theta}}{\partial z}\right|_{z=0}\right\rangle_{\mathcal{A}}, \quad Re \equiv \sqrt{\frac{Ra}{Pr}}\sqrt{\langle\overline{\mathbf{u}^2}\rangle_V},$$
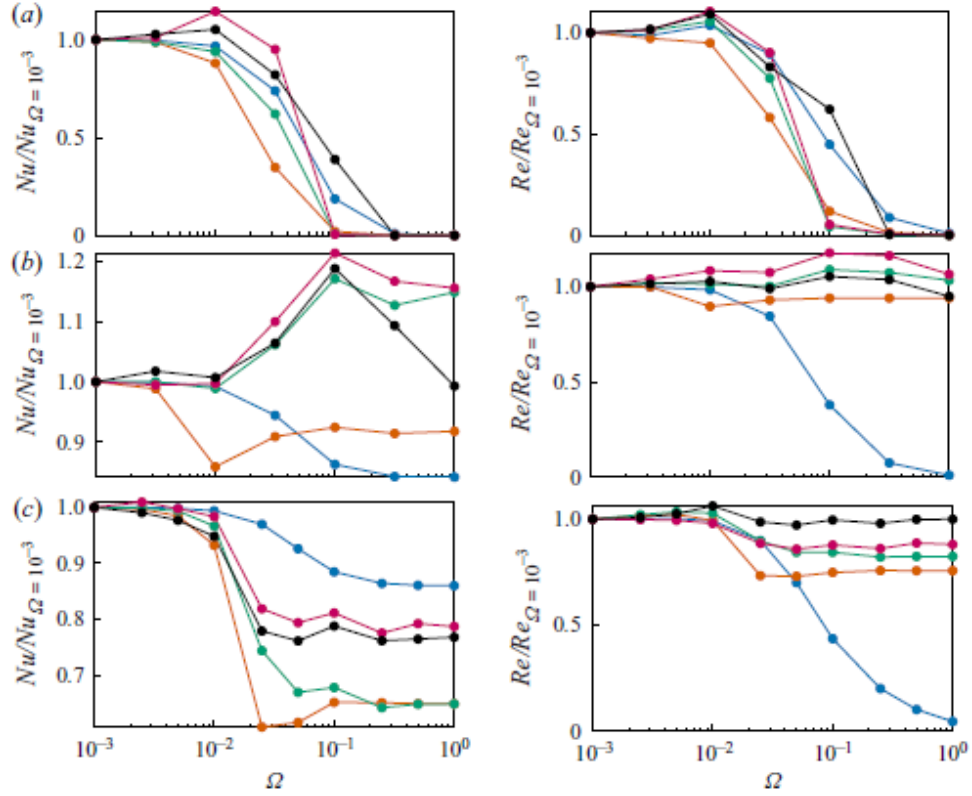
Figure 4.13: Normalised Nu and Re vs. Ω for a) 2-D set-up A, b) 2-D set-up B and c) 3-D Cylinder. $Ra = 10^3$ (●), 10^4 (●), 10^5 (●), 10^6 (●) and 10^7 (●).

where $\mathcal{A}$ denotes the horizontal plane for the cylinder or, respectively, the x-direction for the 2-D simulations. Figure 4.13 shows $Nu(\Omega)$ and $Re(\Omega)$, normalised by their values at $\Omega = 10^{-3}$. Their exact values are given in the supplementary material. The 2-D system (figure 4.13 a,b) shows a significant heat and momentum transport enhancement for certain TW speeds Ω, especially for large Ra. For the 3-D cylindrical system (figure 4.13 c), no clear correlation between the zonal flow maximum (see figure 4.9) and $Nu(\Omega)$ and $Re(\Omega)$ is observed. However, a small Re enhancement is present at $\Omega \approx 10^{-2}$.

4.C Linear stability analysis

In section 4.3.1 a temporal linear stability analysis was conducted to identify the most unstable eigenmode of the 2-D linearised Navier-Stokes equations, where a wave-like form was considered only in time. Thus, any flow quantity $\phi(x, z, t)$ is represented as $\phi(x, z, t) = \hat{\phi}(x, z)e^{-i\omega t}$ and the system of equations for the horizontal velocity u, the vertical velocity w, the pressure p and the temperature θ reads

$$
\begin{bmatrix}
L_{2-D} + D_x U & D_z U & D_x & 0 \\
D_x W & L_{2-D} + D_z W & D_z & -1 \\
D_x & D_z & 0 & 0 \\
D_x \overline{\theta} & D_z \overline{\theta} & 0 & K_{2-D}
\end{bmatrix}
\begin{bmatrix}
\hat{u} \\
\hat{v} \\
\hat{p} \\
\hat{\theta}
\end{bmatrix}
= \omega
\begin{bmatrix}
i & 0 & 0 & 0 \\
0 & i & 0 & 0 \\
0 & 0 & 0 & 0 \\
0 & 0 & 0 & i
\end{bmatrix}
\begin{bmatrix}
\hat{u} \\
\hat{v} \\
\hat{p} \\
\hat{\theta}
\end{bmatrix}, \quad (4.16)
$$

where

$$L_{2-D} = UD_x + WD_z + \sqrt{Pr/Ra}\left(-D_x^2 - D_z^2\right),$$
$$K_{2-D} = UD_x + WD_z + 1/\sqrt{RaPr}\left(-D_x^2 - D_z^2\right).$$

The overline represents the mean field quantity. In our study we applied the Chebyshev method to approximate the vertical gradient (D_z) and the Fourier method for the horizontal gradient (D_x). Conveniently, the corresponding differentiation matrices are available open source, e.g. we used the Python package *dmsuite*.

The linear set of equations (4.16) is solved as a generalized eigenvalue problem of the form $\mathbf{A}\hat{\phi} = \omega\mathbf{B}\hat{\phi}$, where the eigenvectors $\phi(x, z, t)$ represent the wave amplitudes and the eigenvalues ω their respective temporal behaviour. The matrices of the size $4 \times N_x \times N_z$ are very large and therefore an iterative solver has to be used (e.g. Python's *scipy.eigs*). The code has been validated by solving the Blasius boundary layer, pipe flow and Rayleigh–Taylor instability in one and two dimensions, and in closed and periodic domains. For all cases we have found excellent agreement with results in the literature.

5 Flow states and heat transport in Rayleigh–Bénard convection with different sidewall boundary conditions

This work addresses the effects of different thermal sidewall boundary conditions on the formation of flow states and heat transport in two- and three-dimensional Rayleigh–Bénard convection (RBC) by means of direct numerical simulations and steady-state analysis for Rayleigh numbers Ra up to 4×10^{10} and Prandtl numbers $Pr = 0.1, 1$ and 10. We show that a linear temperature profile imposed at the conductive sidewall leads to a premature collapse of the single-roll state, whereas a sidewall maintained at a constant temperature enhances its stability. The collapse is caused by accelerated growth of the corner rolls with two distinct growth rate regimes determined by diffusion or convection for small or large Ra, respectively. Above the collapse of the single-roll state, we find the emergence of a double-roll state in two-dimensional RBC and a double-toroidal state in three-dimensional cylindrical RBC. These states are most prominent in RBC with conductive sidewalls. The different states are reflected in the global heat transport, so that the different thermal conditions at the sidewall lead to significant differences in the Nusselt number for small to moderate Ra. However, for larger Ra, heat transport and flow dynamics become increasingly alike for different sidewalls and are almost indistinguishable for $Ra > 10^9$. This suggests that the influence of imperfectly insulated sidewalls in RBC experiments is insignificant at very high Ra - provided that the mean sidewall temperature is controlled.

5.1 Introduction

Understanding thermally induced convection as it arises in the earth's atmospheric/oceanic circulations and deducing its fundamental aspects from laboratory experiments is an ongoing endeavour which motivated numerous experimental and theoretical studies. In this realm, Rayleigh–Bénard convection (RBC), i.e. a fluid held between two parallel plates heated from below and cooled from above, is the most thoroughly investigated model system to study the complex physics behind natural convection such as pattern formation and the transition to turbulence (Bodenschatz *et al.*, 2000; Ahlers *et al.*, 2009*b*; Lohse & Xia, 2010).

Most of the early theoretical advances were made by considering the system as infinitely extended in the lateral direction. For instance, conventional linear-stability analysis predicts the formation of two-dimensional rolls (Chandrasekhar, 1961), while a weakly non-linear analysis reveals the stability regimes of these rolls and their path to subsequent oscillatory or stationary type bifurcations (Schlüter *et al.*, 1965; Busse, 1967, 1978). In laboratory experiments, however, we must resort to laterally confined systems where our understanding is far less complete. In particular, when the lateral size of the container is close to or less than the height of the cell, the presence of sidewalls plays an important role (Roche, 2020; Shishkina, 2021). Therefore, this study focuses on the effects of different thermal sidewall boundary conditions on heat transfer and the emergence of different flow states.

Different sidewalls are known to affect the critical Rayleigh number Ra_c above which convection sets in (Buell & Catton, 1983; Hébert *et al.*, 2010), and perfectly conducting sidewalls have been found to delay the onset compared to adiabatic sidewalls. In an attempt to better understand the flow regimes above onset, bifurcation analyses were performed in a cubic domain for adiabatic (Puigjaner *et al.*, 2004) and perfectly conducting sidewalls (Puigjaner *et al.*, 2008). The bifurcation diagrams for the conducting sidewalls are generally more complex, and double-toroidal states predominate over the classical single-roll structure found for adiabatic sidewalls. Sidewalls also have a strong influence on pattern formation (Cross & Hohenberg, 1993; de Bruyn *et al.*, 1996; Bodenschatz *et al.*, 2000) and different sidewall boundary conditions lead to differences in observable patterns even in cells with large aspect ratio (Hu *et al.*, 1993).

In RBC experiments, spurious sidewall heat fluxes are a major practical difficulty that can substantially bias global heat transport measurements. Ahlers (2000) reported that naive sidewall corrections can overstate Nusselt number measurements by up to 20% and underestimate the scaling of the Nusselt number Nu with respect to the Rayleigh number Ra ($Nu \sim Ra^{\lambda}$) reflected in the reduction of the scaling exponent λ by about 2%, underscoring the importance of more sophisticated sidewall corrections. Roche *et al.* (2001) further emphasized this conclusion by showing that the sidewall corrections can be considerably larger than assumed, leading to scaling exponents closer to the turbulent scaling of $Nu \sim Ra^{1/3}$ (Grossmann & Lohse, 2000, 2001, 2004) than previously measured. Probably the most important question in convection today is whether the ultimate regime in confined geometries has the same scaling as predicted for unbounded domains, i.e. $Nu \sim Ra^{1/2}$ (up to different logarithmic corrections), as proposed by Kraichnan (1962) and Grossmann & Lohse (2011). Another important question is when and how exactly the transition to the ultimate regime takes place in confined geometries. Laboratory experiments (Chavanne *et al.*, 1997; Niemela *et al.*, 2000; Chavanne *et al.*, 2001; Ahlers *et al.*, 2009*a*,

2012; He *et al.*, 2012*b*; Urban *et al.*, 2014; Roche, 2020) in this extremely high Ra regime are notoriously difficult to perform and potentially sensitive to several unknowns of the system, one of which is the influence of imperfectly isolated/adiabatic sidewalls.

Numerical simulations were performed incorporating thermal conduction in the solid sidewall to clarify the differences between an ideal adiabatic setup and a finite thermal conductivity sidewall (Verzicco, 2002; Stevens *et al.*, 2014; Wan *et al.*, 2019). The results of these studies suggest that different thermal properties of the sidewall alter the mean flow structure, leading to significant differences in global heat transport in the low to mid Ra range. However, this effect vanishes for larger Ra, at least when the sidewall temperature is constant and maintained at the arithmetic mean of upper and lower plate temperatures. Conversely, if the sidewall temperature deviates from the arithmetic mean, differences in heat transport persist even for large Ra. This indicates that it is more important to keep the environment at the correct temperature than to shield the interior of the cell from its surroundings.

Despite extensive previous work, the spatial distribution of flow and heat transport in confined geometries with different thermal boundary condition has not been exhausted, especially the conditions related to real experimental sidewall boundary conditions. In the present work, we investigate RBC with the following thermal sidewall boundary conditions: adiabatic, constant temperature (isothermal) and linear temperature. In the first part of the results, we focus on a steady-state analysis based on an adjoint descent algorithm (Farazmand, 2016) to identify different flow states, their properties and their evolution over Ra. In the second part, the analysis is complemented and extended to higher Ra into the turbulent regime by a set of direct numerical simulations (DNS) for a 2D box and 3D cylindrical setup, covering a range of $10^3 \leq Ra \leq 4 \times 10^{10}$ and $10^3 \leq Ra \leq 10^9$, respectively, aiming for a more complete picture. We first present our numerical methods, discuss the results and conclude with our main findings.

5.2 Numerical methods

5.2.1 Governing equations

The dimensionless control parameters in RBC are the Rayleigh number $Ra \equiv \alpha g \Delta H^3/(\kappa\nu)$, the Prandtl number $Pr \equiv \nu/\kappa$, and the width-to-height aspect ratio of the box, $\Gamma \equiv L/H$. Here, α denotes the isobaric thermal expansion coefficient, ν the kinematic viscosity, κ the thermal diffusivity of the fluid, g the acceleration due to gravity, $\Delta \equiv T_+ - T_-$ the difference between the temperatures at the lower (T_+) and upper (T_-) plates, H the distance between the parallel plates (the container height), and L the length of the container or the diameter in the case of a cylindrical setup. In this study, we focus on variations with Ra, while $Pr = 1$ is fixed for most results in this paper except for a Pr-dependence study in section 5.4.5, and $\Gamma = 1$ is held constant throughout the study.

The governing equations in the Oberbeck–Boussinessq approximation for the dimensionless, incompressible velocity $\mathbf{u}$, temperature θ and kinematic pressure p read as follows:

$$
\begin{aligned}
\partial\mathbf{u}/\partial t + \mathbf{u} \cdot \boldsymbol{\nabla}\mathbf{u} + \boldsymbol{\nabla}p &= \sqrt{Pr/Ra}\boldsymbol{\nabla}^2\mathbf{u} + \theta\mathbf{e}_z, \\
\partial\theta/\partial t + \mathbf{u} \cdot \boldsymbol{\nabla}\theta &= 1/\sqrt{PrRa}\boldsymbol{\nabla}^2\theta, \quad \boldsymbol{\nabla} \cdot \mathbf{u} = 0.
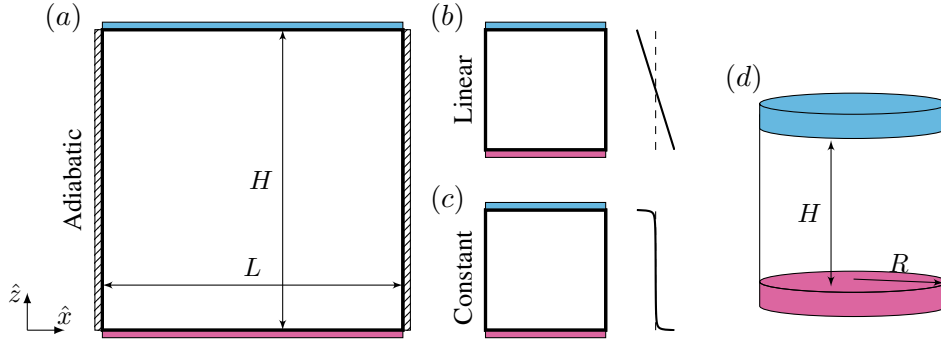\end{aligned}
\tag{5.1}
$$

Figure 5.1: 2D Numerical setup of (a) adiabatic, (b) linear and (c) constant sidewall temperature boundary conditions. (d) Sketch of cylindrical domain. Profiles next to (b) and (c) show the imposed sidewall temperature distribution.

The equations were made dimensionless using the free-fall velocity $u_{ff} \equiv (\alpha g \Delta H)^{1/2}$, the free-fall time $t_{ff} \equiv H/u_{ff}$, the temperature difference $\Delta \equiv T_+ - T_-$ between bottom (T_+) and top (T_-) plates and H the cell height. Here $\mathbf{e}_z$ is the unit vector in the vertical z-direction. This set of equations is solved with the direct numerical solver GOLDFISH, which uses a fourth-order finite volume discretization on a staggered grid and a third order Runge–Kutta time scheme. The code has been widely used in previous studies and validated against other direct numerical simulation codes (Kooij *et al.*, 2018; Reiter *et al.*, 2021*a*).

5.2.2 Boundary conditions

We study 2D RBC in a square box and 3D RBC in a cylindrical domain. The setups and profiles of the sidewall (SW) boundary conditions (BCs) used are shown in figure 5.1. The adiabatic, linear and (almost) constant conditions for the sidewall region δV_S are defined by

$$\text{adiabatic:} \quad \partial\theta/\partial\chi = 0, \tag{5.2}$$

$$\text{linear:} \quad \theta = \theta_+ + z\left(\theta_- - \theta_+\right), \tag{5.3}$$

$$\text{constant:} \quad \theta = \begin{cases} \frac{-k(2z-1)}{k+2z}\left(\theta_+ - \theta_m\right), & 0 \leq z \leq 1/2, \\ \frac{k(2z-1)}{k-2z+2}\left(\theta_- - \theta_m\right), & 1/2 < z \leq 1, \end{cases} \tag{5.4}$$

with the temperature of the lower plate $\theta_+ = 1/2$, the temperature of the upper plate $\theta_- = -1/2$, their arithmetic mean $\theta_m = 0$, $z \equiv z/H \in [0,1]$ and $\chi = x$ for box and $\chi = r$ for cylinder, respectively. As for the constant temperature conditions, most of the sidewall is kept at a nearly uniform temperature (θ_m), except for the transition regions in the vicinity of the top and bottom plates to ensure a smooth temperature distribution. The parameter $0 < k \ll 1$ in eq. (5.4) defines the thickness of the transition layer. Here we used $k = 0.01$, which gives a fairly sharp albeit sufficiently smooth transition, as can be seen in figure 5.1 (c). Moreover, the velocity no-slip conditions apply to all walls, i.e. $\mathbf{u}\big|_{\text{wall}} = 0$.

5.2.3 Adjoint descent method

A complementary analysis to direct numerical simulations is the study of the Boussinesq equations by means of its invariant solutions. Hopf (1948) conjectured that the solution of the Navier–Stokes equations can be understood as a finite but possibly large number of invariant solutions, and turbulence from this point of view is the migration from the neighbourhood of one solution to another. While highly chaotic systems seem hopelessly complex to understand, laminar or weakly chaotic flows can often be captured quite well with this approach. In this work, we focus solely on solutions for steady-states (equilibrium).

Determining steady-state solutions can be quite difficult, especially when the number of dimensions is large as it is the case for most fluid mechanical problems. The most commonly used numerical method for this task is Newton's method, which usually uses the generalized minimal residual (GMRES) algorithm to solve the corresponding systems of linear equations (Saad & Schultz, 1986). This method generally shows fast convergence rates when the initial estimate is close to the equilibrium point. However, if the initial estimate is too far from the equilibrium, Newton's method often fails. In particular, for fluid mechanics, the basin of attraction of Newton's method can be quite small, making the search for steady-states highly dependent on the initial guess. Here we consider an alternative approach recently proposed by Farazmand (2016) based on an adjoint method. Farazmand (2016) has shown that this adjoint-descent method can significantly improve the chance of convergence compared to the Newton–descent method, and thus more reliably capture equilibrium states from a given initial state, but at the cost of a generally slower convergence rate. A detailed derivation of the algorithm can be found in Farazmand (2016). Below we sketch the idea of the method.

Suppose we want to find equilibrium solutions of a particular PDE (in our case the Boussinessq equations)

$$\partial_t \mathbf{u} = F(\mathbf{u}), \tag{5.5}$$

with $\mathbf{u} = \mathbf{u}(\mathbf{x}, t)$. The equilibrium's of $F(\mathbf{u})$ can be generally unstable and therefore difficult to detect. The idea is to search a new PDE, i.e.

$$\partial_\tau \mathbf{u} = G(\mathbf{u}), \tag{5.6}$$

which solutions always converge to the equilibrium solutions of (5.5) when the fictitious time τ goes to infinity

$$\|F(\mathbf{u})\|_{\mathcal{A}}^2 \to 0 \quad \text{as} \quad \tau \to \infty, \tag{5.7}$$

with the weighted energy norm $\|\cdot\|_{\mathcal{A}} \equiv \langle\cdot,\cdot\rangle_{\mathcal{A}} \equiv \langle\cdot,\mathcal{A}\cdot\rangle$ for a certain real self-adjoint and positive definite operator $\mathcal{A}$. $F(\mathbf{u})$ evolves along a trajectory $\mathbf{u}'$ in accordance with

$$\frac{1}{2}\partial_\tau \|F(\mathbf{u})\|_{\mathcal{A}}^2 = \langle\delta F(\mathbf{u},\mathbf{u}'), F(\mathbf{u})\rangle_{\mathcal{A}}, \tag{5.8}$$

where $\delta F(\mathbf{u},\mathbf{u}') \equiv \lim_{\varepsilon\to 0}\frac{F(\mathbf{u}+\varepsilon\mathbf{u}')-F(\mathbf{u})}{\varepsilon}$ of $F(\mathbf{u})$ is the functional Gateaux derivative at $\mathbf{u}$ in the direction $\mathbf{u}'$. In the Newton-descent method, the search direction $\mathbf{u}'$ is approximated from $\delta F(\mathbf{u},\mathbf{u}') = -F(\mathbf{u})$ by using, for example, a GMRES iterative algorithm. For the adjoint-descent method, on the other hand, we rewrite eq. (5.8)

in the form

$$\frac{1}{2}\partial_\tau \|F(\mathbf{u})\|_\mathcal{A}^2 = \langle \mathbf{u}', \delta F^\dagger(\mathbf{u}, F(\mathbf{u}))\rangle_\mathcal{A}, \tag{5.9}$$

where $\delta F^\dagger$ is the adjoint operator of the functional derivative δF. For $\mathbf{u}' = -\delta F^\dagger(\mathbf{u}, F(\mathbf{u}))$ one guarantees that $\|F(\mathbf{u})\|_\mathcal{A}^2$ decays to zero along the trajectory $\mathbf{u}'$, since then $\frac{1}{2}\partial_\tau \|F(\mathbf{u})\|_\mathcal{A}^2 = -\|\delta F^\dagger(\mathbf{u}, F(\mathbf{u}))\|_\mathcal{A}^2$. Letting $\mathbf{u}$ evolve along the adjoint search direction ensures the convergence to an equilibrium, thus we find the desired PDE $G(\mathbf{u}) \equiv \mathbf{u}'$, i.e.

$$G(\mathbf{u}) = -\delta F^\dagger(\mathbf{u}, F(\mathbf{u})). \tag{5.10}$$

The choice of the norm $\|\cdot\|_\mathcal{A}$ is important for the algorithm to be numerically stable and is explained in more detail in the appendix. As mentioned, the operator $\mathcal{A}$ should be real-valued, positive-definite and self-adjoint. Following Farazmand (2016), we use an operator $\mathcal{A}$ that is closely related to the inversed Laplacian, i.e. $\mathcal{A} = (I - \alpha\boldsymbol{\nabla}^2)^{-1}$ where I is the identity operator and α is a non-negative scalar parameter. For $\alpha = 0$ this norm converges to the L^2-norm and for $\alpha > 0$ it effectively dampens smaller scales and provides a better numerical stability.

The linear adjoint equations for the Boussinesq equations (5.1) read

$$-\partial_\tau \mathbf{u} = \left(\boldsymbol{\nabla}\tilde{\mathbf{u}}'' + (\boldsymbol{\nabla}\tilde{\mathbf{u}}'')^{\mathrm{T}}\right)\mathbf{u} - \tilde{\theta}''\boldsymbol{\nabla}\theta - \boldsymbol{\nabla}p'' + \sqrt{Pr/Ra}\boldsymbol{\nabla}^2\tilde{\mathbf{u}}'',$$
$$-\partial_\tau \theta = \mathbf{u} \cdot \boldsymbol{\nabla}\tilde{\theta}'' + 1/\sqrt{PrRa}\boldsymbol{\nabla}^2\tilde{\theta}'' + \vec{\mathbf{e}}_z \cdot \tilde{\mathbf{u}}'',$$
$$\boldsymbol{\nabla} \cdot \mathbf{u}'' = 0, \quad \boldsymbol{\nabla} \cdot \mathbf{u} = 0 \tag{5.11}$$

(see derivations in the appendix). Here the double prime fields $\mathbf{u}''$ and θ'' denote the residuals of the Navier–Stokes eq. (5.1), i.e.

$$\mathbf{u}'' \equiv -\mathbf{u} \cdot \boldsymbol{\nabla}\mathbf{u} - \boldsymbol{\nabla}p + \sqrt{Pr/Ra}\boldsymbol{\nabla}^2\mathbf{u} + \vec{\mathbf{e}}_z\theta,$$
$$\theta'' \equiv -\mathbf{u} \cdot \boldsymbol{\nabla}\theta + 1/\sqrt{PrRa}\boldsymbol{\nabla}^2\theta. \tag{5.12}$$

and $\tilde{\mathbf{u}}'' \equiv \mathcal{A}\mathbf{u}''$ as well as $\tilde{\theta}'' \equiv \mathcal{A}\theta''$. For simplicity, let $\mathbf{q} \equiv (\mathbf{u}, \theta)$, then the adjoint descent method consists of three steps

1. Find the residuals $\mathbf{q}''$ according to eq. (5.12).

2. Solve $\tilde{\mathbf{q}}'' = \mathcal{A}\mathbf{q}''$ for $\tilde{\mathbf{q}}''$.

3. Update $\mathbf{q}$ according to eq. (5.11).

In step (i), we solve the time-stepping eq. (5.1), where we use a standard pressure projection method and treat the diffusion term implicitly. The time step size Δt can be chosen independently of the artificial time step size $\Delta\tau$ of the adjoint equations. For step (ii), using the energy norm $\|\cdot\|_\mathcal{A}$ with the operator $\mathcal{A} = (I - \alpha\boldsymbol{\nabla}^2)^{-1}$, we solve the Helmholtz-type equation $(I - \alpha\boldsymbol{\nabla}^2)\tilde{\mathbf{q}}'' = \mathbf{q}''$. The integration of the adjoint equations in step (iii) is similar to step (i), but all terms are treated explicitly. Through tests, we found that the artificial time step $\Delta\tau$ can be chosen much larger than Δt in some cases, i.e. for large Ra.

The boundary conditions of $\tilde{\mathbf{u}}''$ and $\tilde{\theta}''$ result from integration by parts in the derivation of the adjoint equations. Evaluation of the adjoint operator of the diffusion terms yields

$$\int_V \tilde{\mathbf{u}}''\boldsymbol{\nabla}^2\mathbf{u}'dV = \int_V \mathbf{u}'\boldsymbol{\nabla}^2\tilde{\mathbf{u}}''dV + \int_S \mathbf{u}'(\boldsymbol{\nabla}\tilde{\mathbf{u}}'' \cdot \mathbf{n})dS - \int_S \tilde{\mathbf{u}}''(\boldsymbol{\nabla}\mathbf{u}' \cdot \mathbf{n})dS, \tag{5.13}$$
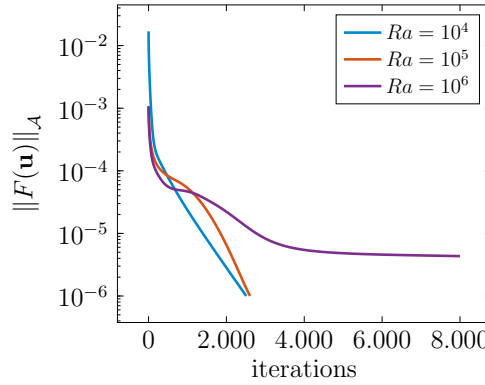
Figure 5.2: Convergence of the adjoint-descent method for three different Ra, starting from the same initial field. The time-step size for which the algorithm is just stable increased with Ra, i.e., for these cases we used $\Delta\tau = 0.5$ ($Ra = 10^4$), $\Delta\tau = 2.0$ ($Ra = 10^5$) and $\Delta\tau = 5.0$ ($Ra = 10^6$). All three cases converged to large-scale circulation flow states as described in section 5.3.2.

where we see the occurrence of two additional boundary terms (the last two terms) evaluated on the boundary domain S. The first boundary term vanishes since the search direction $\mathbf{u}'$ is zero on the boundaries. The second term can be eliminated if we also choose homogeneous Dirichlet boundary conditions for the adjoint field $\tilde{\mathbf{u}}''$ on S. The same logic applies to homogeneous Neumann conditions. For the pressure field p'', we apply Neumann boundary conditions conditions on all walls. In this study, all flow states showed good overall convergence ($\|F(\mathbf{u})\|_{\mathcal{A}}^2 \leq 10^{-5}$) and the velocity fields where almost divergence free ($\|\boldsymbol{\nabla} \cdot \mathbf{u}\|_{L^2} \leq 10^{-3}$). However, the rigorous verification of the chosen pressure BCs has yet to be performed. Another interesting point, reserved for later investigation, is whether a vorticity-streamfunction formulation might be better suited to resolve issues with the boundary conditions.

For the steady-state analysis, we use a Galerkin method with Chebyshev bases in x and z directions and a quasi-inverse matrix diagonalization strategy for better efficiency (Shen, 1995; Julien & Watson, 2009; Oh, 2019; Mortensen, 2018). The code is publicly available (Reiter *et al.*, 2021*b*). We use an implicit backward Euler time discretization and alias the fields using the 2/3 rule by setting the last 1/3 high-frequency spectral coefficients to zero after evaluating the nonlinear terms. When used as a direct numerical solver, we found excellent agreement with our finite-volume code GOLDFISH. In addition, the steady-states from the adjoint descent method showed excellent agreement with those found by an alternative Newton–GMRES iteration. Figure 5.2 shows the convergence rates for three different Ra, starting from the same initial state. Overall, we find that the convergence chance is improved over the Newton-descent method, although the convergence rate suffers and larger Ra are either not feasible with the current approach as implemented in our code or diverge after some time. Therefore, we restrict the steady-state analysis to flows in the range $Ra \leq 10^7$ and investigate larger Ra using direct numerical simulations. One conceivable problem with the current approach is that the currently used energy norm with the operator $\mathcal{A} \equiv (I - \alpha\boldsymbol{\nabla}^2)^{-1}$ dampens smaller scales in order to increase the stability of the algorithm. But for larger Ra, smaller scales
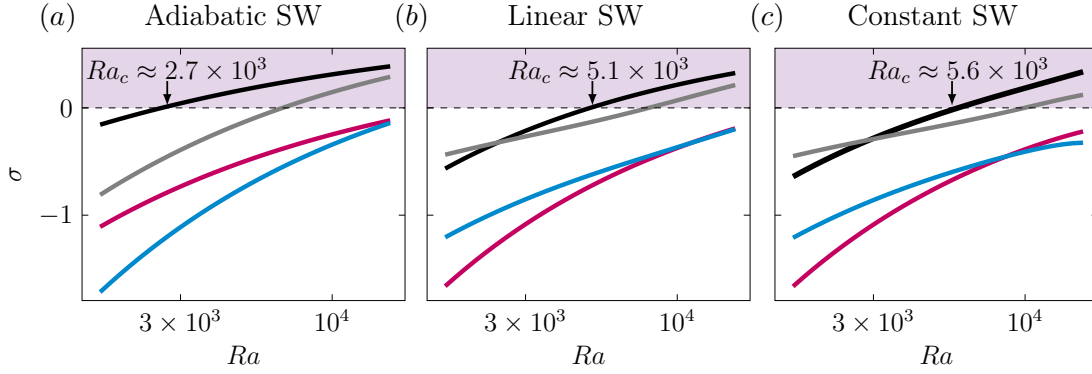
Figure 5.3: Growth rates σ as determined from linear stability analysis for the four most unstable modes at the onset of convection in the 2D cell for (a) adiabatic, (b) linear and (c) constant sidewall boundary conditions. Each line represents a different unstable mode: single roll (black), vertically stacked double roll (red), horizontally stacked double roll (gray) and four-roll (blue).

become important to resolve the boundary layers sufficiently, so the algorithm is likely to take longer to converge or the damping of the smaller scales is too severe to reach convergence overall. Using smaller values of α could lead to better results in that case, as it emphasizes smaller scales more. Preliminary analysis suggests that $\alpha = 10^{-3}$ leads to better convergence to a steady-state than $\alpha = 1$, but requires smaller time steps $\delta\tau$, which currently makes it too costly to apply to a wider range of parameters. In the future, the convergence rate might be improved by employing a hybrid adjoint-descent and Newton-GMRES approach, as proposed by Farazmand (2016). Alternative gradient optimization techniques are also conceivable to boost convergence speed.

5.3 Steady-state analysis

In this section, we study steady-states in 2D RBC for $Ra \leq 10^7$. In what follows, we refer to flow states as single or multiple solutions connected by inherent symmetries of the system. For example, the single-roll state (SRS) in 2D can exist in two forms, either circulating clockwise or counterclockwise, but is considered as a single flow state that is invariant under reflection. Steady-state solutions of the SRS state have been investigated in laterally periodic flows with stress-free velocity boundary conditions on the horizontal walls (Wen *et al.*, 2015, 2020*b*) and with no-slip BCs (Waleffe *et al.*, 2015; Sondak *et al.*, 2015; Wen *et al.*, 2020*a*; Kooloth *et al.*, 2021). Bifurcations and different flow states have already been studied in laterally unbounded RBC (Zienicke *et al.*, 1998), in laterally bounded RBC for a cubic domain (Puig-janer *et al.*, 2008) and a 2D square domain (Venturi *et al.*, 2010). Here we focus on the onset of convection, the SRS and a vertically stacked double-roll state (DRS) in two-dimensional RBC for three different sidewall BCs as shown in figure 5.1.

5.3.1 Onset of convection

In RBC, there is a critical Rayleigh number Ra_c above which the system bifurcates from the conduction state to coherent rolls. We calculate Ra_c using a linear stability
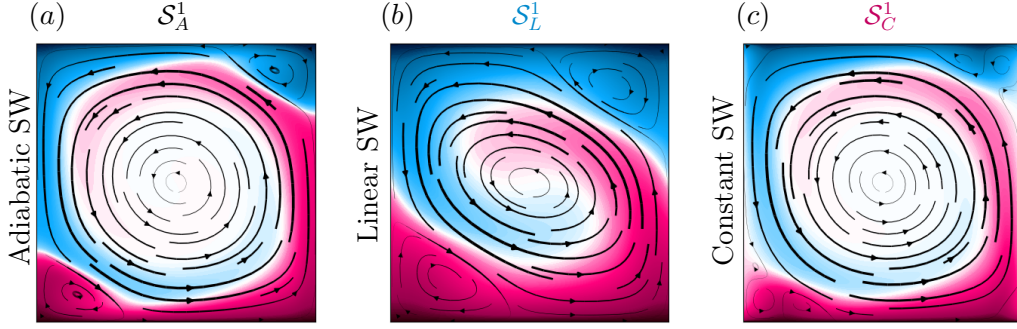
Figure 5.4: Single roll state for (a) adiabatic ($Ra = 10^6$), (b) linear ($Ra = 9 \times 10^4$) and (c) constant ($Ra = 10^6$) sidewall temperature boundary conditions. Contours (streamlines) represent the temperature (velocity) field.

analysis described in more detail in Reiter *et al.* (2021c). For adiabatic or linear (conductive) sidewall BCs, the conduction or base state is characterized by a linear temperature profile in the vertical direction with zero velocity field and independence from control parameters. However, for a constant temperature sidewall distribution, there is always a weak flow due to the horizontal temperature gradients, which resembles a four-roll state. In this case, we perform a steady-state search before analyzing the local stability around this equilibrium point.

Figure 5.3 shows the linear growth rates of the four most unstable modes, which resemble the first four Fourier modes as depicted in the same figure. All three BCs initially bifurcate from the conduction state to a single roll state. Adiabatic sidewalls lead to a lower critical Rayleigh number compared to isothermal sidewalls, which is to be expected (Buell & Catton, 1983; Shishkina, 2021). The onset for the adiabatic sidewall occurs at $Ra_c \approx 2.7 \times 10^3$ which agrees well within our resolution limit with Venturi *et al.* (2010), who reports a critical Ra of about 2582. The onset for the linear SW occurs at 5.1×10^3 and the onset for the constant SW occurs slightly later at 5.6×10^3. This indicates that the interaction of the convective field - as present for the constant sidewall BC - with the unstable modes is weak and its influence on the onset is small.

5.3.2 Single-roll (states $\mathcal{S}_A^1$, $\mathcal{S}_L^1$, $\mathcal{S}_C^1$)

The single roll state (SRS) is arguably the most important state in RBC for aspect ratios around unity. It is the first mode to appear above the conduction state, as we have just seen, and prevails even up to largest Ra in the form of large-scale circulation (LSC) on turbulent superstructures (Zhu *et al.*, 2018a; Reiter *et al.*, 2021a). The SRS is stable and time-independent for small Ra but oscillatory, chaotic, or even completely vanishing for larger Ra, as we will show in section 5.4.3. Here we analyze its properties before collapse and show that the growth of secondary corner rolls plays an important role in its destabilization and that this process can be both suppressed and enhanced by different sidewall boundary conditions.

Figure 5.4 shows the temperature and velocity fields of the SRS for different sidewall BCs. For all three BCs we can identify a large primary roll circulating counterclockwise and two secondary corner rolls. The corner rolls are most pronounced for the linear sidewall BC and the primary roll is nearly elliptical. The dimensionless heat-flux is expressed in form of the Nusselt number $Nu \equiv \sqrt{RaPr}F_f H/\Delta$ with the
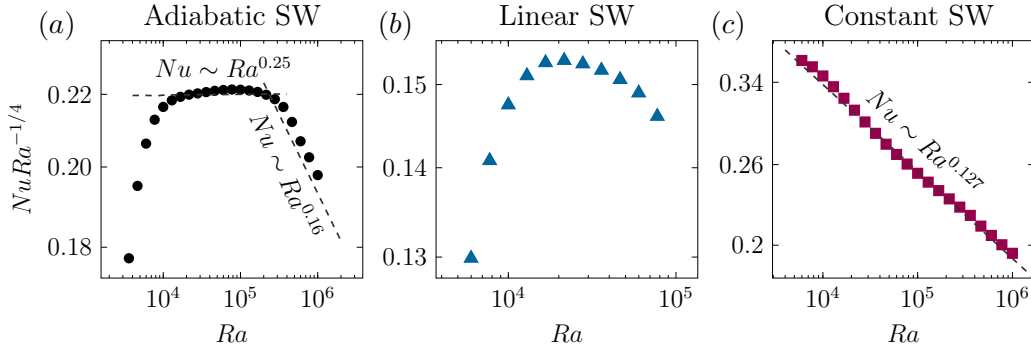
Figure 5.5: Nusselt number Nu for the single-roll states for (a) adiabatic, (b) linear and (c) constant sidewall temperature boundary conditions. Plotted is the range, where steady state convergence is achieved. Further comparison of the steady-state analysis with the DNS results is shown in figure 5.18.

heat-flux F_f entering the fluid and the imposed temperature difference Δ. F_f can be defined in different ways, especially in the presence of sidewall heat-fluxes. Averaging the temperature equation in eq. (5.1) over time, one obtains

$$\boldsymbol{\nabla} \cdot \mathbf{F} = 0, \quad \mathbf{F} \equiv \mathbf{u}\theta - 1/\sqrt{RaPr}\boldsymbol{\nabla}\theta, \tag{5.14}$$

from which it follows that the total heat flux must vanish through the boundaries $S = \delta V$, i.e. $\int_S (F \cdot \mathbf{n}) dS = 0$. (However, local temperature fluxes through the sidewall can and do exist, as we discuss in section 5.4.2.) For isothermal sidewall BCs, asymmetric flow states with net nonzero sidewall heat-fluxes are possible; in this case the heat fluxes through the bottom and top plates would deviate from each other. However, in the present study, we found that all sidewall heat fluxes are approximately equal to zero when integrated vertically and the temperature gradient at the bottom plate is approximately equal to the temperature gradient at the top plate. Therefore, we define Nu based on the lower (hot) plate at $z = 0$:

$$Nu \equiv -\frac{1}{A_+} \int_{S_+} \frac{\partial \theta}{\partial z} dS_+, \tag{5.15}$$

with the bottom plate domain S_+ and its surface area A_+. The dimensionless momentum transport is given by the Reynolds number

$$Re \equiv \sqrt{Ra/Pr}\sqrt{\langle \mathbf{U}^2 \rangle_V}L, \tag{5.16}$$

based on total kinetic energy of the mean field velocity $\mathbf{U}$. Here, $\langle \cdot \rangle_V$ denotes a volume average.

In the laminar regime, where the dissipation of velocity and temperature field is determined by the contributions of the boundary layers, we expect the total heat and momentum scaling $Nu \sim Ra^{1/4}$ and $Re \sim Ra^{1/2}$ (Grossmann & Lohse, 2000), respectively. Figure 5.5 shows that the former scaling shows up only for a very limited Ra range and only for the adiabatic boundary conditions. The SRS of the linear sidewall BCs is stable only up to $Ra \leq 10^5$, then the corner rolls become strong enough to lead to a collapse of the SRS. The stability region where the steady-states
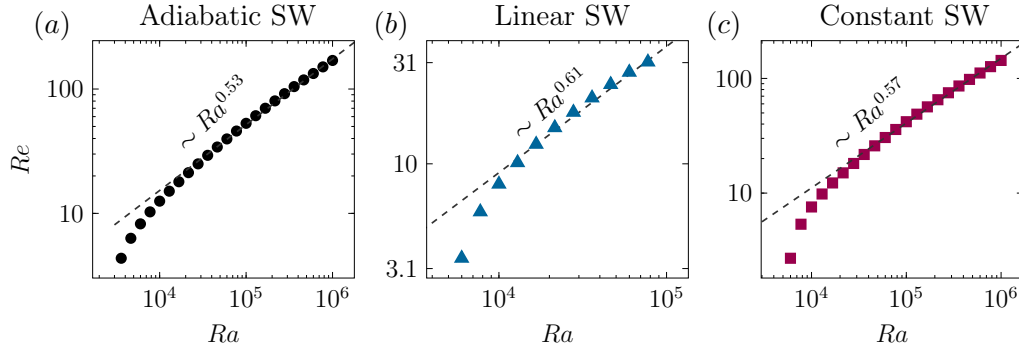
Figure 5.6: Reynolds number Re for the single roll states $\mathcal{S}_A^1$, $\mathcal{S}_L^1$, $\mathcal{S}_C^1$. (a) adiabatic, (b) linear and (c) constant sidewall temperature boundary conditions. Plotted is the range, where steady state convergence is achieved.

converge is too small to observe an unperturbed scaling. On the other hand, for the constant sidewall boundary conditions, corner roll growth is less dominant. In this case, the reason why Nu scaling deviates from $1/4$, is that heat entering through the bottom/top can immediately escape through the sidewalls in the form of a "short-circuit", which dominates the lower Ra regime and is the reason why Nu is relatively large for small Ra. For the adiabatic sidewall BC, we observe $Nu \sim Ra^{0.25}$ for $10^4 \leq Ra \leq 3 \times 10^5$, followed by $Nu \sim Ra^{0.16}$ for $3 \times 10^5 \leq Ra \leq 10^6$. Similarly, the growth of the corner rolls disturbs the convection wind, and Nu deviates from the ideal $1/4$ scaling. Looking at the Re vs. Ra scaling in figure 5.6, we find the theoretically predicted scaling of $1/2$ is better represented in comparison and the different sidewall boundary conditions deviate less among themselves. This suggests that momentum transport is less affected by changing sidewall boundary conditions than heat transport.

Growth of corner rolls

The SRS is stable up to a certain Ra limit. Above this limit, it may fluctuate, reverse orientation, or even disappear altogether. This process occurs at $Ra \approx 10^6$ for the adiabatic and constant temperature sidewall BCs and at $Ra \approx 10^5$ for the linear sidewall BC. While up to this event the dynamic behaviour of the three different sidewall BCs is qualitatively very similar, from there on it differs. The constant sidewall BC case shows a time dependence, but remains in the SRS state without changing its orientation. The adiabatic and linear sidewall BCs, on the other hand, enter a more chaotic regime of regular and chaotic flow reversals (Xi & Xia, 2007; Sugiyama *et al.*, 2010), some of which are discussed in section 5.3.3. Of greatest importance here appears to be the presence and magnification of secondary corner rolls (CRs).

Figure 5.7 (a) shows the vorticity field and stream-function contour of two-dimensional RBC with adiabatic sidewalls at $Ra = 7 \times 10^5$. The existence of two corner vortices is apparent. Here we define the corner roll size δ_{CR} based on the zero crossing, or stagnation point, of the vorticity $\omega \equiv \partial_x u_z - \partial_z u_x$ at the top plate, cf. Shishkina *et al.* (2014). To understand the processes involved in the formation of the corner
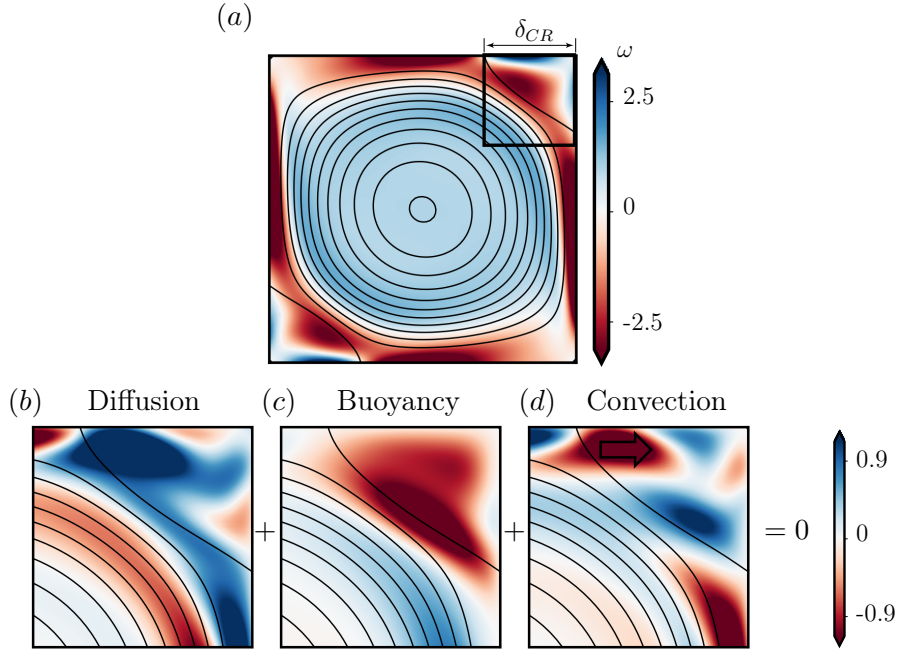
Figure 5.7: (a) Steady-state vorticity field and velocity streamlines for $Ra = 7 \times 10^5$ and adiabatic sidewalls. The corner roll size δ_{CR} is defined as the distance from the corner to the closest stagnation point at the plate. Bottom figures show the vorticity balance contributions according to eq. (5.17) in the corner roll domain, i.e., (b) diffusion, (c) buoyancy and (d) convection. The same contour levers were used for $(b-d)$.

rolls, we write down the evolution equation for vorticity

$$\partial_t \omega = \underbrace{-\mathbf{u} \cdot \boldsymbol{\nabla} \omega}_{\text{convection}} + \underbrace{\sqrt{Pr/Ra} \boldsymbol{\nabla}^2 \omega}_{\text{diffusion}} + \underbrace{\partial_x \theta}_{\text{buoyancy}} . \qquad (5.17)$$

It is evident that for steady-states ($\partial_t \omega = 0$) there must be an equilibrium between convection, diffusion and buoyancy forces. The three corresponding fields are shown in figure 5.7 $(b-d)$ zoomed in on the corner roll region. For this particular Ra, all three contributions appear to be significant. We evaluate the size of the corner rolls (figure 5.8) and analyse contributions of diffusion, buoyancy, and convection for all Ra (figure 5.7). For this purpose, we evaluate the absolute values of the volume averages for each term in the corner roll region, e.g., $\langle |\partial_x \theta| \rangle_{S_{CR}}$ represents the strength of the buoyancy term in the corner roll area S_{CR}, as shown in figure 5.7 (c). The constant BC yields a notable exception because multiple corner rolls can exist. This can be sensed from figure 5.4 (c). For small Ra, the corner roll are dominant in the lower right and upper left corner, where the LSC detaches (ejects). For the other two BCs, these rolls are not present. Looking at eq. (5.17), we realize that the presence of a horizontal temperature gradient can lead to the formation of vortex structures. This condition is present for the constant BCs, e.g., in the lower right corner, where the hot LSC detaches while the temperature is kept constant at zero, resulting in a (strong) negative temperature gradient. The two more "classical" corner rolls first appear at larger Ra, but soon take over in size, as can be seen in
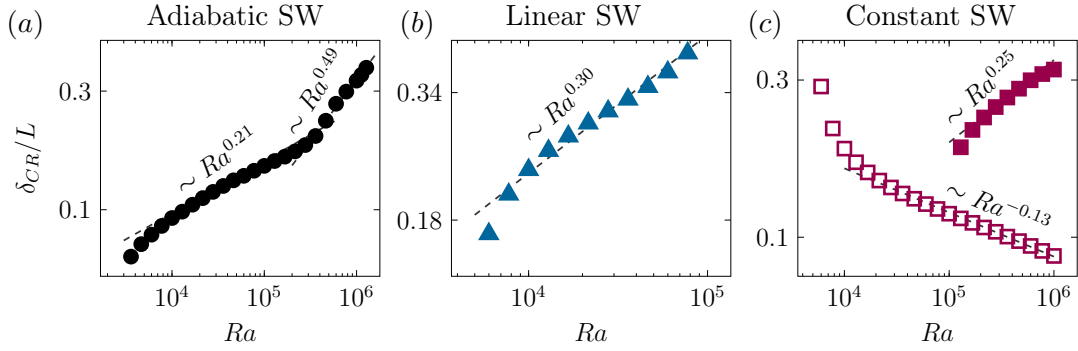
Figure 5.8: Growth of the corner roll size δ_{CR} for (a) adiabatic, (b) linear and (c) constant sidewall temperature boundary conditions. Adiabatic BC show two distinct regions, a buoyant dominated regime and a regime where convective influx leads to a more rapid increase. For the constant BC, the corner rolls appear first in the plume ejecting corner (bottom right and upper left in figure 5.4) which is represented by the open symbols in (c), and only for larger Ra they appear in the plume impacting region (closed symbols). Plotted is the range, where steady state convergence is achieved.

figure 5.8.

The adiabatic and linear sidewall BCs each yield only two corner rolls. These are present from the onset of convection and grow until the collapse of the SRS (figure 5.8). The main difference between the two is that for the adiabatic sidewall, the corner rolls initially grow monotonically with respect to Ra, whereas for the linear sidewall BCs, the corner rolls are already considerable large as soon as the SRS is present. Moreover, they also grow faster with respect to Ra ($\delta_{CR} \sim Ra^{0.3}$) and soon cover almost 40% of the width of the cell. Their large initial size combined with faster growth is the reason for premature SRS instability in linear sidewall BCs. Figure 5.9 (b) shows that vorticity formation for the entire Ra range is mainly governed by buoyancy and balanced by diffusion. Assume the hot plumes carry warm fluid to the upper plate where it meets a cold sidewall, generating strong lateral gradients in the upper right corner and consequently vorticity, according to eq. (5.17).

In the adiabatic case, on the other hand, the sidewall is warmer close to the corner, which leads to less vorticity generation by lateral temperature gradients and therefore smaller corner rolls. In the low Ra regime, the corner rolls of the adiabatic sidewall are also governed by buoyancy, with a growth of the corner rolls of $\delta_{CR} \sim Ra^{0.21}$ (figure 5.8 a). This can be understood by dimensional arguments. Assume convection can be neglected in eq. (5.17), which is justified from the results in figure 5.9 (a). Thus we obtain $\sqrt{Pr/Ra}\boldsymbol{\nabla}^2\omega = \partial_x\theta$, or, in terms of a characteristic temperature θ_{CR} and a characteristic vorticity Ω_{CR}, we have $\nu\frac{\Omega_{CR}}{\delta_{CR}^2} \sim \frac{\theta_{CR}}{\delta_{CR}}$, and thus

$$\delta_{CR} \sim \sqrt{\frac{Pr}{Ra}}\frac{\Omega_{CR}}{\theta_{CR}}. \tag{5.18}$$

The evaluation (not shown here) of the characteristic vorticity in the corner roll regions by means of their root mean square value unveiled $\Omega \sim Ra^{0.7}$. Assuming further that the temperature θ_{CR} is approximately constant over Ra, we obtain
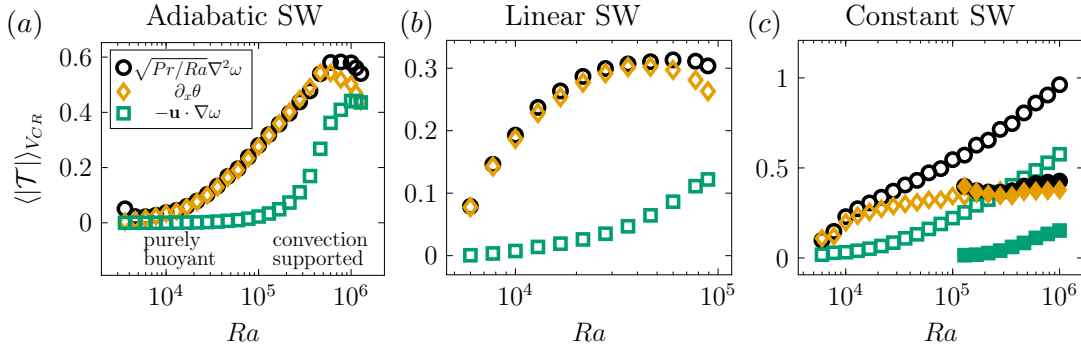
Figure 5.9: Strength of the vorticity balance contributions diffusion (black circles), buoyancy (yellow diamonds) and convection (green squares) in the corner roll region, according to eq. (5.17). (a) adiabatic, (b) linear and (c) constant sidewall temperature boundary conditions. Adiabatic BC show two distinct regions, a buoyancy dominated regime and a regime where convective influx leads to a more rapid increase. For the constant BC, the corner rolls appear first in the plume ejecting corner (bottom right and upper left in figure 5.4) which is represented by the open symbols in (c), and only for larger Ra they appear in the plume impacting region (closed symbols). Plotted is the range, where steady state convergence is achieved.

$\delta_{CR} \sim Ra^{0.20}$, which agrees remarkably well with $\delta_{CR} \sim Ra^{0.21}$. Figure 5.8 (a) discloses a transition at $Ra \approx 3 \times 10^5$, above which the corner roll growth accelerates exhibiting a scaling of $\delta_{CR} \sim Ra^{0.49}$. Figure 5.9 (a) indicates that convective processes begin to affect vorticity generation. Figure 5.7 (d) reveals a region with strong convective vorticity current with the same sign as the buoyancy forces, which enhances the vorticity generation in this region (figure 5.7 c). We interpret that above a certain Ra the primary roll of the SRS begins to feed the corner rolls until they become strong enough, eventually leading to the collapse of the SRS itself. We would like to note that the current analysis describes steady-states up to $Ra \leq 10^6$. An opposite trend was observed for larger Ra by Zhou & Chen (2018), who found a slow shrinkage of the corner rolls that scales approximately with $\sim Ra^{-0.085}$. It would be interesting to consolidate these results in future studies.

5.3.3 Double-roll ($\mathcal{S}_A^2$, $\mathcal{S}_L^2$)

Having discussed the properties of the SRS state, we proceed to the double-roll state (DRS) as shown in figure 5.10. It consists of two vertically stacked hot and cold circulation cells rotating in opposite directions with an almost discrete temperature jump in the mid plane. The DRS was not identified as an equilibrium for the constant sidewall BCs, so we will discuss it exclusively for the adiabatic and linear sidewall setup. The DRS can coexist with the SRS, but is generally found at larger Ra. Here we have tracked it in the range $10^5 \leq Ra < 7 \times 10^6$ for adiabatic and $10^5 \leq Ra < 4 \times 10^6$ for linear sidewall BCs. This range is consistent with Goldhirsch $et\ al.$ (1989) who described a roll-upon-roll state in 2D RBC for $Pr = 0.71$ at $Ra \approx 10^5$, but interestingly it was not found for $Pr = 6.8$.

From figure 5.11 we see that Nu scales close to $Nu \sim Ra^{1/4}$, which corresponds to
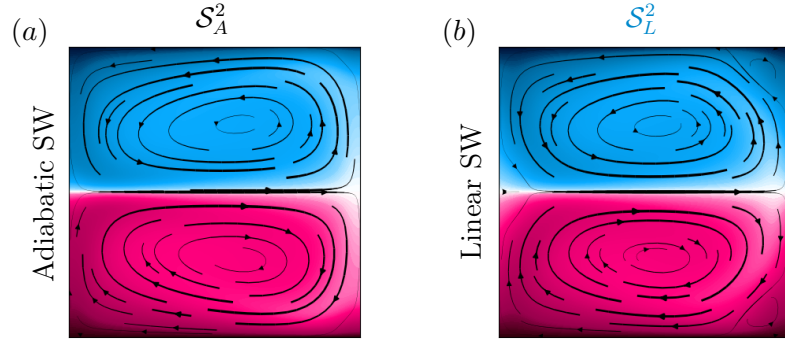
Figure 5.10: Double-roll state (DRS) for (a) adiabatic and (b) linear. Contours (streamlines) represent the temperature (velocity) field.
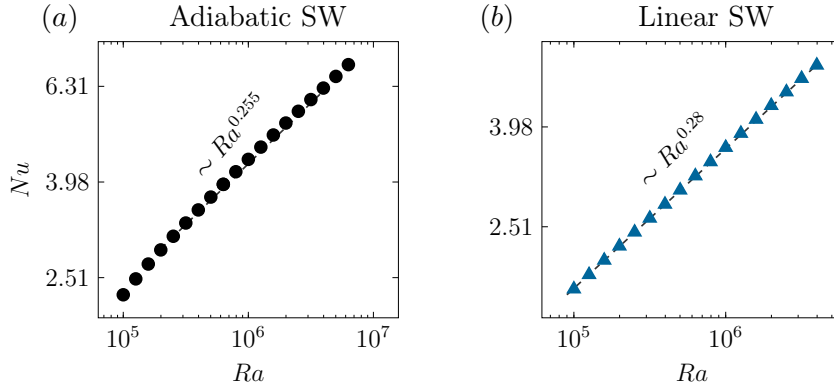
Figure 5.11: Nusselt number Nu for double-roll states $\mathcal{S}_A^2$ and $\mathcal{S}_L^2$. (a) adiabatic and (b) linear sidewall temperature boundary conditions. Plotted is the range, where steady state convergence is achieved. Further comparison of the steady-state analysis with the DNS results is shown in figure 5.18.
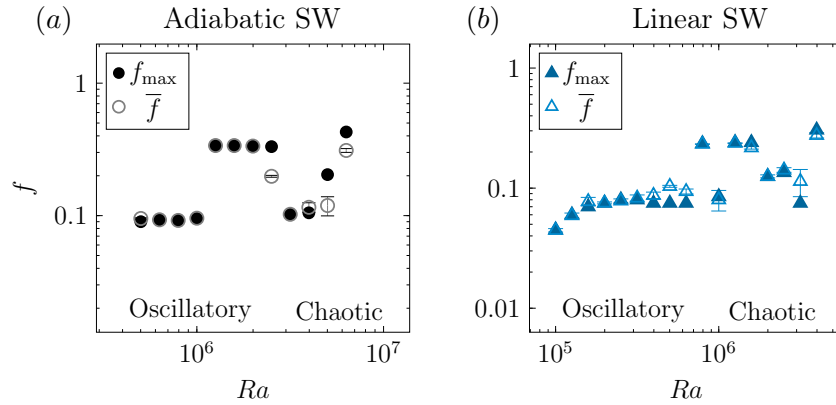
Figure 5.12: Maximum peak frequency $f_{\max}$ and average frequency $\overline{f}$ determined from $Nu(t)$ for double-roll states $\mathcal{S}_A^2$ and $\mathcal{S}_L^2$ for (a) adiabatic and (b) linear sidewall temperature boundary conditions. Plotted is the range, where steady state convergence is achieved.

81
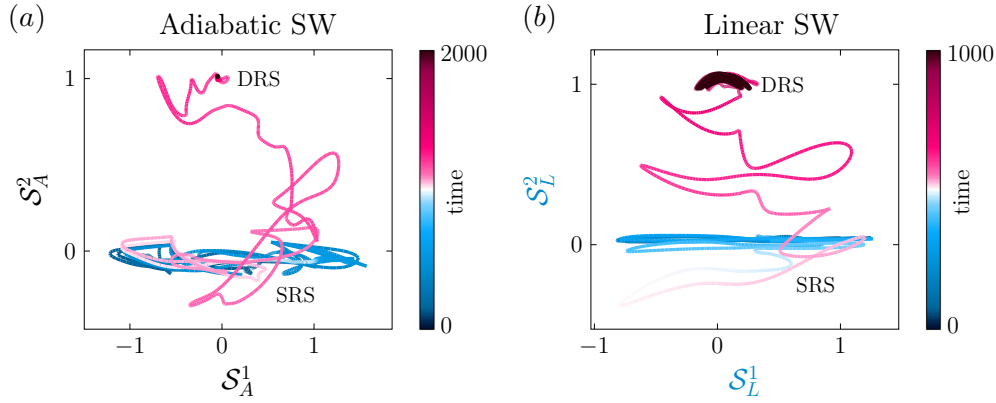
Figure 5.13: Phase space trajectories from a single-roll ($\mathcal{S}_A^1/\mathcal{S}_L^1$) to a double-roll state ($\mathcal{S}_A^2/\mathcal{S}_L^2$) for ($a$) adiabatic sidewall at $Ra = 2 \times 10^6$ and (b) linear sidewall BCs at $Ra = 1.5 \times 10^5$.

laminar scaling for RBC flows governed by boundary layer dissipation. Compared to the single-roll state, it is less effective in transporting heat from wall to wall, as evidenced by an overall smaller Nu. This is actually to be anticipated, since one roll of the DRS can be conceptually viewed as a half-height, half-temperature gradient RBC system, implying a 16 times smaller effective Ra. However, this factor most likely overestimates the difference, since the mid plane velocity is much closer to a free-slip flow than a no-slip flow and the aspect ratio is two rather than one. In reality, a DRS has about the same Nu as a SRS with a 6 times smaller Ra.

The DRS is found to be time-independent (stable) only for the adiabatic sidewall BCs for $Ra \leq 4 \times 10^5$. For other Ra it is either periodically oscillating or chaotic. In figure 5.12 we show characteristic frequencies of the DRS obtained by initializing DNS simulation with the steady-state solutions and evaluating the frequency spectra of $Nu(t)$. The frequency is presented in free-fall time units. The DRS oscillates with a frequency of about 0.1 for $Ra \leq 10^6$ for both the adiabatic and linear setups, i.e., about one cycle every 10 time units. This cycle corresponds to about half the circulation time of a cell, i.e., the characteristic velocity of the circulation is about $0.09 \sim 0.11$ and its size is $\approx 2L$. Thus, the DRS oscillation frequency seems to be initially tied to the circulation time. When Ra exceeds 10^6, we see the emergence of a more chaotic behavior. Despite increasing turbulence, the DRS state persists and does not show transition to a SRS state for $Ra < 10^7$. In section 5.4.3 we will see that for larger Ra the DRS state is eventually replaced by a single roll LSC again.

The DRS state is not merely an equilibrium solution, but more fundamentally there is a regime in Ra where the DRS is the preferred flow state to which all initial states tested in this work tend towards. Starting from random perturbations, one usually first finds a SRS, which soon goes through a series of flow reversals and restabilizations until it evolves to the DRS state. This process is depicted in an SRS-DRS phase space picture in figure 5.13. The horizontal axis represents the SRS, and the vertical axis represents the DRS. This process is qualitatively the same for adiabatic and linear sidewall boundary conditions. We do not address the flow reversal process, as it is described in more detail in Xi & Xia (2007); Sugiyama *et al.* (2010); Castillo-Castellanos *et al.* (2016); Zhao *et al.* (2019), but note that the intermediate flow fields bear striking resemblance to the proper orthogonal decomposition modes
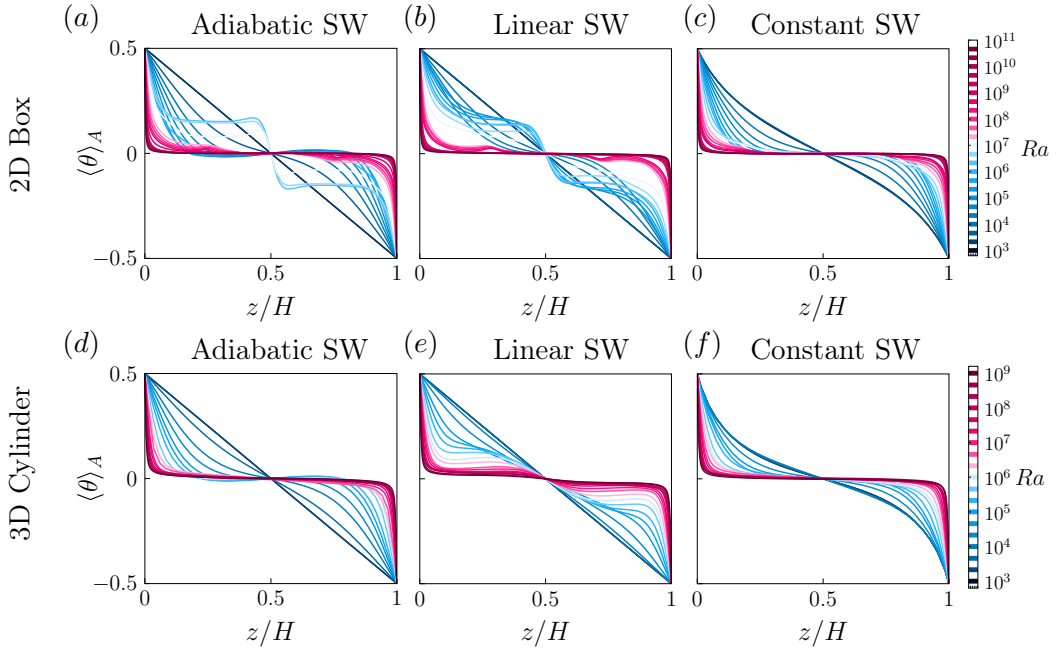
Figure 5.14: Mean temperature profile for cases with (a, d) adiabatic, (b, e) linear and (c, f) constant sidewall boundary conditions for (a-c) 2D box and (d-f) cylinder.

presented in Podvin & Sergent (2015, 2017). We want to stress that the transition time is surprisingly long. It can take up to several thousand free-fall time units for the flow to settle in the DRS state, so it can be missed if the observation window is too small.

5.4 Direct numerical simulations

In addition to the steady-state analysis, we performed a series of DNS of RBC for 2D in a square and 3D in a cylinder with $\Gamma = 1$ and $Pr = 1$, covering Ra from the onset of convection to 4.64×10^{10} and 10^9, respectively. The highest Ra in 2D was simulated on a 1024^2 grid with at least 15 grid points in the thermal boundary layer and performed for several thousand free-fall time units, ensuring adequate spatial resolution and temporal convergence. The largest simulation for the cylindrical setup was performed on a $N_r \times N_\varphi \times N_z = 128 \times 256 \times 320$ grid, with about 10 points inside the thermal and viscous boundary layers and the averaging statistics were collected for at least 600 free-fall time units.

5.4.1 Vertical temperature profiles

Figure 5.14 shows the horizontally averaged temperature profiles $\langle\theta\rangle_A$ for all conducted simulations. We first remark the similarity between 2D and 3D. For example, both show the feature of a weakly stabilizing positive temperature gradient in the mid plane for small Ra and adiabatic boundary conditions (figures 5.14 a,d). This
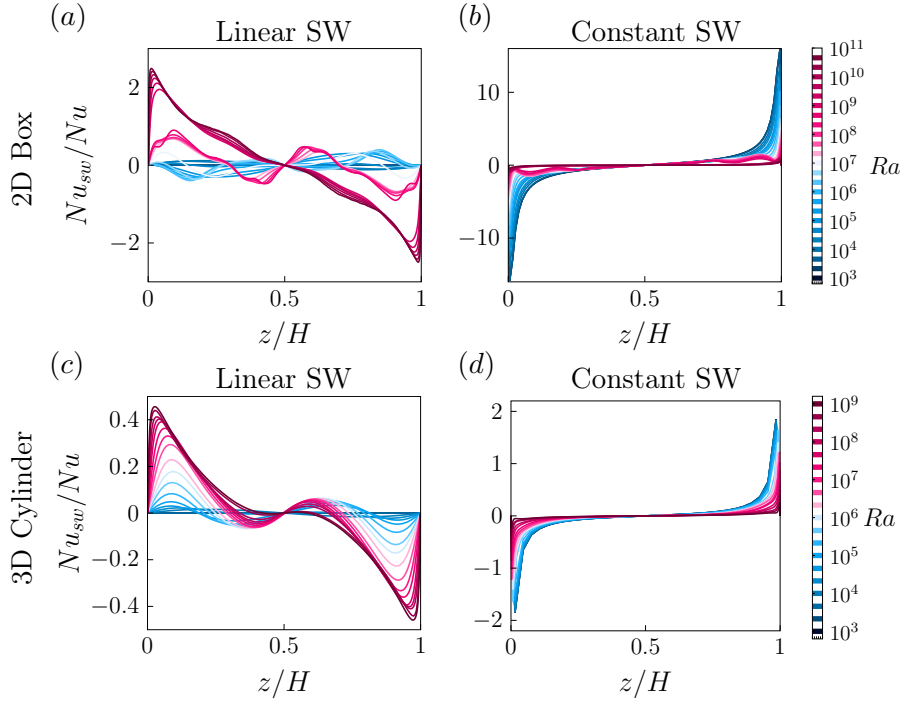
Figure 5.15: Comparison of the lateral sidewall heat flux Nu_{sw} for cases (a, c) linear and (b, d) constant sidewall boundary conditions in (a, b) 2D box and (c, d) cylinder.

phenomenon is often found in the interior of the bulk (Tilgner *et al.*, 1993; Brown & Ahlers, 2007; Wan *et al.*, 2019) and is caused by the thermal signature of the LSC. As the thermal plume of the LSC climbs up along the sidewall, it penetrates deeper into the bulk, thus hot (cold) plumes carry their signature into the top (bottom) part of the cell, which can result in a slightly positive temperature gradient in the center of the bulk.

Another important detail is the apparent non-monotonicity of the profiles in the intermediate Ra range, which is most pronounced for the linear sidewall BCs (figure 5.14 b,e) and also occurs for the 2D adiabatic BCs. The temperature profiles initially drop sharply and then level of at about a quarter of the cell height before dropping sharply again in the cell center. This behaviour was also observed in Stevens *et al.* (2014). These profiles are reminiscent of the DRS state (see section 5.3.3) and indeed caused by transitions in the flow structures, which we analyse in section 5.4.3 in more detail. Finally, all simulations for larger Ra show the classical RBC profile with steep temperature gradients at the bottom and top plates and a well-mixed homogeneous bulk.

5.4.2 Vertical sidewall heat flux profiles

Next we analyse the horizontal heat flux through the vertical sidewall Nu_{sw} which is more elaborately defined in the appendix 5.A. This is shown in figure 5.15 for the linear and constant BCs, while the sidewall heat flux of the adiabatic BC is obviously zero. The linear and constant BCs show two opposite trends. The constant setup has

the largest temperature gradients for small Ra and almost vanishing gradients for large Ra. This can be understood from the temperature profiles in figure 5.14 (c, f). As Ra increases, the bulk is more efficiently mixed and the temperature distribution becomes nearly constant, hence the temperature in the cell becomes more similar to the sidewall temperature imposed by the BCs. On the other hand, the linear sidewall BC corresponds exactly to the temperature profile before the onset of convection and from then on its contrast increases more and more, which is reflected in the relatively strong vertical temperature gradients for large Ra. However, all profiles are symmetrical around the center and consequently, although heat flows in and out locally, there is no net heat flux through the vertical sidewalls. This is supported by the fact that in our simulations the temperature gradients at the top and bottom plates were nearly equal, linked by the heat flux balance

$$Nu_c - Nu_h + \zeta \langle Nu_{sw} \rangle_z = 0 \qquad (5.19)$$

with $\zeta = \frac{1}{\Gamma}$ for the 2D box and $\zeta = \frac{4}{\Gamma}$ for the cylindrical setup (see appendix 5.A). Lastly, we detect at least two transitions in Nu_{sw} for the linear sidewall BCs (figure 5.15 a, c). These are consistent with the transitions in the temperature profiles discussed in the previous section and are elucidated in more detail in the following.

5.4.3 Mode analysis

It is generally difficult to compare the dynamics of flows in different, possibly even turbulent, states without restricting the underlying state space. Therefore, in this section we analyze the DNS results by projecting each snapshot onto four distinct modes and evaluate time averages and standard deviations.

Starting with the 2D simulations, a common choice for the mode are the first four Fourier modes, see e.g. Petschel *et al.* (2011) and (Wagner & Shishkina, 2013), i.e.

$$u_x^{m,k} = -\sin(\pi m x/L)\cos(\pi k z/H),$$
$$u_z^{m,k} = \cos(\pi m x/L)\sin(\pi k z/H). \qquad (5.20)$$

For the cylinder, the choice of modes is less obvious. In this work, we follow Shishkina (2021) and use a combination of Fourier modes in z and φ direction and Bessel functions of the first kind J_n of order n in r for the radial velocity component u_r and the vertical velocity component u_z. The first two (non-axisymmetric) modes are

$$u_r^{1,k} = J_0(\alpha_0 r/R)\cos(\pi k z/H)e^{i\varphi},$$
$$u_z^{1,k} = J_1(\alpha_1 r/R)\sin(\pi k z/H)e^{i\varphi}, \qquad (5.21)$$

and the axisymmetric modes are

$$u_r^{2,k} = J_1(\alpha_1 r/R)\cos(\pi k z/H),$$
$$u_z^{2,k} = -J_0(\alpha_0 r/R)\sin(\pi k z/H), \qquad (5.22)$$

where α_n is the first positive root of the Bessel function J_n for Dirichlet boundary conditions on the sidewall (u_r) and the k-th positive root of the derivative of the Bessel function J_n' for Neumann boundary conditions (u_z). The non-axisymmetric modes are complex-valued to account for different possible azimuthal orientations. Ultimately, however, we are only interested in the energy content and not the orien-

Figure 5.16: Energy and standard deviation of the projection of flow field snapshots onto the modes defined by eq. (5.20) for the 2D box and (*a*) adiabatic, (*b*) linear and (*c*) constant sidewall temperature boundary condition for the 2D box. Below: Streamlines, coloured by vertical velocity, of the modes $\mathcal{F}_1$, $\mathcal{F}_2^=$, $\mathcal{F}_2^\parallel$ and $\mathcal{F}_4$.

tation of the modes, so we evaluate their magnitude. We note further, that a vertical slice through the cylindrical modes is very similar to the first four 2D Fourier modes, albeit with a slightly different dependence in the radial direction. For this reason, we use the same notation for the cylindrical modes as for the Fourier modes in 2D. More precisely, we have $F_1 \equiv (u_r^{1,1}, u_z^{1,1})$, $F_2^= \equiv (u_r^{1,2}, u_z^{1,2})$, $F_2^\parallel \equiv (u_r^{2,1}, u_z^{2,1})$ and $F_4 \equiv (u_r^{2,2}, u_z^{2,2})$. Having defined the modes, we project the velocity field **u** of several snapshots onto a mode $\mathbf{u}^m$ and evaluate the energy content $\mathcal{P}$ of each mode according to

$$\mathcal{P} \equiv \frac{\int_V \mathbf{u}\mathbf{u}^m dV}{\int_V \mathbf{u}^m \mathbf{u}^m dV}, \tag{5.23}$$

and analyse the time average and standard deviation of $\mathcal{P}$.

The energy of the individual Fourier mode for the 2D box is shown in figure 5.16. Above the onset of convection, only the first Fourier mode (single-roll) contains a considerable amount of energy. Because of its similarity to the SRS, this mode will be referred to as the SRS-mode. Following the stable SRS, we find for adiabatic and linear sidewall BCs a flow regime that changes from the SRS to a roll-upon-roll second Fourier mode ($\mathcal{F}_2^\parallel$) state. This state embodies the DRS state, which we discussed in section 5.3.3. The $F_2^=$ regime, or DRS regime, is found in the range $10^6 < Ra \le 10^7$ for an adiabatic sidewall and $10^5 \le Ra \le 10^7$ for a linear sidewall BC. In contrast, the DRS regime is absent for a constant sidewall BC. As a reminder, this state could not be found as an equilibrium solution for the constant sidewall boundary condition either, which is in line with its absence in DNS. The next regime can be regarded as a weakly chaotic SRS regime, with the SRS mode again dominating but being
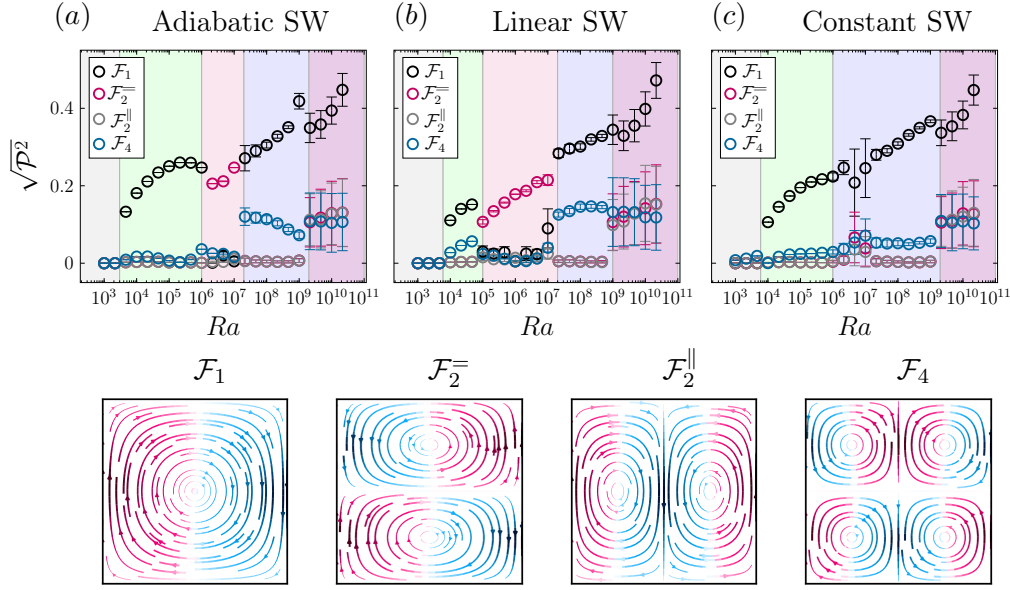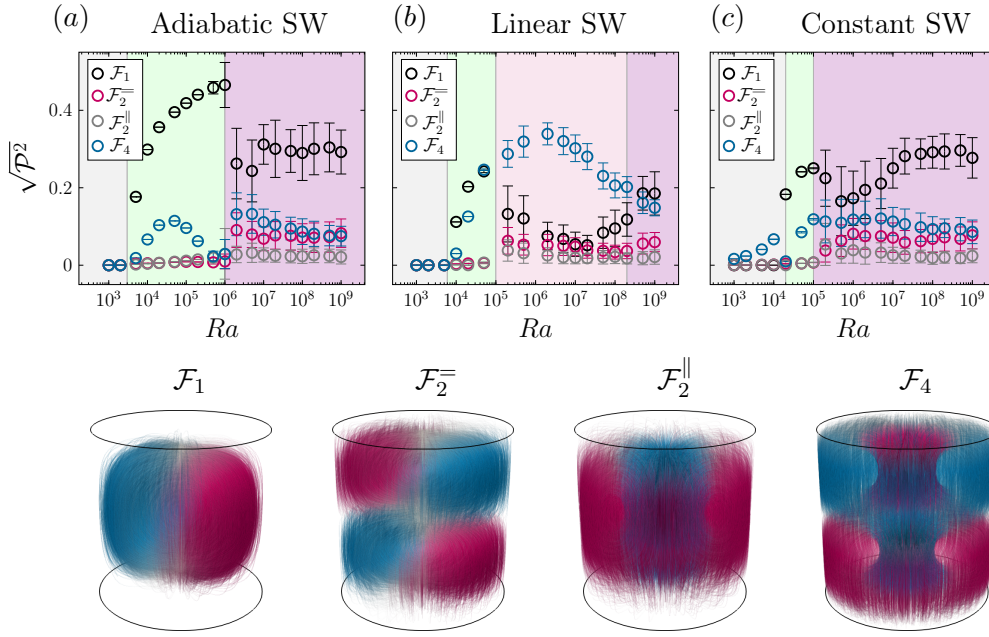
Figure 5.17: Energy and standard deviation of the projection of flow field snapshots onto the modes defined by eq. (5.22) and (5.21) for (*a*) adiabatic, (*b*) linear and (*c*) constant sidewall temperature boundary condition for the cylinder. Below: Streamlines, coloured by vertical velocity, of the modes $\mathcal{F}_1$, $\mathcal{F}_2^{=}$, $\mathcal{F}_2^{\parallel}$ and $\mathcal{F}_4$.

transient and a substantial amount of energy is contained in the F_4 (4-roll) mode, indicative of dynamically active corner rolls. Finally, above $Ra \approx 10^9$ there exists another surprisingly sharp transition. This regime is different from the others as now all Fourier modes contain a significant amount of energy and exhibit strong fluctuations. An inspection of the flow fields revealed an abundance of small-scale plumes and strong turbulent dynamics. Most remarkably, in this regime all three sidewall BCs show a very similar mode signature, i.e., they become increasingly alike, or in other words, RBC becomes insensitive to sidewall BCs for large Ra.

Moving on to the mode analysis for the cylindrical setup, shown in figure 5.17, we see a very similar picture as for the 2D box with some noticeable differences. First, for the constant BC setup we note that the onset of convection is significantly later than in the 2D case, while the other two setups show a closer similarity with the 2D case. The cylindrical setup might be more sensitive to the BCs of the sidewalls in general, since the ratio of sidewall area to cell volume ratio is larger than in the 2D box and therefore the sidewall temperature likely has a larger impact on the interior.

In the adiabatic BCs setup, the transition from a steady to a time-dependent state takes place at $Ra \approx 5 \times 10^5$, which agrees well with results of a recent experimental study that found a transition to chaos at $Ra \approx 2 \times 10^5$ in a cylindrical cell with $Pr = 0.71$ (Wei, 2021). A difference between the cylindrical and 2D box setup is, that the adiabatic setup does not show a transition to a regime with a vanishing SRS; rather, the SRS mode is the most dominant mode over all Ra. In contrast, the linear sidewall BC possess a striking similarity to the observations in 2D. Above $Ra \approx 10^5$ it undertakes a transition from a SRS-dominated regime to a F_4-dominated regime. The F_4-mode is axissymmetric and has a double-donut, or double-toroidal shape.
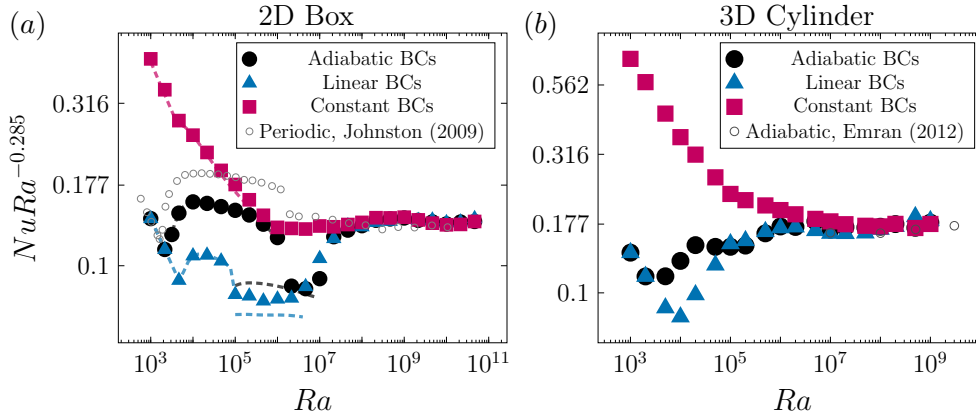
Figure 5.18: Nusselt number Nu for cases with different sidewall boundary conditions in (a) 2D simulations, (b) 3D simulations. For comparison, open symbols shows heat transport in a periodic 2D domain with $\Gamma = 2$ by Johnston & Doering (2009) (a) and for cylindrical setup with adiabatic sidewalls, $\Gamma = 1$ and $Pr = 0.7$ conducted by Emran & Schumacher (2012) (b). Dashed lines in (a) show the results from the steady-state analysis.

Similar flow states were found in a bifurcation analysis by Puigjaner et $al.$ (2008) in a cubic domain with the same lateral boundary conditions. Here, its existence range extends over $10^5 \leq Ra \leq 10^8$. The double-donut state can be considered as the counterpart of the DRS state in 2D RBC, although we see that it outlasts its 2D analog by about a decade in Ra. At the highest Ra available, the SRS again dominates for all BC configurations considered, although the amount of energy and the strength of the fluctuations are somewhat different for the different BCs. At this points, we can only conjecture from their trend and our findings in 2D that their deviation will decrease for even larger Ra in the high-turbulence/high-Ra regime.

We conclude that there exist at least five different flow regimes: conduction state, stable SRS, DRS (or double-donut state in the cylindrical setup), weakly chaotic SRS and highly turbulent state. We find the constant isothermal sidewall generally enhances the SRS dominance, while a linear isothermal sidewall BC suppresses the SRS in the mid Ra regime and induces the DRS or double-donut state. Moreover, although we find strong differences in the flow dynamics in the small to medium Ra range, but these differences eventually disappear and the system becomes increasingly insensitive to the type of sidewall BC at high Ra.

5.4.4 Heat transport

Lastly, the global heat transport is discussed. The results are shown in figure 5.18. For the 2D setup, we include the results from the steady-state analysis from the first part of this study. Here, we find a very good agreement between Nu of the DNS and steady-states for the SRS mode as well as for the DRS state for adiabatic sidewalls. However, the DRS state for linear sidewalls shows slightly larger Nu in the DNS. This is because the DRS state is an unstable equilibrium solution that can oscillate strongly, which apparently enhances heat transport properties.

In the low Ra regime, the heat transport of the constant sidewall case surpasses that of the adiabatic and linear sidewall BCs. Given the observed resemblance of the

flow dynamics (see figure 5.16), this suggests a substantial impact of the lateral heat fluxes on the total heat transport. In contrast, heat transport differences between the linear BCs and the adiabatic BCs are more strongly impacted by transitions in the flow states rather than by the sidewall heat fluxes. We find that Nu degrades strongly when switching from a SRS- to a DRS-dominated regime at $Ra \approx 10^5$ (linear) and $Ra \approx 10^6$ (adiabatic) for the 2D domains (figure 5.18a). In contrast, this does not occur for the cylindrical setup as it transitions from the SRS to the double-toroidal state (figure 5.18b). In fact, this flow transition is hardly observed in the evolution of heat transport.

In the high Ra regime, the heat transport in the cylindrical setup is found to be more efficient than in the 2D setup, with about 30% larger Nu. This agrees well with the observations of van der Poel *et al.* (2013). Both setups show $Nu \sim Ra^{0.285}$ scaling at the largest studied Ra. We also observe that Nu becomes independent of the choice of sidewall BCs for high Ra. This agrees with Stevens *et al.* (2014), at least when the sidewall temperature is equal to the arithmetic mean of bottom and top plate temperature. If this condition is violated, Stevens *et al.* (2014) has shown that Nu differences will exist even for high Ra. This indicates that the effects of an imperfectly insulated sidewall tend to be small in experiments when the mean temperature of the sidewall is well controlled.

5.4.5 Prandtl number dependence

The previous analysis focused on fluids with $Pr = 1$, but thermal convection is relevant in nature in a wide variety of fluids and many experiments are conducted in water ($Pr \approx 4$) or in liquid metals ($Pr \ll 1$) (Zwirner *et al.*, 2020). Therefore, we now explore the Pr parameter space with $Pr = 0.1, 1$ and 10 for Ra up to 10^9 in the 2D RBC setup.

The Nusselt number is shown in figure 5.19. We observe a collapse of all data points for all studied boundary conditions at large Ra. However, the collapse for large Pr is achieved earlier, at $Ra \gtrsim 10^7$, whereas the differences between $Pr = 1.0$ and $Pr = 0.1$ are small. Both indicate heat transport invariance for $Ra \gtrsim 10^8$. This suggests that the size of the thermal boundary layer λ_θ plays a crucial role. For small Pr we expect larger thermal boundary layers, which extend further into the bulk and thus have a stronger influence on the system. As λ_θ gets smaller, the coupling between the sidewall and bulk disappears, and so do the differences in heat transport. And although our results show a small Pr-dependence, the main message remains. Experiments with very high Ra are not affected by different thermal sidewall BCs, regardless of whether they are performed in a low Pr or high Pr medium. This conclusion is related to the global heat transport properties as well as to the flow dynamics that show increasingly resemblance, as we have seen in section 5.4.3. We anticipate a similar trend for smaller aspect ratio cells, but shifted towards larger Ra.

5.5 Conclusions

We have investigated the influence of three different lateral thermal boundary conditions, i.e., adiabatic, linearly distributed in the vertical direction and constant (isothermal) ones, on heat transport and flow states in two- and three-dimensional Rayleigh-Bénard convection (RBC) using direct numerical simulation and steady-
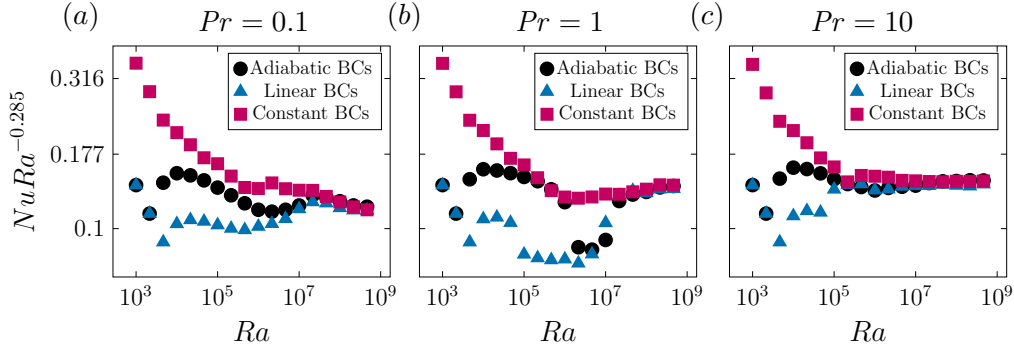
Figure 5.19: Nusselt number Nu for (a) $Pr = 0.1$, (b) $Pr = 1$ and (c) $Pr = 10$ in 2D RBC with different thermal sidewall BCs.

state analysis. The steady-state analysis is based on an adjoint-descent method (Farazmand, 2016). We found superior convergence chance in the laminar and weakly laminar regime compared to Newton's method, but did not achieve convergence at larger Ra. Further studies on the proper boundary conditions, the choice of the energy norm and or a combination with Newton's method are needed to further explore the potential of the method in the study of convective flows.

Investigation of the stability of the single-roll state (SRS) revealed that a linear temperature distribution at the sidewall leads to a premature collapse of the SRS compared to adiabatic BCs. In contrast, the stability of the SRS was enhanced by the introduction of constant temperature sidewall BCs. We find that in 2D and for linear and adiabatic sidewall BCs, the collapse of the SRS is followed by a regime in which the preferred flow state is a double-roll state (DRS), where one roll is located on top of the other. The DRS can be found for adiabatic and linear BCs in the regime $10^6 < Ra \leq 10^7$ and $10^5 \leq Ra \leq 10^7$, respectively, and is associated with suppressed heat transport. The DRS can be stable, it can oscillate periodically with a frequency of ≈ 0.1 free-fall time unit, or it can be chaotic for larger Ra. In 3D cylindrical simulations, a similar flow transition occurs. Imposing linear sidewall BCs leads to the emergence of a double-toroidal structure, that prevails over a wide range of Ra, i.e., $10^5 \leq Ra \leq 10^8$. Unlike in 2D, the double-toroidal structure does not lead to a heat transport recession.

We confirmed that the collapse of the SRS in 2D RBC is strongly related to the enlarging of corner rolls. Examining the setup with adiabatic sidewalls, there seem to be two regimes with distinct corner roll growth rates. For small Ra, the vorticity balance is dominated purely by diffusion and buoyancy in the form of lateral temperature gradients. In this regime, the size of the corner roll δ_{CR} grows as $\delta_{CR} \sim Ra^{0.21}$, which is consistent with dimensional analysis. For larger Ra, the convective flux starts to be of significance and the growth of the corner roll accelerates to $\delta_{CR} \sim Ra^{0.49}$ before the SRS finally collapses and slowly transforms to the DRS state, undergoing several cycles of flow reversals and restabilization.

Analysis of global heat transport and the flow dynamics have shown that for $Ra \leq 10^8$ there are significant differences between the various sidewall BCs. However, for larger Ra and for various Pr these differences disappear and the different sidewall BCs become globally - in terms of their integral quantities - and dynamically similar. In this context, Stevens *et al.* (2011) and Johnston & Doering (2009) showed that regardless of imposition of fixed temperature or fixed heat flux at the

bottom/top plates, high Ra show similar heat transport. Thus, together with our results, we can conclude that the effects of different boundary conditions, at the sidewalls or at the top/bottom plates, are limited for experiments with high Ra. However, there are exceptions. For example, when the sidewall temperature differs from the mean fluid temperature, larger Nu differences can occur (Stevens *et al.*, 2014). Thus, in experiments at high Rayleigh numbers, it appears to be more important to control the mean sidewall temperature than to ensure perfectly insulating conditions. However, close to the onset of convection, the sidewall thermal boundary conditions significantly influence the flow organization and heat transport in the system.

5.A Heat flux

The temperature equation for an incompressible fluid in dimensional units is

$$\partial\theta/\partial t + \boldsymbol{\nabla} \cdot (\mathbf{u}\theta) = \kappa\boldsymbol{\nabla}^2\theta. \tag{5.24}$$

Averaging equation (5.24) over time yields the following relations for the heat flux $\mathbf{F}$:

$$\boldsymbol{\nabla} \cdot \mathbf{F} = 0, \quad \mathbf{F} \equiv \mathbf{u}\theta - \kappa\boldsymbol{\nabla}\theta. \tag{5.25}$$

Using the divergence theorem we obtain

$$\int_S \mathbf{F} \cdot \mathbf{n}dS = 0, \tag{5.26}$$

which states that the net heat flux through the walls must be zero. Expressing the heat fluxes by the Nusselt number and decomposing the contribution of the surface integral into those for a lower plate heat flux Nu_h, for an upper plate heat flux Nu_c and for a side wall heat flux Nu_{sw}, we write

$$Nu_c - Nu_h + \zeta\langle Nu_{sw}\rangle_z = 0, \tag{5.27}$$

where $\langle\cdot\rangle_z$ denotes a vertical mean and ζ a geometric factor defining the ratio of the sidewall surface to the bottom/top plate surface, which is $\zeta = 1/\Gamma$ for the 2D box and $\zeta = 4/\Gamma$ for the cylindrical setup. Note that the lateral heat flux Nu_{sw} is z-dependent as it was shown in section 5.4.2. For the 2D box this is

$$Nu_{sw} = \frac{H}{\Delta}\left[\frac{\partial\theta}{\partial x}\bigg|_{x=L} - \frac{\partial\theta}{\partial x}\bigg|_{x=0}\right] \tag{5.28}$$

and for the 3D cylinder setup it is

$$Nu_{sw} = \frac{H}{2\pi\Delta}\int_0^{2\pi}\frac{\partial\theta}{\partial r}\bigg|_{r=R}d\varphi. \tag{5.29}$$
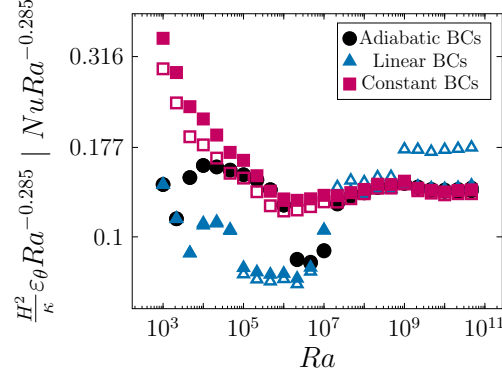
Figure 5.20: Comparison of the normalized Nu (closed symbols) and thermal dissipation rate ε_θ (open symbols) in the 2D box. The connection between thermal dissipation and Nu is given in equation (5.34).

5.B Thermal dissipation rate

Multiplying equation (5.24) with θ and averaging over time yields

$$\frac{1}{2}\partial_t\theta^2 + \frac{1}{2}\boldsymbol{\nabla}\cdot(\mathbf{u}\theta^2) = \kappa\theta\boldsymbol{\nabla}^2\theta. \tag{5.30}$$

Taking a time and volume average of (5.30), the time derivative and the convective part (for impenetrable walls) vanish and using the relation $(\boldsymbol{\nabla}\theta)^2 = \boldsymbol{\nabla}\cdot(\theta\boldsymbol{\nabla}\theta)-\theta\boldsymbol{\nabla}^2\theta$ we obtain

$$\kappa\int_V \overline{(\boldsymbol{\nabla}\theta)^2}dV = \kappa\int_V \boldsymbol{\nabla}\cdot(\overline{\theta\boldsymbol{\nabla}\theta})dV, \tag{5.31}$$

where an overbar denotes a time average and $\varepsilon_\theta = \kappa(\boldsymbol{\nabla}\theta)^2$ is known as the thermal dissipation rate. Using the divergence theorem once more, we find the relation between the total thermal dissipation rate and the wall heat fluxes

$$\int_V \overline{\varepsilon_\theta}dV = \kappa\int_S (\overline{\theta\boldsymbol{\nabla}\theta})\cdot\vec{n}dS. \tag{5.32}$$

For clarification, writing eq. (5.32) more explicitly and only for 2D Cartesian coordinates, we get

$$\langle\overline{\varepsilon_\theta}\rangle_V = \frac{\kappa}{V}\left(L\left[\langle\overline{\theta\partial_z\theta}\rangle_x\right]_{z=0}^{z=H} + H\left[\langle\overline{\theta\partial_x\theta}\rangle_z\right]_{x=0}^{x=L}\right), \tag{5.33}$$

with the horizontal and vertical average $\langle\cdot\rangle_x$ and $\langle\cdot\rangle_z$, respectively. In RBC, the temperatures of the upper and lower plates are spatially homogeneous, i.e. $\theta_h = \frac{\Delta}{2}$ and $\theta_c = -\frac{\Delta}{2}$, and assuming that the vertical wall fluxes are equal (which is not necessarily the case for non-adiabatic sidewalls, but has been shown to be true in all our simulations), i.e., $\partial_z\theta_c = \partial_z\theta_h$, then

$$\langle\overline{\varepsilon_\theta}\rangle_V = \frac{\kappa}{V}\left(-L\Delta\langle\partial_z\theta_h\rangle_x + H\left[\langle\overline{\theta\partial_x\theta}\rangle_z\right]_{x=0}^{x=L}\right),$$

$$\langle\overline{\varepsilon_\theta}\rangle_V = \frac{\kappa\Delta^2}{H^2}Nu + \frac{\kappa}{L}\left[\langle\overline{\theta\partial_x\theta}\rangle_z\right]_{x=0}^{x=L}. \tag{5.34}$$

This results in $\langle\overline{\varepsilon_\theta}\rangle_V = \frac{\kappa\Delta^2}{H^2}Nu$ for adiabatic sidewalls or for zero temperature sidewalls, but adds an additional term to the $\varepsilon_\theta - Nu$ relation otherwise. A comparison of the normalized Nu and ε_θ is shown in figure 5.20. The virtual discontinuity of ε_θ for the linear sidewall temperature reflects the reordering of the flow structures as explained in the main part of this study, but surprisingly Nu shows a rather smooth change in this regime. This is consistent with lateral heat flux profiles presented in figure 5.15 (a). The sudden increase in the lateral heat flux affects the second term in the right-hand side of eq. (5.34), resulting in the virtual discontinuity of the thermal dissipation rate.

5.C Adjoint descent

5.C.1 Derivation

Following Farazmand (2016), we define the right-hand side of the Navier-Stokes equations as the vector $\mathbf{F_0}$, i.e.

$$\mathbf{F_0}(\mathbf{q}) = \begin{pmatrix} -\mathbf{u}\cdot\boldsymbol{\nabla}\mathbf{u} - \boldsymbol{\nabla}p + \nu\boldsymbol{\nabla}^2\mathbf{u} + \vec{e}_z\theta \\ -\mathbf{u}\cdot\boldsymbol{\nabla}\theta + \kappa\boldsymbol{\nabla}^2\theta \\ \boldsymbol{\nabla}\cdot\mathbf{u} \end{pmatrix}. \tag{5.35}$$

The functional Gateaux derivative $\delta F(\mathbf{u}, \mathbf{u}') \coloneqq \lim\limits_{\varepsilon\to 0} \frac{F(\mathbf{u}+\varepsilon\mathbf{u}')-F(\mathbf{u})}{\varepsilon}$ of equation (5.35) is

$$\delta F(\mathbf{q}, \mathbf{q}') = \begin{pmatrix} -\mathbf{u}'\cdot\boldsymbol{\nabla}\mathbf{u} - \mathbf{u}\cdot\boldsymbol{\nabla}\mathbf{u}' - \boldsymbol{\nabla}p' + \nu\boldsymbol{\nabla}^2\mathbf{u}' + \vec{e}_z\theta' \\ -\mathbf{u}'\cdot\boldsymbol{\nabla}\theta - \mathbf{u}\cdot\boldsymbol{\nabla}\theta' + \kappa\boldsymbol{\nabla}^2\theta' \\ \boldsymbol{\nabla}\cdot\mathbf{u}' \end{pmatrix}. \tag{5.36}$$

We want to find the adjoint operator $\delta F^\dagger$ of equation (5.36) with respect to the inner-product

$$\langle\mathbf{q}, \mathbf{q}'\rangle_{\mathcal{A}} = \int_{\mathcal{D}} \left(\mathbf{q}\cdot\mathcal{A}\mathbf{q}'\right) \mathrm{d}\mathbf{x}. \tag{5.37}$$

The adjoint δF of equation (5.36) with respect to the inner product (5.37), with $\tilde{\mathbf{q}} \equiv \mathcal{A}\mathbf{q}$, is derived as follows

$$\langle\delta F(\mathbf{q}, \mathbf{q}'), \tilde{\mathbf{q}}''\rangle_{\mathcal{A}} =$$

$$= \int_V \begin{pmatrix} -\mathbf{u}'\cdot\boldsymbol{\nabla}\mathbf{u} - \mathbf{u}\cdot\boldsymbol{\nabla}\mathbf{u}' - \boldsymbol{\nabla}p' + \nu\boldsymbol{\nabla}^2\mathbf{u}' + \vec{e}_z\theta' \\ -\mathbf{u}'\cdot\boldsymbol{\nabla}\theta - \mathbf{u}\cdot\boldsymbol{\nabla}\theta' + \kappa\boldsymbol{\nabla}^2\theta' \\ \boldsymbol{\nabla}\cdot\mathbf{u}' \end{pmatrix} \begin{pmatrix} \tilde{\mathbf{u}}'' \\ \tilde{\theta}'' \\ \tilde{p}'' \end{pmatrix} \mathrm{d}\mathbf{x}$$

$$= \int_V \begin{pmatrix} \left(\boldsymbol{\nabla}\tilde{\mathbf{u}}'' + \boldsymbol{\nabla}\tilde{\mathbf{u}}''^{\mathrm{T}}\right)\mathbf{u} - \tilde{\theta}''\boldsymbol{\nabla}\theta - \boldsymbol{\nabla}\tilde{p}'' + \nu\boldsymbol{\nabla}^2\tilde{\mathbf{u}}'' \\ \mathbf{u}\cdot\boldsymbol{\nabla}\tilde{\theta}'' + \nu\boldsymbol{\nabla}^2\tilde{\theta}'' + \vec{e}_z\cdot\tilde{\mathbf{u}}'' \\ \boldsymbol{\nabla}\cdot\tilde{\mathbf{u}}'' \end{pmatrix} \begin{pmatrix} \mathbf{u}' \\ \theta' \\ p' \end{pmatrix} \mathrm{d}\mathbf{x}$$

$$= \langle\mathbf{q}', \delta F^\dagger(\mathbf{q}, \tilde{\mathbf{q}}'')\rangle_{\mathcal{A}}, \tag{5.38}$$

where the second line follows from integration by parts. Here we have refrained from writing the boundary terms that follow from the integration by parts step, since they can be eliminated by choosing the boundary conditions on $\tilde{\mathbf{q}}''$ as discussed in section

5.2.3.

5.C.2 Choice of the norm

As mentioned in Farazmand (2016), the most obvious choice for the norm is the L^2 norm, i.e. $\mathcal{A} = I$, where I is the identity operator. However, this norm is rather stiff and leads to restrictive small time steps. As an alternative, Farazmand (2016) uses a norm related to the Laplacian, which effectively smooths the $\tilde{\mathbf{q}}''$ field. Here we use a similar norm based on the inversed Laplacian, i.e. $\mathcal{A} = (I - \alpha\boldsymbol{\nabla}^2)^{-1}$,

$$\langle \mathbf{q}, \mathbf{q}' \rangle_{\boldsymbol{\nabla}^{-2}} = \int_V \left(\mathbf{q} \cdot \mathcal{A}\mathbf{q}' \right) \mathrm{d}\mathbf{x} = \int_{\mathbf{V}} \left(\mathbf{q} \cdot \tilde{\mathbf{q}}' \right) \mathrm{d}\mathbf{x} \tag{5.39}$$

where a is a positive constant. Then, $\tilde{\mathbf{q}}'$ is obtained as the solution of the Helmholtz equation

$$(I - \alpha\boldsymbol{\nabla}^2)\tilde{\mathbf{q}}' = \mathbf{q}', \tag{5.40}$$

which points out the smoothing property of this norm. In practice, we choose $\alpha = 1$. The choice of the operator for the energy norm is somewhat arbitrary, but this peculiar choice leads to improved numerical stability properties. Note that the operator $\mathcal{A}$ should be positive definite and should commute with the divergence operator, i.e. $\mathcal{A}(\boldsymbol{\nabla} \cdot \mathbf{u}) = \boldsymbol{\nabla} \cdot \mathcal{A}\mathbf{u}$.

6 Crossover of the relative heat transport contributions of plume ejecting and impacting zones in turbulent Rayleigh–Bénard convection

Turbulent thermal convection is characterized by the formation of large-scale structures and strong spatial inhomogeneity. This work addresses the relative heat transport contributions of the large-scale plume ejecting versus plume impacting zones in turbulent Rayleigh–Bénard convection. Based on direct numerical simulations of the two dimensional (2-D) problem, we show the existence of a crossover in the wall heat transport from initially impacting dominated to ultimately ejecting dominated at $Ra \approx 3 \times 10^{11}$. This is consistent with the trends observed in 3-D convection at lower Ra, and we therefore expect a similar crossover to also occur there. We identify the development of a turbulent mixing zone, connected to thermal plume emission, as the primary mechanism for the takeover. The mixing zone gradually extends vertically and horizontally, therefore becoming more and more dominant for the overall heat transfer.

6.1 Introduction

Thermally driven turbulence is omnipresent in nature and technology and its deep fundamental understanding is of utmost relevance for answering various environmental or technological questions. As a model system for thermally driven convection, Rayleigh–Bénard convection (RBC) – the flow in a box heated from below and cooled from above – has always been the most paradigmatic and popular one (Ahlers *et al.*, 2009*b*; Lohse & Xia, 2010; Chillà & Schumacher, 2012). It also reflects the intrinsic difficulty of thermally driven flows, namely its spatially inhomogeneity, including in the lateral direction, due to the formation of large-scale structures. Different regions in the flow show different flow features and contribute differently to the overall heat transfer, which is the key global response of the system to some given control parameters. In the presence of sidewalls, the spatial inhomogeneity in horizontal direction is obvious. However, due to the formation of large-scale structures it even holds in the absence of sidewalls, for periodic boundary conditions (van der Poel *et al.*, 2015; Stevens *et al.*, 2018; Pandey *et al.*, 2018; Krug *et al.*, 2020; Blass *et al.*, 2021), or for very large aspect ratios Γ defined as cell width over cell height (Emran & Schumacher, 2015).

The spatial inhomogeneity of the flow must also be reflected in any theoretical approach to understand the heat transfer in RB flow. The simplest example may be the theory of Malkus (1954), which assumes a thermal shortcut in the bulk and laminar type heat transport in the thermal boundary layers (BLs), which leads to the scaling law $Nu \sim Ra^{1/3}$ for the Nusselt number (the dimensionless heat transfer) as function of the Rayleigh number (the dimensionless temperature difference between top and bottom plate). This also holds for the mixing length theory of Castaing *et al.* (1989), the boundary layer theory of Shraiman & Siggia (1990), and the unifying theory of Grossmann & Lohse (2000, 2001, 2004), which splits the kinetic energy and thermal dissipation rates into bulk and boundary-layer/plume contributions, with different scaling behavior. Since the kinetic energy and thermal dissipation rates are additive with respect to these contributions and the total dissipation rates can exactly be connected with the overall Nusselt and Rayleigh numbers, this implies that the system response parameters, i.e., the Nusselt and Reynolds numbers, do not show pure scaling behavior, but a smooth crossover from the dominance of one region to another.

Indeed, different scaling behavior in different regions of the flow were measured in various experiments and direct numerical simulations (DNS). E.g., for the local heat fluxes, Shang *et al.* (2003, 2004, 2008) measured the scaling close to $Nu_{loc} \sim Ra^{1/4}$ near the sidewalls and close to $\sim Ra^{1/2}$ in the bulk. This suggests that for increasing Ra, the latter may take over. This is the so-called asymptotic ultimate regime $Nu \sim Ra^{1/2}$, first suggested by Kraichnan (1962) and Spiegel (1971) and indeed found in so-called homogeneous RB flow (Lohse & Toschi, 2003; Calzavarini *et al.*, 2005; Lepot *et al.*, 2018), where the flow-driving hot and cold temperature boundary conditions at the plates have been replaced by a bulk driving with an overall temperature gradient.

Different scaling behavior of the local heat flux in different regions of the flow in the lateral direction, reflecting the spatial lateral inhomogeneity of the flow, was also observed in numerical simulations with periodic boundary conditions, despite the periodicity. van der Poel *et al.* (2015) distinguishes between plume ejecting and plume impacting regions, and in between regions dominated by wind-shearing. These
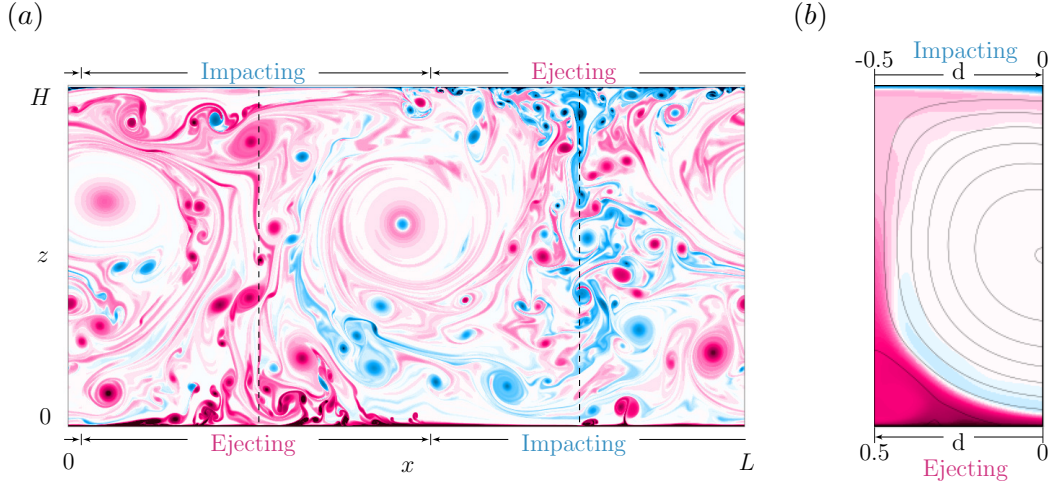
Figure 6.1: (a) A snapshot of the temperature field for $Ra = 10^{11}$. Blue (red) colour corresponds to the temperature below (above) the arithmetic mean of the top and bottom temperatures. The dashed vertical lines show the two locations of the centres of the plume ejecting zones (a hot one on the left and cold a one on the right), which are identified with the conditional averaging algorithm (see the main text). (b) The mean temperature field together with the mean velocity streamlines, as obtained from the conditional averaging algorithm. Bottom (top) corresponds to the ejecting (impacting) zone. The colour scale is the same as in (a).

regions are set by the large-scale convection rolls. In general, these large-scale rolls wiggle laterally due to the turbulent nature of the flow. Therefore, to obtain the local heat flux in the different regions, spatially moving averages have to be performed. In this way, the local dynamics can be disentangled from the slow large-scale movement of the rolls.

Assuming that the large-scale rolls are of similar size and always located at the same places, for very large $Ra \geq 10^{13}$ and in two-dimensional (2-D) direct numerical simulations, Zhu *et al.* (2018a) obtain effective scaling laws: $Nu_{loc} \sim Ra^{0.28}$ in the plume impacting region and $Nu_{loc} \sim Ra^{0.38}$ in the plume ejecting region. This implies that for very large Ra, the latter scaling wins for the overall (global) Nusselt number, $Nu \sim Ra^{0.38}$. This is the so-called ultimate regime, which corresponds to $Nu \sim Ra^{1/2}$ with logarithmic corrections, as predicted by Kraichnan (1962) and by Grossmann & Lohse (2011, 2012). In this regime, the kinetic boundary layer has become turbulent, which is reflected in logarithmic velocity and temperature profiles that allow for an enhanced heat transfer. Note that, without accounting for the movement of the structures in the decomposition, Zhu *et al.* (2018a, 2019a) find that the plume ejecting regions contribute more to the overall heat flux for all Ra explored in their study ($10^{11} \leq Ra \leq 4.64 \times 10^{14}$).

In contrast to the findings by Zhu *et al.* (2018a), for Ra up to 10^9 and in three-dimensional (3-D) DNS, Blass *et al.* (2021) find that the plume impacting regions contribute more to the overall heat flux. These findings in large periodic boxes ($\Gamma = 32$) are in line with earlier findings in more confined geometries of van Reeuwijk *et al.* (2008) ($\Gamma = 4$) and Wagner *et al.* (2012) ($\Gamma = 1$). Indeed, such a situation would be expected from the fact that the boundary layer thickness grows as the fluid

is advected along the plate with correspondingly reduced heat fluxes downstream (i.e. towards the ejecting region). However, Blass *et al.* (2021) also find that the dominance of the plume impacting regions diminishes with increasing Ra. Extrapolating their data to higher Ra, they estimate a crossover from impacting to ejecting dominated at $Ra \approx 10^{12}$, which appears consistent with the findings of Zhu *et al.* (2018a) in 2-D. Blass *et al.* (2021) use a conditional averaging technique which is superior to a spatially moving average because it allows to extract precise statistics despite movement of the structures or even changes in the number and orientation.

In this paper, we want to reconcile the results of Zhu *et al.* (2018a) – the dominance in the heat flux of the plume ejecting regions in 2-D DNS beyond $Ra = 10^{11}$ and of Blass *et al.* (2021) – dominance in the heat flux of the plume impacting regions in 3-D DNS up to $Ra = 10^9$, obtained with the conditional averaging technique. We do this by applying the superior conditional averaging technique to the numerical data obtained by Zhu *et al.* (2018a) and to new 2-D direct numerical simulations (DNS) for Ra down to 10^7. Our main result is that the observations by Blass *et al.* (2021) and Zhu *et al.* (2018a) are consistent and robust, and that we can identify the crossover Rayleigh number in 2-D RBC at which the heat flux from the plume ejecting regions overtakes that one from the plume impacting regions. This analysis is relevant in the context of the findings of Zhu *et al.* (2018a, 2019a), who showed that beyond $Ra \geq 10^{13}$, both, the local heat flux in the plume ejecting regions (which grows with increasing Ra) and the overall heat flux, scale steeper than the classical Malkus scaling $Nu \sim Ra^{1/3}$. This reflects the onset of the ultimate regime around that Rayleigh number, consistent with theoretical predictions (Grossmann & Lohse, 2000, 2002) and experimental measurements (He *et al.*, 2012b,a).

6.2 Numerical simulations

In this letter, we restrict us to 2-D DNS of RB flow, with periodic sidewalls and no-slip velocity boundary conditions (BCs). The governing dimensionless Navier–Stokes equations in the Oberbeck–Boussinesq approximations read

$$
\begin{aligned}
\mathrm{d}\mathbf{u}\,/\mathrm{d}t + \mathbf{u} \cdot \nabla \mathbf{u} &= -\nabla p + \sqrt{Pr/Ra}\nabla^2\mathbf{u} + \theta\mathbf{e}_z, \\
\mathrm{d}\theta\,/\mathrm{d}t + \mathbf{u} \cdot \nabla \theta &= 1/\sqrt{PrRa}\nabla^2\theta, \quad \nabla \cdot \mathbf{u} = 0,
\end{aligned}
\tag{6.1}
$$

where $\mathbf{u}$ is the velocity, θ the temperature, p the pressure, t the time and $\mathbf{e}_z$ denotes the unit vector in the vertical direction. The equations have been non-dimensionalised using the free-fall velocity $u_{ff} \equiv (\alpha g \Delta H)^{1/2}$, the free-fall time H/u_{ff}, the temperature difference Δ between the hot and the cold plate, and the cell height H. The parameters Ra, Pr, and the aspect ratio Γ are

$$
Ra \equiv \alpha g \Delta H^3/(\kappa\nu), \quad Pr \equiv \nu/\kappa = 1, \quad \Gamma \equiv L/H = 2,
$$

where L is the lateral extension of the periodic computational domain, α the fluid thermal expansion coefficient, ν the viscosity, κ the thermal diffusivity and g acceleration due to gravity.

The set of equations (6.1) is solved numerically using the finite volume code GOLD-FISH for Ra from 10^7 to 3×10^{12}. Furthermore, we have reanalysed complementary the flow snapshots from the previously published data series (Zhu *et al.*, 2018a) for Ra from 10^{11} to 10^{14}, which was generated with the finite-difference solver AFID
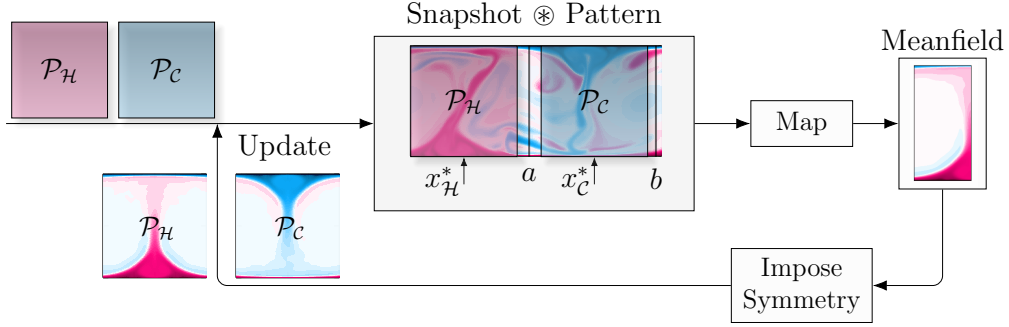
Figure 6.2: Schematic overview of the iterative pattern matching algorithm that is used to identify the hot and cold plumes and the conditional average of the fields, based on the horizontal positions of the plumes.

(Verzicco & Orlandi, 1996; Zhu *et al.*, 2018*b*). Taken together, the present study covers the parameter range $10^7 \leq Ra \leq 10^{14}$. These two computational codes for turbulent RBC were validated against each other, with excellent agreement (Kooij *et al.*, 2018). Besides, we demand the same grid resolution criteria (Shishkina *et al.*, 2010) in simulations with both codes. Thus, for the overlapping Ra-range, we use grids with the same number of nodes for both codes and with a similar grid nodes clustering near and in the boundary layers attached to the isothermal plates. For further details regarding the computational grids we refer to the supplementary material in Zhu *et al.* (2018*a*).

6.3 Conditional averaging

Figure 6.1(a) gives an impression of the complexity of the flow and its large-scale organization into two counter-rotating circulation rolls, driven by a single rising hot plume and a single sinking cold plume. We decompose the flow into plume impacting and ejecting zones (the way to do this is explained later), extract statistical information and analyse their individual heat transport contributions. Evidently, this procedure depends on the robustness of the conditional averaging algorithm, which should be applicable in a broad range of Ra and which, first and foremost, should be able to reliably identify the location of the large-scale rolls.

In a 3-D domain, the first choice for the large-scale roll identification would be the technique of Berghout *et al.* (2021); Krug *et al.* (2020); Blass *et al.* (2021), which was developed to identify 3-D superstructures in turbulent RBC. The method is based on the observation that there exists a well pronounced scale separation between the turbulent thermal superstructures and small-scale turbulent fluctuations so that, after applying a low-pass filter at an intermediate wave-number ($k \approx 2/H$), what remains is a visually convincing representation of the large-scale structures. However, the turbulence cascades (and hence the spectral energy distributions) are different in 2-D and 3-D flows, and as a result, the studied 2-D flows lack the needed distinct scale separation, which impedes the applicability of the technique (Krug *et al.*, 2020; Blass *et al.*, 2021) to 2-D RBC.

On the other hand, one of the advantages of the 2-D confined ($\Gamma = 2$) cell is that the configuration of the large-scale circulation (LSC) is stable, which means that
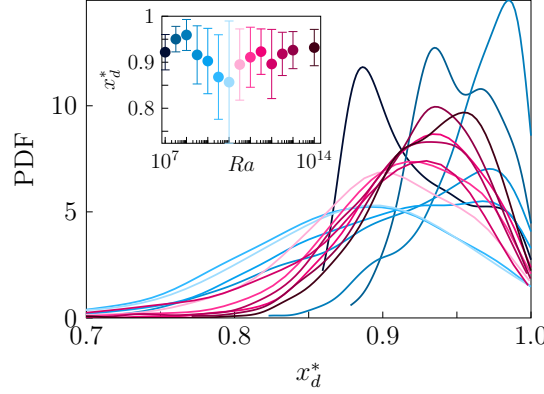
Figure 6.3: Probability density distribution of the minimum plume separation $x_d^* \equiv \min|x_H^* - x_C^*|$. The different curves represent different Ra. The inset figure shows the mean and one standard deviation of the minimal distance between the hot and cold plumes, for different Ra. The colour scale ranges from blue (smaller Ra) to red (larger Ra), according to the inset figure.

one can safely assume the number of the convection rolls to be fixed for all times. This is beneficial in so far, that the problem reduces to find the horizontal positions of the hot and cold large-scale plumes as functions of time, i.e. $x_{\mathcal{H}}^*(t)$ and $x_{\mathcal{C}}^*(t)$. These positions are indicated by the dashed lines in Fig. 6.1(a). The functions $x_{\mathcal{H}}^*(t)$ and $x_{\mathcal{C}}^*(t)$ are generally independent so that, in particular, the distance between the plumes changes with time.

To find $x_{\mathcal{H}}^*(t)$ and $x_{\mathcal{C}}^*(t)$, we employ a pattern (or, equivalently, template) matching algorithm. The idea is simple. We check the flow fields for the presence of some pattern by moving a template (horizontally) over the flow field and measure their similarity via convolution. In doing so, the templates $\mathcal{P}_{\mathcal{H}}$ and $\mathcal{P}_{\mathcal{C}}$ are chosen such that they resemble the structure of the region of interest, i.e. the hot ($\mathcal{H}$) upwelling and cold ($\mathcal{C}$) downwelling plumes. The (circular) convolution can be formally defined as

$$\left(\mathcal{P}_{\mathcal{H}(\mathcal{C})} \circledast \theta\right)(x') = \int_0^L \int_0^H \mathcal{P}_{\mathcal{H}(\mathcal{C})}(x' - x, z)\theta(x, z)dxdz, \qquad (6.2)$$

and the position of the maximal correlation gives the location of the corresponding hot or cold, plume, i.e.

$$x_{\mathcal{H}(\mathcal{C})}^* = \max\left(\mathcal{P}_{\mathcal{H}(\mathcal{C})} \circledast \theta\right). \qquad (6.3)$$

This approach is similar to the one proposed by Kooloth *et al.* (2021) with the difference, that their templates are given by previously computed steady state solutions. In contrast, our templates (patterns) are generated iteratively.

The entire process is schematically depicted in Fig. 6.2. We begin by choosing initial templates $\mathcal{P}_{\mathcal{H}(\mathcal{C})}$: functions, which are independent from the vertical coordinate and are cosines in the horizontal direction. Then we calculate $x_{\mathcal{H}}^*$ and $x_{\mathcal{C}}^*$, according to Eqs. (6.2) and (6.3). Once $x_{\mathcal{H}}^*$ and $x_{\mathcal{C}}^*$ are found, we construct the conditional mean field of the hot plume by mapping the variable width subdomains $[b, x_{\mathcal{H}}^*]$ and

$[a, x^*_{\mathcal{H}}]$ – assuming reflection symmetry – onto the fixed interval $[0, 0.5]$. Here a and b denote locations, halfway between $x^*_{\mathcal{H}}$ and $x^*_{\mathcal{C}}$, as sketched in Fig. 6.2. A similar procedure is applied for the region around $x^*_{\mathcal{C}}$, which gives a second field, i.e., the conditional field of the cold plume. Afterwards, we merge both fields by using the symmetry of the hot and cold plumes. In this way, all snapshots are processed and successively added to the conditional time averaged mean field, as it is shown in Fig. 6.1(b). Finally, from this mean field we can generate new templates $\mathcal{P}_{\mathcal{H}(\mathcal{C})}$, by reapplying the inherent symmetries and then restart the algorithm. In practice, the algorithm converges after one iteration and delivers convincing and robust positions of $x^*_{\mathcal{H}}$ and $x^*_{\mathcal{C}}$. We confirmed that stretching and squeezing of the flow fields while mapping does not distort the global response characteristics like Nu, which were practically unaffected ($< 1\%$ deviation) by these manipulations.

As noted, the templates are first initialised with vertically independent cosine functions. Therefore, the first step of the algorithm is equivalent to a cosine fit method, which is often used to identify the LSC in cylindrical cells (Cioni *et al.*, 1997; Brown & Ahlers, 2006). This method, however, inherently constrains the size of the LSC and fixes the relative size of the large-scale hot and cold plumes and the distance between them. To get an impression about the limitations of the cosine fit method, we evaluate the probability density function (PDF) and the mean and standard deviation of the (minimal) relative distance between $x^*_{\mathcal{H}}$ and $x^*_{\mathcal{C}}$, or, in simple terms, how close do the hot and cold plumes approach each other (see Fig. 6.3). We find that for all Ra this distance varies quite substantially within the range between 0.8 to 1, which shows that the relative motion of the plumes is quite significant. As a consequence, the cosine fit method leads to rather "blurry" looking mean fields, while the mean fields from our conditional averaging algorithm appear more "in-focus".

6.4 Results

In the following analysis, we will make use of two Nusselt number definitions. The first one is based on the global heat transport and defined as

$$Nu = \sqrt{Ra\,Pr}\langle \overline{u_z\theta}\rangle_V - \langle \partial_z\overline{\theta}\rangle_V, \tag{6.4}$$

where the overline represents the conditional time average and $\langle\cdot\rangle_V$ denotes a volume average. The second one is the local wall heat transport, given by

$$\overline{Nu}(d) = -\partial_z\overline{\theta}|_{z=0 \text{ (or } z=H)} \tag{6.5}$$

which is a function of the relative location d and is associated with the plume ejecting (or, respectively, plume impacting) heat transport, as elucidated in Fig. 6.1(b). More precisely, we define the ranges $-0.5 \leq d < 0$ and $0 < d \leq 0.5$, with the plume impacting and plume ejecting regions, respectively (Fig. 6.1b).

We start off by analysing the horizontal distribution of $\overline{Nu}$. Generally, the thermal BL grows as the fluid travels downstream along the plate, i.e. when proceeding from the large scale impacting to the emitting region. Correspondingly, the local heat transfer in the laminar and weakly chaotic regime is expected to decrease along this direction (Bejan, 1993). This is seen in van Reeuwijk *et al.* (2008); Wagner *et al.* (2012); Blass *et al.* (2021) and consistently also here (Fig. 6.4) for small Ra, for which the heat transport reaches its maximum in the impacting zone and then gradually
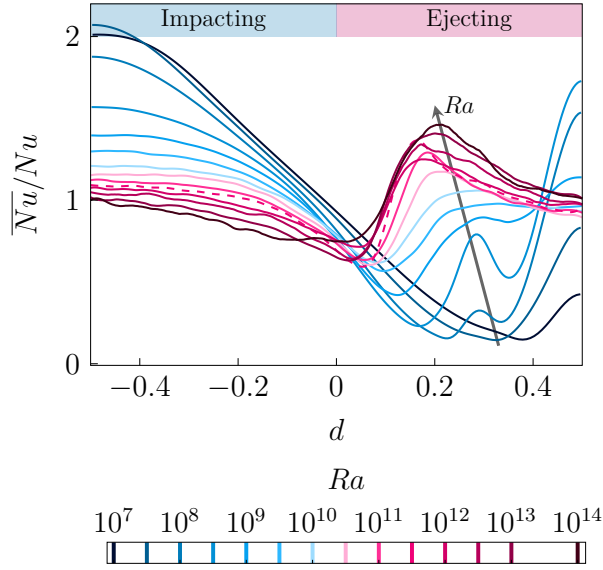
Figure 6.4: Horizontal distribution of the normalized heat flux at the plates for small (blue) to large (red) Ra. Dashed line: $Ra = 3 \times 10^{11}$.

decreases in the ejecting zone. However, as Ra increases, we observe two distinct departures from this picture, which both lead to heat transport enhancements in the ejecting zone.

The first enhancement occurs in the center of the ejecting zone, at $d > 0.35$, where a significant peak in $\overline{Nu}/Nu$ emerges initially as Ra is increased beyond 10^7. However, this peak reaches a maximum at $Ra = 10^9$ and eventually subsides again with even stronger thermal driving. Based on an analysis of instantaneous flow fields, we identified the formation of small recirculation regions, which lead to secondary circulation cells, as the source of this behaviour. These recirculations disappear for $Ra \gtrapprox 10^{10}$ and therefore do not play a role beyond this. Besides that, this phenomenon (and certainly in it's strength) is likely peculiar to 2-D RBC, since it is not observed in comparable 3-D studies van Reeuwijk *et al.* (2008); Wagner *et al.* (2012); Blass *et al.* (2021).

Of more general relevance is the peak that emerges at about $Ra = 10^8$ in the region $0.2 < d < 0.35$ (see Fig. 6.4) and ends up dominating the overall wall heat transport for larger Ra. From Fig. 6.1(b) we can verify that this part of the domain, the "leg" of the large-scale plume, is the predominant origin of small-scale turbulent plumes that emit from the BLs. These turbulent plumes are able to effectively mix their surroundings, thus inducing an increase of the vertical and horizontal heat transport. Hence, this part of the domain can be seen as the turbulent mixing zone, as suggested by Castaing *et al.* (1989). We further note that a similar increase of the heat transfer in streamwise direction is also observed in connection with the shear-driven laminar-turbulent transition of the BL (Wu & Moin, 2010). The peak first occurs at $d \approx 0.35$ at $Ra = 10^8$ but its location gradually shifts towards lower values of d as Ra is increased. This lends some support to the hypothesis of van der Poel *et al.* (2015), who surmised that the transition to ultimate scaling is driven by a spreading by the plume-ejection dominated region. However, especially at the highest Ra studied here, the simultaneous growth in peak magnitude with increasing
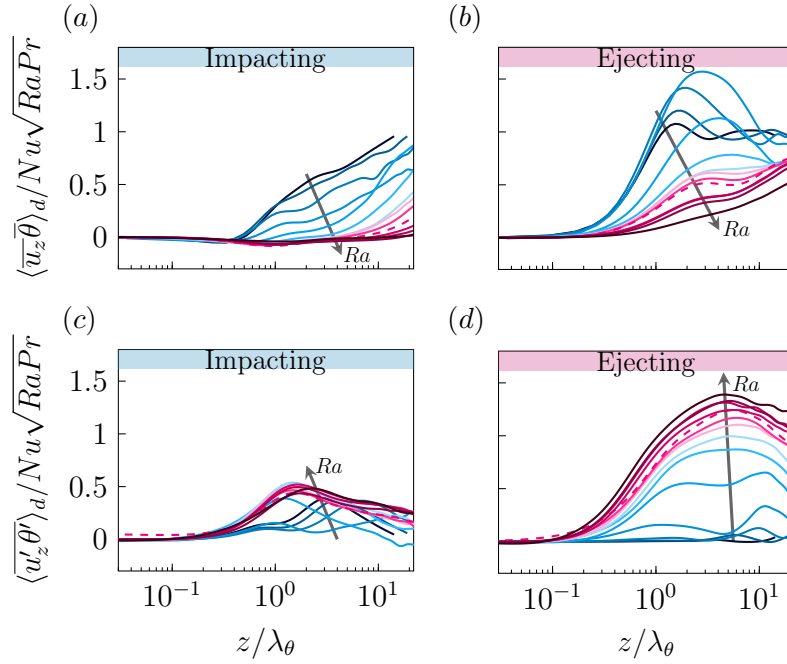
Figure 6.5: Vertical distribution of the horizontally averaged mean (top) and turbulent (bottom) convective heat transport in the impacting (a,c) and ejecting (b,d) zone for small (blue) to large (red) Ra. Dashed line: $Ra = 3 \times 10^{11}$.

Ra appears to be an even more relevant factor in shifting the balance in the heat transfer distribution towards the ejecting side.

To shed more light on the local heat transport mechanisms, we proceed and decompose the convective heat transport $\overline{u_z\theta}$ into its mean $\overline{u}_z\overline{\theta}$ and turbulent fluctuations $\overline{u_z'\theta'}$,

$$\langle\overline{u_z\theta}\rangle_d = \langle\overline{u}_z\overline{\theta}\rangle_d + \langle\overline{u_z'\theta'}\rangle_d, \tag{6.6}$$

where $\langle\cdot\rangle_d$ denotes a horizontal average taken either across the impacting $(d < 0)$ or the ejecting $(d > 0)$ region. The mean and turbulent convective heat transport profiles are shown in Fig. 6.5. Furthermore, we normalize the vertical coordinate z with mean thickness of the thermal BL, $\lambda_\theta = 1/(2Nu)$.

Figures 6.5 (a, b) show that for small Ra, the mean field transport is dominant in the convective heat transfer for both, impacting and ejecting zones. However, its relative contribution weakens with increasing thermal driving such that the large-scale circulation ultimately plays no significant role in the convective heat transport at high Ra. This behaviour is especially apparent in the impacting zone Fig. 6.5 (a), where the mean convective transport vanishes almost completely, whereas in the ejecting zone Fig. 6.5 (b), the mean convective transport remains of significant importance. Moreover, the contribution in the ejecting zone first rises before it starts to decay. This is another manifestation of the recirculation regions mentioned earlier, and therefore it is no coincidence that also here the strongest effect is observed at $Ra = 10^9$.

We turn the focus now to the turbulent convective heat transport shown in Figures 6.5 (c, d). As expected, turbulent mixing becomes the predominant heat transport mechanism at large Ra, but again, the impacting and ejecting zones behave charac-

teristically differently. In the impacting zone (Fig. 6.5 c), the turbulent transport contribution initially increases with increasing Ra before it saturates. Above $Ra \approx 10^{10}$, the curves almost collapse onto a single curve, which was observed similarly in Blass *et al.* (2021). This indicates that above a certain Ra, the turbulent heat transport in the impacting region does not increase significantly anymore. In the ejecting region ($0 \leq d \leq 0.5$), however, the turbulent transport increases gradually with increasing Ra, confirming again the trends observed earlier in 3-D convection (Blass *et al.*, 2021). Evidently, the aforementioned ejecting plumes create an efficient turbulent mixing zone which becomes more and more important and ultimately dominates the heat transport mechanisms. Moreover, the mixing zone increases in size with increasing Ra, compared to the thermal BL thickness, and reaches its maximal effectiveness at $z \approx 5\lambda_\theta$. This complements the observations by Schumacher (2008), who showed that the extension of this mixing zone can be significantly larger than the thermal BL. Surprisingly, the location of this maximum is relatively robust with respect to changes in Ra. It is further noteworthy that turbulent transport is dominant even deep inside the BL ($z < \lambda_\theta$) once $Ra \gtrsim 10^{10}$.

As mentioned in the introduction, for low and intermediate Ra in 3-D RBC, the impacting zones dominate the wall heat transport (Blass *et al.*, 2021), whereas for large Ra in 2-D RBC, the ejecting zones were found to contribute the majority of the heat transport (Zhu *et al.*, 2018a). Yet a direct link between these observations has up to now been missing. With this in mind, we compare contributions of the emitting and ejecting regions to the total wall heat transport in Fig. 6.6. Thanks to the wide range of Ra available here, we now observe a clear crossover of the contributions from the ejecting and impacting regions at $Ra \approx 3 \times 10^{11}$. At this critical Rayleigh number (highlighted as dashed lines in Fig. 6.4 and 6.5), the dominance of the contribution from the impacting zone changes to the dominance of the contribution from the ejecting zone. The data by Zhu *et al.* (2018a) also show such a crossover, if we apply the conditional averaging as proposed in the present study. Therefore, the dynamic tracking of the LSC is the key to a successful individual statistical description of the different zones. Additionally, from Fig. 6.6(a), we find that the 3-D and 2-D cases show increasingly similar behaviour as Ra increases. This gives confidence that the observed trends in the Nu distribution are indeed driven by the increase in Ra and not predominantly related to differences between 2-D and 3-D flows. We would expect a similar crossover to occur in 3-D as well at sufficiently high Ra.

6.5 Conclusions

By means of direct numerical simulations and using a conditional averaging technique we explored the properties of the plume impacting and plume ejecting zones in horizontally periodic 2-D RBC. This study covers the range $10^7 \leq Ra \leq 10^{14}$, thus bridging the Ra gap between the corresponding studies of Blass *et al.* (2021) (3-D) and Zhu *et al.* (2018a) (2-D). We provide an unifying picture of the relative heat transport importance of ejecting and impacting zones across Ra and show the existence of a crossover from an impacting dominated to an ejecting dominated local wall heat transfer at $Ra \approx 3 \times 10^{11}$. This trend is connected to an increase in the convective heat transport at the leg of the large-scale plume. Specifically, we identify the turbulent convective transfer to become the dominant transport mechanism, which is reflected in a gradual growth with Ra of the turbulent convective heat flux

$\overline{u'_z \theta'}$. The turbulent mixing zone reaches its peak efficiency at a vertical distance of about five thermal boundary layer thicknesses from the plate and it gradually expands in size with increasing Ra, thus occupying an ever larger fraction of the domain. Given the differences between 2-D and 3-D RBC (Schmalzl *et al.*, 2004; van der Poel *et al.*, 2013), it remains to be verified whether such a crossover towards the dominance in the heat transport of the thermal plume ejecting regions also exists in 3-D turbulent convection, but our results strongly suggest so.
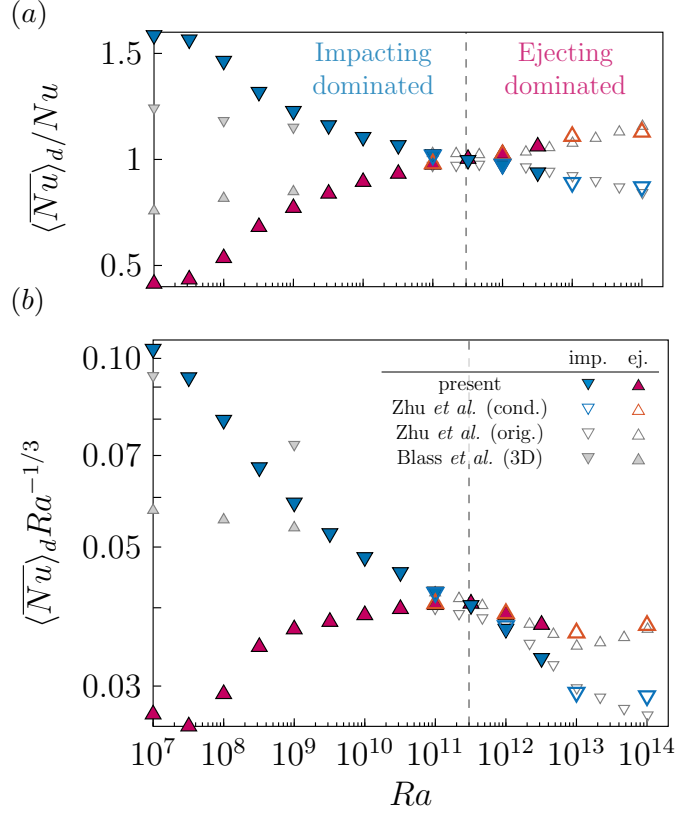
Figure 6.6: Local wall heat flux $\overline{Nu}$ compensated by (*a*) the global Nusselt number Nu and (*b*) $Ra^{-1/3}$. Results from the new simulations (closed colour symbols) and results obtained from the analysis of the flow snapshots from Zhu *et al.* (2018*a*) (open colour symbols) show the Nusselt numbers evaluated in the plume impacting regions (blue downwards triangles) and in the plume ejecting regions (red upwards triangles). For comparison, we show the results for the 2-D case, as reported in Zhu *et al.* (2018*a*) (closed grey symbols), and the results for the 3-D case, as reported in Blass *et al.* (2021) (open grey symbols). A crossover of the heat transport contributions to the total heat flux from the plume impacting regions and from the plume ejecting regions occurs at $Ra \approx 3 \times 10^{11}$.

7 Conclusions and outlook

The aim of this thesis was to add some new insight into the multi-facetted topic of thermal convection. A special focus was laid on different numerical setups, especially different thermal boundary conditions including temporally-modulated boundary conditions, and their impact on integral quantities and flow structures. Different problems have been studied by means of linear stability analysis, steady state methods, theoretical models and direct numerical simulations (DNS). In the following, the main findings of this thesis are summarized and a further outlook is given.

Numerical methods

The second chapter of this thesis presented the numerical methods and the corresponding implemented computational codes. The finite-volume DNS code *goldfish* was advanced towards applicability in massively parallel simulations and higher order temporal approximation schemes. A new pseudospectral direct numerical solver (Reiter, 2021) was developed and validated against *goldfish*. Detailed descriptions of the algorithms were presented along with performance comparisons showing good scalability of both codes. In the second part of this chapter, the linear stability analysis was discussed. The collocation method (Reiter, 2020a) and the Galerkin method (Reiter, 2020b) were compared in one- and two-dimensional stability problems, with the conclusion that the Galerkin method is preferable because it is associated with a smaller number of spurious eigenvalues.

Horizontal convection

In chapter 3, based on the paper Reiter & Shishkina (2020), a scaling model for horizontal convection (Shishkina *et al.*, 2016) was tested by extensive numerical simulations. Evidence was found for multiple scaling regions. It was shown that the inherent asymmetry of horizontal convection complicates the identification of scaling regimes and that a domain decomposition spatially separating the unstable stratified region brought a significant improvement to the interpretation of the data. A central result of this chapter was that a theoretical analysis based on scaling arguments provides a qualitatively good description of the parameter dependence of the occurrence of plumes and oscillations. It turned out that plumes are dominating for large Pr number horizontal convection, while oscillations and early chaos are prevalent for small Pr. The transition between the two regimes occurs at Pr around unity. A theoretical analysis of both structures brings forth a simpler interpretation and a better intuitive insight into the dynamics of horizontal convection and the appearance of different timescales (Yang *et al.*, 2020b).

Further work is needed to clarify the relevant length scale in horizontal convection. Studies for the cell aspect ratios Γ, $0.16 \leq \Gamma \leq 2$, report collapse of Nu for Ra based on the enclosure length, suggesting that the enclosure length is the relevant length scale for large Ra (Sheard & King, 2011). The collapse shifts to larger Ra at smaller aspect ratios. It is also not clear, whether the ocean with its extreme aspect

ratio can be studied as a geometrically unconstrained system. Investigation of the aspect ratios ≤ 0.1 should provide new insights and confidence in the applicability of laboratory studies to natural systems. Further works could also delve deeper into the modeling of the mixing efficiency, i.e., the ratio of irreversible diapycnal mixing to total energy. Measurements in the ocean indicate a mixing efficiency of about 0.2 (Gregg *et al.*, 2018), while purely buoyancy-driven horizontal convection for large Ra asymptotically approaches one (Scotti & White, 2011). Thus, the ocean is clearly not a purely horizontal convection system and other forcing mechanisms such as winds, tides, and rotation should be considered.

Travelling thermal waves

In chapter 4, based on the paper Reiter *et al.* (2021*c*), it was shown that applying travelling thermal waves to laterally periodic two-dimensional and cylindrical Rayleigh–Bénard convection results in an increased heat and momentum transport and leads to the formation of mean zonal flows. An analytical model of the zonal flow strength as a function of the thermal wave propagation speed showed excellent agreement for small Ra in the linear regime. Discrepancies for larger Ra were explained by non-linear effects. While all detailed zonal flows for small Ra were retrograde, i.e. opposite to the propagation direction of the thermal wave, consistent with the model, most simulations for large Ra reverse their direction to a prograde moving zonal flow. Such a behaviour could be expected from an instability mechanism. Stability analysis of steady convection rolls revealed a good resemblance of vertical zonal flow profiles of the most unstable mode with the observed prograde flows, indicating the importance of tilted cell instability for larger Ra.

Although the study has provided useful insights, some observations remain open, especially with respect to the tilted cell instability mechanism. First, why do almost all simulations show prograde flows at large Ra, while the instability of tilted cells does not prefer any direction for symmetric cells? Whether the traveling wave provides an initial tilt of convection cells that favors prograde flows should be determined by examining the dependence on the initial conditions. Further extension of the study to travelling internal thermal waves should be very informative. Preliminary analyses indicate that zonal flow strength increases greatly compared to traveling waves at the surface, with zonal flow strength significantly surpassing the traveling wave propagation speed. Moreover, it would be interesting to study the problem of propagating heat waves in a spherical geometry in combination with rotation, as has been done for classical Rayleigh–Bénard convection (Tilgner & Busse, 1997).

Thermal sidewall boundary conditions

In chapter 5, based on the paper Reiter *et al.* (2021*b*), the influence of various thermal sidewall boundary conditions in two- and three-dimensional Rayleigh–Bénard convection on heat transport and flow structures was investigated. It was shown that the breakdown of the large-scale circulation is caused by the enlargement of the corner rolls. Based on the vorticity fluxes, two different regimes of corner roll growth have been identified, which are diffusively and convectively dominant, respectively, leading to different corner roll growth rates. The sidewall boundary conditions have a profound impact on the global flow structures and on the heat transport for Ra up to $\approx 10^9$. Sidewalls with a linear temperature distribution are particularly suscepti-

ble to vertically stacked double rolls in two-dimensional domains or to double torus cells in cylindrical cells, which exist as the dominant solution for a wide range of Ra. A modal analysis showed the existence of single-roll, double-roll, weakly chaotic single roll and turbulent single roll regimes with respect to Ra depending strongly on the sidewall boundary conditions. However, at large Ra the differences disappear and the simulations with different sidewall boundary conditions become globally - in terms of their integral quantities - and dynamically similar. Our results should strengthen the confidence that imperfectly insulated sidewalls have only a weak influence on the observations in experiments with extremely high Ra, independent of Pr.

Our analysis focused on setups where the mean sidewall temperature was equal to the arithmetic mean of the top and bottom plate temperatures. To quantify experimental measurement errors where ambient temperature cannot be controlled well enough, further studies with different mean sidewall temperatures could be conducted, similar to Stevens *et al.* (2014) in a larger parameter space. In this chapter, an adjoint algorithm for finding stationary states, inspired by Farazmand (2016), was applied to Rayleigh–Bénard convection. It provides a better chance of convergence than a standard Newton method, however, it may fail to converge in the case of larger Ra and confined domains. Preliminary analysis suggests that the choice of the norm, in which the residual is to be minimized, plays an important role and that the convergence is superior in laterally periodic domains.

Heat transport of plume impacting and ejecting regions

In the final chapter of this thesis, based on the paper Reiter *et al.* (2021*a*), the lateral spatial inhomogeneity of two-dimensional Rayleigh–Bénard convection was investigated by dividing the domain into plume impacting and plume ejecting regions. By applying a novel conditional averaging algorithm, the quality of the statistical description of the ejecting and impinging regions was significantly improved compared to previous studies. As previous results indicated, wall heat transport is dominant in the impacting region for small Ra (Blass *et al.*, 2021), while heat transport for large Ra dominates in the ejection regions Zhu *et al.* (2018*a*). An important result was the demonstration of a crossover from the dominance of impacting to the dominance of ejecting regions at $Ra \approx 3 \times 10^{11}$ ($Pr = 1$). The increase in heat transport in the ejection regions is accompanied by an increasing turbulent convective heat transport due to a turbulent mixing zone, which reaches its peak efficiency at about five thermal boundary layer thicknesses. Our study supports the intuition that first signs of turbulent boundary layers should appear above the plume ejection zone.

Further studies of extremely high Ra regimes in thermal convection are desirable, since this regime is most important for astro- and geophysical applications. Moreover, the same study could be applied to Rayleigh–Bénard convection with non-slip horizontal walls to determine whether or not this system is qualitatively different.

7 Conclusions and outlook

Bibliography

AHLERS, G. 2000 Effect of sidewall conductance on heat-transport measurements for turbulent Rayleigh–Bénard convection. *Phys. Rev. E* **63**, 015303.

AHLERS, G., BODENSCHATZ, E., HARTMANN, R., HE, X., LOHSE, D., REITER, P., STEVENS, R. J. A. M., VERZICCO, R., WEDI, M., WEISS, S., ZHANG, X., ZWIRNER, L. & SHISHKINA, O. 2022 Aspect ratio dependence of heat transfer in a cylindrical Rayleigh–Bénard cell. Submitted.

AHLERS, G., FUNFSCHILLING, D. & BODENSCHATZ, E. 2009*a* Transitions in heat transport by turbulent convection at Rayleigh numbers up to 10^{15}. *New J. Phys.* **11**, 123001.

AHLERS, G., GROSSMANN, S. & LOHSE, D. 2009*b* Heat transfer and large scale dynamics in turbulent Rayleigh–Bénard convection. *Rev. Mod. Phys.* **81**, 503–537.

AHLERS, G., HE, X., FUNFSCHILLING, D. & BODENSCHATZ, E. 2012 Heat transport by turbulent Rayleigh–Bénard convection for $Pr \sim 0.8$ and $3 \times 10^{12} \lesssim Ra \lesssim 10^{15}$: Aspect ratio $\Gamma = 0.50$. *New J. Phys.* **14**, 103012.

BARKAN, R., WINTERS, K. B. & SMITH, S. G. LLEWELLYN 2013 Rotating horizontal convection. *J. Fluid Mech.* **723**, 556–586.

BASZENSKI, G. & TASCHE, M. 1997 Fast polynomial multiplication and convolutions related to the discrete cosine transform. *Linear Algebra Appl.* **252**, 1–25.

BATCHELOR, G. K. 1953 *The Theory of Homogeneous Turbulence*. Cambridge University Press.

BEARDSLEY, R. C. & FESTA, J. F. 1972 A Numerical Model of Convection Driven by a Surface Stress and Non-Uniform Horizontal Heating. *J. Phys. Oceanogr.* **2**, 444–455.

BEJAN, A. 1993 *Heat transfer*. New York: John Wiley and Sons. Inc.

BÉNARD, H. 1900 Les tourbillons cellulairs dans une nappe liquide. *Rev. Gén. Sciences Pure Appl.* **11**, 1261–1271, 1309–1328.

BENSIMON, D., CROQUETTE, V., KOLODNER, P., WILLIAMS, H. & SURKO, C. M. 1990 Competing and coexisting dynamical states of travelling-wave convection in an annulus. *J. Fluid Mech.* **217**, 441–467.

BERGHOUT, P., BAARS, W. J. & KRUG, D. 2021 The large-scale footprint in small-scale Rayleigh–Bénard turbulence. *J. Fluid Mech.* **911**, A62.

BLASS, A., VERZICCO, R., LOHSE, D., R. J. A. M. STEVENS, RICHARD & KRUG, D. 2021 Flow organisation in laterally unconfined Rayleigh–Bénard turbulence. *J. Fluid Mech.* **906**, A26.

BODENSCHATZ, E., DE BRUYN, J. R., AHLERS, G. & CANNELL, D. S. 1991 Transitions between patterns in thermal convection. *Phys. Rev. Lett.* **67**, 3078–3081.

BODENSCHATZ, E., PESCH, W. & AHLERS, G. 2000 Recent developments in Rayleigh–Bénard convection. *Annu. Rev. Fluid Mech.* **32**, 709–778.

BROWN, E. & AHLERS, G. 2006 Rotations and cessations of the large-scale circu-

lation in turbulent Rayleigh–Bénard convection. *J. Fluid Mech.* **568**, 351–386.

BROWN, E. & AHLERS, G. 2007 Temperature gradients, and search for non-Boussinesq effects, in the interior of turbulent Rayleigh–Bénard convection. *Eur. Phys. Lett.* **80**, 14001.

DE BRUYN, J. R., BODENSCHATZ, E., MORRIS, S. W., TRAINOFF, S. P., HU, Y., CANNELL, D. S. & AHLERS, G. 1996 Apparatus for the study of Rayleigh–Bénard convection in gases under pressure. *Rev. Sci. Instrum.* **67** (6), 2043–2067.

BUELL, J. C. & CATTON, I. 1983 The effect of wall conduction on the stability of a fluid in a right circular cylinder heated from below. *J. Heat Transfer* **105**, 255–260.

BUSSE, F.H., HARTUNG, G., JALETZKY, M. & SOMMERMANN, G. 1998 Experiments on thermal convection in rotating systems motivated by planetary problems. *Dyn. Atmos. Oceans* **27**, 161–174.

BUSSE, F. H. 1967 On the Stability of Two-Dimensional Convection in a Layer Heated from Below. *J. Math. Phys.* **46**, 140–150.

BUSSE, F. H. 1972 On the mean flow induced by a thermal wave. *J. Atmos. Sci.* **29** (8), 1423–1429.

BUSSE, F. H. 1978 Non-linear properties of thermal convection. *Rep. Prog. Phys.* **41**, 1929–1967.

BUSSE, F. H. 1983 Generation of mean flows by thermal convection. *Phys. D Nonlinear Phenom.* **9**, 287–299.

BUSSE, F. H. & WHITEHEAD, J. A. 1971 Instabilities of convection rolls in a high Prandtl number fluid. *J. Fluid Mech.* **47** (2), 305–320.

CALZAVARINI, E., LOHSE, D., TOSCHI, F. & TRIPICCIONE, R. 2005 Rayleigh and Prandtl number scaling in the bulk of Rayleigh–Bénard turbulence. *Phys. Fluids* **17**, 055107.

CANUTO, C., HUSSAINI, M. Y., QUARTERONI, A. & ZANG, T. A. 1988 *Spectral Methods in Fluid Dynamics*, pp. 31–75. Springer Berlin Heidelberg.

CASTAING, B., GUNARATNE, G., HESLOT, F., KADANOFF, L., LIBCHABER, A., THOMAE, S., WU, X.-Z., ZALESKI, S. & ZANETTI, G. 1989 Scaling of hard thermal turbulence in Rayleigh–Bénard convection. *J. Fluid Mech.* **204**, 1–30.

CASTILLO-CASTELLANOS, A., SERGENT, A. & ROSSI, M. 2016 Reversal cycle in square Rayleigh–Bénard cells in turbulent regime. *J. Fluid Mech.* **808**, 614–640.

CHANDRASEKHAR, S. 1961 *Hydrodynamic and hydromagnetic stability*. Clarendon.

CHANDRASEKHAR, S. 1981 *Hydrodynamic and Hydromagnetic Stability*. Dover Publications.

CHAVANNE, X., CHILLA, F., CASTAING, B., HEBRAL, B., CHABAUD, B. & CHAUSSY, J. 1997 Observation of the ultimate regime in Rayleigh–Bénard convection. *Phys. Rev. Lett.* **79**, 3648–3651.

CHAVANNE, X., CHILLÀ, F., CHABAUD, B., CASTAING, B. & HÉBRAL, B. 2001 Turbulent Rayleigh–Bénard convection in gaseous and liquid He. *Phys. Fluids* **13**, 1300–1320.

CHAWLA, S. S. & PURUSHOTHAMAN, R. 1983 Fluid motion induced by travelling thermal waves in a rotating fluid. *Geophys. Astrophys. Fluid Dyn.* **26**, 303–320.

CHILLÀ, F. & SCHUMACHER, J. 2012 New perspectives in turbulent Rayleigh–Bénard convection. *Eur. Phys. J. E* **35**, 58.

CHIU-WEBSTER, S., HINCH, E. J. & LISTER, J. R. 2008 Very viscous horizontal convection. *J. Fluid Mech.* **611**, 395–426.

CIONI, S., CILIBERTO, S. & SOMMERIA, J. 1997 Strongly turbulent Rayleigh–Bénard convection in mercury: Comparison with results at moderate Prandtl number. *J. Fluid Mech.* **335**, 111–140.

CLEVER, R. & BUSSE, F. 1974 Transition to time-dependent convection. *J. Fluid Mech.* **65**, 625–645.

COMAN, M. A., GRIFFITHS, R. W. & HUGHES, G. O. 2006 Sandström's experiments revisited. *J. Mar. Res.* **64**, 783–796.

CONTE, S. D. & BOOR, C. DE 1972 *Elementary Numerical Analysis: An Algorithmic Approach*. New York: McGraw-Hill.

CROSS, M. C. & HOHENBERG, P. C. 1993 Pattern formation outside of equilibrium. *Rev. Mod. Phys.* **65**, 851–1112.

CROSS, M. C. & TU, Y. 1995 Defect dynamics for spiral chaos in Rayleigh-Bénard convection. *Phys. Rev. Lett.* **75**, 834–837.

CURRY, R. & MAURITZEN, C. 2005 Dilution of the Northern North Atlantic Ocean in Recent Decades. *Science* **308**, 1772–1774.

CUSHMAN-ROISIN, B. & BECKERS, J.-M. 2011 *Introduction to Geophysical Fluid Dynamics*, 2nd edn., *Internation Geophysics Series*, vol. 101. Elsevier.

DAVEY, A. 1967 The motion of a fluid due to a moving source of heat at the boundary. *J. Fluid Mech.* **29**, 137–150.

DECKER, W., PESCH, W. & WEBER, A. 1994 Spiral defect chaos in Rayleigh-Bénard convection. *Phys. Rev. Lett.* **73**, 648–651.

DEVRIES, T., HOLZER, M. & PRIMEAU, F. 2017 Recent increase in oceanic carbon uptake driven by weaker upper–ocean overturning. *Nature* **542**, 215–218.

DING, G.-Y., HE, Y.-H. & XIA, K.-Q. 2022 The effect of tidal force and topography on horizontal convection. *J. Fluid Mech.* **932**, A38.

DOERING, C. R. & CONSTANTIN, P. 1996 Variational bounds on energy dissipation in incompressible flows. III. Convection. *Phys. Review E* **53**, 5957.

DOUGLAS, J. 1962 Alternating direction methods for three space variables. *Numer. Math.* **4**, 41–63.

EMANUEL, K. A. 1994 *Atmospheric convection*. Oxford University Press.

EMANUEL, K. A. 2005 *Divine Wind: The History and Science of Hurricanes*. Oxford University Press.

EMRAN, M. S. & SCHUMACHER, J. 2012 Conditional statistics of thermal dissipation rate in turbulent Rayleigh–Bénard convection. *Eur. Phys. J. E* **108**, 35–42.

EMRAN, M. S. & SCHUMACHER, J. 2015 Large-scale mean patterns in turbulent convection. *J. Fluid Mech.* **776**, 96–108.

FARAZMAND, M. 2016 An adjoint-based approach for finding invariant solutions of Navier–Stokes equations. *J. Fluid Mech.* **795**, 278–312.

FAVIER, B. & KNOBLOCH, E. 2020 Robust wall states in rapidly rotating Rayleigh–Bénard convection. *J. Fluid Mech.* **895**, R1.

FODOR, K., MELLADO, J. P. & WILCZEK, M. 2019 Large-Scale Updrafts and Downdrafts in Deviations From Monin–Obukhov Similarity Theory in Free Convection. *Bound.-Layer Meteorol.* **172**, 371–396.

FRISCH, U. 1995 *Turbulence: The Legacy of A. N. Kolmogorov*. Cambridge Univer-

sity Press.

FULTZ, D., LONG, R. R., OWENS, G. V., BOHAN, W., KAYLOR, R. & WEIL, J. 1959 *Studies of thermal convection in a rotating cylinder with some implications for large-scale atmospheric motions*, *Meteorological Monographs*, vol. 4. Bull. Amer. Meteor. Soc.

GAYEN, B. & GRIFFITHS, R. W. 2022 Rotating Horizontal Convection. *Annu. Rev. Fluid Mech.* **54**, 105–132.

GAYEN, B., GRIFFITHS, R. W. & HUGHES, G. O. 2014 Stability transitions and turbulence in horizontal convection. *J. Fluid Mech.* **751**, 698–724.

GETLING, A. V. 1998 *Rayleigh–Bénard Convection: Structures and Dynamics*, *Advanced Series in Nonlinear Dynamics*, vol. 11. World Scientific Publishing.

GLATZMAIER, G. A. & GILMAN, P. A. 1982 Compressible convection in a rotating spherical shell. V - Induced differential rotation and meridional circulation. *Astrophys. J.* **256**, 316–330.

GOLDHIRSCH, I., PELZ, R. B. & ORSZAG, S. A. 1989 Numerical simulation of thermal convection in a two-dimensional finite box. *J. Fluid Mech.* **199**, 1—28.

GOLUSKIN, D. 2013 Zonal flow driven by convection and convection driven by internal heating. PhD thesis, Columbia University.

GOLUSKIN, D., JOHNSTON, H., FLIERL, G. R. & SPIEGEL, E. A. 2014 Convectively driven shear and decreased heat flux. *J. Fluid Mech.* **759** (6), 360–385.

GOTTLIEB, D. & ORSZAG, S. A. 1977 *Numerical Analysis of Spectral Methods*. SIAM.

GRAMBERG, H. J. J., HOWELL, P. D. & J. R. OCKENDON, JR 2007 Convection by a horizontal thermal gradient. *J. Fluid Mech.* **586**, 41–57.

GREGG, M. C., D'ASARO, E. A., RILEY, J. J. & KUNZE, E. 2018 Mixing efficiency in the ocean. *Annu. Rev. Mar. Sci.* **10**, 443–473.

GRIFFITHS, R. W., HUGHES, G. O. & GAYEN, B. 2013 Horizontal convection dynamics: insights from transient adjustment. *J. Fluid Mech.* **726**, 559–595.

GROSSMANN, S. & LOHSE, D. 2000 Scaling in thermal convection: A unifying theory. *J. Fluid Mech.* **407**, 27–56.

GROSSMANN, S. & LOHSE, D. 2001 Thermal convection for large Prandtl numbers. *Phys. Rev. Lett.* **86**, 3316–3319.

GROSSMANN, S. & LOHSE, D. 2002 Prandtl and Rayleigh number dependence of the Reynolds number in turbulent thermal convection. *Phys. Rev. E* **66**, 016305.

GROSSMANN, S. & LOHSE, D. 2004 Fluctuations in turbulent Rayleigh–Bénard convection: The role of plumes. *Phys. Fluids* **16**, 4462–4472.

GROSSMANN, S. & LOHSE, D. 2011 Multiple scaling in the ultimate regime of thermal convection. *Phys. Fluids* **23**, 045108.

GROSSMANN, S. & LOHSE, D. 2012 Logarithmic temperature profiles in the ultimate regime of thermal convection. *Phys. Fluids* **24**, 125103.

HADLEY, G. 1735 Concerning the cause of the general trade winds. *Phil. Trans. Roy. Soc.* **29**, 58–62.

HALLEY, E. 1687 An historical account of the trade winds, and monsoons, observable in the seas between and near the Tropicks, with an attempt to assign the physical cause of the said winds. *Philos. Trans. R. Soc. London* **16**, 153–168.

HANSEN, C. J., KAWALER, S. D. & TRIMBLE, V. 2004 Heat Transfer by Con-

vection. In *Stellar Interiors: Physical Principles, Structure, and Evolution*, pp. 241–269. Springer New York.

HARTLEP, T., TILGNER, A. & BUSSE, F. H. 2003 Large scale structures in Rayleigh–Bénard convection at high Rayleigh numbers. *Phys. Rev. Lett.* **91**, 064501.

HARTLEP, T., TILGNER, A. & BUSSE, F. H. 2005 Transition to turbulent convection in a fluid layer heated from below at moderate aspect ratio. *J. Fluid Mech.* **544**, 309–322.

HAZEWINKEL, J., PAPARELLA, F. & YOUNG, W. R. 2012 Stressed horizontal convection. *J. Fluid Mech.* **692**, 317–331.

HE, X., BODENSCHATZ, E. & AHLERS, G. 2020 Aspect ratio dependence of the ultimate-state transition in turbulent thermal convection. *Proc. Natl. Acad. Sci.* **117**, 30022–30023.

HE, X., FUNFSCHILLING, D., BODENSCHATZ, E. & AHLERS, G. 2012*a* Heat transport by turbulent Rayleigh–Bénard convection for $Pr \sim 0.8$ and $4 \times 10^{11} \lesssim Ra \lesssim 2 \times 10^{14}$: Ultimate-state transition for aspect ratio $\Gamma = 1.00$. *New J. Phys.* **14**, 063030.

HE, X., FUNFSCHILLING, D., NOBACH, H., BODENSCHATZ, E. & AHLERS, G. 2012*b* Transition to the ultimate state of turbulent Rayleigh–Bénard convection. *Phys. Rev. Lett.* **108**, 024502.

HÉBERT, F., HUFSCHMID, R., SCHEEL, J. & AHLERS, G. 2010 Onset of Rayleigh–Bénard convection in cylindrical containers. *Phys. Rev. E* **81**, 046318.

HESTHAVEN, J. S., GOTTLIEB, S. & GOTTLIEB, D. 2007 *Spectral Methods for Time-Dependent Problems*, pp. 252–259. Cambridge University Press.

HIGNETT, P., IBBETSON, A. & KILLWORTH, P. D. 1981 On rotating thermal convection driven by non-uniform heating from below. *J. Fluid Mech.* **109**, 161–187.

HINCH, E. J. & SCHUBERT, G. 1971 Strong streaming induced by a moving thermal wave. *J. Fluid Mech.* **47**, 291–304.

HOLLAND, M. M. & BITZ, C. M. 2003 Polar amplification of climate change in coupled models. *Climate Dyn.* **21** (3), 221–232.

HOPF, E. 1948 A mathematical example displaying features of turbulence. *Commun. Appl. Maths* **1**, 303–322.

HORINOUCHI, T., HAYASHI, Y.-Y., W., S., Y., M., Y., A., K., T., TAGUCHI, M., FUKUHARA, T., TAKAGI, M., OGOHARA, K., MURAKAMI, S., PERALTA, J., LIMAYE, S. S., IMAMURA, T., NAKAMURA, M., SATO, T. M. & SATOH, T. 2020 How waves and turbulence maintain the super-rotation of Venus' atmosphere. *Science* **368**, 405–409.

HOWARD, L. N. 1963 Heat transport by turbulent convection. *J. Fluid Mech.* **17**, 405–432.

HOWARD, L. N. & KRISHNAMURTI, R. 1986 Large-scale flow in turbulent convection: a mathematical model. *J. Fluid Mech.* **170**, 385–410.

HU, Y., ECKE, R. & AHLERS, G. 1993 Convection near threshold for Prandtl numbers near 1. *Phys. Rev. E* **48**, 4399–4413.

HUGHES, G. O. & GRIFFITHS, R. W. 2008 Horizontal convection. *Ann. Rev. Fluid Mech.* **40**, 185–208.

HUGHES, G. O., GRIFFITHS, R. W., MULLARNEY, J. C. & PETERSON, W. H.

2007 A theoretical model for horizontal convection at high Rayleigh number. *J. Fluid Mech.* **581**, 251–276.

IBBEKEN, G., GREEN, G. & WILCZEK, M. 2019 Large-Scale Pattern Formation in the Presence of Small-Scale Random Advection. *Phys. Rev. Lett.* **123**, 114501.

JEFFREYS, H. 1925 On fluid motions produced by differences of temperature and humidity. *Q. J. R. Meteorol. Soc.* **51**, 347–356.

JOHNSTON, H. & DOERING, C. R. 2009 Comparison of Turbulent Thermal Convection between Conditions of Constant Temperature and Constant Flux. *Phys. Rev. Lett.* **102**, 064501.

JULIEN, K. & WATSON, M. 2009 Efficient multi-dimensional solution of PDEs using Chebyshev spectral methods. *J. Comput. Phys.* **228**, 1480–1503.

KAIMAL, J. C., WYNGAARD, J. C., HAUGEN, D. A., COTÉ, O. R., IZUMI, Y., CAUGHEY, S. J. & READINGS, C. J. 1976 Turbulence Structure in the Convective Boundary Layer. *J. Atmos. Sci.* **33**, 2152–2169.

KELLY, R. E. & VREEMAN, J. D. 1970 Excitation of waves and mean currents in a stratified fluid due to a moving heat source. *Zeitschrift für Angew. Math. und Phys.* **21**, 1–16.

KERSWELL, R. R. 2002 Elliptical instability. *Annu. Rev. Fluid Mech.* **34**, 83–113.

KILLWORTH, P. D. 1983 Deep convection in the World Ocean. *Rev. Geophys.* **21** (1), 1–26.

KNOBLOCH, E. & SILBER, M. 1990 Travelling wave convection in a rotating layer. *Geophys. Astrophys. Fluid Dyn.* **51**, 195–209.

KOLODNER, P., BENSIMON, D & SURKO, C. M. 1988 Travelling-wave convection in an annulus. *Phys. Rev. Lett.* **60**, 1723–1726.

KOLODNER, P. & SURKO, C. M. 1988 Weakly nonlinear traveling-wave convection. *Phys. Rev. Lett.* **61**, 842–845.

KONG, D., ZHANG, K., SCHUBERT, G. & ANDERSON, J. D. 2018 Origin of Jupiter's cloud-level zonal winds remains a puzzle even after Juno. *Proc. Natl. Acad. Sci.* **115**, 8499–8504.

KOOIJ, G. L., BOTCHEV, M. A., FREDERIX, E. M.A., GEURTS, B. J., HORN, S., LOHSE, D., VAN DER POEL, E. P., SHISHKINA, O., STEVENS, R. J. A. M. & VERZICCO, R. 2018 Comparison of computational codes for direct numerical simulations of turbulent Rayleigh–Bénard convection. *Comp. Fluids* **166**, 1–8.

KOOLOTH, P., SONDAK, D. & SMITH, L. M. 2021 Coherent solutions and transition to turbulence in two-dimensional Rayleigh–Bénard convection. *Phys. Rev. Fluids* **6**, 013501.

KRAICHNAN, R. 1962 Turbulent thermal convection at arbitrary Prandtl number. *Phys. Fluids* **5**, 1374–1389.

KRISHNAMURTI, R. & HOWARD, L. 1981 Large-scale flow generation in turbulent convection. *Proc. Nat. Academy of Sci.* **78**, 1981–1985.

KRUG, D., LOHSE, D. & STEVENS, R. J. A. M. 2020 Coherence of temperature and velocity superstructures in turbulent Rayleigh–Bénard flow. *J. Fluid Mech.* **887**, A2.

LEIGH, M. A., TSAI, T. & SHEARD, G. J. 2016 Probing horizontal convection instability via perturbation of the forcing boundary layer using a synthetic jet. *Int. J. Therm. Sci.* **110**, 251–260.

LEPOT, S., AUMAÎTRE, S. & GALLET, B. 2018 Radiative heating achieves the ultimate regime of thermal convection. *Proc. Nat. Acad. Sci.* **115**, 8937–8941.

LEVEQUE, R. J. 2002 *Finite Volume Methods for Hyperbolic Problems*. Cambridge University Press.

LI, N. & LAIZET, S. 2010 2DECOMP&FFT – A highly scalable 2D decomposition library and FFT interface. *Cray User Group 2010 conference* .

LOHSE, D. & TOSCHI, F. 2003 The ultimate state of thermal convection. *Phys. Rev. Lett.* **90**, 034502.

LOHSE, D. & XIA, K.-Q. 2010 Small-scale properties of turbulent Rayleigh–Bénard convection. *Annu. Rev. Fluid Mech.* **42**, 335–364.

LORD RAYLEIGH 1916 On convection currents in a horizontal layer of fluid, when the higher temperature is on the under side. *Phil. Mag.* **32**, 529–546.

LORENZ, E. N. 1963 Deterministic Nonperiodic Flow. *J. Atmos. Sci.* **20** (2), 141.

MALKUS, M. V. R. 1954 The heat transport and spectrum of thermal turbulence. *Proc. R. Soc. London A* **225**, 196–212.

MALKUS, W. V. R. 1970 Hadley-Halley circulation on Venus. *J. Atmos. Sci.* **27** (4), 529–535.

MAMOU, M, ROBILLARD, L, BILGEN, E & VASSEUR, P 1996 Effects of a moving thermal wave on Bénard convection in a horizontal saturated porous layer. *Int. J. Heat Mass Transf.* **39**, 347–354.

MANNEVILLE, P. 2006 Rayleigh–Bénard Convection: Thirty Years of Experimental, Theoretical, and Modeling Work. In *Dynamics of Spatio-Temporal Cellular Structures: Henri Bénard Centenary Review*, pp. 41–65.

MARSHALL, J. & SCHOTT, F. 1999 Open-ocean convection: Observations, theory, and models. *Rev. Geophys.* **37**, 1–64.

MAXIMENKO, N. A., BANG, B. & SASAKI, H. 2005 Observational evidence of alternating zonal jets in the world ocean. *Geophys. Res. Lett.* **32** (12).

MORIZE, C., BARS, M. LE, GAL, P. LE & TILGNER, A. 2010 Experimental Determination of Zonal Winds Driven by Tides. *Phys. Rev. Lett.* **104**, 214501.

MORRIS, S. W., BODENSCHATZ, E., CANNELL, D. S. & AHLERS, G. 1993 Spiral defect chaos in large aspect ratio Rayleigh–Bénard convection. *Phys. Rev. Lett.* **71**, 2026–2029.

MORTENSEN, M. 2018 Shenfun: High performance spectral Galerkin computing platform. *J. Open Source Softw.* **3**, 1071.

MULLARNEY, J. C., GRIFFITHS, R. W. & HUGHES, G. O. 2004 Convection driven by differential heating at a horizontal boundary. *J. Fluid Mech.* **516**, 181–209.

MUNK, W. H. 1966 Abyssal recipes. *Deep-Sea Res. Oceanogr. Abstr.* **13** (4), 707–730.

NADIGA, B. T. 2006 On zonal jets in oceans. *Geophys. Res. Lett.* **33** (10).

NG, C. S., OOI, A., LOHSE, D. & CHUNG, D. 2015 Vertical natural convection: application of the unifying theory of thermal convection. *J. Fluid Mech.* **764**, 0349–361.

NIEMELA, J. J., SKRBEK, L., SREENIVASAN, K. R. & DONNELY, R. J. 2000 Turbulent convection at very high Rayleigh numbers. *Nature* **404**, 837–841.

NIEMELA, J. J. & SREENIVASAN, K. R. 2008 Formation of the "superconducting" core in turbulent thermal convection. *Phys. Rev. Lett.* **100**, 184502.

OH, S. 2019 An Efficient Spectral Method to Solve Multi-Dimensional Linear Partial

Different Equations Using Chebyshev Polynomials. *Mathematics* **7**, 90.

ORSZAG, S. A. 1969 Numerical Methods for the Simulation of Turbulence. *Phys. Fluids* **12**, II–250–II–257.

PANDEY, A., SCHEEL, J. D. & SCHUMACHER, J. 2018 Turbulent superstructures in Rayleigh–Bénard convection. *Nat. Commun.* **9**, 2118.

PAPARELLA, F. & YOUNG, W. R. 2002 Horizonal convection is non-turbulent. *J. Fluid Mech.* **466**, 205–214.

PASSAGGIA, P.-Y., SCOTTI, A. & WHITE, B. 2017 Transition and turbulence in horizontal convection: linear stability analysis. *J. Fluid Mech.* **821**, 31–58.

PASSAGGIA, P.-Y., SCOTTI, A. & WHITE, B. 2018 Heat and momentum transport in turbulent horizontal convection at low Prandtl numbers, arXiv: 1805.11741.

PEDLOSKY, J. 1987 *Geophysical Fluid Dynamics*, 2nd edn. Springer, Berlin.

PETSCHEL, K., WILCZEK, M., BREUER, M., FRIEDRICH, R. & HANSEN, U. 2011 Statistical analysis of global wind dynamics in vigorous Rayleigh–Bénard convection. *Phys. Rev. E* **84**, 026309.

PIERCE, D. W. & RHINES, P. B. 1996 Convective building of a pycnocline: laboratory experiments. *J. Phys. Oceanogr.* **26**, 176–190.

PODVIN, B. & SERGENT, A. 2015 A large-scale investigation of wind reversal in a square Rayleigh–Bénard cell. *J. Fluid Mech.* **766**, 172–201.

PODVIN, B. & SERGENT, A. 2017 Precursor for wind reversal in a square Rayleigh–Bénard cell. *Phys. Rev. E* **95**, 013112.

VAN DER POEL, E. P., OSTILLA-MÓNICO, R., VERZICCO, R., GROSSMANN, S. & LOHSE, D. 2015 Logarithmic mean temperature profiles and their connection to plume emissions in turbulent Rayleigh-Bénard convection. *Phys. Rev. Lett.* **115**, 154501.

VAN DER POEL, E. P., STEVENS, R. J. A. M. & LOHSE, D. 2013 Comparison between two- and three-dimensional Rayleigh–Bénard convection. *J. Fluid Mech.* **736**, 177–194.

PUIGJANER, D., HERRERO, J., GIRALT, F. & SIMÓ, C. 2004 Stability analysis of the flow in a cubical cavity heated from below. *Phys. Fluids* **16**, 3639–3655.

PUIGJANER, D., HERRERO, J., SIMÓ, C. & GIRALT, F. 2008 Bifurcation analysis of steady Rayleigh–Bénard convection in a cubical cavity with conducting sidewalls. *J. Fluid Mech.* **598**, 393–427.

RAHMSTORF, S. 2003 Thermohaline circulation: The current climate. *Nature* **421**, 699–699.

RAI, M. M. & MOIN, P. 1991 Direct simulations of turbulent flow using finite-difference schemes. *J. Comput. Phys.* **96**, 15–53.

RAMME, L. & HANSEN, U. 2019 Transition to time-dependent flow in highly viscous horizontal convection. *Phys. Rev. Fluids* **4**, 093501.

VAN REEUWIJK, M., JONKER, H. & HANJALIĆ, K. 2008 Wind and boundary layers in Rayleigh–Bénard convection. II. Boundary layer character and scaling. *Phys. Rev. E* **77**, 036312.

REITER, P. 2020*a* https://github.com/preiter93/pylsa.

REITER, P. 2020*b* https://github.com/preiter93/pypde.

REITER, P. 2021 https://github.com/preiter93/rustpde.

REITER, P. & SHISHKINA, O. 2020 Classical and symmetrical horizontal convection:

detaching plumes and oscillations. *J. Fluid Mech.* **892**, R1.

REITER, P., SHISHKINA, O., LOHSE, D. & KRUG, D. 2021*a* Crossover of the relative heat transport contributions of plume ejecting and impacting zones in turbulent rayleigh-bénard convection (a). *Europhys. Lett.* **134**, 34002.

REITER, P., ZHANG, X. & SHISHKINA, O. 2021*b* Flow states and heat transport in Rayleigh–Bénard convection with different sidewall boundary conditions, arXiv: 2111.00971.

REITER, P., ZHANG, X., STEPANOV, R. & SHISHKINA, O. 2021*c* Generation of zonal flows in convective systems by travelling thermal waves. *J. Fluid Mech.* **913**, A13.

ROCHE, P. E. 2020 The ultimate state of convection: a unifying picture of very high Rayleigh numbers experiments. *New J. of Phys.* **22**, 073056.

ROCHE, P.-E., CASTAING, B., CHABAUD, B., HÉBRAL, B. & SOMMERIA, J. 2001 Side wall effects in Rayleigh–Bénard experiments. *Eur. Phys. J. B* **24**, 405–408.

ROSSBY, H. T. 1965 On thermal convection driven by non-uniform heating from below: an experimental study. *Deep Sea Res.* **12**, 9–16.

ROSSBY, T. 1998 Numerical experiments with fluid heated non-uniformly from below. *Tellus* **50A**, 242–257.

SAAD, Y. & SCHULTZ, M. H. 1986 GMRES: A Generalized Minimal Residual Algorithm for Solving Nonsymmetric Linear Systems. *SIAM J. Sci. Comput.* **7**, 856–869.

SALTZMAN, B. 1962 Finite Amplitude Free Convection as an Initial Value Problem—I. *J. Atmos. Sci.* **19** (4), 329–341.

SANDSTROM, J.W. 1908 Dynamische Versuche mit Meerwasser. *Ann. Hydrog. Mar. Meteorol.* **36**, 6.

SCHLÜTER, A., LORTZ, D. & BUSSE, F. 1965 On the stability of steady finite amplitude convection. *J. Fluid Mech.* **23**, 129–144.

SCHMALZL, J., BREUER, M. & HANSEN, U. 2004 On the validity of two-dimensional numerical approaches to time-dependend thermal convection. *Europhys. Lett.* **67**, 390–396.

SCHUBERT, G., TURCOTTE, D. L. & OLSON, P. 2001 *Mantle Convection in the Earth and Planets*. Cambridge University Press.

SCHUBERT, G. & WHITEHEAD, J. A. 1969 Moving flame experiment with liquid Mercury: Possible implications for the Venus atmosphere. *Science* **163**, 71–72.

SCHUMACHER, J. 2008 Lagrangian dispersion and heat transport in convective turbulence. *Phys. Rev. Lett.* **100**, 134502.

SCOTT, JEFFERY R, MAROTZKE, JOCHEM & ADCROFT, ALISTAIR 2001 Geothermal heating and its influence on the meridional overturning circulation. *Journal of Geophysical Research: Oceans* .

SCOTTI, A. & WHITE, B. 2011 Is horizontal convection really "non-turbulent?". *Geophys. Res. Lett.* **38**, L21609.

SHANG, X. D., QIU, X.-L., TONG, P. & XIA, K.-Q. 2003 Measured local heat transport in turbulent Rayleigh–Bénard convection. *Phys. Rev. Lett.* **90** (7), 074501.

SHANG, X. D., QIU, X.-L., TONG, P. & XIA, K.-Q. 2004 Measurements of the local convective heat flux in turbulent Rayleigh–Bénard convection. *Phys. Rev. E*

70, 026308.

Shang, X. D., Tong, P. & Xia, K.-Q. 2008 Scaling of the local convective heat flux in turbulent Rayleigh–Bénard convection. *Phys. Rev. Lett.* **100**, 244503.

Sheard, G. J. & King, M. P. 2011 Horizontal convection: Effect of aspect ratio on Rayleigh number scaling and stability. *Appl.Math. Model.* **35**, 1647.

Shen, J. 1995 Efficient Spectral-Galerkin Method II. Direct Solvers of Second- and Fourth-Order Equations Using Chebyshev Polynomials. *SIAM J. Sci. Comput.* **16**, 74–87.

Shen, J., Tang, T. & Wang, L. L. 2011 *Spectral Methods: Algorithms, Analysis and Applications*. Springer Berlin Heidelberg.

Shishkina, O. 2017 Mean flow structure in horizontal convection. *J. Fluid Mech.* **812**, 525–540.

Shishkina, O. 2021 Rayleigh–Bénard convection: The container shape matters. *Phys. Rev. Fluids* **6**, 090502.

Shishkina, O., Grossmann, S. & Lohse, D. 2016 Heat and momentum transport scalings in horizontal convection. *Geophys. Res. Lett.* **43**, 1219–1225.

Shishkina, O., Horn, S., Wagner, S. & Ching, E. S. C. 2015 Thermal boundary layer equation for turbulent Rayleigh–Bénard convection. *Phys. Rev. Lett.* **114**, 114302.

Shishkina, O., Stevens, R. J. A. M., Grossmann, S. & Lohse, D. 2010 Boundary layer structure in turbulent thermal convection and its consequences for the required numerical resolution. *New J. Phys.* **12**, 075022.

Shishkina, O. & Wagner, S. 2016 Prandtl-number dependence of heat transport in laminar horizontal convection. *Phys. Rev. Lett.* **116**, 024302.

Shishkina, O., Wagner, S. & Horn, S. 2014 Influence of the angle between the wind and the isothermal surfaces on the boundary layer structures in turbulent thermal convection. *Phys. Rev. E* **89**, 033014.

Shraiman, B. I. & Siggia, E. D. 1990 Heat transport in high-Rayleigh-number convection. *Phys. Rev. A* **42**, 3650–3653.

Shukla, P. K., Yu, M. Y., Rahman, H. U. & Spatschek, K. H. 1981 Excitation of convective cells by drift waves. *Phys. Rev. A* **23**, 321–324.

Siggia, E. 1994 High Rayleigh number convection. *Annu. Rev. Fluid Mech.* **26**, 137–168.

Sondak, D., Smith, L. M. & Waleffe, F. 2015 Optimal heat transport solutions for Rayleigh–Bénard convection. *J. Fluid Mech.* **784**, 565–595.

Spiegel, E. A. 1971 Convection in stars, I. Basic Boussinesq convection. *Annu. Rev. Astron. Astrophys.* **9**, 323–352.

Sreenivasan, K. R. & Donnelly, R. J. 2001 Role of cryogenic helium in classical fluid dynamics: Basic research and model testing. *Adv. Appl. Mech.* **37**, 239–276.

Stern, M. E. 1959 The moving flame experiment. *Tellus* **11**, 175–179.

Stern, M. E. 1960 The "Salt-Fountain" and Thermohaline Convection. *Tellus* **12**, 172–175.

Stern, M. E. 1971 Generalizations of the rotating flame effect. *Tellus* **23**, 122–128.

Stevens, R., Lohse, D. & Verzicco, R. 2014 Sidewall effects in Rayleigh–Bénard convection. *J. Fluid Mech.* **741**, 1–27.

Stevens, R. J. A. M., Blass, A., Zhu, X., Verzicco, R. & Lohse, D. 2018

Turbulent thermal superstructures in Rayleigh–Bénard convection. *Phys. Rev. Fluids* **3**, 041501.

STEVENS, R. J. A. M., LOHSE, D. & VERZICCO, R. 2011 Prandtl and Rayleigh number dependence of heat transport in high Rayleigh number thermal convection. *J. Fluid Mech.* **688**, 31–43.

STEVENS, R. J. A. M., LOHSE, D. & VERZICCO, R. 2020 Toward DNS of the Ultimate Regime of Rayleigh–Bénard Convection. In *Direct and Large Eddy Simulation XII* (ed. M. García-Villalba et al.), pp. 215–224. Springer International Publishing.

STEVENS, R. J. A. M., VAN DER POEL, E. P., GROSSMANN, S. & LOHSE, D. 2013 The unifying theory of scaling in thermal convection: The updated prefactors. *J. Fluid Mech.* **730**, 295–308.

STOMMEL, H. 1962 On the smallness of sinking regions in the ocean. *Proc. Natl. Acad. Sci.* **48**, 766–772.

SUGIYAMA, K., NI, R., STEVENS, R. J. A. M., CHAN, T. S., ZHOU, S.-Q., XI, H.-D., SUN, C., GROSSMANN, S., XIA, K.-Q. & LOHSE, D. 2010 Flow reversals in thermally driven turbulence. *Phys. Rev. Lett.* **105**, 034503.

SUKHANOVSKY, A., FRICK, P., TEYMURAZOV, A. & BATALOV, V. 2012 Horizontal rolls in convective flow above a partially heated surface. *Eur. Phys. J. B* **85**, 9.

TEXTOR, C., GRAF, H. F., HERZOG, M., OBERHUBER, J. M., ROSE, W. I. & ERNST, G. G. J. 2006 Volcanic particle aggregation in explosive eruption columns. Part I: Parameterization of the microphysics of hydrometeors and ash. *J. Volcanol. Geotherm. Res.* **150**, 359–377.

THOMPSON, R. 1970 Venus general circulation is a merry-go-round. *J. Atmos. Sci.* **27**, 1107–1116.

THOMSON, J. 1892 On the Grand Currents of Atmospheric Circulation. *Trans. Roy. Soc. London* **183**, 653–684.

TILGNER, A. 2007 Zonal Wind Driven by Inertial Modes. *Phys. Rev. Lett.* **99**, 194501.

TILGNER, A. 2019 Time evolution equation for advective heat transport as a constraint for optimal bounds in Rayleigh–Bénard convection. *Phys. Rev. Fluids* **4**, 014601.

TILGNER, A., BELMONTE, A. & LIBCHABER, A. 1993 Temperature and velocity profiles of turbulent convection in water. *Phys. Rev. E* **47**, 2253–2257.

TILGNER, A. & BUSSE, F. H. 1997 Finite-amplitude convection in rotating spherical fluid shells. *J. Fluid Mech.* **332**, 359–376.

TREFETHEN, L. N. 2000 *Spectral Methods in MATLAB*. SIAM.

TSAI, T., HUSSAM, W. K., FOURAS, A. & SHEARD, G. J. 2016 The origin of instability in enclosed horizontally driven convection. *Int. J. Heat Mass Transfer* **94**, 509–515.

TSAI, T., HUSSAM, W. K., KING, M. P. & SHEARD, G. J. 2020 Transitions and scaling in horizontal convection driven by different temperature profiles. *Int. J. Therm. Sci.* **148**, 106166.

UHLMANN, M. 2004 Linear stability analysis of flow in an internally heated rectangular duct.

UHLMANN, M. & NAGATA, M. 2006 Linear stability of flow in an internally heated rectangular duct. *J. Fluid Mech.* **551**, 387–404.

Bibliography

Urban, P., Hanzelka, P., Musilova, V., Kralik, T., Mantia, M. L., Srnka, A. & Skrbek, L. 2014 Heat transfer in cryogenic helium gas by turbulent Rayleigh–Bénard convection in a cylindrical cell of aspect ratio 1. *New J. Phys.* **16**, 053042.

Venezian, G. 1969 Effect of modulation on the onset of thermal convection. *J. Fluid Mech.* **35**, 243–254.

Venturi, D., Wan, X. & Karniadakis, G. 2010 Stochastic bifurcation analysis of Rayleigh–Bénard convection. *J. Fluid Mech.* **650**, 391–413.

Verzicco, R. 2002 Sidewall finite-conductivity effects in confined turbulent thermal convection. *J. Fluid Mech.* **473**, 201–210.

Verzicco, R. & Orlandi, P. 1996 A finite-difference scheme for three-dimensional incompressible flow in cylindrical coordinates. *J. Comput. Phys.* **123**, 402–413.

Wagner, S. & Shishkina, O. 2013 Aspect ratio dependency of Rayleigh–Bénard convection in box-shaped containers. *Phys. Fluids* **25**, 085110.

Wagner, S., Shishkina, O. & Wagner, C. 2012 Boundary layers and wind in cylindrical Rayleigh–Bénard cells. *J. Fluid Mech.* **697**, 336–366.

Waleffe, F., Boonkasame, A. & Smith, L. M. 2015 Heat transport by coherent Rayleigh–Bénard convection. *Phys. Fluids* **27**, 051702.

Wan, Z., Wei, P., Verzicco, R., Lohse, D., Ahlers, G. & Stevens, R. 2019 Effect of sidewall on heat transfer and flow structure in Rayleigh-–Bénard convection. *J. Fluid Mech.* **881**, 218—243.

Wang, B. F., Ma, D. J., Chen, C. & Sun, D. J. 2012 Linear stability analysis of cylindrical Rayleigh–Bénard convection. *J. Fluid Mech.* **711**, 27–39.

Wang, Q., Chong, K. L., Stevens, R. & Lohse, D. 2020*a* From zonal flow to convection rolls in Rayleigh–Bénard convection with free-slip plates. *J. Fluid Mech.* **905**, A21.

Wang, Q., Reiter, P., Lohse, D. & Shishkina, O. 2021 Universal properties of penetrative turbulent Rayleigh–Bénard convection. *Phys. Rev. Fluids* **6**, 063502.

Wang, Q., Verzicco, R., Lohse, D. & Shishkina, O. 2020*b* Multiple states in turbulent large-aspect-ratio thermal convection: What determines the number of convection rolls? *Phys. Rev. Lett.* **125**, 074501.

Wang, W. & Huang, R. X. 2005 An experimental study on thermal circulation driven by horizontal differential heating. *J. Fluid Mech.* **540**, 49–73.

Wang, Y., Baboulin, M., Dongarra, J., Falcou, J., Fraigneau, Y. & Le Maître, O. 2013 A parallel solver for incompressible fluid flows. *Procedia Comput. Sci.* **18**, 439–448.

Wei, P. 2021 The persistence of large-scale circulation in Rayleigh–Bénard convection. *J. Fluid Mech.* **924**, A28.

Wen, B., Chini, G. P., Kerswell, R. R. & Doering, C. R. 2015 Time-stepping approach for solving upper-bound problems: Application to two-dimensional Rayleigh–Bénard convection. *Phys. Rev. E* **92**, 043012.

Wen, B., Goluskin, D. & Doering, C. R. 2020*a* Steady Rayleigh–Bénard convection between no-slip boundaries, arXiv: 2008.08752.

Wen, B., Goluskin, D., LeDuc, M., Chini, G. P. & Doering, C. R. 2020*b* Steady Rayleigh-–Bénard convection between stress-free boundaries. *J. Fluid Mech.* **905**, R4.

122

WHITEHEAD, J. A. 1972 Observations of rapid mean flow produced in mercury by a moving heater. *Geophys. Fluid Dyn.* **3**, 161–180.

WHITEHEAD, J. A. 1975 Mean flow generated by circulation on a beta-plane: An analogy with the moving flame experiment. *Tellus* **27**, 358–364.

WHITEHEAD, J. P. & DOERING, C. R. 2011 Ultimate state of two-dimensional Rayleigh–Bénard convection between free-slip fixed-temperature boundaries. *Phys. Rev. Lett.* **106**, 244501.

WINCHESTER, P., DALLAS, V. & HOWELL, P. D. 2021 Zonal flow reversals in two-dimensional Rayleigh-Bénard convection. *Phys. Rev. Fluids* **6**, 033502.

WU, X. & MOIN, P. 2010 Transitional and turbulent boundary layer with heat transfer. *Phys. Fluids* **22**, 085105.

WUNSCH, C. 2000 Moon, tides and climate. *Nature* **405**, 743–744.

XI, H.-D. & XIA, K.-Q. 2007 Cessations and reversals of the large-scale circulation in turbulent thermal convection. *Phys. Rev. E* **75**, 066307.

YANG, R., CHONG, K. L., WANG, Q., VERZICCO, R., SHISHKINA, O. & LOHSE, D. 2020*a* Periodically Modulated Thermal Convection. *Phys. Rev. Lett.* **125**, 154502.

YANG, R., ZHANG, X., REITER, P., LINKMANN, M., LOHSE, D. & SHISHKINA, O. 2020*b* Data-driven identification of the spatio-temporal structure of turbulent flows by streaming Dynamic Mode Decomposition, arXiv: 2006.05552.

YANO, J., TALAGRAND, O. & DROSSART, P. 2003 Origins of atmospheric zonal winds. *Nature* **36**.

YOUNG, R. E., SCHUBERT, G. & TORRANCE, K. E. 1972 Nonlinear motions induced by moving thermal waves. *J. Fluid Mech.* **54**, 163–187.

ZHANG, X., VAN GILS, D. P. M., HORN, S., WEDI, M., ZWIRNER, L., AHLERS, G., ECKE, R. E., WEISS, S., BODENSCHATZ, E. & SHISHKINA, O. 2020 Boundary zonal flow in rotating turbulent Rayleigh–Bénard convection. *Phys. Rev. Lett.* **124**, 084505.

ZHAO, J., CAI, W. & JIANG, Y. 2019 Study on corner vortex enlarging process of 2D square Rayleigh–Bénard cells filled with air in transient states. *Int. J. Heat Mass Transfer* **129**, 599–609.

ZHOU, W.-F. & CHEN, J. 2018 Letter: Similarity model for corner roll in turbulent Rayleigh–Bénard convection. *Phys. Fluids* **30**, 111705.

ZHU, X., MATHAI, V., STEVENS, R., VERZICCO, R. & LOHSE, D. 2018*a* Transition to the ultimate regime in two-dimensional Rayleigh–Bénard convection. *Phys. Rev. Lett.* **120**, 144502.

ZHU, X., MATHAI, V., STEVENS, R., VERZICCO, R. & LOHSE, D. 2019*a* Reply. *Phys. Rev. Lett.* **123**, 259402.

ZHU, X., PHILLIPS, E., SPANDAN, V., DONNERS, J., RUETSCH, G., ROMERO, J., OSTILLA-MÓNICO, R., YANG, Y., LOHSE, D., VERZICCO, R., FATICA, M. & STEVENS, R. J. A. M. 2018*b* AFiD-GPU: a versatile Navier–Stokes solver for wall-bounded turbulent flows on GPU clusters. *Comp. Phys. Commun.* **229**, 199–210.

ZHU, X., STEVENS, R. J. A. M., SHISHKINA, O., VERZICCO, R. & LOHSE, D. 2019*b* $Nu \sim Ra^{1/2}$ scaling enabled by multiscale wall roughness in Rayleigh–Bénard turbulence. *J. Fluid Mech.* **869**, R4.

ZIENICKE, E., SEEHAFER, N. & FEUDEL, F. 1998 Bifurcations in two-dimensional

Rayleigh–Bénard convection. *Phys. Rev. E* **57**, 428–435.

ZWIRNER, L., KHALILOV, R., KOLESNICHENKO, I., MAMYKIN, A., MANDRYKIN, S., PAVLINOV, A., SHESTAKOV, A., TEIMURAZOV, A., FRICK, P. & SHISHKINA, O. 2020 The influence of the cell inclination on the heat transport and large-scale circulation in liquid metal convection. *J. Fluid Mech.* **884**, A18.